CHEMIRESISTIVE DETECTION OF METAL CATIONS IN WATER

CHEMIRESISTIVE DETECTION OF METAL CATIONS IN WATER

By JOHNSON DALMIEDA, B.Sc.

A thesis submitted to the School of Graduate Studies in partial fulfillment of the requirements for the degree of Master of Science in Chemistry

McMaster University

McMaster University

MASTER OF SCIENCE (2020)

Hamilton, Ontario (Chemistry and Chemical Biology)

TITLE: Chemiresistive Detection of Metal Cations in Water

AUTHOR: Johnson Dalmieda, B.Sc. (McMaster University)

SUPERVISOR: Dr. Peter Kruse

NUMBER OF PAGES: XV, 159

ABSTRACT

Metal cations serve an important physiological purpose in humans, and one of the most abundant sources of these cations is water. Many cations beneficial to human life are found in water. However, many cations that are deemed detrimental to health may also be present in these water sources. Currently, many methods exist to detect, quantify, and monitor metal cations in water ranging from simple visual tests to more elaborate lab-based methods. The method of metal cation detection employed in this thesis relies on the use of chemiresistive sensors. These sensors monitor the changes in the transductive portion of the sensor, which can be observed through the changes in the current resistance of the sensor. One example of a transducing film is graphene, which is known for its high conductivity. Herein, chemiresistive sensors based on a few layer graphene transducing film have been employed for the detection of metal cations, namely copper, silver, lead, and mercury. The films were functionalized with molecules specific to each cation to ensure selectivity. Charge transfer between the metal-molecule complex and the few layer graphene film drives the sensing mechanism. An investigation was also made into the efficient selection of sensor molecules to be used for functionalization by observing four different phenanthroline derivatives. This was done to allow for a smarter way to select sensor molecules. The work presented in this thesis suggests that the detection of metal cations using these few layer graphene based chemiresistive sensors is a viable pathway towards cheap online water quality monitoring.

ACKNOWLEDGEMENTS

I would first like to thank my supervisor Dr. Peter Kruse for allowing me to work in his research group. His mentorship and knowledge have proven invaluable to me during my tenure as a graduate student and for that, I am grateful.

I would also like to thank Dr. P. Ravi Selvaganapathy for his guidance during my time as a graduate student. His insight has allowed me to see the impact of my research through a broader lens. I would also like to thank Dr. David Emslie and Dr. Randall Dumont for their valuable advice throughout these years

I would like to thank my colleagues in the Kruse research group, both past and present, for being there for me and helping me out with my experiments during these two years. Special thanks go out to Ana Zubiarrain Laserna and Dipankar Saha for helping me get started in the lab, as well as Maryam Darestani-Farahani, Mae Masters, Arjun Rego, and Devanjith Ganepola for their contributions to this thesis. I would also like to thank Jonah Halili for helping me get prepared for my graduate research by lending me his undergraduate thesis and providing his input during my time in the Kruse group (the Timbits didn't hurt either).

Although I am unsure of where I will go next, I know that everything I have learned here will lead me toward a bright future.

BLACK LIVES MATTER

TABLE OF CONTENTS

LIST OF FIGURES

LIST OF TABLES

LIST OF EQUATIONS

LIST OF ABBREVIATIONS AND SYMBOLS

ASV	Anodic Stripping Voltammetry
B3LYP	Becke 3-parameter Lee Yang Parr
bcp	Bathocuproine
bphen	Bathophenanthroline
DAP	2,3-diaminophenazine
DAQ	1,2-diaminoanthraquinone
DFT	Density Functional Theory
DMSO	Dimethylsulfoxide
ECP	Effective Core Potential
EtOH	Ethanol
FAAS	Flame Atomic Absorption Spectroscopy
FLG	Few Layer Graphene
FTIR	Fourier Transform Infrared
GGA	Generalized Gradient Approximation
HEG	Homogeneous Electron Gas
HOMO	Highest Occupied Molecular Orbital
ICP-MS	Inductively Coupled Plasma-Mass Spectrometry

ISE	Ion Selective Electrode
L(S)DA	Local (Spin) Density Approximation
LANL2DZ	Los Alamos National Laboratory 2-double Zeta
LMCT	Ligand Metal Charge Transfer
LUMO	Lowest Unoccupied Molecular Orbital
MeCN	Acetonitrile
MeOH	Methanol
MLCT	Metal Ligand Charge Transfer
ncp	Neocuproine
PDE	Partial Differential Equation
PDMS	Polydimethylsiloxane
PGR	Pyrogallol Red
phen	Phenanthroline
ppb	Parts per billion (μg/L)
ppm	Parts per million (mg/L)
SAM	Self Assembled Monolayer
XPS	X-Ray Photoelectron Spectroscopy

DECLARATION OF ACADEMIC ACHIEVEMENT

In CHAPTER 2, research aggregation and text editing was done by the author. Peter Kruse contributed to the editing of the text. In CHAPTER 5, Ana Zubiarrain Laserna provided the *Sensor Fabrication* section. Devanjith Ganepola provided the nitrate data used in Figure 7b. Peter Kruse and Ravi Selvaganapathy contributed to the editing of the overall text and the discussion of ideas and concepts. XPS was performed by Mark Biesinger of Surface Science Western. ICP-MS and ion chromatography was performed by Activation Laboratories Ancaster. All other work was performed by the author. In CHAPTER 6, Mae Masters provided some replicate data for Receptor 1. All other data and experimentation was done by the author. In CHAPTER 7, Maryam Darestani-Farahani provided the UV/vis data. All other data and experimentation was done by the author.

1 - INTRODUCTION

Cations in water are an important parameter for the insurance of water quality. Aqueous metal cations can have many effects, positive and negative, on human physiology, aquatic life, and the overall ecosystem. In CHAPTER 2, *Metal Cation Detection in Drinking Water*, the importance of water quality detection and various parameters and methods are discussed in finer detail.

1.1 - Approach for Cation Detection

Many methods currently exist for the detection of cations that range from simple colorimetric assays to more elaborate spectrometric methods meant for ultra-trace (sub-ppb) detection.[5] Although these methods are sufficient for the detection of many cations, there are several drawbacks that need to be addressed. Colorimetric methods, although cheap and portable, do not allow for ultra-trace detection of cations, and may also suffer from matrix effects which affect the colorimetric response. Many electrochemical methods, such as ion-selective electrodes (ISE) and anodic stripping voltammetry (ASV) require counter electrodes which will need to be calibrated and maintained, not to mention their fragility. Government standard methods such as inductively coupled plasma mass spectrometry (ICP-MS) and flame atomic absorption spectroscopy (FAAS) allow for ultra-trace detection of cations, but are rather expensive and due to the size of the instrumentation experiments will need to be performed *ex situ*.

Here we utilize chemiresistive sensors because they allow for sensitive, portable and cost effective designs.[6] Chemiresistive sensors are relatively cheap to produce, do not require any sample preparation or reference electrodes, and can provide sufficient sensitivity for the

detection of cations in water. The transducing element of the sensor can be functionalized to tune sensor selectivity towards different cations. The method of functionalization used here is ligand adsorption (non-covalent physisorption in this case, rather than chemisorption which is more indicative of covalent interaction). In this method, the sensors are dipped into a ligand solution for a set amount of time. This allows for a self-assembled monolayer (SAM) to form on the surface.[7] Coordination of the metal cations to these ligands can be detected by the chemiresistive sensor, which will allow for the quantification of the selected metal cation.

1.1.1 - Coordination Complexes

When a metal atom or ion receives electrons from a neutral or negatively charged compound (known as a ligand), it forms what is called a coordination complex. The atom in the ligand that is bonded to the metal is known as the donor atom. Multiple donor atoms within a ligand can be bonded to the metal ion or atom and form what is called a chelation complex, which has a certain denticity. Denticity occurs when two or more donor atoms in a ligand bond to the metal.[8] In the following example, 2,3-diaminophenazine (a well known copper chelating ligand) is shown bonding to copper (II) chloride (Figure 1).[9]

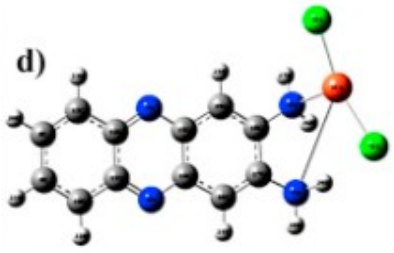

Figure 1. 2,3-diaminophenazine binding to copper (II) chloride.[1]

The two amine groups in the 2 and 3 position on the phenazine backbone bond to the copper (II) chloride metal centre, which indicates that the two nitrogen atoms in the amines

are the donor atoms, each donating a lone pair to form a bond with the copper. Since copper is bound to two atoms on the 2,3-diaminophenazine, this would be a bidentate chelation complex. Since there are two donor atoms from the 2,3-diaminophenazine attached to copper, as well as two chlorides, the coordination number of the complex would be four.

One characteristic of coordination complexes is their coloured appearance after complexing. This is due to the change in electronic configuration of the ligand alone versus the ligand-metal complex, which occurs through charge transfer. In charge transfer, electrons from a filled orbital in the ligand can move to a higher empty orbital in the metal (ligand-to-metal charge transfer [LMCT]) or vice versa (metal-to-ligand charge transfer [MLCT]), which is more common for d^0 and d^{10} configuration metals. Another transition that can occur is d-d transitions, in which an electron in a metal d orbital is excited to a higher energy d orbital by photons (common in d^1-d^9 configuration metals). The colour changes can be quantified using a UV/vis spectroscopy.[10] Using the example above, the colour change of the ligand once complexation occurs can be seen through its UV/vis spectra (Figure 2).

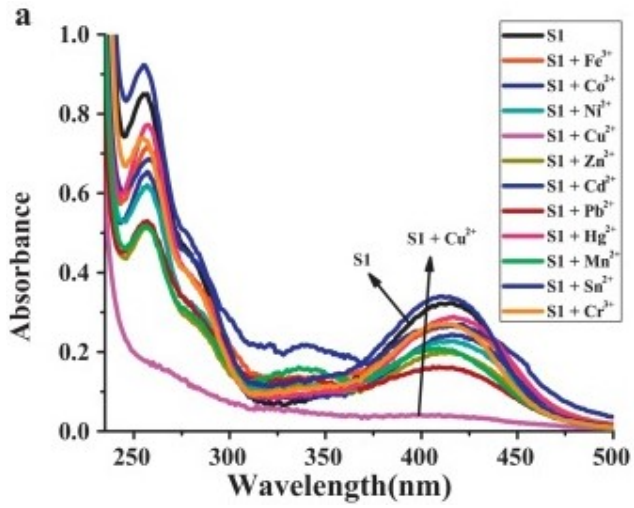

Figure 2. UV/vis spectra of 2,3-diaminophenazine with copper and various other metal ions.[1]

The ligand alone can be seen having a peak at ~400 nm in the visible range. Once copper chelates to the ligand, however, the complex causes the ligand to undergo a

bathochromic shift, which could be due to the fact that the transition between the ligand and the metal is lower energy than the shift within the ligand itself.

1.1.2 - Phenanthrolines

One class of ligands that can aid in the detection of cations is phenanthrolines, which are derivatives of the phenanthroline molecule. Phenanthroline itself is a heterocyclic aromatic hydrocarbon commonly used as a ligand in organometallic chemistry due to its high binding constant with many metals.[11] Its aromaticity makes it very susceptible to adsorption onto a chemiresistive film; however its selectivity is brought into question due to its preference to bind to many different cations. Due to this, the effects of substituents on the phenanthroline molecule must be investigated (Figure 3).

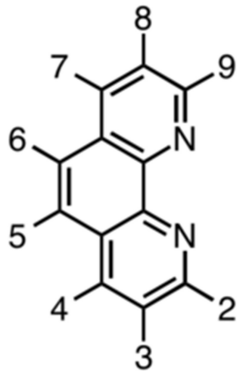

Figure 3. Numbering for 1,10-phenanthroline derivatives. Reprinted with permission under the Creative Commons Attribution-Share Alike 3.0 Unported license.

Many phenanthroline derivatives exist, such as 2,9-dimethyl-1,10-phenanthroline (neocuproine), 4,7-diphenyl-1,10-phenanthroline (bathophenanthroline), 2,9-dimethyl-4,7-diphenyl-1,10-phenanthroline (bathocuproine), and many more. These substituents will have an effect on the charge transfer that occurs between the metal and the ligand. Substituents in the 2,9-positions, such as methyl groups, will hinder charge transfer even if they are electron donating due to sterics (they will hinder the approach of the metal cation).[12] Based on binding

preference, a combination of substituents in the 4,7- positions and the 2,9-positions can be used to finely tune the ligand binding preference to a selected metal. This would be based on properties such as the size of the metal centre, and the coordination number of the metal centre (less substituted phenanthrolines will form tri-complexes whereas more substituted phenanthrolines will form mono-complexes).[13] This would allow for the fabrication of multiple sensors based on the phenanthroline backbone alone.

1.2 - Chemiresistivity

Chemiresistivity is the phenomenon that occurs when a change in the nearby environment causes a change in resistance of a conductive material. This change in resistance can be measured by two contacts at either end measuring the current passing through the material at a given voltage.[14] The basic components of a chemiresistor are a conducting material, two contacts at either end to facilitate conduction, and an electrical readout which displays changes in the resistance of the conducting material.[15] The property of changing resistance can be utilized to detect concentrations of different analytes by correlating the changes in resistance to the concentration or pressure of a target species. Various interactions can lead to a change in resistance, such as adsorption, molecular binding, and changes with regards to the material itself.[6] The first time a chemiresistivity was utilized for sensing was in 1985 when Wohltjen et. al. developed a vapour-sensitive Langmuir-Blodgett film to detect ammonia in air at sub-ppm levels. This was done by using a copper phthalocyanine film, which is selective to ammonia. Exposure to ammonia induces a change in the current which can be plotted against the concentration.[16] More recently, chemiresistors with functionalizable sensor films have been developed (Figure 4).

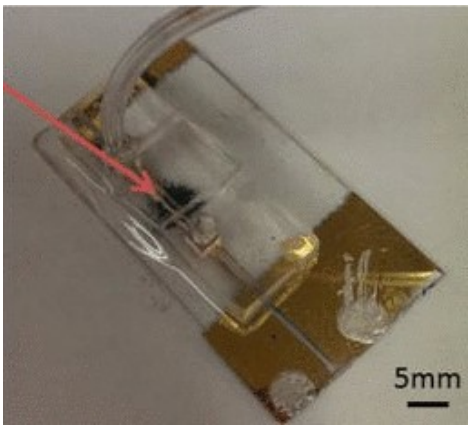

Figure 4. A chemiresistive sensor with a nanotube film and a microfluidic channel for liquid to flow through.[2]

One such example is a free chlorine sensor developed by Kruse et. al. which utilizes carbon nanotubes as a conductive film. The carbon nanotubes themselves detect free chlorine, however they are not selective to chlorine, and interfering molecules will affect the signal. By adsorbing phenyl-capped aniline tetramer onto the nanotube film, the response size and selectivity of the film to free chlorine was improved.[2]

1.2.1 - Graphene

For the functioning of a chemiresistive sensor, an appropriate conducting film is required. One film that has the appropriate conductivity and adsorptive properties required for a chemiresistive film is graphene multilayers. Graphene is an allotrope of carbon in which the carbon is arranged in a 2-dimensional hexagonal lattice. When a sufficient number of layers are stacked on top of each other (at least 10), they form a new allotrope of carbon known as graphite.[17] The individual graphene layers are arranged in a hexagonal lattice with C-C distances of 1.42 Å within each layer, and an interplanar distance of 3.35 Å.[18] Due to the sp^2 hybridization of the graphene layers, the electrons are highly delocalized, making

graphene a very conductive material. This is what allows graphene to be used as an electrode material.[19]

Graphene can be cast onto a two-dimensional surface through exfoliation. The process of exfoliation involves suspending a two dimensional layered material in a specific solvent such that the layers do not recombine.[20] When sonicating graphite powder into a water-alcohol mixture, the alcohol molecules will aggregate in water, forming micelles.[21] These micelles will separate the individual layers, keeping them in suspension as long as they are separated at a distance larger than the critical distance (beyond which the Leonard-Jones potential will no longer cause the layers to move together, creating an aggregate of the layered material) (Figure 5).[22]

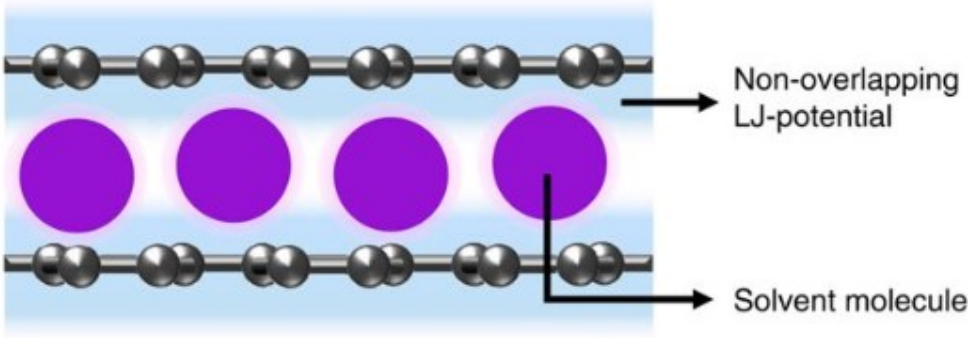

Figure 5. Visualization of the solvent molecules separating the graphene layers in solution.[3]

Using the exfoliated graphite, one can create a two dimensional graphene multilayer with more control over the sheet resistance and thickness by drop casting the suspension onto a heated substrate.[3]

1.3 - Structure of the Thesis

In this chapter, existing methods of detection for the metal cations are discussed. The approach considered in this thesis for the detection of cations is a chemiresistive platform with a tunable few-layer graphene (FLG) conductive film to adjust selectivity toward various cations. Tuning is done by modifying the ligand adsorbed onto the surface of the FLG film. In CHAPTER 2 a published review article, *Metal Cation Detection in Drinking Water*, introduced and elaborated upon the importance of the detection of metal cations in water. In CHAPTER 3 details pertaining to experimental techniques (particularly density functional theory (DFT), UV/vis spectroscopy, and x-ray photoelectron spectroscopy (XPS)) will be discussed. Sensor fabrication and data acquisition will also be elaborated upon. In CHAPTER 4, the results of a copper selective sensor will be discussed. The development of this copper sensor builds on Ana Zubiarrain Laserna's undergraduate and graduate research, which was performed from 2016-2019. My contributions include DFT calculations, UV/vis spectroscopy, sensor data, calibration curves, sensor resetting, and ligand deposition optimization. CHAPTER 5 is a submitted full paper, *Chemiresistive Detection of Silver Ions in Aqueous Media*, which introduces the use of bathocuproine-functionalized FLG chemiresistive devices for the detection of silver ions in water. UV/vis spectroscopy, XPS, and sensor data (pH/conductivity, calibration curves, resetting, ligand deposition optimization) are discussed. In CHAPTER 6, an attempt to fabricate a lead sensor was made in collaboration with Mae Masters, an undergraduate thesis student in the 2019-2020 academic year. The development of this sensor builds on Jonah Halili's undergraduate thesis work, which was performed in the 2017-2018 academic year. Three lead ligands (one commercial, two synthesized) were tested on the FLG chemiresistive sensor platform. Along with sensor data acquisition and analysis, DFT calculations and UV/vis spectroscopy was also performed for the three ligands. CHAPTER 7 introduces an initial attempt at a

chemiresistive mercury sensor, done in collaboration with Maryam Darestani-Farahani, a PhD student in the Kruse research group. Once again, UV/vis spectroscopy, and sensor data are discussed. In CHAPTER 8, a systematic approach towards cation sensor development is elaborated upon. Four different phenanthroline derivatives are investigated for their potential as ligands to be used on a chemiresistive sensor platform. UV/vis and sensor screening tests are performed and discussed, as well as DFT calculations, calibration curves, and the pH/conductivity response of each ligand. Finally, in CHAPTER 9, the findings of this thesis are summarized, and future work is outlined.

2 - METAL CATION DETECTION IN DRINKING WATER

sensors

MDPI

Review

Metal Cation Detection in Drinking Water

Johnson Dalmieda [1] and Peter Kruse [1,*]

Department of Chemistry and Chemical Biology, McMaster University, Hamilton L8S 4M1, ON Canada
* Correspondence: pkruse@mcmaster.ca

Received: date18 October 2019; Accepted: date21 November 2019; Published: date23 November 2019

Abstract: Maintaining a clean water supply is of utmost importance for human civilization. Human activities are putting an increasing strain on Earth's freshwater reserves and on the quality of available water on Earth. To ensure cleanliness and potability of water, sensors are required to monitor various water quality parameters in surface, ground, drinking, process, and waste water. One set of parameters with high importance is the presence of cations. Some cations can play a beneficial role in human biology, and others have detrimental effects. In this review, various lab-based and field-based methods of cation detection are discussed, and the uses of these methods for the monitoring of water are investigated for their selectivity and sensitivity. The cations chosen were barium, cadmium, chromium, copper, hardness (calcium, magnesium), lead, mercury, nickel, silver, uranium, and zinc. The methods investigated range from optical (absorbance/fluorescence) to electrical (potentiometry, voltammetry, chemiresistivity), mechanical (quartz crystal microbalance), and spectrometric (mass spectrometry). Emphasis is placed on recent developments in mobile sensing technologies, including for integration into microfluidics.

Keywords: water quality; chemical sensors; cations; heavy metals; lead; mercury

1. Introduction

Water is an important part of human physiology. It is not only necessary for various bodily functions; it has various uses from agriculture to cleaning, food processing, chemical processes, and many more. The human body consists of 50% to 70% of water, and water intake is necessary for adequate kidney health. To maintain proper hydration, humans need at least one liter of water a day [1]. Water is also necessary for irrigation, and up to 42% of water in the United States is used for that purpose [2]. Together with soap, water is used to maintain personal hygiene and general cleanliness. Water is used for various cooking methods such as boiling or simmering (in its liquid state) or steaming (in its gaseous state as steam) [3]. In the chemical industry, water is used as a common solvent for aqueous soluble reagents due to its ability to dissolve many ionic species. Water vapor can also be used in some processes, such as the production of acrylic acid [4]. Since water is used in so many different ways around the world, it is important to maintain water to a safe standard for consumption and for use in the fields where it is required. Many countries and international agencies have guidelines for various parameters to maintain. In this review, the importance of cation maintenance and detection is discussed. Maximum allowable concentration (MAC) guideline values are listed in Table 1 for various jurisdictions.

Table 1. Guidelines for water quality and standard detection methods.

	Canada [1]	US [2]	Europe [3]	WHO [4]	Standard Method *
pH	7.0–10.5	6.5–8.5	6.5–9.5	-	
Barium	1 ppm	2 ppm	-	1.3 ppm	ICP-MS[a] (200.8, 7440-39-3) ICP-AES[b] (200.7, 7440-39-3) FAAS[c] (7000B, 7440-39-3)
Cadmium	5 ppb	5 ppb	5 ppb	3 ppb	ICP-MS (200.8, 7440-43-9) ICP-AES (200.7, 7440-43-9) FAAS (7000B, 7440-43-9)
Chromium	50 ppb	100 ppb	50 ppb	50 ppb	ICP-MS (200.8, 7440-47-3) ICP-AES (200.7, 7440-47-3) FAAS (7000B, 7440-47-3)
Copper	2 ppm	1.3 ppm	2 ppm	2 ppm	ICP-MS (200.8, 7440-50-8) ICP-AES (200.7, 7440-50-8) FAAS (7000B, 7440-50-8)
Hardness	-	-	-	-	ICP-AES (200.7, 7440-70-2 (Ca), 7439-95-4 (Mg)) FAAS (7000B, 7440-70-2 (Ca), 7439-95-4 (Mg))
Lead	5 ppb ALARA	15 ppb ALARA	10 ppb	10 ppb	ICP-MS (200.8, 7439-92-1) ICP-AES (200.7, 7439-92-1) FAAS (7000B, 7439-92-1)
Mercury	1 ppb	2 ppb	1 ppb	6 ppb	ICP-MS (200.8, 7439-97-6) ICP-AES (200.7, 7439-97-6)
Nickel	-	-	20 ppb	70 ppb	ICP-MS (200.8, 7440-02-0) ICP-AES (200.7, 7440-02-0) FAAS (7000B, 7440-02-0)
Silver	-	-	-	100 ppb REC	ICP-MS (200.8, 7440-22-4) ICP-AES (200.7, 7440-22-4) FAAS (7000B, 7440-22-4)
Uranium	20 ppb	30 ppb	-	30 ppb	ICP-MS (200.8, 7440-61-1)
Zinc	5 ppm	-	-	-	ICP-MS (200.8, 7440-66-6) ICP-AES (200.7, 7440-66-6) FAAS (7000B, 7440-66-6)

[1] Health Canada: Guidelines for Canadian Drinking Water Quality. 2018. [2] United States Environmental Protection Agency (EPA): National Primary Drinking Water Regulations. 2018. [3] European Union: European Drinking Water Directive. 2019. [4] World Health Organization: Guidelines for Drinking Water Quality. 2017.

* Listed are the EPA methods in this format: [method] ([method number], [CASRN]). [a]Inductively coupled plasma mass spectrometry. [b] Inductively coupled plasma absorption emission spectroscopy. [c]Flame atomic absorption spectroscopy.

ALARA = as low as reasonably achievable; REC = recommended

Cations in water serve an important physiological purpose in humans. Elements such as copper, iron, calcium, magnesium, and many more contribute to various biological processes such as oxygen transport, enzymatic catalysis, DNA synthesis, and cell maturation. Many of these elements are provided through food intake; however, for areas in which meat consumption is low, the most abundant source of these elements is water [5]. Conversely, many other elements such as silver, lead, mercury, and cadmium can have detrimental effects on humans, such as nerve damage, growth defects, and even death.

There are many different methods used to determine the concentration of cations present in water. These methods can be divided into four categories: mechanical, optical, electrochemical, and spectroscopic/spectrometric. Mechanical methods use the mass or physical change an analyte induces to generate a signal that can correlate to the concentration. This can be done by using a piezoelectric material or through swelling of a film [6]. This allows for a very simple set-up in terms of portability and signal output but may not be very selective to the target analyte. Optical methods rely on the visual change in the properties of the sensor, whether it is a change in color, induced fluorescence of a non-fluorescent material, or quenching of fluorescence of a naturally fluorescing material. Almost all chemosensors follow the same formula in their molecular design: a receptor specific to the analyte, and a portion that generates a colorimetric signal [7]. This method is quick and selective and can be performed in situ. However, it lacks the sensitivity of more elaborate techniques. Electrochemical sensors induce a change in electrical property (current or voltage) proportional to the amount of analyte in solution. This allows for sensitive and selective quantification for many analytes in water, while still being quite portable [8]. Spectroscopic/spectrometric methods utilize the characteristic response of each atom to electromagnetic radiation to determine concentrations of those analytes in solution. This method is highly sensitive and selective but lacks the portability as it requires elaborate instrumentation [9].

As a range of methods are becoming available for water quality monitoring, we review state-of-the-art research that was recently published in the area of cation monitoring for aqueous environments. For the purpose of this review, we firstly discuss each detection method in some detail, followed by individual sections for the most important cationic species of relevance to water quality monitoring.

2. Methods

2.1. Mechanical

2.1.1. Quartz Crystal Microbalance (QCM)

QCM measures changes in mass by measuring changes in the frequency of a quartz crystal resonator. This change in frequency occurs due to the piezoelectric effect, which is the generation of electricity as a response to mechanical stress, or vice versa. The measurement occurs through a change in the resonance frequency caused by deposition of the analyte onto the surface of the quartz crystal. By functionalizing the surface of the quartz disc, selectivity to a particular analyte is achieved, and its binding affinity can be determined [10]. As the analyte adsorbs onto the piezoelectric crystal, the change in mass causes a change in the resonance frequency of the crystal. This relationship is defined by the Sauerbrey equation (Equation (1)), which indicates that the correlation between the change in mass and the change in frequency is linear [11].

$$\Delta \boldsymbol{f} = -\frac{\boldsymbol{2f_0^2}}{\boldsymbol{A\sqrt{\rho_q \mu_q}}} \Delta \boldsymbol{m}, \quad (1)$$

where Δf is the change in frequency, f_0 is the resonant frequency of the quartz crystal, Δm is the change in mass, A is the active area of the crystal, ρ_q is the density of quartz (2.65 g/cm^3), and μ_q is the shear modulus (2.95×10^{11} g/cm·s^2). For a quartz crystal with a resonance frequency in the MHz range, changes in frequency can be measured with a sensitivity of 1 Hz [12]. The Sauerbrey equation assumes that depositing a certain mass of the analyte onto the crystal is equivalent to the crystal itself increasing in mass. This means that the equation is subject to three constraints: the adsorbed analyte remains rigid on the film once adsorbed, the mass of the analyte is small compared to the crystal itself, and the analyte is evenly distributed onto the crystal [13]. In liquid media, adsorption of the analyte may not fully couple to the frequency of the crystal, which leads to losses in energy. This loss in energy is due to the fact that, in liquids, the analyte forms softer films that do not remain rigid on the surface of the quartz crystal, which leads to non-resonant oscillations. In this case, the change in

the rate of energy transfer (dissipation) from the crystal to the analyte also needs to be considered. This technique is known as QCM-D [14]. By taking the change in dissipation into account, information about the adsorbed analyte's density, thickness, viscosity, and elasticity can also be known. To do this, the Voigt viscoelastic model is used, which relates the change in frequency and the change in dissipation to the viscoelastic properties of the adsorbed analyte and the liquid medium [15]. The ratio of the changes in dissipation compared to frequency can be used to determine the rigidity of the adsorbed analyte onto the quartz crystal. Ideally, a film would be considered viscoelastic if there is no change in dissipation. However, in real samples there are criteria, such as a $\Delta D/\Delta f$ ratio (the ratio of change in dissipation to the frequency change) of 10^{-8} Hz^{-1}. Below this ratio, the film would be considered rigid, and, above this, it would be considered viscoelastic [16]. A typical QCM consists of a quartz disc with electrodes attached to the front and the back, an oscillator which oscillates at the resonant frequency, and a monitor that shows real-time frequency changes. As the analyte adsorbs onto the quartz crystal, the change in mass results in an electrical signal, which is output onto a monitor.

The advantage of QCM lies in its portability, its quick and sensitive response, and its ability to be functionalized to improve selectivity. However, non-specific adsorption or physisorption can lead to interference within the signal, decreasing its effectiveness in more complex matrices such as environmental samples.

2.2. Optical

2.2.1. Colorimetry

Colorimetry is one of the most widely used analytical methods in chemistry. The main principle of colorimetry focuses on the detection of analyte based on the color change of the analyte solution or a surface (such as litmus paper). Detection is performed in various ways, such as with the eye or with instrumentation (such as a UV/vis spectrophotometer). Sensitivity of detection can range from a simple yes/no response to a proportional visual response or a change in concentration [17]. The concentration of an analyte can be determined by comparing the absorbance of a colored solution of analyte at a specific wavelength to a blank or a control solution. Solutions with known concentrations of analyte can be used to create a calibration equation which follows the Beer–Lambert law (Equation (2)).

$$A = \varepsilon l c, \quad (2)$$

where A is the absorbance of the sample, l is the path length of the cuvette, and c is the concentration of analyte in sample. The molar extinction coefficient, ε, can be obtained using the results from the calibration given that the concentration, c, and the path length (distance that the incident light travels through the sample, usually the diameter of the analyte containing cuvette), l, are known [18]. The concentration of an unknown analyte sample can now be determined using the obtained function.

Colorimetry is probably the easiest of all the methods for implementation, since it gives a visual indication of the presence of target analytes in a sample. This method is highly portable and inexpensive (some colorimetry kits can be bought at retail stores), and it may not require any additional instrumentation. However, for quantitative measurements, a UV/vis spectrophotometer is required, which substantially increases cost. In addition, the color change that occurs may only be detectable at higher concentrations (in some cases, much higher than regulation), meaning that this method lacks sensitivity. The color change may also be induced by interferences in the sample matrix, affecting the selectivity of the method.

2.2.2. Fluorescence

In contrast to colorimetry, which measures the decrease in transmission of the incident light, fluorescence spectroscopy measures the increase in the emission of light as a result of excitation. Fluorescence occurs when an excited electron relaxes back to its ground state, emitting a photon [19].

The emitted photon can have an energy that is lower than the excitation energy (Stokes shift due to vibrational relaxation), higher than the excitation energy (two-photon absorption leading to a transition equal to the sum of the two photons), or the same as the excitation energy (resonance fluorescence) [20]. Fluorescence also has a certain efficiency associated with it, known as its quantum yield. Quantum yield is the ratio of the photons emitted by the analyte to the photons absorbed by the analyte. This can give important information about the number of molecules in the solution interacting with the incident photons [21]. Through the binding of the selected analyte to a fluorescent compound, one can detect he concentration of the analyte quite accurately based on the degree of quenching of the fluorescence signal (decrease in quantum yield). By using a fluorometer with a single exciting and detection wavelength, one can monitor changes in quantum efficiency and correlate them to concentrations of analyte in solution [22]. Compared to colorimetry, fluorescence can also be used in bioimaging and in intracellular detection [23].

Many of the advantages and drawbacks listed for colorimetry also apply to fluorescence. The main difference between the two, however, is that fluorescence requires a light source to excite the analyte within the sample. This light source may lead to other interferences in the sample becoming excited as well, affecting the quantum yield of the analyte in the sample. To avoid this, a sample workup step may be required.

2.2.3. Surface-Enhanced Raman Spectroscopy (SERS)

SERS enhances the Raman scattering of molecules by having those molecules adsorbed onto metal or organic surfaces [24]. There is debate on the nature of the SERS effect; however, the strongest theory for its mechanism is the electromagnetic (EM) theory. This theory states that the enhancement in the signal is caused by surface plasmon resonance (SPR). When the incident light impacts the analyte adsorbed onto the surface, the collective electronic states at the surface (plasmons) become excited. Enhancement of the EM field (from the incident light) is at its highest when the frequency of the surface plasmon oscillations is equal to the frequency of the incident light [25]. This field enhancement increases the intensity of the incident light, which enhances the Raman signal. The oscillations that occur on the surface also enhance the Raman signal. The electric field is enhanced by a factor of two at each step; thus, the signal is enhanced by a power of four [26]. Samples for SERS are commonly prepared by depositing the analyte solution onto a dielectric with a noble-metal surface (usually silver or gold nanoparticles) [27]. An important property of the surface is the structure and size of the nanoparticles themselves. For ideal enhancement, the surface must be uniform. If the nanoparticles are too big, higher-order transitions may lead to non-radiative scattering, decreasing the enhancement. If they are too small, they may not have the ability to oscillate upon the impact of incident light. When combined with SPR, SERS can be used to identify and quantify analytes in liquids [28].

SERS allows for quantification of analytes at ultra-trace levels due to the multiplying effect of the analyte on the enhancement of the surface plasmon resonance. The method is also quite portable and can be used for in situ analysis. However, the plasmonic material used (usually gold or silver) is expensive and inaccessible for wide-scale use.

2.2.4. Atomic Absorption Spectroscopy (AAS)

The principle behind AAS is that the wavelength of the optical absorption of the analyte in the gas phase provides the identity of the analyte, while the intensity of the absorbance correlates to the concentration of that analyte in the sample. Unlike the colorimetric absorbance method, the sample is atomized first before being exposed to light. Various methods exist to atomize the sample, the most common being flame atomizers and electrothermal atomizers. When using flame atomizers, a nebulizer turns the liquid or gaseous samples into a fine mist. They are then subjected to mixture with a combustible gas, which produces a flame containing the atomic aerosol for analysis [29]. Electrothermal atomization utilizes a graphite furnace which contains a graphite tube that has a small

cavity for holding the sample. Through the Joule effect, the graphite tube is heated (and can reach temperatures of 3000 K). This decomposes and atomizes the sample for analysis. Due to the high atom density, the graphite furnace has a higher sensitivity than the flame atomizer [30]. For some heavy metals, it is difficult to reduce them to their elemental state through flame or high heat. In these cases, the sample needs to be reacted with a reducing agent before analysis (a metal hydride is usually formed). These metallic hydrides then thermalize at 1000 K. This is used for samples such as arsenic and mercury. Measurements are made using the Beer–Lambert law (Equation (2)). A calibration curve can be prepared with the target analyte at the specific wavelength for the analyte. This provides the correction coefficient for the unknown sample (there is no molar extinction coefficient since there is no cuvette length; thus, these two parameters are replaced by a correction factor k). The concentration of the analyte in the unknown sample can then be determined using this correction factor and the obtained absorbance.

This method allows for detection at ultra-trace levels of analyte, and, since each atom has a specific wavelength on the spectrum, interference is eliminated, making this a highly selective and sensitive method which is also capable of simultaneous detection. However, AAS instrumentation is quite large and, therefore, cannot be used outdoors in the field. The method is also destructive to the samples, since analysis requires the sample to be atomized.

2.3. Electrical

2.3.1. Chemiresistivity/ChemFET

Chemiresistivity is a change in resistance of a conductive material due to a change in its chemical environment. This change in resistance can be determined by placing contacts at either end of a thin film made from the material to measure the current passing through the material at a given voltage [31]. The basic components of a chemiresistor are a conducting material, the contacts at either end to facilitate conduction, and an electrical readout device which displays changes in the resistance of the conducting material [32]. The property of changing resistance can be utilized to detect concentrations of different analytes by correlating the changes in resistance to the concentration or pressure of a target species. Various interactions can lead to a change in resistance, such as adsorption, molecular binding, and changes with regard to the material itself [33]. Common conducting materials include but are not limited to metal oxides [34], conducting polymers [35], and carbon allotropes [36]. Chemiresistors can be used for either gas-phase [37] or liquid-phase sensing [38]. When using chemiresistive sensors, one must take into account the film thickness and the voltage. As the films get thicker, the size of the response to the analyte increases, and the film is more stable. However, the response time is much slower. With thinner films, the opposite effect is seen, with fast response times, less stable films, and smaller response sizes. For gas sensors, higher voltages can be used for thinner films to achieve larger responses. In liquids such as water, however, the voltage cannot be too high, since electrochemical side reactions or hydrolysis could occur. Functionalization of the conducting material, either through covalent or physical interactions, can be used to improve selectivity of the sensor to a certain analyte [39].

ChemFETs, on the other hand, utilize an indirect method of ion detection. For this method, the ions collected on the selective membrane apply an electric field perpendicular to the actual conductive material. This electric field changes the current going from the source through the gated channel to the drain of the device, which can be correlated to the concentration of ions. A positive electric field (generated by cations) attracts electrons and repels electron holes in the channel. A negative electric field (generated by anions) attracts electron holes and repels electrons in the channel. In a p-type device, cations decrease the conductivity of the channel and anions increase it, and vice versa for n-type devices [40]. These devices can be made selective by using an ion-selective membrane over the gate that modulates the channel, which generates an electric field as specific ions are captured [41].

These sensors are quite simple to fabricate and give good current responses for low concentrations of analyte. They also do not require a counter electrode or a reference electrode, simplifying the set-up greatly compared to other methods such as potentiometry. Due to its small size, it can also be used in situ. However, in complex sample matrices, pH and conductivity affect the sensor response, as well as non-specific binding (physisorption).

2.4. Electrochemical

2.4.1. Potentiometry (Ion-Selective Electrodes, ISEs)

Potentiometry is the observation of changes in the electrochemical potential of an electrode in solution with respect to a reference potential in order to determine analyte concentration. This method requires both a working electrode and a reference electrode. The working electrode can either be a blank electrode for redox potential (ORP) measurements, or have a membrane selective to the desired analyte, while the reference electrode remains at a constant potential. The most commonly used reference electrodes are the saturated calomel electrode (SCE) and the silver/silver chloride (Ag/AgCl) electrode. For the blank electrode, the double layer formed on the surface causes a change in potential. As the conductance of a sample solution increases, shrinkage of the double layer is induced, which results in a change in potential with respect to the reference electrode [42]. For the ion-selective electrode, the membrane on the working electrode can have two possible modes of performance: redox equilibrium and ion capture. Redox equilibrium works through the redox interaction between the analyte and the membrane on the working electrode. The redox interaction between the analyte and the membrane either oxidizes or reduces the analyte, generating a potential difference as the reaction approaches equilibrium. Ion capture utilizes ion-selective membranes to trap analyte molecules onto the electrode. The concentration of ions on the electrode generates a potential difference [43]. The potential differences can be correlated to concentration using the Nernst equation (Equation (3)).

$$E_{cell} = E^0_{cell} - \frac{RT}{nF} lnQ_r. \quad (3)$$

Using this equation, one can use the potential differences to obtain the concentrations in solution [44]. The method is quite sensitive, since the potential differences in the electrodes are normally in the hundred-millivolt range, which allows for readouts through inexpensive commercial voltmeters.

Electrochemical methods have the advantage over chemiresistive sensors as they are invariant to changes in the bulk of the electrode, even though they are equally sensitive to changes in the surface chemistry. Their main drawback is the requirement for a reference electrode, which requires frequent maintenance and calibration. Similar to other solid-state sensors, they may be miniaturized for use in microfluidics. They can be used for continuous online monitoring, but are also subject to interferences by pH, conductivity, and other analyte species.

2.4.2. Anodic Stripping Voltammetry (ASV)

Anodic stripping voltammetry (ASV) is a method that allows for preconcentration of the analyte to obtain a lower limit of detection. ASV utilizes three electrodes (as opposed to two in the case of potentiometry). These are the working electrode, the reference electrode, and a counter electrode. To prepare for analysis, the potential between the working and the counter electrode is kept higher than the oxidizing potential of the analyte to remove residual ions from the electrode. Then, the potential is lowered so that the analyte electroplates onto the electrode. Finally, the potential is slowly raised to oxidize the electroplated analyte and dissolve it back into solution. This provides the stripping current as a function of the oxidation potential. Oxidation releases electrons, which is measured as current [45]. The current given by the deposition can be correlated to the concentration through the

Levich equation (Equation (4)), which gives the deposition current as a function of the electroplated analyte.

$$i(t)_{dep} = 0.62nFAD^{\frac{2}{3}}\omega^{\frac{1}{2}}\mu^{-\frac{1}{6}}C(t), \quad (4)$$

where i is the current, n is the number of electrons in the half reaction of the analyte, F is the Faraday constant, A is the active area, D is the diffusion coefficient, ω is the rate of stirring of sample solution, μ is the kinematic viscosity, and C is the analyte concentration. There are three different ways to strip the electroplated analyte from the working electrode: linear ramp stripping voltammetry, alternating current (AC) stripping voltammetry, and differential pulse stripping voltammetry (DPV). Linear ramp stripping increases the potential linearly as a function of time. This is sufficient for identifying different adsorbed species; however, there is a large non-Faradaic contribution to the current, which contributes to the noise. AC voltammetry is phase-sensitive, which means that it can separate the Faradaic current (current related to redox processes) from the non-Faradaic current. This is because the reversible processes occur within the timescale of the alternating potential. Irreversible processes are, therefore, eliminated [46]. DPV is similar to the linear ramp in that there is a linear potential increase. However, at fixed time interval, the potential pulses to a higher potential before returning to the linear ramp. This is good for small amounts of analyte at sub-ppb levels [47].

ASV is highly sensitive, and the stripping potential is different for each cation, meaning interference is minimized and simultaneous detection of analytes is possible. However, three electrodes are required for analysis (a working electrode, a counter electrode, and the reference), which complicates the set-up and results in the need for frequent maintenance and re-calibration.

2.5. Spectrometry

2.5.1. Inductively Coupled Plasma Mass Spectrometry (ICP-MS)

ICP-MS is a very common method for determination of metals in drinking water. This method allows for ppt levels of detection for many elements. Samples for ICP-MS are in the liquid phase and are incorporated into argon plasma through the use of a nebulizer. The electrically charged argon plasma (charged via induction heating) dissociates the molecules, and then ionizes them by removing one electron. These ions are then scanned using a quadrupole mass spectrometer, which separates the ions based on mass-to-charge ratio (m/z). It does this by setting its voltage and radio frequency to allow certain ions to pass through to the detector while all others are ejected. Copper(I) ions, for example, have a mass-to-charge ratio of 63/1. When a specific voltage and radio frequency are applied, only copper ions pass through. Since some molecules do not get fully atomized, there can be interferences if a molecular fragment is of the same mass as the analyte. To remove interferences, one can use either a collision cell or a reaction cell. The collision cell uses the fact that molecular fragments are bigger than elements and, therefore, undergo more collisions in an inert gas. This means that the molecular fragment loses its kinetic energy faster than the element, which retains most of its kinetic energy. This allows for the passage of elements, while stopping interfering molecular fragments from passing through to the detector. The reaction cell focuses on the thermodynamics of the interaction between an element or molecular fragment and a reactive gas. A molecular fragment reacts exothermally with a reactive gas, whereas an element reacts endothermally. This allows for passage of elements to the mass spectrometer while ejecting the molecular fragments. Both these methods increase the resolution and selectivity of ICP-MS [48].

This method is the most sensitive out of all of the methods since it is able to detect individual atoms as they are passed through the quadrupole mass analyzer. Since atoms have different masses, simultaneous detection is also possible using mass spectrometry. However, the method is destructive since it requires atomization of the sample. The method also requires large and very expensive instrumentation, making in situ measurements impossible.

3. Analytes

3.1. Barium

Barium is a soft metal used to make various things such as paint, bricks, ceramics, and tiles. It is also used as an additive for fuels, sealants, and the passivation of limestone. Barium occurs in water naturally through soil erosion and leeching of barium ore, but it can also occur through other means such as industrial emissions. In humans, high intake of barium can affect kidney function and promote cardiovascular disease. The World Health Organization has a guideline value (not a maximum limit) of 1.3 ppm. Health Canada has a higher proposed maximum allowable concentration (MAC) of 2 ppm [49,50].

A fluorescent method based on imination of an anthracene molecule for the detection of barium(II) was developed by Basa et al. This method uses a 1,2-phenylenediamine host with an anthraquinone macrocycle to improve selectivity toward barium(II) in solution. When tested with barium(II) titration in acetonitrile, a linear increase was seen in fluorescence intensity going from 0–133 μM (0 ppm to 18 ppm), after which the sensor molecule saturated. Although there are no other analytical data available, this sensor shows potential for the detection of barium(II) in aqueous media [51].

A potentiometric sensor based on dimethyl-4,4-dimethoxy-5,6,5′,6′-dimethylene dioxy biphenyl-2,2-dicarboxylate (DDB)—a liver drug—for the detection of barium(II) was developed by Hassan et al. This method consists of using DDB as the barium(II)-selective ionophore and coating it onto an Ag/AgCl internal reference electrode for use as the working electrode. An Ag/AgCl external electrode was used as the reference for this test. When testing this barium(II)-sensing method, a linear range of 10 μM to 0.1 M (1.4 ppm to 13 733 ppm) was found with a limit of detection of 5 μM (0.7 ppm). When tested against other cations for interference, barium(II) gave the highest slope for potential changes compared to other metal cations, making this method quite selective. In real samples, the values obtained by this method were in good agreement with those obtained by the standard AAS method [52].

A potentiometric method based on 3-deoxy-D-erythro-hexos-2-ulose bis (thiosemicarbazone) (DHUT) as the ionophore for detection of barium(II) was developed by Zamani et al. The electrode was prepared using a solution of DHUT in plasticizer and coating it onto an Ag/AgCl wire for use as the working electrode. An Ag/AgCl electrode was used as the external reference for this method. When tested for sensitivity to barium(II) by titration, the potential of the electrode changed proportionally to the amount of barium(II) added. A linear range of 1 μM to 0.01 M (0.1 ppm to 1373 ppm) was obtained. A limit of detection of 0.56 μM (77 ppb) was observed for this method. When testing against other cations, the response slope for barium(II) was much higher compared to the other cations, meaning that this method is sufficiently selective. In real samples, the values obtained were in good agreement with the standard AAS method [53].

An AAS method for detection of barium(II) in water was developed by Silva et al. This method uses a tungsten coil to atomize the samples for analysis by AAS. As the concentration of barium(II) changed in the solution, the peak height for the characteristic barium(II) wavelength would increase proportional to the amount of barium(II) in solution. Although a linear range is not available, a detection limit of 0.2 ppb was obtained, which is much lower than the limits set by the World Health Organization (WHO) and Health Canada. Interference studies with other cations showed that only calcium(II) interfered with the peak, but the interference could be corrected with addition of Ethylenediaminetetraacetic acid (EDTA). In real water samples, the values obtained with this method were in good agreement with the standard ICP-AES method used for comparison [54].

3.2. Cadmium

Cadmium is a heavy metal that is harmful to human health. It is classified as a carcinogen, and can have adverse effects on the kidneys, bones, and respiratory system. Cadmium occurs naturally in

water through volcanic activity and erosion, but it also occurs through human activities such as mining, fossil fuel combustion, and recycling of electronic waste. Although cadmium levels in drinking water are usually low, the increase in these human activities may affect levels currently found. For water to be considered safe to drink, the World Health Organization recommends a maximum limit of 3 ppb, whereas Health Canada set a higher limit of 5 ppb [55,56].

A colorimetric method for the detection of cadmium(II) using gold nanoparticles (AuNPs) modified with 4-amino-3-hydrazino-5-mercapto-1,2,4-triazoles was developed by Wang et al. This sensor functions through the cadmium(II) chelation-induced aggregation of the functionalized AuNPs, which results in a change in color of the solution from red to blue. The addition of cadmium(II) into solution led to a shift in the absorbance peak from 520 nm to 650 nm, which was proportional to the concentration of cadmium(II) in solution. The ratiometric response obtained was correlated to the concentration added to the solution, and a linear range from 60 nM to 480 nM (7 ppb to 54 ppb) was obtained, with an R^2 value of 0.9963. A limit of detection of 30 nM (3.5 ppb) was observed for this sensor. When comparing to other cations for interference, the ratiometric response given by the cadmium(II) chelation was twice as large as the response by other cations, making this a selective colorimetric method for the determination of cadmium(II) [57].

A napthalimide-based fluorescent sensor for determination of cadmium(II) was developed by Wang et al. This sensor utilizes an *N*,*N*′-bis(salicylidene)diethylenetriamine receptor to turn on fluorescence in the presence of cadmium(II) in solution. This sensor is pH-dependent; at low pH ranges (<4.5 pH), the free molecule fluoresces, and shows no enhancement of emission after interaction with cadmium(II). Within the pH range of 7.0 to 13.5, the free molecule does not fluoresce. However, upon addition of cadmium(II), fluorescence is enhanced in solution, which would make this a viable method in environmental conditions. In a 1:1 ethanol (EtOH)/H_2O solution buffered with 4-(2-hydroxyethyl)-1-piperazineethanesulfonic acid (HEPES) buffer at pH 7.2, the fluorescence enhancement of the molecule at 525 nm was linearly proportional to the concentration of cadmium(II) in solution. A linear range of 50 nM–10 μM (6 ppb to 1 ppm) was obtained with an R^2 value of 0.9902 and a limit of detection of 520 nM (58 ppb). When compared against other cations, only cadmium(II) led to a fluorescence enhancement, making this sensor quite selective [58].

A protein-based fluorescent sensor for cadmium(II) was developed by Varriale et al. This method utilizes a column packed with zinc(II)-saturated Chelex resin with a rhodamine-labeled metallothionein. Cadmium(II) was flowed through the column, displacing the rhodamine-labeled metallothionein, and leading to a fluorescence enhancement. When water with no metal ions was flowed through, there was no fluorescence detected in the fluorometer. Once cadmium(II) aqueous solution was flowed through, however, the metallothionein was eluted, resulting in a fluorescence enhancement at 575 nm, which was proportional to the concentration of cadmium(II) flowed through the column. Cadmium(II) solutions with a concentration range of 2.5 ppb to 10 ppm were flowed through the column, which resulted in a limit of detection of 0.5 μM (56 ppb). When testing against other cations, no other cations led to the elution of the metallothionein, meaning that this method is selective toward cadmium(II) [59].

A potentiometric method for the detection of cadmium(II) was developed by Ion et al. This method uses a cadmium(II)-specific ionophore to change the potential of the working electrode. Changes in the potential can be correlated to the concentration of cadmium(II) in solution. The ISE membrane containing the ionophore, *N*,*N*,*N*′,*N*′-tetradodecyl-3,6-dioxaoctanedithioamide (ETH 5435), was glued to a plasticized polyvinyl chloride (PVC) tubing with a PVC/tetrahydrofuran (THF) slurry. The reference used was an Ag/AgCl electrode. In a 0.1 mM sodium ion background at pH 7, cadmium(II) resulted in a change in potential proportional to its concentration in solution. A limit of detection of 11 ppt was obtained, which is much lower than the values set by the WHO and Health Canada [60].

A thermally enhanced ASV method for the determination of cadmium(II) was developed by Marken et al. This method utilizes the microwave radiation-enhanced deposition of cadmium(II) onto the working electrode, which enhances the stripping peak and the detection limit. A microwave

working electrode with a 100-μm Pt disc was used as the working electrode, along with a Pt-mesh counter electrode and an SCE as the reference electrode. With no heating, there was no detectable stripping peak present for 400 μM (45 ppm) of cadmium(II) in 4.6 pH acetate buffer. When heated up to 205 °C, the peak was present at −0.603 V for the same concentration. The enhancement in the peak was proportional to the temperature going from 30–205 °C. Although there was no quantitative analysis in this study, this method shows potential for a highly sensitive cadmium(II) sensor [61].

An SERS method for determination of cadmium(II) was developed by Yin et al. This method is dependent on Raman-active AuNPs tagged with a Raman-active dye, and a cadmium(II)-selective polymer. Upon chelation of cadmium(II) onto the nanoparticle, the AuNPs aggregate, which turns on the Raman signal and leads to a 90-fold enhancement of the Raman signal (Figure 1).

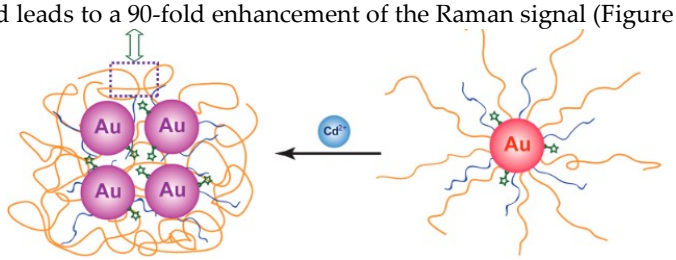

Figure 1. Mechanism of the cadmium(II)-induced aggregation of gold nanoparticles (AuNPs). Reprinted with permission from Reference [59]; Copyright 2011 American Chemical Society.

When cadmium(II) was added to an aqueous solution of functionalized AuNPs, a Raman peak enhancement was seen at 525 cm^{-1}, proportional to the amount of cadmium(II) added. A detection limit of 1 μM (112 ppb) was observed for this method. When testing against other cations, cadmium(II) gave the biggest Raman peak enhancement at 525 cm^{-1}, with zinc(II) giving a much smaller response, and all other cations not enhancing the peak at all [62].

An alizarin-based SERS probe for detection of trace levels of cadmium(II) in drinking water was developed by Dasary et al. Alizarin was functionalized onto the AuNP as a Raman reporter, while 3-mercaptopropionic acid was used as a cadmium(II) chelating agent. Upon addition of cadmium(II), aggregation of AuNPs induced by the chelation of cadmium(II) onto the 3-mercaptopropionic acid leads to a Raman enhancement, which can be used to determine the concentration of cadmium(II) in water. In a pH 8.5 buffer, enhancement of the Raman peak at 1335 cm^{-1} was seen, which was proportional to the amount of cadmium(II) added into the solution. A linear range of 25 ppb to 200 ppb was obtained, with a saturation point at 250 ppb. The detection limit of this method was found to be 10 ppt, which is quite sensitive. Comparison of the cadmium(II) response to other cations showed that there is no Raman peak enhancement present with the other cations. When testing in real water samples by spiking cadmium(II), recovery was shown to be adequate, and the detection limit in environmental water was found to be 70 ppt [63].

An AAS method using preconcentration in a knotted reactor was developed by Wen et al. For this method, the solution of cadmium(II) was mixed with an ammonia solution, and then injected into the knotted reactor, where the now precipitated cadmium hydroxide was adsorbed onto the knotted reactor walls. Then, a 1 M nitric acid solution was passed through the reactor, eluting the cadmium hydroxide and moving it into the nebulizer for analysis by FAAS. This method gave a linear correlation for the absorbance of the cadmium peak with the concentration of cadmium(II) eluted from the reactor. The linear range obtained went from 40 ppt (the detection limit) to 2 ppb, with an R^2 value of 0.999. Interference tests showed that there was no significant effect on recovery of cadmium(II) when in the presence of various different cations and anions. When tested in various certified reference and real samples, the values obtained by this method were in good agreement with the certified reference samples, and with the standard ICP-MS method of detection [64].

An AAS method for cadmium(II) detection through solidification of floating organic drop microextraction was developed by Dadfarnia et al. For this method, the sample containing cadmium(II) was mixed with 0.2 M iodide at pH 1.2. This solution was transferred into a solution of

0.02 M methyltrioctylammonium chloride in 1-undecanol. This was mixed until the CdI_4^{2-} formed previously reacted with the methyltrioctylammonium chloride, and then precipitated in an ice bath. This precipitate was then melted and dissolved in ethanol for analysis. When using this method, a linear correlation between the absorbance and concentration of cadmium(II) was obtained, with a range of 80 ppt to 30 ppb, and an R^2 value of 0.9998. A limit of detection of 8 ppt was observed, which makes this method highly sensitive. When compared against other cations and anions, the recovery of cadmium(II) was not significantly affected, making this method quite selective to cadmium(II). When this method was tested in real samples, recovery values were normally above 97%, and the values obtained were in good agreement with the standard graphite furnace (GF) AAS method used for comparison [65].

3.3. Chromium

Chromium is an element found in the Earth's crust, most commonly in its trivalent state. Chromium, as an element and as its various salts, is used for tanning, pigments, photography, and alloy production. Most chromium occurring in the environment comes from human activity, such as refineries and thermal generating stations. Humans actually require 0.5–2.0 µg of chromium(III) daily. Chromium(III) does not have any harmful effects that are known, but chromium(VI) is a known carcinogen. The World Health Organization set a provisional guideline value of 50 ppb, which is the same as the maximum allowable concentration for Health Canada [66,67]. Since this review is focused on cation detection, only chromium(III) detection is discussed here, since chromium(VI) is usually found as a chromate anion.

A colorimetric method based on citrate chelation on Tween-20-stabilized AuNPs for the detection of chromium(III) was developed by Wang et al. In this method, the Tween-20-stabilized AuNPs functionalized with citrate are dispersed in a phosphate buffer solution. Upon interaction with chromium(III), the AuNPs aggregate, causing a visual color change from red to blue. This method only induces the color change when exposed to chromium(III) and not chromium(VI) (Figure 2).

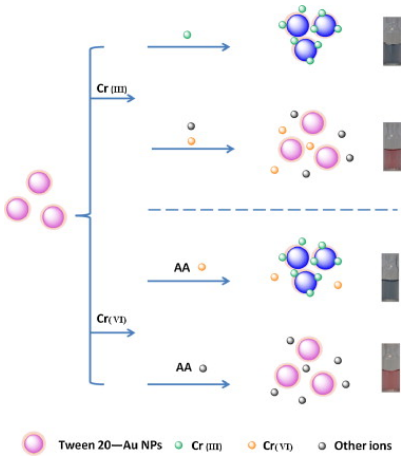

Figure 2. The sensing mechanism of the functionalized AuNPs. Reprinted with permission from Reference [65]; Copyright 2015 Elsevier.

When chromium(III) was tested with this method, the absorption peak at 520 nm decreased while the peak at 660 nm increased. This change in the absorbance spectrum was proportional to the concentration of chromium(III) ions in solution. The ratiometric response was correlated with the concentration of chromium(III), showing a linear range of 0.05–5.0 µM (3 ppb to 260 ppb), and an R^2 value of 0.989. A detection limit of 0.016 µM (0.8 ppb) was obtained for this method. When tested with other cations, no other cations interfered with the signal or led to aggregation of the AuNPs,

making this method quite selective. This method was also used for testing in real water samples using the sample addition method, and the recovery values remained above 91% [68].

A colorimetric method that utilizes dithiocarbamate-modified *N*-benzyl-4-(pyridin-4-ylmethyl)aniline ligand (BP-DTC)-functionalized AuNPs for the detection of chromium(III) was developed by Zhao et al. This method, much like the one before, also works through the aggregation of AuNPs via chelation of chromium(III) to the BP-DTC ligand (Figure 3a).

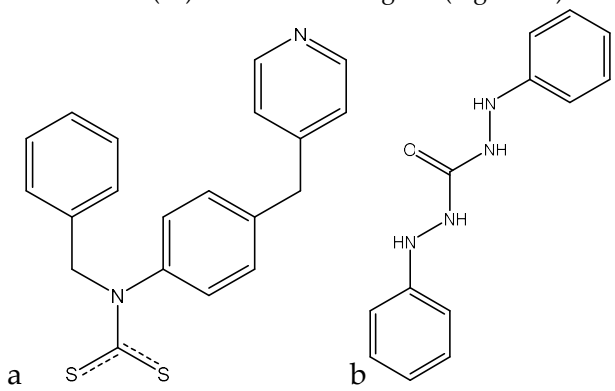

Figure 3. The structure of (**a**) the dithiocarbamate-modified *N*-benzyl-4-(pyridin-4-ylmethyl)aniline (BP-DTC) ligand and (**b**) 1,5-diphenylcarbazide.

When exposed to chromium(III) in aqueous solution, a color change from red to blue is visually observed. In the absorbance spectrum, the absorbance peak at 520 nm decreases upon addition of chromium(III), and a new peak at 630 nm arises, with the peak heights being proportional to the amount of chromium(III) added. A linear range for the ratiometric response was found between 0 and 8.0 μM (0 ppb and 416 ppb) with an R^2 value of 0.9958. A limit of detection of 31 ppb was obtained for this method. When testing against other cations, the response of the chromium(III) was five times larger than any of the other interfering cations, making this method quite selective. When tested with real water samples, the values obtained were in good agreement with the standard ICP-MS method, and sample addition gave recovery values above 103% [69].

A fluorescent method for the detection of chromium(III) through the use of a distyryl boron-dipyrromethene (BODIPY) derivative was developed by Wang et al. For this method, the BODIPY derivative by itself does not have an emission peak due to the amine groups transferring electrons to the BODIPY backbone, quenching fluorescence. Once chromium(III) is in solution, the electrons from the amine groups now transfer to the chromium(III) metal center, turning on the fluorescence for the molecule. When this molecule is exposed to chromium(III) in aqueous acetonitrile solution, an emission peak at 643 nm arises, and the peak height is proportional to the chromium(III) in solution. Although no analytical data are available, the sensor had a quantitative fluorescence enhancement from 0–200 μM (0 ppb to 10 ppm), indicating that this sensor has a large range. When tested against other cations for interference, the BODIPY derivative only bound to chromium(III) and did not give any fluorescence enhancement with other cations. However, iron(III), copper(II), and mercury(II) did affect the ability of chromium(III) to enhance fluorescence (although concentrations of 10 ppm were required) [70].

A potentiometric method based on carbon nanotube (CNT) -coated Pt electrodes for the detection of chromium(III) was developed by Abbaspour et al. In this method, an multi-walled (MW) CNT/PVC membrane is used as the working electrode, with 1,5-diphenylcarbazide as the chromium(III)-selective ionophore, and an SCE as the reference electrode (Figure 3b). When this sensor was tested with chromium(III) in solution, a pH range of 3–7 was found to be optimal, since higher pH values lead to chromium hydroxide being formed, while lower pH values lead to protonation of the ionophore. The potential changes with respect to the SCE reference were correlated with the concentration of chromium(III) in solution, and a Nernstian response for the concentration

range of 30 nM to 0.01 M (1.5 ppb to 520 ppm) was found, with a limit of detection of 32 nM (1.6 ppb). When tested against other cations, chromium(III) displayed better Nernstian responses than any of the other interferences tested. In real samples, the values obtained by this method were in good agreement with the standard AAS method [71].

An SERS method of detecting chromium(III) through the use of citrate-functionalized AuNPs was developed by Ye et al. This method utilizes the chromium(III)-induced aggregation of the functionalized AuNPs to enhance the Raman signal generated by the bare AuNPs. When tested with chromium(III) in aqueous solution, the Raman peak at 555 cm^{-1} saw an enhancement proportional to the amount of chromium(III) added. A calibration curve was obtained with a range of 50 nM to 0.2 μM (2.6 ppb to 10 ppb), with an R^2 value of 0.936. The limit of detection for this method is 50 nM (2.6 ppb). When tested against other cations, only chromium(III) led to a visual color change form red to blue and an enhancement in the Raman spectra, making this method quite selective. When tested in real water samples using the sample addition method, recovery values were all above 94% [72].

An SERS method for detection of chromium(III) using silver nanoparticles (AgNPs) was developed by Liang et al. This method utilizes AgNPs along with lateral flow immunoassays to quench the Raman peak intensity proportional to the concentration of chromium(III). When the sample solution of functionalized AgNPs was flowed through the immunoassay, they were bound by the antigen Cr-EDTA-bis(trimethylsilyl)acetamide (BSA). When a mixture of chromium(III) solution and AgNPs was flowed through, the chromium(III) prevented the AgNPs from being bound by the antigen, decreasing the Raman peak signal. When tested with chromium(III), a decrease in the characteristic peak at 1077 cm^{-1} is seen, which is proportional to the concentration of chromium(III) in solution. A linear range of 0.01 ppt to 0.01 ppb was seen, with an R^2 value of 0.99774. A limit of detection of 0.01 ppt was obtained. When tested against other cations, only chromium(III) led to the quenching of the Raman peak at 1077 cm^{-1}, making this method quite selective. In real water samples, however, the values were much lower than what was obtained by ICP-MS, meaning that there is still some optimization required for this method [73].

An AAS method with preconcentration of a packed minicolumn for the determination of chromium(III) was developed by Rao et al. This method uses flow injection to adsorb the chromium(III) in solution to the C_{18}-packed minicolumn. Here, 5 ppm manganese(II) is added to the chromium(III) solution to enhance the absorbance signal, and the pH is adjusted to 7. This solution is then flowed through the minicolumn for preconcentration. The chromium(III) is then eluted with methanol and flowed into the nebulizer for analysis with FAAS. When this method was tested with chromium(III), a linear range was obtained for 20 ppt to 200 ppb. The limit of detection obtained was 20 ppt. When tested with other cations, there was no effect on the recovery of the chromium(III) from the minicolumn. In real samples, the value obtained by this method was in good agreement with the certified value for the sample [74].

3.4. Copper

Copper is an essential element for human life. The recommended intake for adults is 900 μg/day, and, for children, it is between 340 and 890 μg/day. Deficiency in copper intake can lead to various adverse effects, such as anemia and low white blood cell count [75]. This is not a concern, however, since food intake supplies enough copper for a human. Overexposure to copper can lead to gastrointestinal issues (nausea, diarrhea, etc.). High levels of copper in water also stain clothing and plumbing. In Canada, drinking water has a maximum allowable concentration of 2 ppm copper, with an aesthetic objective of 1 ppm [76].

Kaur et al. developed a colorimetric sensor based on 1-aminoanthracene-9,10-dione-based molecules for the detection of copper cations (Figure 4a).

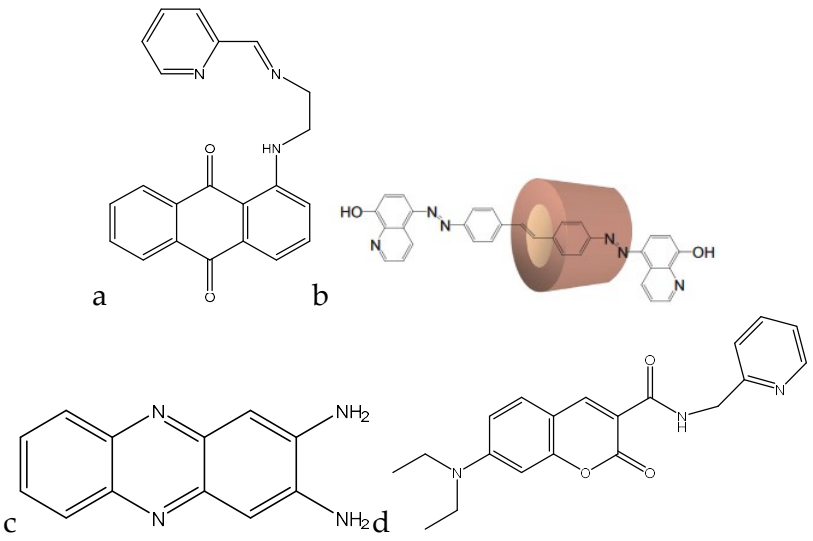

Figure 4. Structure of (**a**) the copper(II)-selective anthraquinone derivative, (**b**) rotaxane with 8-hydroxyquinoline as the blocking group (reprinted with permission from Reference [75]; Copyright 2010 Elsevier), (**c**) 2,3-diaminophenazine, and (**d**) coumarin-based fluorophore.

When copper(II) was added to the chemosensor in a methanol (MeOH)/H_2O (1:1) mixture at pH 7.0 (10 mM HEPES), the λ_{max} shifted from 494 nm to 604 nm, which was accompanied by a color change from red to blue. Below pH 5, the chemosensor protonates and does not form a complex with copper(II). Between pH 5 and 8.75, a complex is formed, with the complex formation reaching completion around pH 7. Above pH 8.75, the complex separates into $Cu(OH)_2$ and the free chemosensor. This chemosensor also had a ratiometric response to copper(II). When copper(II) was titrated against the chemosensor, a decrease in the peak at 494 nm was seen, accompanied by a proportional increase in the peak at 604 nm. A calibration curve was able to be made, correlating the ratio of the peak heights to the added concentration of copper(II), which ranged from 5–150 μM (0.318–9.533 ppm) [77].

Park et al. developed a colorimetric detection method using a rotaxane dye (Figure 4b). The rotaxane coupled with the hydroxyquinoline allowed for a 43% enhancement in absorbance. At a pH of 7.5 in dimethylformanilide (DMF)/H_2O (80:20, wt.%), the λ_{max} shifted from 440 nm to 520 nm. The color change was also able to be detected down to 170 ppb, with the upper limit being dependent on the concentration of the dye. Since the color change was also ratiometric (similar to the previous chemosensor), a calibration curve can be formed with this dye as well, allowing for interpolation of concentration values in unknown samples [78].

Udhayakumari et al. utilized 2,3-diaminophenazine for fluorometric detection of copper(II). With the addition of 100 μL of a 1.5×10^{-5} M Cu^{2+} solution in water to 3 mL of 5×10^{-5} M 2,3-diaminophenazine in acetonitrile, a quenching in fluorescence was observed, with the emission peak at 500 nm decreasing in intensity with the addition of the copper(II) (Figure 4c). The sensing is feasible at a pH range of 4–8. Below pH 4, the amine groups protonate, and the complex is unable to form. Above pH 8, the complex dissociates to form the sensor molecule and $Cu(OH)_2$. The molecule is reported to have a detection limit of 0.015 ppb and was shown to be selective to copper(II) when tested against various interfering cations [79].

A coumarin-based fluorogenic probe was developed by Jung et al. for determination of copper(II) in living cells (Figure 4d). The excitation peak of the fluorophore is located at ~480 nm in an aqueous HEPES/dimethylsulfoxide (DMSO) (9:1, *v*/*v*) solution. Once copper(II) is added, the fluorescence is nearly fully quenched. The quenching of the fluorescence is also proportional to the amount of copper(II) present in solution, with a negative linear correlation with respect to the emission intensity. The linear range of the sensor goes from 0.5 μM to 50 μM (32 ppb to 3.2 ppm) [80].

An ASV method for determining trace amounts of copper(II) was developed by Zhao et al. This method involves using a carbon nanotube (CNT) thread as the working electrode, a platinum wire as the counter electrode, and an Ag/AgCl reference electrode. CNT thread was used as the working electrode since it has high conductivity, good mechanical strength, and a large surface area. The copper(II) was deposited using a deposition potential of −1.5 V. Osteryoung square wave stripping was used for stripping the metals from the CNT thread. When copper from the working electrode is oxidized to copper(II), a peak in the current-voltage (I–V) curve appears at +24 mV. The current peak at this potential is proportional to the concentration of the copper(II) in solution, with a linear response from 0.5–3.5 μM (32 ppb to 222 ppb, R^2 = 0.99). The effects of dissolved oxygen on the response of copper(II) were also investigated. When oxygen is present in solution, the copper(II) stripping peak moves to −56 mV, and the peak becomes sharper and more pronounced. The slope of the calibration curve also increases, going from 0.33 to 0.60 from a range of 1.5–5.0 μM (96 ppb to 320 ppb). Since the copper(II) stripping potential is quite specific to copper(II), this is a very sensitive method for copper(II) detection in water [81].

SERS was utilized to detect copper in aqueous media by Ndokoye et al. through the use of cysteine-functionalized gold nanostars (Cys-AuNSs). When the Cys-AuNSs are adsorbed onto a colloidal gold surface, the signals from 1500–900 cm^{-1} are enhanced, and the symmetric vibration mode of COO is observed strongly at 1400 cm^{-1}. A 2:1 Cys-AuNS:Cu^{2+} complex is formed, which causes the aggregation of the AuNSs (Figure 5).

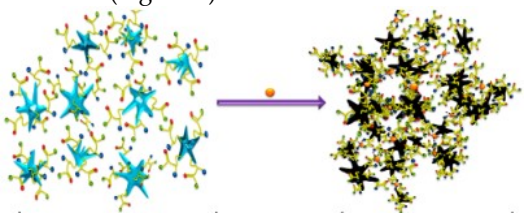

Figure 5. Complexation induced aggregation of cysteine-functionalized gold nanostars (Cys-AuNSs). Reprinted with permission from Reference [79]; Copyright 2014 American Chemical Society.

This greatly enhances the SERS signal due to plasmon coupling. When tested with other metals, they complexed with the Cys-AuNS, but did not induce the aggregation, which indicated selectivity to copper(II). The method was tested over a range of 8.5–40 μM (544 ppb to 2.56 ppm) and saw a proportional increase in the symmetric vibration mode of the COO group at 1400 cm^{-1} [82].

A flame atomization AAS (FAAS) method was developed by Cassella et al. This method utilizes a flow injection method to preconcentrate a minicolumn, and then elutes the copper(II) from the column for analysis by FAAS. The sample, which is maintained at pH 9, is pumped into the minicolumn packed with a polystyrene/divinylbenzene resin functionalized with (*S*)-2-[hydroxyl-bis-(4-vinyl-phenyl)-methyl]-pyrrolidine-1-carboxylic acid ethyl ester, which chelates to copper(II). Here, 2 M HCl was then flowed through the minicolumn to desorb the copper(II) from the resin for analysis by FAAS, which measured at a wavelength of 324.8 nm. Absorbance values were measured for concentrations between 10 ppb and 200 ppb, and the increases in absorbance were linear with respect to copper(II) concentration (R^2 = 0.9995). Environmental samples were also tested and spiked to determine recovery, and they were found to be in agreement with the standardized method, electrothermal AAS (ET AAS). Recoveries were also quite good, ranging from 91% to 106% (only sea water samples had a low recovery value of 79.5% compared to the rest of the samples) [83].

An online concentration determination method based on AAS was developed by Porento et al. Aqueous copper samples were injected via syringe pump into the nitrogen plasma jet for atomization, and then were flowed into the AAS for analysis. For a range of concentrations from 0.4 to 3.9 ppm, a linear correlation was observed between copper(II) concentration and the absorbance at 324.8 nm, with an R^2 value of 0.99. The limit of detection for this method was 0.25 ppm. Response was also compared against magnesium(II), which did not give any discernible response at 324.8 nm [84].

3.5. Hardness

Water hardness is the amount of combined calcium and magnesium (and various other divalent cations at lower concentrations) in water. The WHO defines it as the capacity of water to react with soap, i.e., the harder the water is, the more soap it needs to form a lather. The most common expression for hardness is the concentration of calcium carbonate per liter. The hardness of water is quantified as follows: <60 ppm is soft, 60–120 ppm is moderately hard, 120–180 ppm is hard, and >180 ppm is very hard [85]. The most common sources of ions that contribute to water hardness are from sedimentary rock (limestone and chalk) and soil runoff. Both calcium and magnesium are essential for human biology. Calcium increases bone mass and reduces the risk of fracture. Calcium deficiency can increase the chances of osteoporosis, hypertension, stroke, and various other cardiovascular issues. On the other hand, an excess of calcium can lead to hypercalcemia in those who are prone to milk alkali syndrome [86]. Magnesium is a cofactor for 350 cellular enzymes and is involved in protein and DNA/RNA synthesis. Magnesium deficiency can lead to hypertension, while excessive intake can have a laxative effect [87]. Although there is no strict guideline, hardness levels between 80 ppm and 100 ppm are recommended [88].

A method of determining water hardness through the use of acoustic wave sensors was developed by Veríssimo et al. A 9-MHz quartz crystal coated with an ionophore solution (1,3,5-tris [10(1-adamantyl)-7,9-dioxo-6,10-diazaundecyl] benzene (Mg ionophore), 10,19-bis[bis(octadecylcarbamoyl) methoxyacetyl]-1,4,7,13,16-pentaoxa-10,19-diaza cycloheneicosane (Ca ionophore), polyvinyl chloride (PVC), plasticizer, and lipophilic salt in 5 mL THF) was used to deposit the calcium(II) or magnesium(II) onto the coated quartz crystals. Calibration solutions were flowed through the quartz crystal cells through flow injection analysis to create a calibration curve to interpolate real sample values. The change in frequency of the quartz crystal was correlated to the calibration concentration that was injected. By doing this, linear calibrations for both calcium(II) and magnesium(II) were obtained, with R^2 values of 0.9990 and 0.9994, respectively. These calibration curves were then used to analyze real water samples in Portugal, and the results were compared to the standard EDTA titration method. Both methods were in agreement with each other, with no discrepancies being present between the two [89].

An optical test strip for the determination of water hardness was developed by Capitán-Vallvey et al. This test strip utilizes an ion exchange mechanism which quantifies calcium(II) and magnesium(II) simultaneously. The strips were prepared on Mylar, upon which the 4,13-[bis(*N*-adamantylcarbamoyl)acetyl]-1,7,10,16-tetraoxa-4,13-diazacyclooctadecane (K22B5 ionophore) in THF was spin-coated. The strip was then fully submerged into the sample solution for 5 min. The strip was then removed, and its absorbance was measured against a background of Mylar. By using equimolar solutions of calcium(II) and magnesium(II), a calibration curve was made using calibration solutions, and was fit to a theoretical response function using the logarithm of the concentration as the independent variable. A detection limit of 1.9 ppm was obtained, with a linear range of 1.9 ppm to 14 800 ppm. This method was also used in real samples and was compared to a standard complexometric titration. The results obtained with the test strips were quite comparable to the values obtained by the titration, making this an easy method to sense water hardness [90].

A complexometric method of determining water hardness was developed by Bhattacharjee et al. The method is based on the properties of EDTA titration. A channel is three-dimensionally (3D) printed from acrylonitrile butadiene styrene (ABS). It contains a red and blue light emitting diode (LED), with a photodiode for each. An inlet and outlet were present to inject the sample. A calgamite solution was prepared at pH 10 as the indicator. The sample was then injected into the device. Afterward, the calgamite solution was injected, changing the color to red, and dropping the voltage output by the blue LED. Once EDTA-Na_2 was added, the solution turned blue, and the voltage output from the blue LED increased. By measuring the absorbance of the blue light emitted, a calibration curve was created with a linear range of 0 ppm to 120 ppm, and an R^2 value of 0.9163. Although the sensor is not very precise, it can be used to differentiate between soft and hard water at the 60-ppm threshold [91].

A hardness determination method based on fluorescence resonance energy transfer (FRET) was developed by Dey et al. For the energy transfer, two dyes, acriflavine (Acf) and rhodamine B (RhB), are used as the energy donor and acceptor, respectively. FRET efficiency (efficiency of energy transfer) can be affected by metal ions in water, such as calcium(II) and magnesium(II), and the changes in efficiency can be correlated to water hardness. It is seen that, when Acf and RhB are both in solution with calcium(II) and magnesium(II), the efficiency of the FRET decreases from 11.37% to 4.38%. The changes in FRET efficiency were observed from 30 ppm to 200 ppm in clay dispersion, although it was not a linear correlation; thus, a calibration curve could not be created. A FRET efficiency of 48.2% was determined as the threshold above which water would be considered soft, and below which water would be considered hard [92].

A fluorometric method of hardness determination using a molecular aptamer beacon was developed by Lerga et al. (Figure 6).

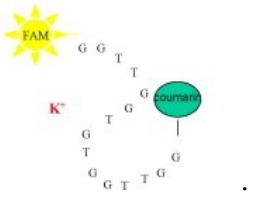

Figure 6. The molecular aptamer beacon used for detection. Reprinted with permission from Reference [90]; Copyright 2008 Elsevier.

For the analysis, a calibration curve was created ranging from 0–3000 μM (0 ppm to 300 ppm) in a 0.15-mL solution containing 100 nM beacon in 10 mM HEPES (pH 8.4). The concentration of the calcium(II) and magnesium(II) was plotted against the quenching of the fluorescence at 518 nm, and a calibration curve was created with an R^2 value of 0.998. Real samples were also tested, and the method was compared with AAS. The values obtained with the beacon were quite comparable to those obtained with AAS, with maximum variation being in the range of 0.5 mM (50 ppm) [93].

A method of hardness determination using a potentiometric sensor array was developed by Saurina et al. This method used a working electrode with a selective ionophore mixture (calcium ionophore II, ammonium ionophore I, potassium ionophore III, sodium ionophore III, lithium ionophore VI, magnesium ionophore I, and hydrogen ion ionophore III) to detect calcium(II) and magnesium(II) in solution. To obtain the calibration curve, different volumes of the standard ion solution were added to a 0.01 M Tris solution, and the changes in potential were correlated with the concentration. For calcium(II), this resulted in a dynamic range of 20 μM to 300 μM (2 ppm to 30 ppm), with a limit of detection (LOD) of 0.006 mEq/L (milliequivalents per liter, 120 ppb). For magnesium(II), the range was from 2 mM to 10 mM (200 ppm to 1000 ppm) with an LOD of 1.7 mEq/L (21 ppm). Although the magnesium LOD is higher than what is recommended, this method is good for testing the general hardness of a water sample [94].

A PVC-based membrane sensor for water hardness was developed by Singh et al. This sensor utilizes α-furildioxime as a neutral carrier for a calcium(II)-selective electrode (Figure 7).

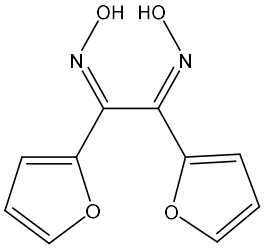

Figure 7. Structure of α-furildioxime.

Various parameters for the construction of the ion-selective membrane were investigated, such as the type of plasticizer and the ratios of each component. The optimal result was obtained by using α-furildioxime/PVC/dibutylphthalate/potassium(tetrakis-4-chlorophenyl)borate (KTpClPB) in a 4:32:62:2 (wt.%) solution in THF. By running the calibration solutions to obtain a curve, a linear range of 2.56×10^{-7} M to 1 M (26 ppb to 100,000 ppm) was observed, as well as an LOD of 1.25×10^{-7} M (13 ppb). This range is stable between pH 3.5 and 9.0, which would indicate that, below pH 3.5, the ionophore begins to protonate, and, above pH 9, the calcium(II) forms its hydroxide $Ca(OH)_2$. When measuring real samples, the calcium(II)-selective electrode obtained similar concentrations to those obtained by AAS [95].

3.6. Lead

Lead enters drinking water when lead-containing service pipes begin to corrode. Since lead has the ability to bioaccumulate in the body overtime, there is no safe maximum concentration. For practical purposes, a maximum allowable concentration of 5 ppb was set by Health Canada [96]. Infants and young children are the most susceptible to lead poisoning due to the effects on their physical and mental development. Lead exposure in children is linked to growth defects, nerve damage, and decreased function of blood cells. In adults, lead exposure can lead to adverse cardiovascular effects, impaired kidney function, and reproductive problems [97].

A DNAzyme-based QCM-D method for measurement of lead(II) ions was developed by Teh et al. This sensor uses a 5-MHz gold-coated quartz crystal as the microbalance. The crystal was firstly functionalized with a thiol-modified GR-5 strand, then filled with 6-mercaptohexanol, a blocking agent. An AuNP-hybridized DNAzyme was then introduced to bind with the immobilized GR-5. Upon the addition of lead(II), the bound AuNP/DNAzyme is released, which increases the frequency and decreases the dissipation factor of the QCM. This can be correlated to the concentration of lead(II) in solution (Figure 8).

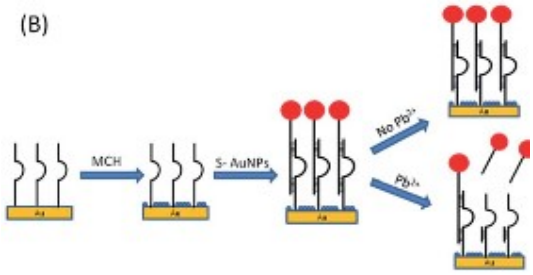

Figure 8. Sensing mechanism of the lead(II)-selective quartz crystal microbalance (QCM) method. Reprinted with permission from Reference [95]; Copyright 2014 Royal Society of Chemistry.

The increases in frequency were correlated to the concentrations of lead(II), and a linear relationship was obtained for the range of 46–3000 nM (10 ppb to 622 ppb) with an R^2 value of 0.997. The detection limit of the sensor was determined to be 14 nM (3 ppb). When the dissipation was correlated with the concentration, a range of 66–3000 nM (14 ppb to 622 ppb) and a detection limit of 20 nM (4 ppb) were observed ($R^2 = 0.994$). When tested against other interferences, the DNAzyme was only released in the presence of lead(II), making it quite selective. Tap-water samples were also tested and gave comparable values to the standard ICP-MS method [98].

A colorimetric method for lead(II) detection using polyazomacrocycles was developed by Ranyuk et al. When using a triamide-substituted diaminoanthraquinine-linked polyazomacrocycle, a blue shift was seen in the presence of lead(II) from 571 nm to 524 nm (in a 50 μM solution of HEPES buffer, pH 7.4). This blue shift accompanies a visual change of the solution from violet to pink. This change is quantitative, as different concentrations of lead(II) in solution proportionally blue-shift the absorbance peak. Through UV/vis titration, the detection limit was determined to be 21 ppb, with a

molar extinction coefficient of 4.9×10^3 L·mol^{-1}·cm^{-1}. When tested against silver(I) and cobalt(II), no distinct changes were observed, showing that this sensor is selective to lead(II) [99].

A colorimetric method of lead(II) detection based on tetrathiafulvalene (TTF)-π-pyridine derivatives was developed by Xue et al. The interaction between the pyridyl groups and lead(II) leads to the color change seen in the molecule solution (Figure 9a).

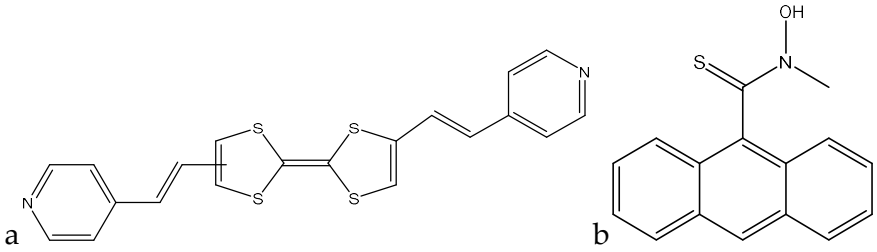

Figure 9. The (**a**) TTF-π-pyridine derivative used for lead(II) sensing and (**b**) the fluorescent anthracene derivative for lead(II) detection.

The absorbance peaks at 301 nm and 440 nm decrease proportionally with the increase of the new peaks at 330 nm and 55 nm with increasing concentrations of lead(II). This is accompanied by a visual color change in the solution from yellow to purple. A linear range for this sensor was obtained going from 0–6.1×10^{-5} M (0 ppb to 13 ppm) [100].

A fluorescence method based on anthracene derivatives for the detection of lead(II) was developed by Chae et al. This molecule is complexometric, and binding to lead(II) enhances fluorescence in an aqueous solution (Figure 9b). Prior to exposure to lead(II), the sensor molecule possesses weak fluorescence at 420 nm due to the lone pairs on the thioamide group. When lead(II) complexes at the thioamide group, fluorescence is enhanced due to the lone pairs being used for complexation. The fluorescence is only linearly proportional up to 0.5 equivalents of lead(II), which indicates that the sensor molecule binds to the lead(II) in a 2:1 fashion. Although analytical data are not available for this sensor molecule, it shows promise as a quantitative fluorometric method to measure lead(II) in aqueous solution [101].

A method of fluorescent lead detection through the use of catechin-synthesized Au nanoparticles was developed by Wu et al. This sensor is based on the lead(II)/catechin complexes and the lead/gold alloy that forms on the catechin/AuNP surface, mimicking the catalytic activity of the hydrogen peroxide oxidation of Amplex UltraRed. This enhances the emission peak at 588 nm when excited with a 540-nm source. This enhancement is linearly proportional to the concentration of lead(II) ranging from 10 nm to 10 μM (2 ppb to 2 ppm, $R^2 = 0.99$). A limit of detection of 1.5 nM (0.3 ppb) was achieved for this method. When compared to other cations, only lead(II) gave the fluorescence enhancement at 588 nm, indicating the selectivity of the probe. When comparing the method to AAS for real sample analysis, a *t*-test indicated that the results were not significantly different [102].

The ASV method used by Ruecha et al. mentioned for zinc(II) detection was also used for lead(II) detection. By using square wave ASV, the stripping current was correlated to the lead(II) concentration in solution at a stripping voltage of −0.75 V. A linear range of 1 ppb to 300 ppb was achieved for the method, as well as a detection limit of 0.1 ppb. In human serum, detection of lead(II) using the sample addition method gave recovery values close to 100%, suggesting that this method is quite accurate for detection of lead(II) [103].

The ASV method of copper(II) detection used by Zhao et al. was also used for lead(II) detection. The lead(II) was deposited at −1.5 V, and it exhibited a sharp stripping peak at −0.488 V. A linear correlation between the stripping current and the concentration of lead(II) was obtained over the range of 1.0–4.0 μM (207 ppb to 829 ppb) with an R^2 of 0.99. The calculated limit of detection was 1.5 nM (0.3 ppb) [81].

A method of lead(II) detection using a gold nanoparticle/reduced graphene oxide (AuNP/rGO) colloid for SERS was developed by Zhao et al. This sensor utilizes lead(II)-enhanced gold leaching.

This reduced the amount of AuNPs on the rGO, which decreased the SERS intensity of the rGO. These decreases in the Raman intensity at 1350 cm^{-1} were correlated to the concentration of lead(II). A linear range of 5–4000 nM (1 ppb to 829 ppb) was obtained with an R^2 value of 0.9926. The limit of detection obtained for this method was 1 nM (0.2 ppb). When testing in real samples, the sample addition method provided recoveries above 90%. When testing against an array of other cations, only lead(II) was able to induce gold leaching on the AuNP/rGO surface, which means that this method is quite selective to lead(II) [104].

An SERS method of detecting lead(II) based on a DNAzyme was developed by Wang et al. This method takes advantage of the catalytic reaction that occurs when the DNAzyme binds to lead(II). Onto a gold surface, the DNAzyme was immobilized. A substrate-modified gold nanoconjugate was bound to the substrate. When lead(II) was present, the bond between the substrate and the DNAzyme was cleaved, decreasing the intensity in the Raman signal. The decrease in the peak at 1584 cm^{-1} was correlated to the concentration of the lead(II), which gave a detection range of 20 nM to 1 μM (4 ppb to 207 ppb), with a detection limit of 4 ppb. When tested against other cations for interference, there was no significant decrease in the signal (although some of the cations, such as zinc(II), are known to cleave the substrate–DNAzyme bond), indicating that this method is selective [105].

A flow injection method for the determination of lead(II) through FAAS was developed by Rodriguez et al. This method uses a packed microcolumn to preconcentrate the lead(II), which is then eluted and run through the nebulizer, using AAS for analysis. The microcolumn is packed with silica gel treated with a mixture of Aliquot 336 and nitroso-R-salt. When testing the effects of pH on the adsorption of the lead(II) by preconcentrating between pH 3 and 7, an optimal range of pH 5.2 to 5.9 was obtained; thus, the tests were carried out at pH 5.5. Different eluents (HCl, $HClO_4$, and EDTA) were also tested for removal of lead(II) from the column, and HCl was found to be the best eluent, since EDTA was inefficient in the removal of lead(II), and $HClO_4$ removed the nitroso-R-salt from the column. Using the 217-nm resonance line, a calibration curve was obtained over the range of 0 ppb to 100 ppb, and was found to have a linear correlation, with a limit of detection of 4 ppb. When tested against various other cations and anions for interference, only nickel(II) and fluoride caused any interference. However, since the concentrations of these ions in water are negligible, there is no need to take any extra precaution. When tested with real water samples, the values obtained were in line with the values obtained by the standard ET AAS method, with no significant difference at 95% confidence [106].

An FAAS method for the determination of lead(II) using a microcolumn was developed by Ensafi et al. This method, just like the one previously described, utilizes a microcolumn to preconcentrate the lead from solution. However, rather than silica gel, this microcolumn is packed with activated carbon loaded with pyrogallol red. Pyrogallol red has a high binding constant with lead(II) between pH 5 and 6.5, and, since pyrogallol red is a polycyclic and aromatic, it can adsorb onto the activated carbon through π–π stacking interactions. To elute the lead(II) from the column, a 0.5 M solution of HNO_3 was used, since higher concentrations did not improve recovery from the column. When testing a wide array of cations, no other cation was observed to interfere, since pyrogallol red is quite specific to lead(II). When testing real samples using the sample addition method, recoveries between 97% and 104% were obtained, showing that this method is quite reliable for sensing [107].

3.7. Mercury

The main source of mercury in water is through atmospheric deposition or the discharge of industrial wastes. In water, mercury, usually in the form of methylmercury, is bioconcentrated by fish. Health Canada recommends an MAC of 1 ppb for mercury, due to the fact that long-term exposure leads to adverse neurological effects. Large doses can cause irreversible damage to the central nervous system. Dermal exposure can cause toxic dermatitis and eczema [108].

Rasheed et al. developed three rhodamine-based methods for the colorimetric detection of mercury(II) in aqueous solution. The first two methods are based on the fluorescence enhancement of

rhodamine B derivatives from complexation with mercury(II) in solution. The first rhodamine B derivative (TS) uses a mercury(II)-selective 2-aminothiazole receptor with the rhodamine backbone as the fluorophore. When tested in acetonitrile/water (7:3 *v*/*v*, 10 mM HEPES at pH 7.0) solution, an enhancement was seen in both the absorbance and the fluorescence spectra at 580 nm and 559 nm, respectively. This was accompanied by a visual color change from colorless to pink upon complexation (due to the complexation-induced spirolactam ring opening). The limit of detection for this sensor is 0.326 μM (65 ppb), and the linear range goes up to 12 μM (2 ppm). The second rhodamine B derivative (PST) replaces the 2-amiinothiazole receptor with a 2-amino-5-bromopyridine receptor. When tested in acetonitrile/water (8:2 *v*/*v*), the same absorbance and fluorescence peaks were observed at 580 nm and 559 nm, respectively. This was also accompanied by a visual change in color from colorless to pink. The limit of detection for this derivative is 0.63 μM (126 ppb), and the linear range goes up to 10 μM (2 ppm). When both derivatives were tested against other ions for interference, none gave the colorimetric response that mercury(II) exhibited, making these sensors quite selective [109,110]. The third method is based on the functionalization of an alternating copolymer vesicle using a rhodamine B derivative for the detection of mercury(II). The previously mentioned derivative PST was immobilized onto the self-assembled copolymer vesicle through the nucleophilic substitution of the bromide on the pyridine ring. When tested in aqueous solution, the same absorbance and fluorescence peaks were seen at 580 nm and 559 nm, which was accompanied by the same color change from colorless to pink. The limit of detection for this method, however, is much lower at 53 nM (10 ppb), with the linear range going up to 10 μM (2 ppm) ($R^2 = 0.998$) [111].

A ratiometric method of detecting mercury(II) was developed by Kim et al. This method uses the change in the absorbance spectrum induced by the complexation of mercury(II) to deduce the concentration of mercury(II) in a sample (Figure 10a).

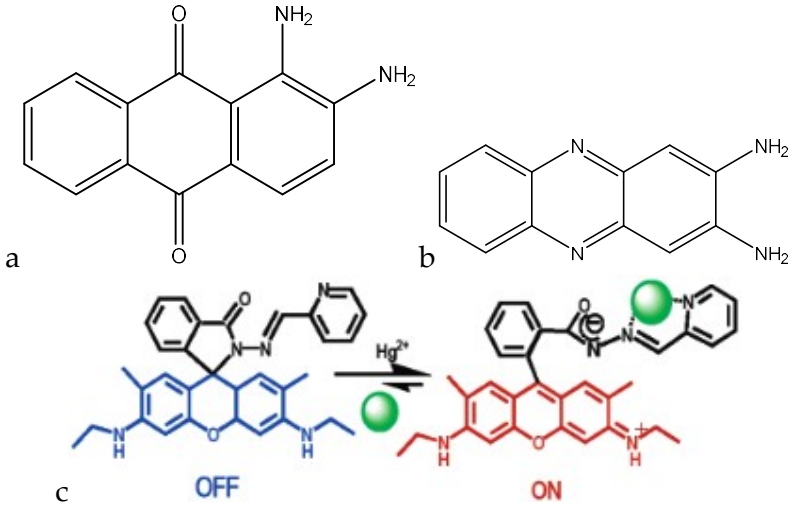

Figure 10. The structures of (**a**) 1,2-diaminoanthraquinone and (**b**) 2,3-diaminophenazine, and (**c**) the detection mechanism of the rhodamine 6G fluorophore (reprinted with permission from Reference [109]; Copyright 2007 American Chemical Society).

Upon the titration of mercury(II) into a 10^{-4} M solution of 1,2-diaminoanthraquinone in DMSO, the absorbance peak at 528 nm decreases proportionally to the amount of mercury(II) added. In addition, an increase in the absorbance peak at 461 nm is seen. When compared to other cations, none gave the change in the absorbance spectrum that mercury(II) gave, which shows the selectivity of this sensor molecule. Although there are no analytical data with regard to this molecule, it shows promise as a selective mercury(II) colorimetric sensor [112].

A method of colorimetric detection of mercury(II) using silver nanoparticles (AgNP) was developed by Firdaus et al. This method takes advantage of the fact that mercury(II) has a higher reduction potential than silver(I). Thus, the AgNPs ionize in the presence of mercury(II), changing the

color of the solution from yellow-brown (due to aggregation of AgNPs) to colorless. Upon addition of mercury(II) to the sensor molecule, a decrease in the absorbance peak at 420 nm was observed, which was proportional to the amount of mercury(II) added. A linear range of 5 μM to 300 μM (1 ppm to 60 ppm) was obtained with an R^2 value of 0.9988, and a limit of detection of 0.85 μM (170 ppb) was achieved. When comparing to other interfering cations, only the mercury(II) gave a significant decrease in absorbance at 420 nm, making this a very selective molecule for mercury(II) detection (although the LOD is too high for public use). Real sample tests using the sample addition method gave recovery values of above 95%, which demonstrates the selectivity of the molecule in a matrix full of interfering ions [113].

A fluorescent method of detecting mercury(II) through the use of 2,3-diaminophenazine (DAP) particles was developed by Liu et al. The nanoparticles were fabricated through the UV irradiation of *o*-phenylenediamine (oPD) in aqueous solution. This irradiation leads to a yellow dispersion, which has a distinct emission wavelength (Figure 10b). DAP emits at a wavelength of 554 nm, which is quenched by the presence of mercury(II) in solution. When the mercury(II) was titrated into solution, the fluorescence intensity at 554 nm decreased proportionally to the concentration of mercury(II) over the range of 1 nm to 500 μM (0.2 ppb to 100 ppm), with a detection limit of 1 nM (0.2 ppb). When testing other cations for interferences, no other interfering cation gave the fluorescence quenching that mercury(II) did, which shows that the DAP nanoparticles are selective toward mercury(II) [114].

A rhodamine 6G-based fluorophore for the detection of mercury(II) was developed by Wu et al. This probe is complexometric and exhibits a fluorescence enhancement upon binding to mercury(II) (Figure 10c). Unbound, the fluorophore is found in the spirolactam phase, making it colorless in DMF/H_2O media. Upon the complexation of mercury(II), the spirolactam ring opens, inducing fluorescence. When mercury(II) was titrated into a solution of the fluorophore, proportional emission enhancements were seen at 560 nm. A linear range was obtained going from 2 ppb to 20 ppb, with a limit of detection of 2 ppb. When comparing the response of mercury(II) to other cations for interference, only mercury(II) complexation led to ring opening, which provides enhanced fluorescence. This demonstrates the selectivity of the fluorophore for use as a mercury(II) sensor [115].

A potentiometric method using calixarene ionophores for mercury(II) detection was developed by Tyagi et al. The working electrode is made of a *p-tert*-butyl-calix[4]arenethioether derivative along with PVC and a sodium tetraphenylboraten (NaTPB) anion excluder in THF, and an SCE is used as the reference electrode. Since the ionophore has a high binding constant with mercury(II), the potential changes due to the sulfur donor atoms in the calixarene ionophore complexing with mercury(II). This causes an increase in the potential, which can be correlated to the concentration of mercury(II) in solution. A linear range was obtained going from 72 nM to 1 mM (14 ppb to 201 ppm). The sensor was not physically tested with other interferences; rather, ab initio calculations were used to determine the interactions. Soft metals show the strongest interaction, of which mercury(II) is the strongest [116].

An ASV method using AuNP/CNT composites for the detection of mercury(II) was developed by Xu et al. This method used a glassy carbon electrode modified with the AuNP/CNT nanocomposites to increase the number of electroactive sites for mercury(II) detection. Differential pulse (DP) ASV was used to strip the electroplated mercury from the electrode. A distinct stripping peak at +0.63 V is seen, which corresponds to the oxidation of mercury(II) from the electrode. This peak was proportional to the amount of mercury(II) in the solution, and it was correlated to the concentration to create a calibration curve. This calibration curve gave a linear range of 0.5 nM to 1.25 μM (0.1 ppb to 251 ppb) with an R^2 value of 0.99. The detection limit of this method was determined to be 0.3 nM (0.06 ppb), which is much lower than the maximum allowable concentration of many countries [117].

A chemiresistive sensor based on single-walled (SW) CNTs and structure-switching DNA for the detection of mercury(II) was developed by Gong et al. This method is based on the adsorption of amino-labeled polyT onto a SWCNT, followed by hybridization with polyA (Figure 11).

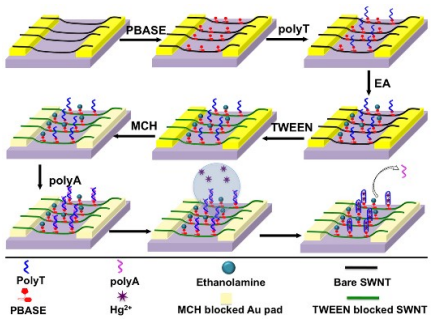

Figure 11. Schematic of the fabrication and sensing mechanism. Reprinted with permission from Reference [18]; Copyright 2013 AIP Publishing.

Once mercury(II) is exposed to the sensor surface, the polyT/polyA duplex is dehybridized, which releases the polyA from the surface and increases the conductivity of the sensor. The changes in conductivity were correlated to the concentration of mercury(II), and a linear correlation was found for the range going from 100 nM to 1 μM (20 ppb to 201 ppb). When tested against other cations, mercury(II) gave the largest change in conductivity of the film, having more than double the response, which proves the selectivity of this method [118].

An SERS method using gold nanostar dimers for mercury(II) detection was developed by Ma et al. This method functions through the mercury(II)-induced conjunction of the thymine base pair, which dimerizes the DNA-functionalized gold nanostars and enhances the Raman peak. A 60-nm gold nanostar dimer was chosen as the substrate for this experiment, and 4-aminothiophenol was used as the Raman reporter molecule. Upon addition of mercury(II), the 4-aminothiophenol peak at 1083 cm^{-1} was enhanced proportionally to the amount of mercury(II) added, due to the effect of mercury(II) on the dimerization of the gold nanostars. A linear range of 2 ppt to 1 ppb was obtained, with an R^2 value of 0.99. The limit of detection obtained was 0.8 ppt, demonstrating the incredible sensitivity of this method. When comparing to other cations for interference, mercury(II) gave a Raman peak enhancement five times greater than the other cations, which shows that this method is selective as well [119].

A SERS method based on gold microshells for the detection of mercury(II) was developed by Han et al. This method uses an oligonucleotide-modified gold microshell, which undergoes a conformational change through exposure to mercury(II) ions. This conformational change occurs due to the mercury(II) ion being able to selectively bind to the thymine bases of two strands to form stable base pairs. This generates an enhancement of the Raman peak. Tetramethylrhodamine was used as the SERS signal generator for this method. With the addition of mercury(II), enhancement of the Raman peak at 1650 cm^{-1} is seen, which is proportional to the amount of mercury(II) added. A detection range was obtained going from 50 nM to 10 μM (10 ppb to 2 ppm), and, when the response was compared against other cations for interference, mercury(II) gave the highest enhancement even when the concentration of mercury(II) was five times less [120].

An AAS method based on solid-phase extraction to detect mercury(II) was developed by Pourreza et al. This method utilizes a minicolumn packed with 2-mercaptobenzimidazole and agar–agar. The sample is preconcentrated into the column, then eluted through the use of 3 M HCl, and analyzed via cold vapour (CV) AAS. Citrate buffer at pH 2.5 was found to be the optimal condition for the sorption of mercury(II) onto the column. The maximum absorbance signal was also obtained when the reducing agent concentration (concentration of $SnCl_2$) was at 2.0%. A linear range for this method was obtained going from 40 ppt to 2.4 ppb, with an R^2 value of 0.9994. The limit of detection for this method was also determined to be 20 ppt, much lower than limits set by many countries. When interference studies were performed, no other ion (except for Cl^- due to the formation of $HgCl_4^{2-}$) had any significant response. Real water samples were also tested using the sample addition method, and the recovery for each trial was above 95% [121].

3.8. Nickel

Nickel occurs in drinking water through the leaching of metals in the fittings found in household piping. The boiling of water in electric kettles can also introduce nickel into drinking water, specifically in decalcified kettles. Common adverse effects of nickel overconsumption include gastrointestinal issues, dermatitis, and oral hyposensitization. Based on the effects of nickel on the digestive system, a maximum limit of 70 ppb is recommended by the World Health Organization [122].

A colorimetric method for the determination of nickel(II) in aqueous solution was developed by Liu et al. This method utilizes a quinolone based chemosensor, which undergoes a color change from yellow to red upon exposure to nickel(II) (Figure 12a).

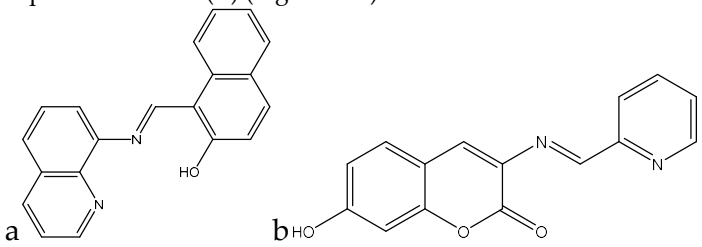

Figure 12. The (**a**) quinolone-based nickel(II) chemosensor and (**b**) the coumarin derivative used for nickel(II) detection.

When tested in DMSO/H_2O (1:1 *v*/*v*) in HEPES buffer at pH 7.4, the absorbance at 525 nm increased, following a linear correlation with an R^2 value of 0.9887. A limit of detection of 0.22 μM (13 ppb) was obtained with a linear range of 8.6 μM to 15.2 μM (505 ppb to 892 ppb). When tested against other cations for interference, only nickel(II) was able to induce the yellow-to-red color change along with the increase in absorbance at 525 nm. Test strips were also fabricated with this chemosensor, with a limit of detection of 5.0 μM [123].

A coumarin-based colorimetric sensor for nickel(II) ions was developed by Jiang et al. This molecule experiences a red shift from 341 nm to 540 nm upon interaction with nickel(II), which is accompanied by a visual color change going from colorless to pink (Figure 12b). When tested with nickel(II) in EtOH/H_2O (1:1 *v*/*v*), a ratiometric response was observed, with a simultaneous decrease in absorbance at 341 nm and an increase in absorbance at 540 nm. A detection limit of 0.5 μM (29 ppb) was obtained, and a linear range from 4 μM to 20 μM (235 ppb to 1 ppm) was observed with an R^2 value of 0.995. When tested against other cations for interference, copper(II) and mercury(II) did induce red shifts of 50 nm and 84 nm, respectively. However, the red shift induced by nickel(II), as well as the enhancement in absorption, was much larger, making this molecule quite selective to nickel(II) [124].

A potentiometric method for the determination of nickel(II) was developed by Tomar et al. The nickel(II)-specific ionophore used was the novel Schiff base 3-aminoacetophenonesemicarbazone (AASC). To construct the nickel(II) ion-selective electrode (ISE), AASC, PVC, plasticizer (dibutylphosphate, DBP), and anion additive (sodium tetraphenyl borate, NaTPB) were combined in a ratio of 4:30:64:2 *w*/*w* in 5 mL of THF. This mixture was evaporated until an oily mixture remained. A Pyrex tube was coated with this mixture, and conditioned for 24 h by soaking it in a 0.01 M solution of $Ni(NO_3)_2$, while using a saturated calomel electrode (SCE) as an internal reference. When tested with nickel(II) in aqueous solution, a Nernstian slope was obtained for a range spanning 0.1 μM to 0.01 M (6 ppb to 587 ppb), with a detection limit of 51 nM (3 ppb). When tested against other cations for interference, nickel(II) gave the largest Nernstian slope, making this electrode quite selective to nickel(II). The electrode is stable between pH 2.0 and 9.8. Below a pH of 2.0, the ionophore begins protonating, preventing selective binding of nickel(II). Above pH 9.8, $Ni(OH)_2$ formation occurs, preventing binding to the electrode. This electrode was also used in real samples (milk powder and

chocolate), and the values obtained by the ISE were comparable to values obtained by the standard AAS method of detection, making this a reliable method for nickel(II) detection [125].

An ASV method for the detection of nickel ions using boron-doped diamond electrodes was developed by Musyarofah et al. The experiment was performed in 0.1 M phosphate buffer solution, using Pt wire as the counter electrode and an Ag/AgCl electrode as the reference. Deposition of the nickel(II) ions onto the electrode was performed at a potential of −100 mV for 5 min. When the potential was increased to strip the nickel from the electrode, a peak was seen at +1.1 V, with the current at that potential correlating to the concentration of nickel(II) in solution. A linear calibration curve going from 5 mM to 200 mM (293 ppm to 11,739 ppm) was obtained, with an R^2 value of 0.9929. Although this method of detection is not very sensitive with respect to regulation, it shows potential as an electrochemical method for determination of nickel(II) in aqueous media [126].

An AAS method of detecting nickel(II) by chemical vapor generation in situ was developed by Matusiewicz et al. The sample is firstly vaporized by continuous flow hydride generation (using $NaBH_4$ as the hydride donor). The vaporized nickel hydride is then trapped in an integrated atom trap and heated by an air–acetylene flame. Using this method, the detection limit was determined to be 0.21 ppb, with a linear range of 1 ppb to 50 ppb (R^2 = 0.9922). When tested with certified NIST (National Institute of Standards and Technology) samples, the values obtained by the AAS method were comparable to the certified values provided. Real samples were also tested and provided good recovery, making this a highly sensitive method for detection of nickel(II) in aqueous solutions [127].

3.9. Silver

Silver is commonly used as a disinfectant for commercial water filters. Leaching of the silver ions from the metallic silver used in the filter can introduce silver ions into drinking water sources. Although there is no evidence of silver having any adverse effect on human physiology (aside from argyria, which causes a blue discoloration of the skin), since it is not an essential element, any exposure to silver is unwanted. There is no strict guideline for silver in drinking water; however, the World Health Organization recommends an upper limit of 0.1 ppm [128].

Lee et al. developed a QCM method for detecting silver(I) in situ. For this, they use a quartz crystal functionalized with 5′–CCCCCCCCCCCCCCCCCCCCCCCCCCCCCC-3ThioMC–3′, a silver-specific nucleotide. For detection, a silver(I) containing solution was combined with a 1 mM solution of cytosine in a 1000:1 ratio. Calibration solutions ranged from 10 pM to 1 μM (0.001 ppb to 108 ppb) (Figure 13).

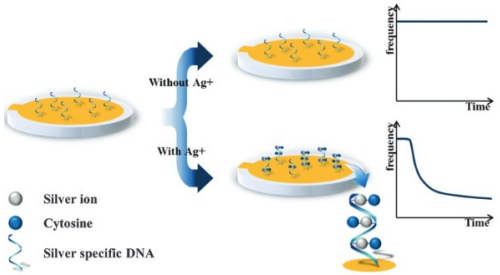

Figure 13. Illustration of the detection mechanism of silver(I). Reprinted with permission from Reference [117]; Copyright 2015 Royal Society of Chemistry.

The limit of detection for this sensor is 100 pM (0.01 ppb), with a limit of quantification (LOQ) of 1 nM (0.1 ppb). However, when reusability was tested, a decrease in the change in frequency was observed (repeated exposure to 1 μM gave lower frequency shifts each time); thus, the sensor can only be used twice. Selectivity was also tested for this sensor by conducting the same experiment with various ions in the solution matrix. Only silver(I) was able to give a discernible signal at 1 μM (other ions were negligible). The sensor was also tested in real drinking water, where it maintained the same LOD and LOQ, although the frequency shifts were smaller [129].

A direct colorimetric detection method in aqueous solution for silver(I) was developed by Qin et al. This method utilizes a water-soluble organometallic polyelectrolyte which goes from colorless to yellow upon exposure to silver(I) ions. Upon the addition of 10 μM silver(I) (1.08 ppm), a red shift of 25 nm was seen at the λ_{max} of 390 nm. A calibration curve was made, correlating the red shift in the λ_{max} of the silver(I)-specific molecule to the logarithm of the concentration. A linear correlation was found between the two, with an R^2 value of 0.99 (using 5×10^{-6} M sensor molecule). The linear range was determined to be 1 μM to 4 mM (108 ppb to 432 ppm) with a limit of detection of 0.5 μM (54 ppb) [130].

A detection method using gold nanoparticles for the colorimetric detection of silver(I) was developed by Lin et al. Gold nanoparticles are capped with citrate ions, which are then functionalized with Tween-20. Silver(I) is reduced and plated onto the surface of the gold nanoparticles, which causes Tween-20 to be removed from the gold nanoparticle, inducing aggregation. In the absorbance spectrum, this is seen as a drop in absorbance at 520 nm, and an increase in absorbance at 650 nm. The ratio of the absorbance was correlated to the concentration of silver(I) in solution. A calibration curve was made going from 0–1000 nM (0 ppb to 108 ppb), and it gave a linear range of 4×10^{-7} to 1×10^{-6} M (43 ppb to 108 ppb), with an R^2 of 0.9935 [131].

A fluorogenic probe for detecting silver(I) ions in water was developed by Chatterjee et al. The molecule used for detection, a rhodamine B derivative, is colorless in a 20% ethanol solution. Upon the addition of silver(I) ions, the solution turns pink, and a fluorescence peak arises at 584 nm. This occurs due to the spirolactam ring opening of the rhodamine B derivative induced by the silver(I) ions (Figure 14).

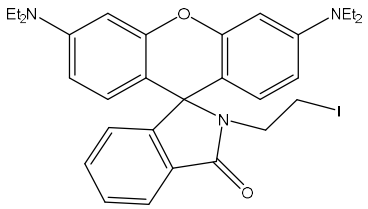

Figure 14. Structure of the rhodamine B derivative.

When tested against other cations, only the silver(I) led to ring opening of the molecule and induced a fluorescence enhancement. The fluorescence enhancement was linear with respect to the concentration of silver(I) over the range of 11 ppb to 540 ppb, and a limit of detection of 14 ppb was obtained [132].

Chae et al. developed a fluorometric method for determination of silver(I) using an anthracene derivative. This anthracene derivative utilizes the oxidation of a thioamide group to enhance fluorescence of the analyte solution proportionally to the concentration of the analyte (Figure 15).

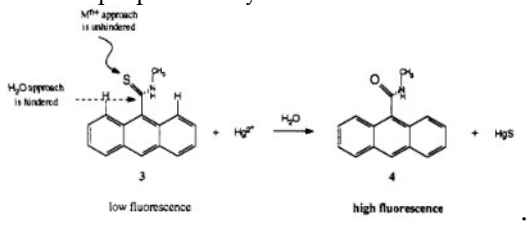

Figure 15. Mechanism of the oxidation of the thioamide group using mercury(II) as a reference. Reprinted with permission from Reference [121]; Copyright 1992 American Chemical Society.

When silver(I) was titrated into a 23 μM solution of the fluorescent molecule in 0.01 M 4-(2-hydroxyethyl)-1-piperazineethanesulfonic acid (HEPES) buffer (pH 7), a fluorescence enhancement was seen that was proportional to the silver(I) present in solution. The enhancement was linear up to two equivalents, indicating that this enhancement occurs in a 2:1 stoichiometry for silver(I) [133].

Polymer electrodes for the potentiometric detection of silver(I) in solution were developed by Rubinova et al. The selective membrane consists of *o*-xylylenebis(*N*,*N*-diisobutyldithiocarbamate) (copper(II) ionophore (I)), lipophilic cation exchanger, tetradodecylammonium tetrakis(4-chlorophenyl)borate (ETH 500), and methylmethacrylate–decylmethacrylate (MMA–DMA)/polyvinyl chloride/bis(2-ethylhexyl) sebacate (PVC/DOS) in a 9:1 ratio in THF. In methylene chloride solution, the PVC/DOS was omitted. Both solvents were used to determine which would be best for coating the gold wire for use in small volumes. The electrode was constructed by taking a gold wire and soldering it to a copper wire for electrical contact. The gold wire was then cleaned with sulfuric acid, then rinsed with acetone and left in chloroform for 3 min. A solution of poly(3-octylthiophene) was then added to the gold wire until the color of the wire was black. The membrane was then added by coating the wire with the membrane solution, and then evaporating the THF (or methylene chloride). The membrane made using methylene chloride solution was found to be best for microelectrode fabrication, and it was used for the experiment. A sodium-selective liquid-contact electrode was used for reference. Using this method, the electrode made in methylene chloride solution gave a detection limit of 0.63 nM (65 ppt), with a Nernstian response over the range of 1 nM to 10 μM (0.1 ppb to 1 ppm). These results were reproducible, and alternating concentrations showed that the response is reversible [134].

A calixarene-based ion-selective electrode for potentiometric detection of silver(I) was developed by O'Connor et al. The set-up was a conventional electrode utilizing a PVC membrane with various calixarene derivatives incorporated (with different ratios of sulfur and nitrogen groups). Using an SCE reference electrode, a detection limit of 100 μM (10 ppm), with a linear response slope of 51.74 mV/decade up to 0.01 M (1079 ppm), was obtained when the membrane was deposited onto glassy carbon electrode. When tested against various interferences, with the main interferences being sodium, lead(II), and mercury(II), mercury(II) and lead(II) poisoned the electrodes, with the silver(I) response decreasing after exposure to these ions (due to these ions being thiophilic). Sodium did not poison the electrode, however, and its presence did not affect the silver(I) response [135].

A square wave ASV method to determine silver(I) ions in surface water was developed by Schildkraut et al. This method utilizes a carbon paste electrode as the working electrode, with an SCE being used as a reference. Carbon paste was chosen over glassy carbon electrode and platinum electrode due to better sensitivity and less interference from the background. Water hardness was seen to have an effect on the stripping peak of the silver(I) at +0.170 V, which was seen through the decrease of the full width-half maximum (FWHM) as the hardness increased. Over the range of 0.2 ppb to 2 ppb, a linear correlation between peak current and silver(I) concentration in potassium hydrogen phthalate (KHP) buffer was found, with an R^2 value of 0.991. Calibration curves were also made for different matrices, such as an NIST 1643c trace metal standard, a moderately hard synthetic water solution, and an SLRS-3 (St. Lawrence river) water reference. The calibration curves in the SLRS-3 and the moderately hard water were comparable to the original calibration curve in KHP buffer, but the calibration curve for the NIST 1643c had a much lower slope. This was found to be due to the higher acidity of the NIST 1643c (0 pH) compared to the SLRS-3 (1.6 pH). The NIST 1643c sample also splits the peak into two, with a smaller stripping peak appearing at +0.040 V. Due to this, a calibration curve correlating peak charge to concentration was created, which gave better slopes and higher correlation coefficients than the current measurements (R^2 = 0.993). The detection limit of this method was 0.2 ppb [136].

An ASV method using polythiophene-modified platinum electrodes was developed by Zejli et al. The platinum thiophene electrode was placed in a stirred solution of 0.2 M KNO_3 at pH 5 along with a platinum counter electrode and an Ag/AgCl reference electrode, and silver(I) was pipetted into the solution. The silver(I) was preconcentrated onto the electrode at a potential of −0.500 V, and the stripping current was scanned from +0.0 to +0.700 V. The characteristic silver(I) stripping peak was seen at +0.170 V. The pH of the solution was seen to have an effect on the stripping current seen, with the current increasing from pH 2 to pH 5 (the maximum), and then decreasing above pH 5 (possibly due to the formation of AgOH). A linear correlation of the current with respect to the silver(I)

concentration was seen from 70 ppb to 1 ppm, with an R^2 value of 0.995. The detection limit for this method was found to be 60 ppb. When testing various interferences, their stripping peaks were well separated from that of silver(I), which indicates that this method is quite selective [137].

BNAS, a new Schiff base ligand, was used in an AAS method for the detection of silver(I) ions developed by Shamspur et al. This method utilizes a C_{18}-bonded silica membrane that BNAS adsorbs onto to preconcentrate the membrane with silver(I) ions. The silver(I) is then eluted, and the concentration of silver(I) in solution is determined by FAAS (Figure 16).

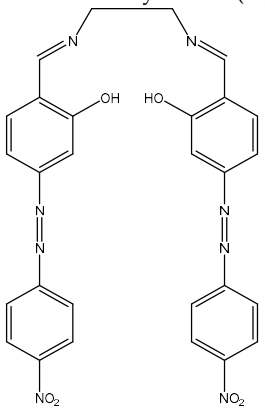

Figure 16. The structure of BNAS.

A 0.5 M thiosulfate solution was used to elute the silver(I) ion, and the optimal pH for extraction was found to be between pH 5 and 7.5. A linear range was obtained from 1 ppb to 50 ppb, with a limit of detection of 10 ppt. Interferences were also investigated to observe their effects on the recovery of silver(I). Although the interferences were in the ppm range, the recovery of silver(I) ions remained above 90% [138].

An AAS method using a silica gel modified with 2,4,6-trimorpholino-1,3,5-triazin was developed by Madrakian et al. This method utilizes preconcentration in a packed column followed by elution and determination of the silver(I) concentration by FAAS at 328.1 nm (Figure 17).

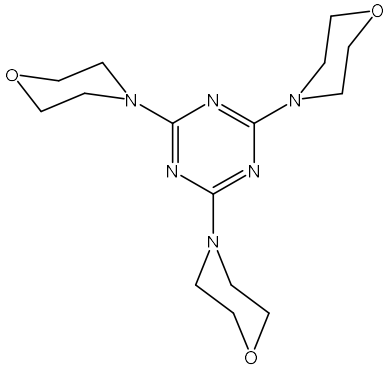

Figure 17. The structure of 2,4,6-trimorpholino-1,3,5-triazin.

The optimal pH range for adsorption onto the column was found to be pH 3–6, since the molecule protonates below pH 3 and silver(I) hydrolyzes above pH 6. For the experiment, the pH was kept at 3.5. Using 0.05 M thiosulfate for elution of solvent, a linear correlation was seen over the range of 125 ppb to 2.25 ppm. Interference studies also showed that there was no strong interference affecting the signal, and recovery of silver(I) remained above 94% [139].

3.10. Uranium

In the environment, uranium is commonly found in its hexavalent form as uranyl (UO_2^{2+}). The most common use of uranium is as fuel in nuclear power stations and for catalysis. Uranium finds its way into water through emissions from nuclear plants, as well as leeching from natural deposits, and the use of uranium containing fertilizers. In humans, uranium is linked to nephritis, which is inflammation of the kidneys. The World Health Organization set a provisional guideline value of 30 ppb, while Health Canada has a maximum allowable concentration of 20 ppb [140,141].

A colorimetric sensor for uranium(VI) based on a DNAzyme/AuNP system was developed by Lee et al. In this method, the DNAzyme-functionalized AuNPs aggregate to form a purple-colored solution. Once exposed to uranium(VI), the aggregate disassembles, and the solution turns red. This colorimetric shift can be correlated to the concentration of uranium(VI) in solution. Using this method, the ratiometric shift between 490 nm and 550 nm was correlated to the concentration of uranium(VI) in solution, and a linear dependence was observed. The sensor had a linear response from 50 nM to 2 μM (12 ppb to 476 ppb), with a detection limit of 12 ppb. When tested against other cations for interference, only uranium(VI) led to the de-aggregation of the functionalized AuNPs and, consequently, the colorimetric response [142].

A colorimetric method based on a peroxidase memetic assay for the detection of uranium(VI) was developed by Zhang et al. This method of detection is based on the inhibition of peroxidase-like activity that bovine serum albumin (BSA)-functionalized gold nanoclusters (AuNSs) naturally exhibit. When exposed to uranium(VI), the peroxidase-like activity is inhibited, and a colorimetric response is generated which can be correlated to the concentration of uranium(VI) in solution. Due to the peroxidase-like activity, an absorbance peak at 652 nm is present for the free functionalized AuNS. Once uranium(VI) is added to the solution, the peak decreases proportional to the concentration of uranium(VI) in solution. A linear correlation was seen for the decrease with a range of 12–160 μM (3 ppm to 38 ppm) with an R^2 value of 0.9957. The limit of detection for this method was 1.86 μM (443 ppb). When compared to other cations that may interfere, uranium(VI) gave the largest response. Mercury(II) also gave a response, although it was not as significant as the uranium(VI). When tested in real water samples using the sample addition method, recovery for the method was 98% [143].

A fluorescent method for detecting uranium(VI) in water based on coprecipitation with calcium fluoride was developed by Perry et al. In this method, uranium was precipitated along with calcium fluoride; then, the precipitate was heated to 800 °C to calcify the sample. The samples were then pressed into pellets and analyzed using laser-induced fluorescence spectroscopy. The excitation wavelength was set to 488 nm for the test. The presence of uranium(VI) in the pellet led to a fluorescence enhancement at 530 nm. The enhancement was correlated to the concentration of uranium(VI) in solution, which yielded a linear range of 1 pM to 1 μM (0.2 ppt to 200 ppb) and a limit of detection of 0.04 pM (0.008 ppt), which is much lower than both WHO and Health Canada limits. Interference studies showed that the presence of other cations limits the linear range of the sensor, which only goes from 0.01 μM to 1 μM (2 ppb to 238 ppb) in a mixed solution. Analyses of real samples were in good agreement with their certified concentrations [144].

A fluorescent method based on an amidoximated polymer for the detection of uranium(VI) was developed by Ma et al. Upon binding to uranium(VI) in solution through the amidoxime groups on poly(diimino-2,2-dicyanoethylene), fluorescence of the polymer is quenched. This quenching is quantitative and can be correlated to the concentration of uranium(VI) in solution (Figure 18).

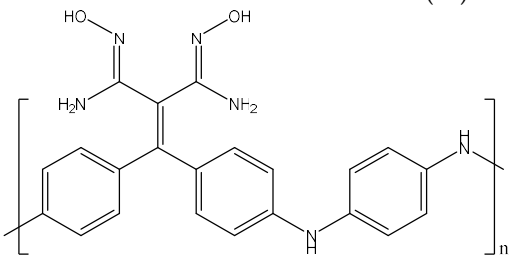

Figure 18. Structure of the amidoximated fluorescent polymer.

When uranium(VI) was titrated into a solution of polymer in dimethylacetamide (DMA)/H_2O (95/5, *v*/*v*), fluorescence quenching of the peak at 547 nm was seen proportional to the amount of uranium(VI) added to solution. A linear range was obtained going from 10 nM (the detection limit) to 150 nM (2 ppb to 36 ppb) with an R^2 value of 0.986. When tested against other ions, no other ions gave the quenching response that the uranium(VI) did, making this a very selective method for uranium(VI) detection. When real water samples were tested using the sample addition method, recovery values were above 98%, and the values obtained were in good agreement with the standard ICP-MS method [145].

A selective PVC membrane for potentiometric detection of uranium(VI) was developed by Hassan et al. This membrane incorporates tris(2-ethylhexyl)phosphate (TEHP) as the electroactive material and sodium tetraphenylborate (NaTPB) as the ion discriminator selective toward uranium(VI). An Ag/AgCl electrode was used as the reference for this test. When the electrode is exposed to uranium(VI), the TEHP acts as the ionophore and binds to the uranium(VI), leading to a change in potential. Between the pH values of 2.8 and 3.6, a linear correlation between the potential and concentration was obtained, with a range of 20 μM to 10 mM (5 ppm to 2360 ppm). A limit of detection of 13 μM (3 ppm) was observed for this sensor. When comparing with other cations for interference, there was no response generated except for high concentrations of calcium(II), iron(II), and fluoride, which means that this sensor can be applicable for testing in soft water [146].

A CNT-modified glassy carbon electrode (GCE) for detection of uranium(VI) through ASV was developed by Golikand et al. When the deposition potential of −0.40 V is applied, the CNTs adsorb the reduced uranium from solution. Once the voltage is swept in the positive direction (using square wave), the uranium oxidizes at its oxidation potential, and goes back into solution. The current given by the stripping peak can be correlated to the concentration of uranium(VI) in solution. When testing the effect of pH on the stripping response, the optimal response was found to be at pH 4.4. When uranium(VI) was added to a solution of 0.2 M acetate buffer (pH 4.4) and 0.01 M magnesium(II), the oxidation peak had a peak current that increased with increasing concentrations of uranium(VI). A linear calibration was obtained with a range of 5 nM to 120 nM (1 ppb to 29 ppb) with an R^2 value of 0.968. The detection limit for this method was determined to be 1 nM (0.2 ppb). When testing other cations and anions, their stripping peaks were quite distinct from the uranium(VI) peak, which makes this method very selective. When tested in real water samples, the sample addition method gave recoveries above 98% [147].

An SERS method for the detection of uranium(VI) was developed by Ruan et al. This method utilizes (aminomethyl)phosphonic acid (APA)-modified AuNPs as the active substrate. When uranium(VI) interacts with this substrate, an enhancement in the Raman peak can be seen, which can be correlated to the concentration of uranium(VI) in solution. Using the characteristic peak at 830 cm^{-1}, the level of enhancement was correlated with the concentration of uranium(VI). The peak height increased linearly up to 2 ppm, where it began leveling off. This method gave a limit of detection of 200 ppb when tested. When using this method in simulated and in actual groundwater, uranium(VI) was still able to be detected at sub-ppm levels [148].

An SERS method based on functionalized silver colloids for the detection of uranium(VI) was developed by Trujillo et al. Glutathione is used to functionalize the silver colloid, which gives a Raman peak enhancement when interacting with uranium(VI) in solution. When the uranium(VI) interacts with the functionalized silver colloid, a new peak at 834 cm^{-1} arises, indicating that the uranium(VI) is bound to the colloid. The height of this peak is related to the concentration of uranium(VI) in the colloid solution, and a linear calibration can be obtained. The linear range of this method is 250–650 nM (60 ppb to 155 ppb), with an R^2 value of 0.979. The detection limit for this method was determined to be 102 nM (24 ppb). When other cations were tested along with uranium(VI), a recovery of 88% was obtained, which, despite indicating a decrease in detection, is still suitable for use in a more complex matrix [149].

An AAS method for the detection of uranium(VI) using a crown ether was developed by Agrawal et al. For this method, the uranium(VI) in solution is extracted through the use of 5,14-N,N'-

hydroxyphenyl-4,15-dioxo-1,5,14,18-tetraaza hexacosane (NHDTAHA), and the extract is analyzed using GF AAS (Figure 19).

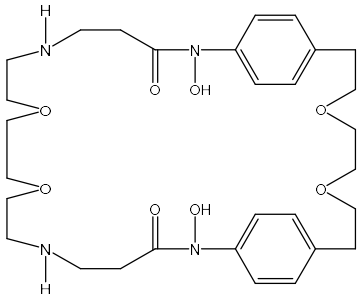

Figure 19. The structure of NHDTAHA.

The effect of pH was observed when extracting the uranium(VI). What was observed was that the maximum extraction for uranium(VI) occurred at pH 6–7. For the test, pH 6 was used. Many other ions were tested in the solution matrix to observe any effects on the recovery of uranium(VI), and none affected the extraction to a great degree. The limit of detection for this method was 10 ppb. When tested in real samples, the values obtained with this method were in good agreement with the certified values for the samples [150].

3.11. Zinc

Zinc is an essential element in human metabolism. Many enzymes in the body such as dehydrogenases, phosphatases, and more contain zinc [151]. The recommended daily intake of zinc is 0.3 mg/kg, with a maximum tolerance of 1 mg/kg of body weight. Adults require 15–22 mg of zinc per day [152]. When excess zinc is consumed, however, gastrointestinal issues (stomach cramps, vomiting, diarrhea) can occur within 3–12 h [153]. Zinc is also used for corrosion inhibition in various alloys, and is also used for galvanizing steel and iron, which is where the leaching of zinc into tap water is present [154]. As of present, there is no health guideline regarding zinc in drinking water; however, at 3 ppm, the water tends to be opalescent [155].

A colorimetric method of zinc(II) determination was developed by Kaur et al. using a hetarylazo derivative. The sensor that was developed is water-soluble and stable in pH >5, which makes it suitable for drinking water analysis (Figure 20a).

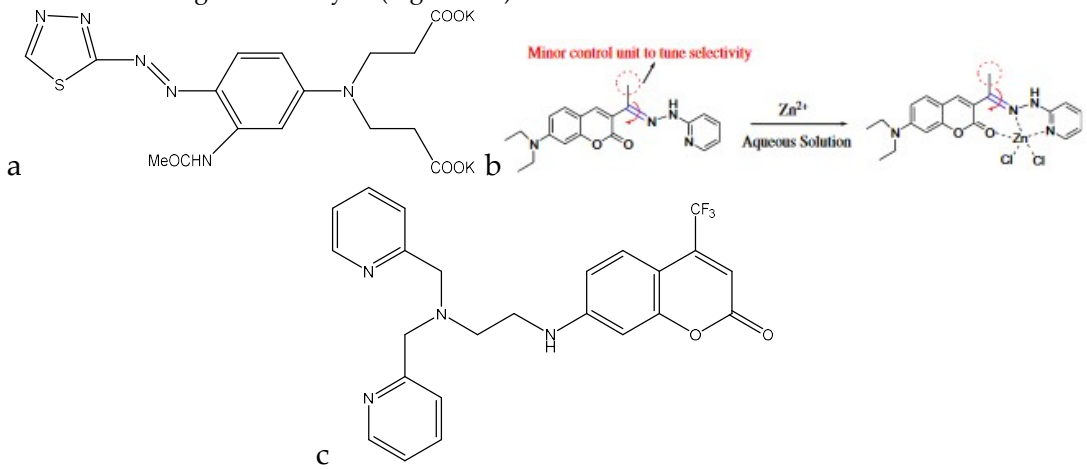

Figure 20. (**a**) Zinc(II)-selective hetarylazo derivative, (**b**) the detection mechanism of the sensor molecule (reprinted with permission from Reference [145]; Copyright 2012 Elsevier), and (**c**) structure of the fluorescent probe.

When zinc(II) was titrated into the sensor-containing solution (pH 7.5 and 0.01 M HEPES in the presence of 0.15 M NaCl), the absorbance peak at 518 nm dropped in intensity, while the peak at 481 nm increased. This ratiometric change was used to create a calibration curve ranging from 0.006–0.015 M (392 ppm to 980 ppm). The sensor was also able to be reset using excess EDTA, which means that the sensor molecule is reusable again for another sample. Interference studies showed that cadmium, calcium, and magnesium did not affect sensor performance, which indicates selectivity to zinc(II) [156].

A fluorescence-based sensor utilizing an imine derivative was developed by Wu et al. The sensing mechanism is based on the C=N isomerization that occurs when the sensor is exposed to zinc(II) (Figure 20b). The sensor has an enhancement in fluorescence when exposed to zinc(II) in CH_3CN/H_2O buffer solution, as well as a shift in the emission peak from 519 nm to 509 nm after exposure to zinc(II) over a range of 1–10 μM (65 ppb to 654 ppb). The quantum yield of the fluorescence increased after exposure to zinc(II) from 0.014 to 0.26. When tested against other metal ions, only zinc(II) gave a significant enhancement to the fluorescence. Cadmium enhances the fluorescence as well (although not as much as the zinc), and all other metals either had no effect on the fluorescence or quenched the fluorescence [157].

A coumarin-derived fluorescent probe for zinc(II) based on photo-induced electron transfer was developed by Li et al. (Figure 20c). In 0.1 M phosphate buffer at pH 7 and at 30 °C, the fluorescence was quite weak at 510 nm for the sensor itself, with a quantum efficiency of 0.15. Once zinc(II) was titrated into the solution, the fluorescence intensity increased 13-fold, and the quantum efficiency went up to 0.47. The linear range for this sensor went from 0.44–10 μM (29 ppb to 654 ppb). Interferences were also tested to determine selectivity, and most did not give any fluorescence enhancement, even at high concentrations. Copper, cobalt, and nickel quenched the fluorescence rather than enhanced it, which is beneficial for the signal resolution of zinc. The only interfering ions for the sensor were mercury and cadmium, since they are in the same transition metal group. Their fluorescence enhancement, however, was not as significant, which indicates that the sensor is selective to zinc(II). The sensor was also tested at various pH levels, and it was found to perform the best between pH 6 and 9 (due to low pH protonating the sensor, and high pH forming $Zn(OH)_2$) [158].

A thin film-based ASV method was developed by Ruecha et al. Both plastic film and paper were used as substrates, and the graphene/polyaniline (G/PANI) electrodes were deposited using drop casting and electrospraying. When testing with the two substrates, peak currents for the plastic film far exceeded that of the paper. Electrospraying the G/PANI electrode rather than drop casting also afforded higher sensitivity due to forming a more uniform film. The stripping mode used was a square wave ramp for all tests. At −1.31 V, the current showed a linear response with respect to the zinc(II) concentration, having a linear range of 1 ppb to 300 ppb. Interferences were tested for peak inhibition, and it was determined that there were no interferences from the range of −1.6 V to −0.5 V. The sensor was also tested in human serum and spiked to determine recovery. For each spike, the recovery remained within the range of 93.8% to 109.7%, which means that this system is reproducible [103].

A bismuth film electrode ASV method was developed by Kefala et al. For this method, three different substrates were considered: glassy carbon electrode (GCE), carbon paste, and impregnated graphite. In 0.1 M acetate buffer (4.5 pH), the GCE gave the highest stripping peaks, as well as the lowest noise; therefore, it was used for further analysis. When comparing bismuth film electrodes (BFEs) to the more common mercury film electrodes (MFEs), the sensitivity on the MFE was higher than the BFE. However, since the sensor was going to be used in situ, the BFE was used for analysis. At −1.31 V, the zinc stripping peak increased proportionally to the concentration of zinc(II), and a limit of detection of 0.7 ppb was obtained. The effects of surfactants (specifically Triton X-100) on the BFE were investigated, and it was found that the zinc(II) stripping peak decreased dramatically in its presence, which indicated that it would not be useful for urinalysis. Tap water was tested with this

method and gave a result of 204 ppb, compared to 211 ppb obtained by AAS, which shows that this method is in good agreement with other analytical methods [159].

A method of zinc(II) determination in seawater using graphite furnace (GF) AAS was developed by Sturgeon et al. To ensure no background interference from the covolatilization of NaCl on the zinc(II) signal as the sample was being heated, NH_4NO_3 was added. This converted NaCl to $NaNO_3$, which separated the zinc(II) peak from the background peak. Adding 10 mg per mL of NH_4NO_3 to a diluted 1:1 sample of seawater was found to be the optimal concentration. The graphite tube was also modified by making the walls at the ends of the tube thinner to improve detection limits. In the case of zinc(II), this allowed for a clean peak with minimal background or interfering peaks. Zinc(II) was analyzed through direct injection and a solvent preconcentration and extraction method. Using both methods, zinc(II) gave very similar results, only differing by 0.2 ppb. The LOD for this method was found to be 0.4 ppb [160].

A flow injection and preconcentration method for analyzing zinc(II) in seawater using FAAS was developed by Tony et al. The samples were adjusted to pH 3.0 ± 1.0 using NH_4OAc. To ensure preconcentration, the zinc(II) was complexed with 5,7-dichlorooxine to adsorb onto the C_{18}-bonded silica gel packed within the preconcentration column. The samples were run by themselves with a 2-ppb spike to ensure good recovery of adsorbed zinc(II). The working range was found to be 0 ppb to 50 ppb, with an LOD of 0.5 ppb. When spiked with 2 ppb of zinc(II), a recovery of 101% was obtained, and, when compared with samples with certified values, the analysis values came quite close, with the FAAS method finding 209 ppb in the MESS sample (certified 191 ± 17 ppb) and 165 ppb in the TORT sample (certified 171 ± 10 ppb) [161].

3.12. Simultaneous Detection of Analytes

Simultaneous detection of analytes is important for the wide-scale use of water quality assurance methods. Being able to detect more than one cation at the same time using only one method reduces the amount of instrumentation and workup required for the samples, and it allows one to collect data for multiple cations at the same time, which reduces workload.

Rasheed et al. developed two colorimetric/fluorescent methods for the simultaneous detection of copper(II) and mercury(II) in aqueous media. The first method utilizes a rhodamine-based colorimetric probe for naked eye and colorimetric detection (Figure 21).

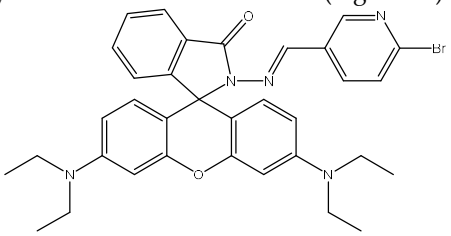

Figure 21. Structure of the rhodamine B-based chemosensor.

In acetonitrile/water (4:1 *v*/*v*, pH 7.2 with 10 mM HEPES) solution, a visual color change was seen going from colorless to pink for both cations. This occurs due to the spirolactam ring opening that occurs when copper(II) or mercury(II) bind at the azo group. This visual change was accompanied by an increase in absorbance at 559 nm for both cations. To distinguish the two cations, fluorescence spectroscopy was used. It was found that copper(II) did not induce fluorescence at 580 nm due to fluorescence quenching from the paramagnetic effect of copper(II)'s d^9 system. Mercury(II), however, did induce fluorescence at 580 nm. The limits of detection for copper(II) and mercury(II) were 3.9 nM and 2.4 nM (0.2 ppb and 0.5 ppb), respectively. Both sensors had a linear range going from the limit of detection up to 10 μM (635 ppb for copper(II) and 2 ppm for mercury(II)). When tested against other cations for interference, no other cations interfered with the copper(II) or mercury(II) signal, making this quite a selective method [1621]. The second method utilizes a chromogenic vesicle functionalized with a rhodamine derivative for the detection of copper(II) and

mercury(II) in water. An alternating copolymer is functionalized with a rhodamine B derivative. When in contact with copper(II) or mercury(II), coordination occurs, causing a spirolactam ring opening of the xanthene backbone. This induces a color change from colorless to pink. When exposed to copper(II) and mercury(II) in aqueous solution, a color change from colorless to pink occurred, as well as an increase in the fluorescence at 558 nm and absorbance at 583 nm. The limits of detection for both copper(II) and mercury(II) were 30 nM and 20 nM (2 ppb and 4 ppb, respectively). The linear range of the sensors went from the detection limit up to 10 μM (635 ppb for copper(II) and 2 ppm for mercury(II)). In seawater samples, spiking the sample gave recovery values above 95%, making this a suitable sensor for more complex matrices [1632].

A "periodic table style" paper device for simultaneous detection of copper(II), nickel(II), and chromium(VI) was developed by Li et al. This method utilizes chromatography paper which is coated in hydrophobic wax except for the detection area, which exposes the hydrophilic paper in the shape of the chemical symbol for the analyte. For the copper(II)-sensing portion, hydroxylamine (0.1 g/mL) in acetic buffer (6.3M, pH 4.3) was applied to the hydrophilic region. Then, 50 mg of bathocuproine in 1 mL of chloroform was added to the region along with 40 mg of polyethylene glycol (PEG) 400 (to preserve the hydrophilicity of the device). When exposed to copper(II) in solution, the "Cu" symbol printed onto the paper began changing color from yellow to brown. This color change occurred at 0.8 ppm, below which the color change was not discernible. For nickel(II), dimethylglyoxime dissolved in ethanol (80 mM) was applied as the sensor molecule. A solution of NaF followed by $Na_2S_2O_3$ was then applied to prevent interference from copper(II). When exposed to nickel(II) in solution, the color of the "Ni" symbol changed from colorless to pink at 0.5 ppm. For chromium(VI), 1,5-diphenylcarbazide (1 mg/mL in 50% acetone) was applied as the sensor molecule, followed by H_2SO_4. When exposed to 0.5 ppm chromium(VI) in water, the color changed from colorless to purple, indicating the presence of chromium(VI). When interference tests were conducted with this device, no other ions seemed to interfere with the signal, and when pseudo-environmental samples were tested and compared to the standard ICP-AES method, the values obtained were in good agreement [1643].

A method for simultaneous detection of mercury(II), lead(II), and copper(II) was developed by Guo et al. This method utilizes gold nanoparticles (AuNPs) functionalized with papain. The AuNPs, when in contact with either lead(II), mercury(II), or copper(II), display different colorimetric responses due to the differences in aggregation of the AuNPs. When aggregation was observed at various pH levels, a pH of 6 gave the biggest color change when exposed to mercury(II), with a red shift in the absorbance going from 524 nm to 626 nm. Below pH 6, aggregation was induced through the protonation of papain, whereas, at higher pH values, the hydroxyl groups interacted with the cations, preventing aggregation. When tested with mercury(II), a visual color change from pink to blue was observed, accompanied by the previously mentioned red shift in the absorbance spectrum. The lowest concentration to induce a color change was 4 μM (802 ppb), which is much higher than the WHO maximum limit. Copper(II) and lead(II) also induce aggregation of the AuNPs, albeit at lower intensity. When tested against other cations, the AuNP solution remained pink, indicating that aggregation was not induced. When testing a real water sample, spiking the water gave good recovery and induced a color change, making this method feasible for more complex matrices [1654].

An ASV method for simultaneous detection of lead(II) and cadmium(II) was developed by Promphet et al. This method uses graphene/polyaniline/polystyrene (G/PANI/PS) screen-printed carbon electrodes for electrochemical detection. To modify the surface of the electrode, G/PAN/PS nanoporous fibers were electrospun onto the electrode. This was used as the working electrode, along with a Pt wire and the counter electrode, and a reference Ag/AgCl electrode. The cadmium(II) and the lead(II) ions were deposited onto the electrode by applying a −1.2 V potential, and bismuth(III) ions were used to improve the response of the electrode. At a bismuth(III) concentration of 900 ppb, cadmium(II) and lead(II) voltammograms were able to be distinguished. Both cadmium(II) and lead(II) had a linear range going from 10 ppb to 500 ppb, with R^2 values of 0.992 and 0.991, respectively. The limits of detection were 3.3 ppb for lead(II) and 4.43 ppb for cadmium(II). When tested against other ions for interference, the voltammograms did not interfere with the cadmium(II)

or lead(II) signal, with the exception of copper(II) and zinc(II) at very high concentrations. When measuring real samples and comparing to the standard ICP-AES method, the values obtained were in good agreement with each other [166].

An electrochemical method for the simultaneous determination of silver(I) and mercury(II) was developed by Miao et al. This method uses DNA1-modified Fe_3O_4@Au nanoparticles. Upon exposure to either silver(I) or mercury(II), the DNA1 immobilized on the nanoparticle hybridizes either to DNA2 (labeled with ferrocene) or DNA3 (labeled with methylene blue) based on whether it binds to silver(I) or mercury(II), respectively. This occurs through the cytosine–Ag^+–cytosine bond and the thymine–Hg^{2+}–thymine bond between the DNA strands. Square wave voltammetry is then used to quantify the amount of silver(I) or mercury(II) in solution, with a magnetic glassy carbon electrode as the working electrode, a Pt wire as the counter electrode, and an SCE reference. The presence of aqueous silver(I) and mercury(II) resulted in a specific current peak for silver at 0.36 V and for mercury(II) at −0.39 V vs. SCE. The linear range for silver(I) went from 10 to 150 nM (1 ppb to 16 ppb), and that for mercury(II) went from 10 nM to 100 nM (2 ppb to 20 ppb), with R^2 values of 0.982 and 0.985, respectively. The limit of detection for silver(I) was 0.37 ppb, and that for mercury(II) was 0.34 ppb. When testing against other ions for interference, none interfered with the silver(I) or the mercury(II) signal. In real water samples, spiking the water samples showed good recovery, and the values obtained were in good agreement with the standard AAS method [167].

4. Conclusion

In this review, the importance of the detection of cations in drinking water was discussed with respect to the effects that various cations have on human physiology, as well as the sources of these cations in water. A number of methods for analysis were investigated in terms of all the analytes presented, as well as modifications to those methods specific to each analyte. Examples of the methods discussed were presented for each analyte, along with their applicability to real life water quality detection. While some methods were more simplistic in their approach (colorimetric yes/no assay), others were much more complex (spectroscopy), which was reflected in the accuracy of the results obtained. Overall, it can be concluded that lighter transition metals (copper, zinc, chromium, nickel) are detectable using relatively simple methods such as colorimetry or fluorescence with sufficiently low detection limits (below regulation). This could be due to the fact that lighter metals are more reactive and interact more readily with colorimetric and fluorescent indicators; this could also be due to the higher limits compared to the heavier metals. Heavier metals (lead, mercury, cadmium, uranium) tend to have higher detection limits when using colorimetric methods due to their lower reactivity, which means that more complex methods such as AAS and ASV are more appropriate to measure these elements. In general, mechanical and optical methods have higher detection limits with large linear ranges, making them appropriate for high-range detection of analytes. Methods such as potentiometry, ASV, SERS, and AAS are better at detecting low-range analytes due to the high sensitivity and lower linear range compared to optical and mechanical methods. For the future, one must look toward sensor networks for continuous in situ monitoring of water supplies and the detection of short-term changes, automation of sample preparation prior to analysis, and analysis of elemental species (ionic salt vs. organic, complexes, changes in oxidation state) [168].

The field of water quality monitoring is very diverse, and, with many other analytes and parameters to consider, the opportunities for development in this area are limitless.

Acknowledgments: The authors acknowledge financial support from the Natural Sciences and Engineering Research Council of Canada through the Discovery Grant Program (award number RGPIN06145-18), as well as the Canada First Research Excellence Fund project “Global Water Futures”.

Funding: This research received no external funding.

Conflicts of Interest: The authors declare no conflicts of interest.

References

1. Rhoades, R.A.; Tanner, G.A. *Medical Physiology*; Lippincott Williams & Wilkins: Philadelphia, PA, USA, 2003.
2. Dieter, C.A.; Maupin, M.A.; Caldwell, R.R.; Harris, M.A.; Ivahnenko, T.I.; Lovelace, J.K.; Barber, N.L.; Linsey, K.S. *Estimated Use of Water in the United States in 2015*; *Circular* **2018**.
3. Duff, L.B. *A Course in Household Arts/Part I*; Whitcomb & Barrows: Boston, MA, USA, 1920.
4. D'Alnoncourt, R.N.; Csepei, L.-I.; Hävecker, M.; Girgsdies, F.; Schuster, M.E.; Schlögl, R.; Trunschke, A. The Reaction Network in Propane Oxidation over Phase-Pure MoVTeNb M1 Oxide Catalysts. *J. Catal.* **2014**, *311*, 369–385.
5. World Health Organization. *Essential Nutrients in Drinking Water*; World Health Organization: Geneva, Switzerland, 2018
6. Godin, M.; Tabard-Cossa, V.; Grütter, P.; Williams, P. Quantitative Surface Stress Measurements Using a Microcantilever. *Appl. Phys. Lett.* **2001**, *7*, 551–553.
7. Rasheed, T.; Li, C.; Bilal, M.; Yu, C.; Iqbal, H.M. Potentially Toxic Elements and Environmentally-Related Pollutants Recognition Using Colorimetric and Ratiometric Fluorescent Probes. *Sci. Total Environ.* **2018**, *640*, 174–193.
8. Skoog, D.A.; Holler, F.J.; West, D.M. *Fundamentals of Analytical Chemistry*; Brooks/Cole/Thomson Learning: South Melbourne, Australia, 2002.
9. Skoog, D.A.; Holler, F.J.; Crouch, S.R. *Principles of Instrumental Analysis*; Brooks/Cole: Belmont, Australia, 2007.
10. King, W.H. Piezoelectric Sorption Detector. *Anal. Chem.* **1964**, *36*, 1735–1739.
11. Sauerbrey, G.N. Verwendung Von Schwingquarzen Zur Wägung dünner Schichten Und Zur Mikrowägung. *Z. Für. Phys.* **1959**, *155*, 206–222.
12. Bottom, V. A History of the Quartz Crystal Industry in the USA. In Proceedings of the Thirty Fifth Annual Frequency Control Symposium, Philadelphia, PA, USA,1981; pp. 3–12.
13. Quartz Crystal Microbalance (QCM). Available online: https://www.nanoscience.com/techniques/quartz-crystal-microbalance/#theory (accessed on September 13, 2019).
14. Rodahl, M.; Kasemo, B. A Simple Setup to Simultaneously Measure the Resonant Frequency and the Absolute Dissipation Factor of a Quartz Crystal Microbalance. *Rev. Sci. Instrum.* **1996**, *67*, 3238–3241.
15. Reviakine, I.; Johannsmann, D.; Richter, R.P. Hearing What You Cannot See and Visualizing What You Hear: Interpreting Quartz Crystal Microbalance Data from Solvated Interfaces. *Anal. Chem.* **2011**, *83*, 8838–8848.
16. Cho, N.-J.; Frank, C.W.; Kasemo, B.; Höök, F. Quartz Crystal Microbalance with Dissipation Monitoring of Supported Lipid Bilayers on Various Substrates. *Nat. Protoc.* **2010**, *5*, 1096–1106.
17. Kruse, P. Review on Water Quality Sensors. *J. Phys. Appl. Phys.* **2018**, *51*, 203002.
18. Ingle, J.D.; Crouch, S.R. *Spectrochemical Analysis*; Prentice-Hall: Englewood Cliffs, NJ, USA, 1988.
19. Lakowicz, J.R. *Principles of Fluorescence Spectroscopy*; Springer Science Business Media: New York, NY, USA, 2010.
20. Skoog, D.A.; Holler, F.J.; Crouch, S.R. *Principles of Instrumental Analysis*; Brooks/Cole: Belmont, Australia, 2007.
21. Valeur, B.; Berberan-Santos Màrio Nuno. *Molecular Fluorescence: Principles and Applications*; Wiley-VCH: Weinheim, German, 2012.
22. Rye, H.; Dabora, J.; Quesada, M.; Mathies, R.; Glazer, A. Fluorometric Assay Using Dimeric Dyes for Double- and Single-Stranded DNA and RNA with Picogram Sensitivity. *Anal. Biochem.* **1993**, *208*, 144–150.
23. Rasheed, T.; Bilal, M.; Nabeel, F.; Iqbal, H.M.; Li, C.; Zhou, Y. Fluorescent Sensor Based Models for the Detection of Environmentally-Related Toxic Heavy Metals. *Sci. Total Environ.* **2018**, *615*, 476–485.
24. Xu, X.; Li, H.; Hasan, D.; Ruoff, R.S.; Wang, A.X.; Fan, D.L. Near-Field Enhanced Plasmonic-Magnetic Bifunctional Nanotubes for Single Cell Bioanalysis. *Adv. Funct. Mater.* **2013**, *23*, 4332–4338.
25. Smith, E.; Dent, G. *Modern Spectroscopy: A Practical Approach*; Wiley: Chichester, UK, 2005.
26. Kneipp, K. Surface-Enhanced Raman Scattering. *Physics and Applications*; Springer: Berlin, Germany, 2006.
27. Shrestha, L.K.; Wi, J.-S.; Williams, J.; Akada, M.; Ariga, K. Facile Fabrication of Silver Nanoclusters as Promising Surface-Enhanced Raman Scattering Substrates. *J. Nanosci. Nanotechnol.* **2014**, *14*, 2245–2251.

28. Xu, Z.; Jiang, J.; Wang, X.; Han, K.; Ameen, A.; Khan, I.; Chang, T.-W.; Liu, G.L. Large-Area, Uniform and Low-Cost Dual-Mode Plasmonic Naked-Eye Colorimetry and SERS Sensor with Handheld Raman Spectrometer. *Nanoscale* **2016**, *8*, 6162–6172.
29. Rouessac, F.; Rouessac, A.; Brooks, S. *Chemical Analysis: Modern Instrumentation Methods and Techniques*; John Wiley and Sons, Ltd.: Chichester, UK, 2014.
30. Lvov, B.V. Recent Advances in Absolute Analysis by Graphite Furnace Atomicabsorption Spectrometry. *Spectrochim. Acta Part B Spectrosc.* **1990**, *45*, 633–655.
31. Bănică, F.-G. *Chemical Sensors and Biosensors: Fundamentals and Applications*; John Wiley & Sons: Chichester, UK, 2014.
32. Khanna, V.K. *Nanosensors: Physical, Chemical, and Biological*; Taylor & Francis: Boca Raton, FL, USA, 2012.
33. Mohtasebi, A.; Kruse, P. Chemical Sensors Based on Surface Charge Transfer. *Phys. Sci. Rev.* **2018**, *3*, 1-13, doi: 10.1515/psr-2017-0133
34. Albert, K.J.; Lewis, N.S.; Schauer, C.L.; Sotzing, G.A.; Stitzel, S.E.; Vaid, T.P.; Walt, D.R. Cross-Reactive Chemical Sensor Arrays. *Chem. Rev.* **2000**, *100*, 2595–2626.
35. Rahman, M.; Kumar, P.; Park, D.-S.; Shim, Y.-B. Electrochemical Sensors Based on Organic Conjugated Polymers. *Sensors* **2008**, *8*, 118–141.
36. Llobet, E. Gas Sensors Using Carbon Nanomaterials: A Review. *Sens. Actuators B Chem.* **2013**, *179*, 32–45.
37. Wohltjen, H.; Barger, W.; Snow, A.; Jarvis, N. A Vapor-Sensitive Chemiresistor Fabricated with Planar Microelectrodes and a Langmuir-Blodgett Organic Semiconductor Film. *IEEE Trans. Electron. Devices* **1985**, *32*, 1170–1174.
38. Hsu, L.H.H.; Hoque, E.; Kruse, P.; Selvaganapathy, P.R. A Carbon Nanotube Based Resettable Sensor for Measuring Free Chlorine in Drinking Water. *Appl. Phys. Lett.* **2015**, *106*, 063102.
39. Rasheed, T.; Nabeel, F.; Adeel, M.; Rizwan, K.; Bilal, M.; Iqbal, H.M. Carbon Nanotubes-Based Cues: A Pathway to Future Sensing and Detection of Hazardous Pollutants. *J. Mol. Liq.* **2019**, *292*, 111425.
40. Janata, J. Thirty Years of CHEMFET—A Personal View. *Electroanalysis* **2004**, *16*, 1831–1835.
41. Wróblewski, W.; Wojciechowski, K.; Dybko, A.; Brzózka, Z.; Egberink, R.J.; Snellink-Ruël, B.H.; Reinhoudt, D.N. Durability of Phosphate-Selective CHEMFETs. *Sens. Actuators B Chem.* **2001**, *78*, 315–319.
42. Heller, I.; Chatoor, S.; Männík, J.; Zevenbergen, M.A.G.; Dekker, C.; Lemay, S.G. Influence of Electrolyte Composition on Liquid-Gated Carbon Nanotube and Graphene Transistors. *J. Am. Chem. Soc.* **2010**, *132*, 17149–17156.
43. Qin, Y.; Kwon, H.-J.; Howlader, M.M.R.; Deen, M.J. Microfabricated Electrochemical PH and Free Chlorine Sensors for Water Quality Monitoring: Recent Advances and Research Challenges. *Rsc. Adv.* **2015**, *5*, 69086–69109.
44. Stock, J.T.; Electrochemistry, Past and Present: Developed from a Symposium Sponsored by the Division of the History of Chemistry and the Division of Analytical Chemistry of the American Chemical Society; at the Third Chemical Congress of North America (195th National Meeting of the American Chemical Society), Toronto, Ontario, Canada, 5–11 June 1988; American Chemical Society: Washington, DC, ,USA, 1989.
45. Ellis, W.D. Anodic Stripping Voltammetry. *J. Chem. Educ.* **1973**, *50*, A131-A147
46. Copeland, T.R.; Skogerboe, R.K. Anodic Stripping Voltammetry. *Anal. Chem.* **1974**, *46*, 1257A–1268A
47. García-Armada, P.; Losada, J.; Vicente-Pérez, S.D. Cation Analysis Scheme by Differential Pulse Polarography. *J. Chem. Educ.* **1996**, *73*, 544.
48. The 30-Minute Guide to ICP-MS.; Perkin Elmer, 2011. Available online: https://www.perkinelmer.com/CMSResources/Images/44-74849tch_icpmsthirtyminuteguide.pdf
49. World Health Organization. *Barium in Drinking-Water*; World Health Organization: Geneva, Switzerland, 2016.
50. Health Canada. Barium in Drinking Water-Guideline Technical Document for Public Consultation. Available online: https://www.canada.ca/en/health-canada/programs/consultation-barium-drinking-water/document.html (accessed on 28 September 2019).
51. Basa, P.N.; Bhowmick, A.; Schulz, M.M.; Sykes, A.G. Site-Selective Imination of an Anthracenone Sensor: Selective Fluorescence Detection of Barium (II). *J. Org. Chem.* **2011**, *76*, 7866–7871.
52. Hassan, S. DDB Liver Drug as a Novel Ionophore for Potentiometric Barium (II) Membrane Sensor. *Talanta* **2003**, *59*, 161–166.

53. Zamani, H.A.; Hamed-Mosavian, M.T.; Aminzadeh, E.; Ganjali, M.R.; Ghaemy, M.; Behmadi, H.; Faridbod, F. Construction of Barium (II) PVC Membrane Electrochemical Sensor Based on 3-Deoxy-d-Erythro-Hexos-2-Ulose Bis (Thiosemicarbazone) as a Novel Ionophore. *Desalination* **2010**, *250,* 56–61.
54. Silva, M.M.; Silva, R.B.; Krug, F.J.; Nobrega, J.A.; Berndt, H. Determination of Barium in Waters by Tungsten Coil Electrothermal Atomic Absorption Spectrometry. *J. Anal. Spectrom.* **1994**, *9,* 861.
55. World Health Organization. *Exposure to Cadmium: A Major Public Health Concern*; World Health Organization: Geneva, Switzerland, 2010.
56. Health Canada. Cadimum in drinking water-for public consultation. Available online: https://www.canada.ca/content/dam/hc-sc/images/programs/consultation-cadmium-drinking-water/Cadmium_in_Drinking_Water_01-29-2019_ENG.pdf (accessed on 28 September 2019).
57. Wang, A.-J.; Guo, H.; Zhang, M.; Zhou, D.-L.; Wang, R.-Z.; Feng, J.-J. Sensitive and Selective Colorimetric Detection of Cadmium (II) Using Gold Nanoparticles Modified with 4-Amino-3-Hydrazino-5-Mercapto-1,2,4-Triazole. *Microchim. Acta* **2013**, *180,* 1051–1057.
58. Wang, W.; Wen, Q.; Zhang, Y.; Fei, X.; Li, Y.; Yang, Q.; Xu, X. Simple Naphthalimide-Based Fluorescent Sensor for Highly Sensitive and Selective Detection of Cd^{2+} and Cu^{2+} in Aqueous Solution and Living Cells. *Dalton Trans.* **2013**, *42,* 1827–1833.
59. Varriale, A.; Staiano, M.; Rossi, M.; Dauria, S. High-Affinity Binding of Cadmium Ions by Mouse Metallothionein Prompting the Design of a Reversed-Displacement Protein-Based Fluorescence Biosensor for Cadmium Detection. *Anal. Chem.* **2007**, *79,* 5760–5762.
60. Ion, A.C.; Bakker, E.; Pretsch, E. Potentiometric Cd2-Selective Electrode with a Detection Limit in the Low Ppt Range. *Anal. Chim. Acta* **2001**, *440,* 71–79.
61. Marken, F.; Matthews, S.L.; Compton, R.G.; Coles, B.A. Microwave Activated Voltammetry: The Thermally Enhanced Anodic Stripping Detection of Cadmium. *Electroanalysis* **2000**, *12,* 267–273.
62. Yin, J.; Wu, T.; Song, J.; Zhang, Q.; Liu, S.; Xu, R.; Duan, H. SERS-Active Nanoparticles for Sensitive and Selective Detection of Cadmium Ion (Cd2). *Chem. Mater.* **2011**, *23,* 4756–4764.
63. Dasary, S.S.; Jones, Y.K.; Barnes, S.L.; Ray, P.; Singh, A.K. Alizarin Dye Based Ultrasensitive Plasmonic SERS Probe for Trace Level Cadmium Detection in Drinking Water. *Sens. Actuators B Chem*. **2016**, *224*, 65–72.
64. Wen, X.; Wu, P.; Xu, K.; Wang, J.; Hou, X. On-Line Precipitation–Dissolution in Knotted Reactor for Thermospray Flame Furnace AAS for Determination of Ultratrace Cadmium. *Microchem. J.* **2009**, *91,* 193–196.
65. Dadfarnia, S.; Shabani, A.M.H.; Kamranzadeh, E. Separation/Preconcentration and Determination of Cadmium Ions by Solidification of Floating Organic Drop Microextraction and FI-AAS. *Talanta* **2009**, *79,* 1061–1065.
66. World Health Organization. *Chromium in Drinking-Water*; World Health Organization: Geneva, Switzerland, 2003.
67. Health Canada. Guidelines for Canadian Drinking Water Quality: Guideline Technical Document-Chromium. Available online : https://www.canada.ca/en/health-canada/programs/chromium-drinking-water/chromium-drinking-water.html (accessed on 28 September 2019).
68. Wang, X.; Wei, Y.; Wang, S.; Chen, L. Red-to-Blue Colorimetric Detection of Chromium via Cr (III)-Citrate Chelating Based on Tween 20-Stabilized Gold Nanoparticles. *Colloids Surf. A Physicochem. Eng. Asp.* **2015**, *472*, 57–62.
69. Zhao, L.; Jin, Y.; Yan, Z.; Liu, Y.; Zhu, H. Novel, Highly Selective Detection of Cr (III) in Aqueous Solution Based on a Gold Nanoparticles Colorimetric Assay and Its Application for Determining Cr (VI). *Anal. Chim. Acta* **2012**, *731*, 75–81.
70. Wang, D.; Shiraishi, Y.; Hirai, T. A Distyryl BODIPY Derivative as a Fluorescent Probe for Selective Detection of Chromium (III). *Tetrahedron Lett.* **2010**, *51,* 2545–2549.
71. Abbaspour, A.; Izadyar, A. Carbon Nanotube Composite Coated Platinum Electrode for Detection of Cr (III) in Real Samples. *Talanta* **2007**, *71,* 887–892.
72. Ye, Y.; Liu, H.; Yang, L.; Liu, J. Sensitive and Selective SERS Probe for Trivalent Chromium Detection Using Citrate Attached Gold Nanoparticles. *Nanoscale* **2012**, *4,* 6442.
73. Liang, J.; Liu, H.; Lan, C.; Fu, Q.; Huang, C.; Luo, Z.; Jiang, T.; Tang, Y. Silver Nanoparticle Enhanced Raman Scattering-Based Lateral Flow Immunoassays for Ultra-Sensitive Detection of the Heavy Metal Chromium. *Nanotechnology* **2014**, *25,* 495501.

74. Rao, T.P.; Karthikeyan, S.; Vijayalekshmy, B.; Iyer, C. Speciative Determination of Chromium (VI) and Chromium (III) Using Flow-Injection on-Line Preconcentration and Flame Atomic-Absorption Spectrometric Detection. *Anal. Chim. Acta* **1998**, *369*, 69–77.
75. Halfdanarson, T.R.; Kumar, N.; Li, C.-Y.; Phyliky, R.L.; Hogan, W.J. Hematological Manifestations of Copper Deficiency: A Retrospective Review. *Eur. J. Haematol.* **2008**, 80, 523–531.
76. Health Canada. Copper in Drinking Water: Guideline Technical Document for Consultation. Available online: https://www.canada.ca/en/health-canada/programs/consultation-copper-drinking-water/document.html (accessed on 25 March 2019).
77. Kaur, K.; Kumar, S. 1-Aminoanthracene-9,10-Dione Based Chromogenic Molecular Sensors: Effect of Nature and Number of Nitrogen Atoms on Metal Ion Sensing Behavior. *Tetrahedron* **2010**, *66*, 6990–7000.
78. Park, J.S.; Jeong, S.; Dho, S.; Lee, M.; Song, C. Colorimetric Sensing of Cu2 Using a Cyclodextrin–Dye Rotaxane. *Dyes Pigments* **2010**, *87*, 49–54.
79. Udhayakumari, D.; Velmathi, S.; Sung, Y.-M.; Wu, S.-P. Highly Fluorescent Probe for Copper (II) Ion Based on Commercially Available Compounds and Live Cell Imaging. *Sens. Actuators B Chem.* **2014**, *198*, 285–293.
80. Jung, H.S.; Kwon, P.S.; Lee, J.W.; Kim, J.I.; Hong, C.S.; Kim, J.W.; Yan, S.; Lee, J.Y.; Lee, J.H.; Joo, T.; et al. Coumarin-Derived Cu2-Selective Fluorescence Sensor: Synthesis, Mechanisms, and Applications in Living Cells. *J. Am. Chem. Soc.* **2009**, *131*, 2008–2012.
81. Zhao, D.; Guo, X.; Wang, T.; Alvarez, N.; Shanov, V.N.; Heineman, W.R. Simultaneous Detection of Heavy Metals by Anodic Stripping Voltammetry Using Carbon Nanotube Thread. *Electroanalysis* **2014**, *26*, 488–496.
82. Ndokoye, P.; Ke, J.; Liu, J.; Zhao, Q.; Li, X. l-Cysteine-Modified Gold Nanostars for SERS-Based Copper Ions Detection in Aqueous Media. *Langmuir* **2014**, *30*, 13491–13497.
83. Cassella, R.; Magalhaes, O.; Couto, M.; Lima, E.; Neves, M.; Coutinho, F. Synthesis and Application of a Functionalized Resin for Flow Injection/F AAS Copper Determination in Waters. *Talanta* **2005**, *67*, 121–128.
84. Porento, M.; Sutinen, V.; Julku, T.; Oikari, R. Detection of Copper in Water Using On-Line Plasma-Excited Atomic Absorption Spectroscopy (AAS). *Appl. Spectrosc.* **2011**, *65*, 678–683.
85. McGowan, W.; Harrison, J.F. *Residential Water Processing: A Reference Handbook*; Water Quality Association: Lisle, IL, USA, 2000.
86. Neri, L.C.; Johansen, H.L. Water Hardness and Cardiovascular Mortality. *Ann. N. Y. Acad. Sci.* **1978**, *304*, 203–219.
87. Neri, L.; Johansen, H.; Hewitt, D.; Marier, J.; Langner, N. Magnesium and Certain Other Elements and Cardiovascular Disease. *Sci. Total Environ.* **1985**, *42*, 49–75.
88. Bean, E.L. Quality Goals for Potable Water. *J. Am. Water Work. Assoc.* **1968**, *60*, 1317–1322.
89. Verissimo, M.; Oliveira, J.; Gomes, M. Determination of the Total Hardness in Tap Water Using Acoustic Wave Sensors. *Sens. Actuators B Chem.* **2007**, *127*, 102–106.
90. Capitán-Vallvey, L.; Fernández-Ramos, M.; Gálvez, P.A.D.C.; Santoyo-González, F. Characterisation of a Transparent Optical Test Strip for Quantification of Water Hardness. *Anal. Chim. Acta* **2003**, *481*, 139–148.
91. Bhattacharjee, T.; Jiang, H.; Behdad, N. A Fluidic Colorimetric Sensor Design for Water Hardness Detection. *IEEE Sens. J.* **2015**, *15*, 819–826.
92. Dey, D.; Bhattacharjee, D.; Chakraborty, S.; Hussain, S.A. Development of Hard Water Sensor Using Fluorescence Resonance Energy Transfer. *Sens. Actuators B Chem.* **2013**, *184*, 268–273.
93. Lerga, T.M.; O'Sullivan, C.K. Rapid Determination of Total Hardness in Water Using Fluorescent Molecular Aptamer Beacon. *Anal. Chim. Acta* **2008**, *610*, 105–111.
94. Saurina, J.; López-Aviles, E.; Moal, A.L.; Hernández-Cassou, S. Determination of Calcium and Total Hardness in Natural Waters Using a Potentiometric Sensor Array. *Anal. Chim. Acta* **2002**, *464*, 89–98.
95. Singh, A.K.; Mehtab, S. Calcium (II)-Selective Potentiometric Sensor Based on α-Furildioxime as Neutral Carrier. *Sens. Actuators B Chem.* **2007**, *123*, 429–436.
96. Health Canada. Lead in Drinking Water. Available online: https://www.canada.ca/en/health-canada/programs/consultation-lead-drinking-water/document.html (accessed on 28 November 2018).
97. Environmental Protection Agency. Basic Information about Lead in Drinking Water. (accessed on 28 November 2018).
98. Teh, H.B.; Li, H.; Li, S.F.Y. Highly Sensitive and Selective Detection of Pb2 Ions Using a Novel and Simple DNAzyme-Based Quartz Crystal Microbalance with Dissipation Biosensor. *Analyst* **2014**, *139*, 5170–5175.

99. Ranyuk, E.; Douaihy, C.M.; Bessmertnykh, A.; Denat, F.; Averin, A.; Beletskaya, I.; Guilard, R. Diaminoanthraquinone-Linked Polyazamacrocycles: Efficient and Simple Colorimetric Sensor for Lead Ion in Aqueous Solution. *Org. Lett.* **2009**, *11*, 987–990.
100. Xue, H.; Tang, X.-J.; Wu, L.-Z.; Zhang, L.-P.; Tung, C.-H. Highly Selective Colorimetric and Electrochemical Pb2 Detection Based on TTF-π-Pyridine Derivatives. *J. Org. Chem.* **2005**, *70*, 9727–9734.
101. Chae, M.; Yoon, J.; Czarnik, A. Chelation-Enhanced Fluorescence Chemosensing of Pb (II), An Inherently Quenching Metal Ion. *J. Mol. Recognit.* **1996**, *9*, 297–303.
102. Wu, Y.; Huang, F.; Lin, Y. Fluorescent Detection of Lead in Environmental Water and Urine Samples Using Enzyme Mimics of Catechin-Synthesized Au Nanoparticles. *ACS Appl. Mater. Interfaces* **2013**, *5*, 1503–1509.
103. Ruecha, N.; Rodthongkum, N.; Cate, D.M.; Volckens, J.; Chailapakul, O.; Henry, C.S. Sensitive Electrochemical Sensor Using a Graphene–Polyaniline Nanocomposite for Simultaneous Detection of Zn (II), Cd (II), and Pb (II). *Anal. Chim. Acta* **2015**, *874*, 40–48.
104. Zhao, L.; Gu, W.; Zhang, C.; Shi, X.; Xian, Y. In Situ Regulation Nanoarchitecture of Au Nanoparticles/Reduced Graphene Oxide Colloid for Sensitive and Selective SERS Detection of Lead Ions. *J. Colloid Interface Sci.* **2016**, *465*, 279–285.
105. Wang, Y.; Irudayaraj, J. A SERS Dnazyme Biosensor for Lead Ion Detection. *Chem. Commun.* **2011**, *47*, 4394.
106. Rodriguez, D.; Fernandez, P.; Perez-Conde, C.; Gutierrez, A.; Camara, C. Determination of Lead in Natural Waters Using Flow Injection with on-Line Preconcentration and Flame AAS Detection. *Fresenius J. Anal. Chem.* **1994**, *349*, 442–446.
107. Ensafi, A.; Khayamian, T.; Karbasi, M. On-Line Preconcentration System for Lead (II) Determination in Waste Water By Atomic Absorption Spectrometry Using Active Carbon Loaded With Pyrogallol Red. *Anal. Sci.* **2003**, *19*, 953–956.
108. Health Canada. Guidelines for Canadian Drinking Water Quality: Guideline Technical Document-Mercury. Available online: https://www.canada.ca/en/health-canada/services/publications/healthy-living/guidelines-canadian-drinking-water-quality-guideline-technical-document-mercury.html (accessed on 28 November 2018).
109. Rasheed, T.; Li, C.; Nabeel, F.; Qi, M.; Zhang, Y.; Yu, C. Real-Time Probing of Mercury Using an Efficient "Turn-on" Strategy with Potential as in-Field Mapping Kit and in Live Cell Imaging. *New J. Chem.* **2018**, *42*, 10940–10946.
110. Rasheed, T.; Nabeel, F.; Li, C.; Bilal, M. Rhodamine-Assisted Fluorescent Strategy for the Sensitive and Selective in-Field Mapping of Environmental Pollutant Hg (II) With Potential Bioimaging. *J. Lumin.* **2019**, *208*, 519–526.
111. Rasheed, T.; Li, C.; Nabeel, F.; Huang, W.; Zhou, Y. Self-Assembly of Alternating Copolymer Vesicles For The Highly Selective, Sensitive and Visual Detection and Quantification of Aqueous Hg2+. *Chem. Eng. J.* **2019**, *358*, 101–109.
112. Kim, S.; Gwon, S.; Bae, J. A Highly Selective Ratiometric Chemosensor For Hg2+ Based on 1,2-Diaminoanthraquinone. *Sen'i Gakkaishi* **2014**, *70*, 254–257.
113. Firdaus, M.; Fitriani, I.; Wyantuti, S.; Hartati, Y.; Khaydarov, R.; McAlister, J.; Obata, H.; Gamo, T. Colorimetric Detection of Mercury (II) Ion in Aqueous Solution Using Silver Nanoparticles. *Anal. Sci.* **2017**, *33*, 831–837.
114. Liu, S.; Qin, X.; Tian, J.; Wang, L.; Sun, X. Photochemical Preparation of Fluorescent 2,3-Diaminophenazine Nanoparticles for Sensitive and Selective Detection of Hg (II) Ions. *Sens. Actuators B Chem.* **2012**, *171*, 886–890.
115. Wu, D.; Huang, W.; Duan, C.; Lin, Z.; Meng, Q. Highly Sensitive Fluorescent Probe for Selective Detection of Hg2+in DMF Aqueous Media. *Inorg. Chem.* **2007**, *46*, 1538–1540.
116. Tyagi, S.; Agarwal, H.; Ikram, S. Potentiometric Polymeric Membrane Electrodes for Mercury Detection Using Calixarene Ionophores. *Water Sci. Technol.* **2010**, *61*, 693–704.
117. Xu, H.; Zeng, L.; Xing, S.; Shi, G.; Xian, Y.; Jin, L. Microwave-Radiated Synthesis of Gold Nanoparticles/Carbon Nanotubes Composites and Its Application to Voltammetric Detection of Trace Mercury (II). *Electrochem. Commun.* **2008**, *10*, 1839–1843.
118. Gong, J.; Sarkar, T.; Badhulika, S.; Mulchandani, A. Label-Free Chemiresistive Biosensor For Mercury (II) Based on Single-Walled Carbon Nanotubes and Structure-Switching DNA. *Appl. Phys. Lett.* **2013**, *102*, 013701.

119. Ma, W.; Sun, M.; Xu, L.; Wang, L.; Kuang, H.; Xu, C. A SERS Active Gold Nanostar Dimer for Mercury Ion Detection. *Chem. Commun.* **2013**, *49*, 4989.
120. Han, D.; Lim, S.; Kim, B.; Piao, L.; Chung, T. Mercury (II) Detection by SERS Based on A Single Gold Microshell. *Chem. Commun.* **2010**, *46*, 5587.
121. Pourreza, N.; Ghanemi, K. Determination of Mercury in Water and Fish Samples By Cold Vapor Atomic Absorption Spectrometry After Solid Phase Extraction on Agar Modified With 2-Mercaptobenzimidazole. *J. Hazard. Mater.* **2009**, *161*, 982–987.
122. World Health Organization. *Nickel in Drinking-Water*; World Health Organization: Geneva, Switzerland, 2018.
123. Liu, X.; Lin, Q.; Wei, T.-B.; Zhang, Y.-M. A Highly Selective Colorimetric Chemosensor for Detection of Nickel Ions in Aqueous Solution. *New J. Chem.* **2014**, *38*, 1418–1423.
124. Jiang, J.; Gou, C.; Luo, J.; Yi, C.; Liu, X. A Novel Highly Selective Colorimetric Sensor for Ni (II) Ion Using Coumarin Derivatives. *Inorg. Chem. Commun.* **2012**, *15*, 12–15.
125. Tomar, P.K.; Chandra, S.; Malik, A.; Kumar, A. Nickel Analysis in Real Samples by Ni2 Selective PVC Membrane Electrode Based on a New Schiff Base. *Mater. Sci. Eng. C* **2013**, *33*, 4978–4984.
126. Musyarofah, N.R.R.; Gunlazuardi, J.; Einaga, Y.; Ivandini, T.A. Anodic Stripping Voltammetry of Nickel Ions and Nickel Hydroxide Nanoparticles at Boron-Doped Diamond Electrodes. *IOP Conf. Ser. Mater. Sci. Eng.* **2017**, *188*, 012020.
127. Matusiewicz, H.; Krawczyk, M. Determination of Nickel by Chemical Vapor Generation in Situ Trapping Flame AAS. *Open Chem.* **2011**, *9*, 648–659.
128. World Health Organization. *Silver as a Drinking-Water Disinfectant*; World Health Organization: Geneva, Switzerland, 2018.
129. Lee, S.; Jang, K.; Park, C.; You, J.; Kim, T.; Im, C.; Kang, J.; Shin, H.; Choi, C.-H.; Park, J.; et al. Ultra-Sensitive in Situ Detection of Silver Ions Using a Quartz Crystal Microbalance. *New J. Chem.* **2015**, *39*, 8028–8034.
130. Qin, C.; Wong, W.-Y.; Wang, L. A Water-Soluble Organometallic Conjugated Polyelectrolyte for the Direct Colorimetric Detection of Silver Ion in Aqueous Media with High Selectivity and Sensitivity. *Macromolecules* **2011**, *44*, 483–489.
131. Lin, C.-Y.; Yu, C.-J.; Lin, Y.-H.; Tseng, W.-L. Colorimetric Sensing of Silver (I) and Mercury (II) Ions Based on an Assembly of Tween 20-Stabilized Gold Nanoparticles. *Anal. Chem.* **2010**, *82*, 6830–6837.
132. Chatterjee, A.; Santra, M.; Won, N.; Kim, S.; Kim, J.K.; Kim, S.B.; Ahn, K.H. Selective Fluorogenic and Chromogenic Probe for Detection of Silver Ions and Silver Nanoparticles in Aqueous Media. *J. Am. Chem. Soc.* **2009**, *131*, 2040–2041.
133. Chae, M.; Czarnik, A. Fluorometric Chemodosimetry. Mercury (II) and Silver (I) Indication in Water Via Enhanced Fluorescence Signaling. *J. Am. Chem. Soc.* **1992**, *114*, 9704–9705.
134. Rubinova, N.; Chumbimunitorres, K.; Bakker, E. Solid-Contact Potentiometric Polymer Membrane Microelectrodes for the Detection of Silver Ions at the Femtomole Level. *Sens. Actuators B Chem.* **2007**, *121*, 135–141.
135. O'Connor, K.; Svehla, G.; Harris, S.; McKervey, M. Calixarene-Based Potentiometric Ion-Selective Electrodes for Silver. *Talanta* **1992**, *39*, 1549–1554.
136. Schildkraut, D.; Dao, P.; Twist, J.; Davis, A.; Robillard, K. Determination of Silver Ions At Submicrogram-Per-Liter Levels Using Anodic Square-Wave Stripping Voltammetry. *Environ. Toxicol. Chem.* **1998**, *17*, 642–649.
137. Zejli, H.; Cisneros, J.; Naranjo-Rodriguez, I.; Temsamani, K. Stripping Voltammetry of Silver Ions At Polythiophene-Modified Platinum Electrodes. *Talanta* **2007**, *71*, 1594–1598.
138. Shamspur, T.; Mashhadizadeh, M.; Sheikhshoaie, I. Flame Atomic Absorption Spectrometric Determination of Silver Ion After Preconcentration on Octadecyl Silica Membrane Disk Modified With Bis [5-(4-Nitrophenyl) Azosalicylaldehyde)] As A New Schiff Base Ligand. *J. Anal. At. Spectrom.* **2003**, *18*, 1407.
139. Madrakian, T.; Afkhami, A.; Zolfigol, M.; Solgi, M. Separation, Preconcentration and Determination of Silver Ion From Water Samples Using Silica Gel Modified With 2,4,6-Trimorpholino-1,3,5-Triazin. *J. Hazard. Mater.* **2006**, *128*, 67–72.
140. Health Canada. Uranium in Drinking Water. Available online: https://www.canada.ca/en/health-canada/programs/consultation-uranium-drinking-water/document.html (accessed on 28 September 2019).

141. World Health Organization. *Uranium in Drinking-Water*; World Health Organization: Geneva, Switzerland, 2012.
142. Lee, J.H.; Wang, Z.; Liu, J.; Lu, Y. Highly Sensitive and Selective Colorimetric Sensors for Uranyl (UO_2^{2+}): Development and Comparison of Labeled and Label-Free DNAzyme-Gold Nanoparticle Systems. *J. Am. Chem. Soc.* **2008**, *130*, 14217–14226.
143. Zhang, D.; Chen, Z.; Omar, H.; Deng, L.; Khashab, N.M. Colorimetric Peroxidase Mimetic Assay for Uranyl Detection in Sea Water. *ACS Appl. Mater. Interfaces* **2015**, *7*, 4589–4594.
144. Perry, D.L.; Klainer, S.M.; Bowman, H.R.; Milanovich, F.P.; Hirschfeld, T.; Miller, S. Detection of Ultratrace Levels of Uranium in Aqueous Samples by Laser-Induced Fluorescence Spectrometry. *Anal. Chem.* **1981**, *53*, 1048–1050.
145. Ma, J.; He, W.; Han, X.; Hua, D. Amidoximated Fluorescent Polymer Based Sensor for Detection of Trace Uranyl Ion in Aqueous Solution. *Talanta* **2017**, *168*, 10–15.
146. Hassan, S. PVC Membrane Based Potentiometric Sensors for Uranium Determination. *Talanta* **2001**, *54*, 1153–1161.
147. Golikand, A.N.; Asgari, M.; Maragheh, M.G.; Lohrasbi, E. Carbon Nanotube-Modified Glassy Carbon Electrode for Anodic Stripping Voltammetric Detection of Uranyle. *J. Appl. Electrochem.* **2008**, *39*, 65–70.
148. Ruan, C.; Luo, W.; Wang, W.; Gu, B. Surface-Enhanced Raman Spectroscopy for Uranium Detection and Analysis in Environmental Samples. *Anal. Chim. Acta* **2007**, *605*, 80–86.
149. Trujillo, M.J.; Jenkins, D.M.; Bradshaw, J.A.; Camden, J.P. Surface-Enhanced Raman Scattering of Uranyl in Aqueous Samples: Implications for Nuclear Forensics and Groundwater Testing. *Anal. Methods* **2017**, *9*, 1575–1579.
150. Agrawal, Y.K.; Shrivastav, P.; Menon, S.K. Solvent Extraction, Separation of Uranium (VI) with Crown Ether. *Sep. Purif. Technol.* **2000**, *20*, 177–183.
151. O'Dell, B.L. History and Status of Zinc in Nutrition. *Fed. Proc.* **1984**, *43*, 2821-2822.
152. World Health Organization. *Evaluation of Certain Food Additives and Contaminants: Twenty-Seventh Report of the Joint FAO/WHO Expert Committee on Food Additives*; World Health Organization: Geneva, Switzerland, 1983.
153. Friberg, L.; Nordberg, G.F.; Vouk, V.B. *Handbook on the Toxicology of Metals*; Elsevier: Amsterdam, The Netherlands, 1986.
154. NRIAGU, J.O. Zinc in the Environment. Pt. 1. *Ecological Cycling*; Wiley: New York, NY, USA, 1980.
155. Zinc in Drinking-water. *Guidelines for Drinking-Water Quality*; WHO: Geneva, Switzerland, 1996.
156. Kaur, P.; Kaur, S.; Mahajan, A.; Singh, K. Highly Selective Colorimetric Sensor for Zn2 Based on Hetarylazo Derivative. *Inorg. Chem. Commun.* **2008**, *11*, 626–629.
157. Wu, J.; Sheng, R.; Liu, W.; Wang, P.; Zhang, H.; Ma, J. Fluorescent Sensors Based on Controllable Conformational Change for Discrimination of Zn2 over Cd2. *Tetrahedron* **2012**, *68*, 5458–5463.
158. Li, J.; Zhang, C.-F.; Ming, Z.-Z.; Hao, G.-F.; Yang, W.-C.; Yang, G.-F. Coumarin-Based Novel Fluorescent Zinc Ion Probe in Aqueous Solution. *Tetrahedron* **2013**, *69*, 4743–4748.
159. Kefala, G. A Study of Bismuth-Film Electrodes for the Detection of Trace Metals by Anodic Stripping Voltammetry and Their Application to the Determination of Pb and Zn in Tapwater and Human Hair. *Talanta* **2003**, *61*, 603–610.
160. Sturgeon, R.E.; Berman, S.S.; Desaulniers, A.; Russell, D.S. Determination of Iron, Manganese, and Zinc in Seawater by Graphite Furnace Atomic Absorption Spectrometry. *Anal. Chem.* **1979**, *51*, 2364–2369.
161. Tony, K.A.; Kartikeyan, S.; Vijayalakshmy, B.; Rao, T.P.; Iyer, C.S.P. Flow Injection on-Line Preconcentration and Flame Atomic Absorption Spectrometric Determination of Iron, Cobalt, Nickel, Manganese and Zinc in Sea-Water. *Analyst* **1999**, *124*, 191–195.
162. Rasheed, T.; Li, C.; Zhang, Y.; Nabeel, F.; Peng, J.; Qi, J.; Gong, L.; Yu, C. Rhodamine-Based Multianalyte Colorimetric Probe with Potentialities as on-Site Assay Kit and in Biological Systems. *Sens. Actuators B Chem.* **2018**, *258*, 115–124.
163. Rasheed, T.; Nabeel, F.; Shafi, S. Chromogenic Vesicles for Aqueous Detection and Quantification of Hg2/Cu2 in Real Water Samples. *J. Mol. Liq.* **2019**, *282*, 489–498.
164. Li, M.; Cao, R.; Nilghaz, A.; Guan, L.; Zhang, X.; Shen, W. "Periodic-Table-Style" Paper Device for Monitoring Heavy Metals in Water. *Anal. Chem.* **2015**, *87*, 2555–2559.

165. Guo, Y.; Wang, Z.; Qu, W.; Shao, H.; Jiang, X. Colorimetric Detection of Mercury, Lead and Copper Ions Simultaneously Using Protein-Functionalized Gold Nanoparticles. *Biosens. Bioelectron.* **2011**, *26*, 4064–4069.
166. Promphet, N.; Rattanarat, P.; Rangkupan, R.; Chailapakul, O.; Rodthongkum, N. An Electrochemical Sensor Based on Graphene/Polyaniline/Polystyrene Nanoporous Fibers Modified Electrode for Simultaneous Determination of Lead and Cadmium. *Sens. Actuators B Chem.* **2015**, *207*, 526–534.
167. Miao, P.; Tang, Y.; Wang, L. DNA Modified Fe3O4@Au Magnetic Nanoparticles as Selective Probes for Simultaneous Detection of Heavy Metal Ions. *ACS Appl. Mater. Interfaces* **2017**, *9*, 3940–3947.
168. Schmidt, T.C. Recent Trends in Water Analysis Triggering Future Monitoring of Organic Micropollutants. *Anal. Bioanal. Chem.* **2018**, *410*, 3933–3941.

3 - EXPERIMENTAL

3.1 - Density Functional Theory

Density Functional Theory, or DFT, is a quantum chemical model which theorizes that the properties of a many body system can be derived simply from the electron density itself through the use of functionals (functions of the electron density). This theory has its foundation in the Hohenberg-Kohn theorems, which state that (I) *any property of any electronic system can be expressed as a functional of the ground state electron density, ρ(r), for that system* and that (II) *for an N-electron system with external potential $v_0(r)$, the energy of an N-electron trial density, $\rho_1(r)$, is always greater than or equal to the true ground state energy of the system, and that equality is achieved if and only if $\rho_1(r)$ is a ground state density for this system*.[23] Using the Kohn-Sham model system[24], the ground state energy of a system is given by the following equation (1).

$$\boldsymbol{E = \sum_{i}^{occ} \varepsilon_i - \int \left(\frac{1}{2} v_J[\rho] + v_{xc}[\rho]\right) \rho[r] dr + E_{xc}[\rho]} \quad (1)$$

In this equation, E is the total ground state energy, ε_i are the energy eigenvalues for the occupied orbitals, $v_J[\rho]$ and $v_{xc}[\rho]$ are the electrostatic potential and exchange correlation potential respectively, and $E_{xc}[\rho]$ is the exchange correlation energy. The eigenvalues for the Kohn-Sham model system can be found by solving the Kohn-Sham equations (2).

$$\boldsymbol{\left(\frac{-\nabla^2}{2} + v(r) + v_J[\rho; r] + v_{xc}[\rho; r]\right) \phi_k(r) = \varepsilon_k \phi_k(r)} \quad (2)$$

In this case, v(r) is the external potential. The Kohn-Sham eigenfunctions ϕ_k, when summed up, form the Kohn-Sham wavefunction Φ^{KS}, which is given by the Slater

determinant of all the spin orbitals with lowest energy eigenvalues. The only unknown variable in the ground state energy equation is then the exchange correlation potential $v_{xc}[\rho]$ and its corresponding energy functional $E_{xc}[\rho]$. One can estimate the exchange correlation energy functional and potential through the use of local density (spin) approximations (L[S]DA) or generalized gradient approximations (GGA). L(S)DA approximates exchange correlation by utilizing the homogeneous electron gas (HEG) model. This allows one to separate the exchange and correlation terms, where the exchange term is a form of the HEG, and the correlation term is approximated. The main drawback of LDA, however, is that it assumes electron density is constant. This underestimates the exchange energy and overestimates the correlation energy.[25] To account for this, GGA allows for corrections based on the non-uniformity of the electron gas.[26] To increase the accuracy of the exchange correlation energy, hybrid functionals are regularly employed such as the Becke 3-parameter Lee-Yang-Parr functional (B3LYP), which is one of the most popular exchange correlation energy functionals (3).

$$\boldsymbol{E_{xc}^{B3LYP} = E_x^{LDA} + 0.2(E_x^{HF} - E_x^{LDA}) + 0.72(E_x^{GGA} - E_x^{LDA}) + E_c^{LDA} + 0.81(E_c^{GGA} - E_c^{LDA})} \quad (3)$$

This combines the exchange functional from Hartree-Fock theory[27] with exchange and correlation functionals from LDA and GGA.[28]

One more component needed for the determination of the properties of a molecule is a basis set. Basis sets are functions used to represent wavefunctions in DFT to turn the partial differential equation (PDE) needed to solve for the energy eigenvalues into an algebraic equation, which is easier to solve through computational methods. A common family of basis sets are Pople valence basis sets, which utilize Gaussian-type orbitals as the eigenfunctions.[29] One example of a Pople valence basis set is 6-31g. What this indicates is that there are six primitive Gaussian functions which make up the core orbitals, and that the valence orbitals

are made up of two basis functions: one with 3 Gaussian functions and the other with 1 Gaussian function.[30] Additional functions can be added, such as polarization functions and diffuse functions. Polarization functions (*) will include asymmetry of the electron density in the molecular orbital as a function of the dipole. Diffuse functions (+) are used to describe anionic molecules more accurately. For large atoms (such as transition metals), a compromise must be made between accuracy of the results and computational cost. In this case, basis sets that include effective core potentials (ECP) are employed to increase efficiency of the calculation at the cost of accuracy. One such basis set is the Los Alamos National Library 2-double zeta (LANL2DZ), which will replace the Gaussian-type orbitals in the core for an effective potential up to the 2p orbitals and use two basis functions for everything above.[31]

In this thesis, optimization and frequency calculations utilizing DFT were performed using the Gaussian09 software (via Sharcnet's Graham cluster), and visualized using Gaussview 5.0. All calculations were done in gas phase. Optimization calculations were utilized to visualize the movement of electron density in the highest occupied molecular orbital (HOMO) and the lowest unoccupied molecular orbital (LUMO) of the ligands upon complexation with a chosen metal cation. Frequency calculations were done to ensure that the resulting structure was a global minimum (absence of negative frequencies). B3LYP was used as the exchange correlation energy functional for all calculations. Basis set specifications are included in the chapters pertaining to each metal cation.

3.2 - UV/vis spectroscopy

Ultraviolet-visible spectroscopy is a form of spectroscopy that involves observing the attenuation of light of a species at different wavelengths in the ultraviolet and visible region. The attenuation, or absorbance, at a specific wavelength corresponds to an electronic

transition in the molecule that occurs when a photon of that wavelength is absorbed by an electron in its relaxed state in the molecule. This electron then gets excited, and moves to a higher energy level, leading to absorption. As the electron relaxes back down to the ground state energy, photons are emitted (fluorescence).[32] This is illustrated by a Jablonski diagram (Figure 6).

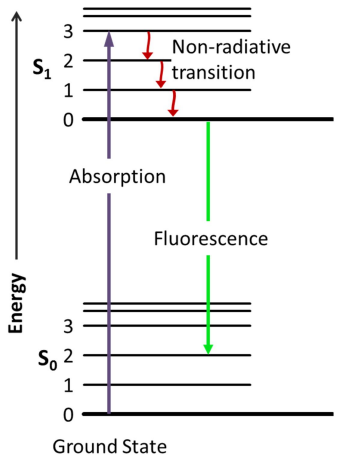

Figure 6. A Jablonski diagram illustrating absorbance, non-radiative decay, and fluorescence. Reprinted with permission under the Creative Commons CC0 1.0 Universal Public Domain Dedication.

With regards to organic molecules, there are four types of transitions that occur: $\sigma \rightarrow \sigma^*$, $n \rightarrow \sigma^*$, $n \rightarrow \pi^*$, and $\pi \rightarrow \pi^*$. $\sigma \rightarrow \sigma^*$ transitions occur below 200 nm, in the far UV range. This transition requires a great amount of energy and is destructive to the molecule since it involves the breaking of a σ bond. $n \rightarrow \sigma^*$ transitions occurs between 180 nm and 220 nm and involves the excitation of a non-bonding electron on a pnictogen, chalcogen, or halogen substituent. $n \rightarrow \pi^*$ transitions are similar, with the key difference being that the excited electron goes into a π^* orbital. This transition is lower in energy and occurs between 220 nm to 280 nm. Finally, $\pi \rightarrow \pi^*$ transitions are transitions of a delocalized π electron to the π^* orbital. Although these are higher energy than the $n \rightarrow \pi^*$ transitions, they are higher in probability (this is due to the solvent stabilization of the non-bonding orbital).

As mentioned in Section 1.2.1, upon complexation to a metal centre, the newly formed coordination complex can also undergo MLCT or LMCT, as well as d-d transitions. These transitions are low in energy and will appear either in the red region in the UV/vis spectrum, or even further in the near-infrared region.

The concentration of a species in solution can be correlated to its absorbance through the Beer-Lambert law (4).[33]

$$\boldsymbol{A = \varepsilon l c} \tag{4}$$

Through this law, one can determine the molar attenuation coefficient (ε) assuming that the cuvette path length (l) and the concentration of their species in solution (c) are known. This can be used to determine the oscillator strength of a certain transition and can also be used to create calibration curves to correlate absorption at a certain wavelength with the concentration of the species.

In this thesis, UV/vis spectroscopy was done using an Orion Aquamate 8000 purchased from Thermo Scientific. A quartz cuvette with a 1 cm path length was used for the testing of all samples. Specifications on the solvents, range, and concentrations used are elaborated on in their corresponding chapters.

3.3 - X-ray Photoelectron Spectroscopy

XPS is a surface sensitive technique in which a sample species is bombarded by X-rays. These X-rays have enough energy to expel an electron from the surface (known as photoelectrons). Measurement of the kinetic energy of the emitted electrons can be used to determine the composition of the surface since it is specific to each element.[34]

During an XPS experiment, the sample is illuminated by a low energy X-ray, most commonly Al K_α X-rays. This will excite a core electron of the sample species, which will then be emitted from the atom (Figure 7a, 7b). The binding energy can be calculated as the difference between the energy of the incident X-ray and the kinetic energy of the electron along with the work function of the spectrometer (5).

$$\boldsymbol{E_{binding} = E_{photon} - (E_{kinetic} + \phi)} \quad (5)$$

The binding energy of the electrons emitted will provide the identity of the elements present in the sample, and the intensity of the emission will provide the quantity of the element in the sample.[4]

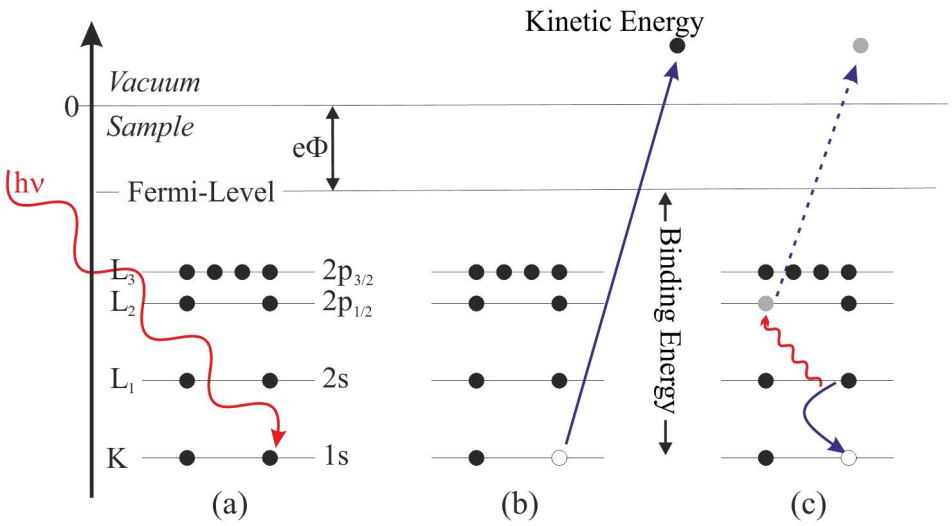

Figure 7. (a) and (b) depict the absorption of the X-ray and subsequent emission of a photoelectron from a core orbital, while (c) shows the Auger relaxation effect.[4]

An XPS spectrum plots the calculated binding energy against the counts per second of the emitted photoelectrons. The peaks that result are labelled according to the nomenclature nl_j, where n is the principal quantum number, l is the angular momentum quantum number, and $j=l+s$ where $s=\pm 1/2$. For orbitals where $l>0$, peaks will split into a doublet due to the presence of both a singlet state and a triplet state. For example, an electron emitted from the

3d orbital of silver will give rise to a doublet due to there being both a singlet and a triplet state (j=3/2 or 5/2). The peak intensities for each spin state are also related to each other through their degeneracy ($2j$+1). Using Ag 3d as an example, the doublet will have an intensity ratio of 2:3 for the $3d_{3/2}$ and $3d_{5/2}$ states, respectively.[35]

When performing an XPS experiment, a survey spectrum should first be obtained. This will allow for the determination of all elements present in the sample species, as well as their relative percent compositions. Once this is known, high resolution spectra can be obtained by focusing on the peaks of interest. The binding energy corresponding to these peaks are dependent on two things: the oxidation state of the atom of interest and the surrounding environment. An atom that is more electropositive will have a higher binding energy since there is extra Coulombic interaction between the electrons and the nuclei. An atom that is more electronegative will have a lower binding energy due to the electron repulsion interaction.[36] With additional insight from different methods such as Raman and Fourier transform infrared spectroscopy (FTIR), this will give important information such as coordination number, chemical environment surrounding the element, and aromaticity.

When an atom emits a photoelectron, the atom becomes ionized. In the example shown in 7c an electron from the 2s orbital drops down to fill the hole in the 1s orbital. The energy from this transfer is absorbed by an electron in the $2p_{1/2}$ orbital, which is then emitted as a photoelectron.[37] The peak resulting from this transition would be given the label KL_1L_2, or KLL for short. This is known as the Auger effect and can provide valuable information on the oxidation state of an element.[38] Another possibility is that an electron from the $2p_{1/2}$ orbital fills the hole in the 1s orbital, releasing a photon in the process. This is known as fluorescence, and is a competing process to the Auger effect. Auger is more prevalent than fluorescence for smaller atoms with Z<50, after which fluorescence dominates. The label

KLL represents a hole initially formed in the 1s orbital (K) filled by an electron from the 2s orbital (L_1) followed by emission of an Auger electron from the $2p_{1/2}$ orbital (L_2). The kinetic energy of the Auger electron is not related to the incident X-ray energy, but the difference in energy between the initially formed ion and the now doubly charged ion. The kinetic energy can be correlated to the oxidation state of the target element through the kinetic energy of the emitted electron. The higher the oxidation state, the lower the kinetic energy of the emitted electron (due to the higher binding energy from a higher oxidation state).

For this thesis, the silver sensors in CHAPTER 5 were observed through XPS using a Kratos AXIS Ultra X-ray photoelectron spectrometer. The XPS survey spectra were obtained using a pass energy of 160 eV for an area of ~300-700 μm. The high resolution spectra used the same area with a pass energy of 20 eV.

3.4 - Sensor Fabrication

3.4.1 - Chemicals Required

- Graphite powder
- Isopropanol
- 18.2 MΩ·CM water
- Methanol
- Sylgard 184 Silicone Elastomer Kit

3.4.2 - Materials Required

- Bath sonicator
- Centrifuge
- Hotplate
- Pasteur pipettes with bulb
- 20 mL vials
- Centrifuge tubes
- Kimwipes
- Weigh boats
- VWR twin frosted glass slides
- 9B pencil
- 3M copper foil tape
- Ohmmeter
- Wood stick applicator
- Permanent marker
- Scoopula
- Analytical balance

3.4.3 - Synthesis of Exfoliated Graphene

Exfoliated FLG flakes were prepared using a literature procedure. 40 mg graphite was added to 15 g of 30% (w/w) isopropanol:water mixture in a 20 mL capped glass vial and sonicated in a bath sonicator (Elmasonic P30H Ultrasonic Cleaner) for six hours at 80 kHz (100% power) and 30 °C using the sweep setting. The suspended FLG flakes were then

centrifuged for 5 minutes at a relative centrifugal force (RCF) of 14100 x g (14500 rpm) in an Eppendorf MiniSpin plus centrifuge to separate the bulk unexfoliated graphite. The supernatant (with the exfoliated FLG) was retained, and recentrifuged for 15 minutes at 14100 x g. The supernatant of the second centrifugation step (containing smaller, defect-rich graphene flakes) was discarded and the precipitate retained for sensor fabrication.

3.4.4 - Fabrication of FLG Chemiresistive Sensors

1. Take a glass slide and drop methanol on one end such that the whole surface is covered. Using a Kimwipe, dab the surface (do not wipe), and let whatever remains evaporate.

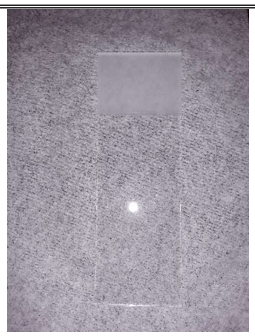

2. Using a 9B pencil, etch two rectangles parallel to each other on the frosted end of the cleaned side of the glass slide. Ensure that the rectangles are separated by about 9 mm of space.

3. Place the glass slide on a hotplate with the pencil etch side up and heat the glass slide to 100^{o}C. Once the hotplate reaches 100^{o}C, take a Pasteur pipette, and draw some of the exfoliated graphite. Drop the graphite in between the rectangles one drop at a time (allow the previous drop to completely dry off before placing another one). Use the voltmeter with the resistance measurement setting at 2MΩ. As you drop the graphite, measure the resistance of the graphite film by

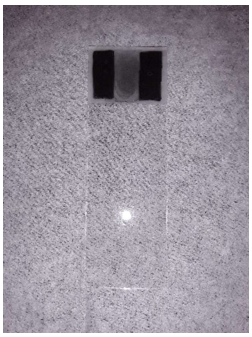

placing the voltmeter contacts on the rectangles, one on each end. The optimal resistance is between 0.01-0.02 MΩ.

4. Allow the slide and the hotplate to cool down to room temperature. Take the copper tape and place it over the pencil rectangle all the way down the length of the glass slide. The copper tape should be parallel to each other on either end. Measure the new resistance.

5. Prepare a PDMS coating by placing ~1 g of methylsiloxane and ~0.1 g of PDMS curing agent in a weigh boat. Stir this mixture with a wooden stick. Place the glass slide on the hotplate and heat to 60^{o}C. Using the wooden stick, coat the copper 2/3 of the way down from the top with the PDMS mixture, being careful not to cover the graphite film in the centre. Allow the PDMS to cure at 60^{o}C until the PDMS is hardened. Once hardened, turn off hotplate, remove slide from hotplate and allow cooling to room temperature. Measure the resistance.

4 - COPPER

As discussed in Chapters 1 and 2, the detection of copper in drinking water is quite important due to the adverse effects of both copper deficiency and excess copper consumption. To aid in the quantification of copper in drinking water, the few-layer graphene (FLG) film was functionalized with a copper selective ligand. Two different ligands, 2,3-diaminophenazine (DAP) and 1,2-diaminoanthraquinone (DAQ), were tested. DAP was shown to exhibit a fluorescent turn-off due to the paramagnetic effect, and DAQ was shown to exhibit a fluorescence turn-on due to photoinduced electron transfer.[1] Prior to the chemiresistive detection of copper computational methods, as well as UV/vis spectroscopy, were used to determine the feasibility of the two selected ligands. After this, the functionalized sensors were run (along with a non-functionalized sensor for control) using the methods described below. The results and discussion in this chapter builds upon research done by Anastasia Benfield-Dexter in the 2017-2018 school year, as well as the research done by Ana Zubiarrain Laserna during 2016-2019. In this chapter we discuss the results obtained.

4.1 - Experimental

4.1.1 - Computational Details

Theoretical calculations were performed using Gaussian09 and visualized in Gaussview 5.0. To optimize the structures of both DAP and DAQ, ground state DFT calculations were used with the B3LYP functional and the 6-31G(d,p) basis set. In the case of the metal complexes, the non-metallic components of the complexes (C, H, N, O, Cl) were

optimized with the 6-31G(d,p) basis set, while the copper metal centre was optimized with LANL2DZ for the sake of computational efficiency.[28] Optimization was done in gas phase in a vacuum.

4.1.2 - UV/vis Spectroscopy

UV/vis spectroscopy was done using an Orion Aquamate 8000. Solutions of both DAP and DAQ in acetonitrile were made such that their concentrations were $5x10^{-5}$ M. A stock solution of $1.57x10^{-3}$ M (100 ppm) was made by adding the requisite amount of copper (II) chloride into 100 mL of ultrapure water (obtained from a Millipore Simplicity UV). The UV/vis spectrophotometer was calibrated to a 1:1 solution of acetonitrile:water. To obtain the spectra of the ligand in its own, 1 mL of the prepared ligand solution was mixed with 1 mL of ultrapure water. For the complex, 1 mL of the ligand solution was mixed with 1 mL of the stock copper solution and left for 2 minutes to ensure that the copper and the ligand has ample time to interact. The spectrum was obtained between a range of 225 nm to 500 nm for DAP and 250 nm to 600 nm for DAQ (as well as their complexes).

4.1.3 - Sensor Testing

To functionalize these sensors, the films were first dipped into acetonitrile and left for five minutes to wet the surface. After this, they were removed from the acetonitrile and dipped into a saturated solution of either DAP or DAQ for one and a half hours. This would allow the DAP and DAQ in solution to form a self-assembled monolayer (SAM) onto the FLG surface of the sensor (Figure 8).[39] This dip-coating method to form a SAM has been

used before to coat a treated silicon substrate with octadecyltrichlorosilane and 3-aminopropyltrimethoxysilane.[40]

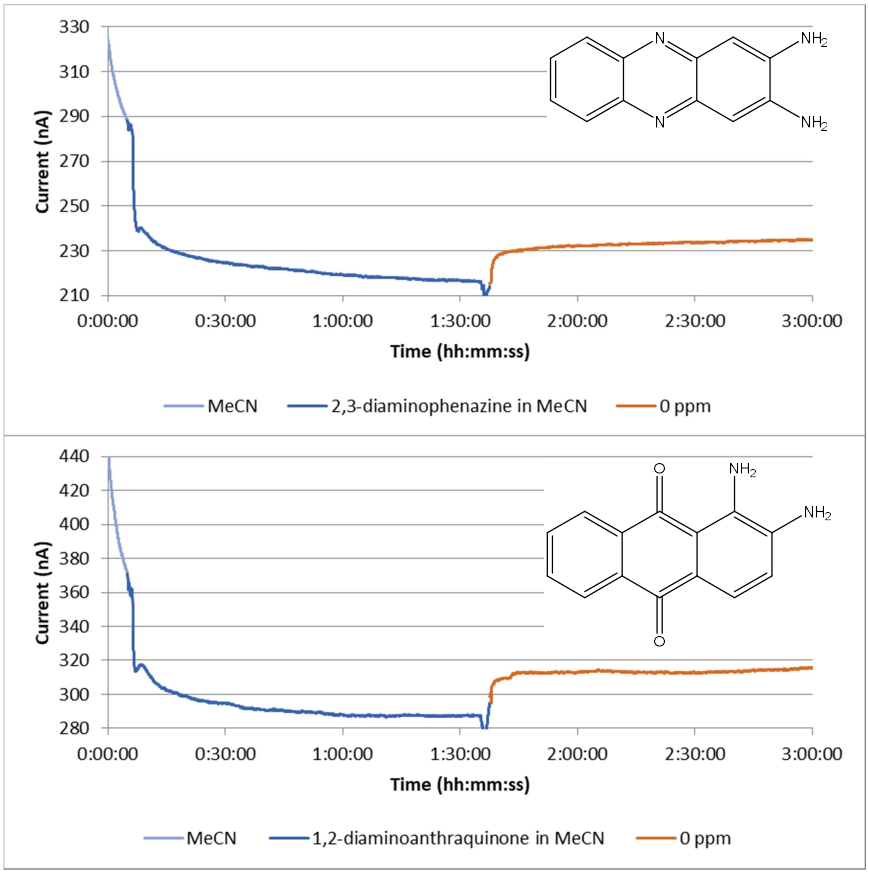

Figure 8. Functionalization of the sensors with DAP (top) and DAQ (bottom). Insets are the corresponding molecular structures. A decrease in current is observed when the sensors were dipped in acetonitrile (first five minutes), followed by a larger decrease in current during functionalization.

As the SAM forms on the FLG surface, the current decreases due to the increasing electron density on the surface. As explained in Chapter 3, the FLG contains edge defects which indicate that the graphene flakes are inherently p-doped. This indicates that electron holes are the primary charge carriers in the film. As the SAM forms, resistance increases on the surface due to the delocalized electrons from the adsorbed DAP and DAQ, which induces a coulombic attraction onto the electron holes moving within the film and consequently decreases the current.[41] After functionalization, the ligand solution was removed, and the

sensor was dried. The sensors were then dipped into a stirring vial filled with 18.2 MΩ·cm water and left overnight to equilibrate (the ultrapure water will absorb CO_2 when exposed to air, changing the pH over time). Once equilibrated, a known amount of the stock copper solution was pipetted into the water. This increased the concentration of copper in the water solution, changing the current which was displayed on the computer output. Using this output, a calibration curve was created to plot current change versus the concentration of the analyte in the water.

4.2 - UV/vis and DFT calculations

For both DAP and DAQ, copper is expected to coordinate to the two -NH_2 lone pairs present on each ligand. The complexation of copper to these sites should induce a change in the optical transitions of the ligand. Since copper is a d^9 metal, d-d transfer within the copper metal centre is the primary mechanism that induces colour change (Figure 9).[8]

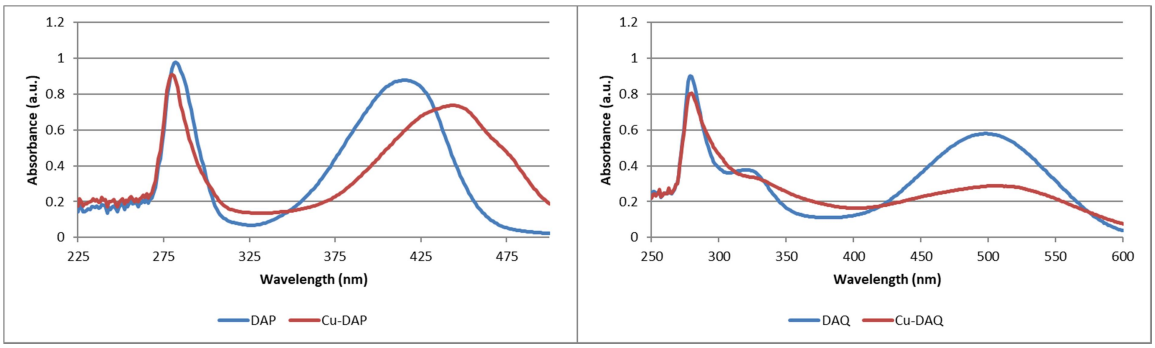

Figure 9. UV/vis spectrum of DAP and its copper complex (left) as well as DAQ and its copper complex (right).

In both cases, a slight quenching of the $\pi \rightarrow \pi^*$ transition at ~280 nm (282 nm for DAP and 279 nm for DAQ) occurs after complexation. However, the most significant change occurs in the $n \rightarrow \pi^*$ transition (415 nm for DAP and 498 nm for DAQ), where a redshift of 29 nm is seen for DAP after complexation. For DAQ, a slight redshift of 7 nm is seen, as well as

quenching of the absorbance that occurs due to this transition. This indicates that the changes to the electronic structure mainly occur in the non-bonding orbitals of the ligand-copper complex in both cases. This can also be seen when comparing the changes in the HOMO electron density of DAP and DAQ before and after complexation (Figure 10).

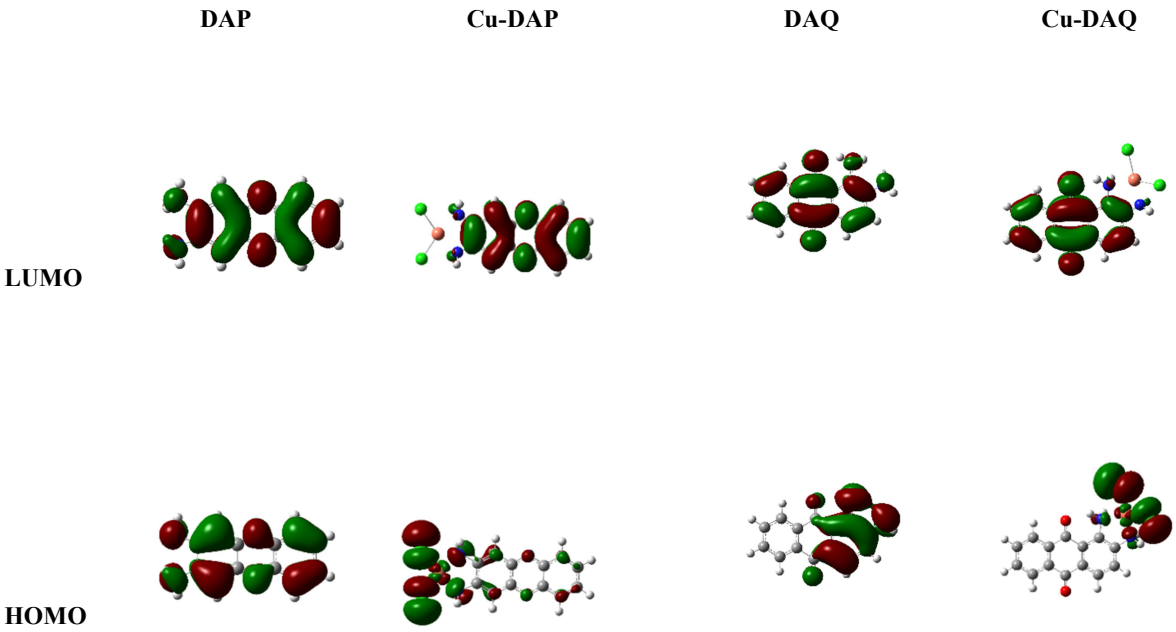

Figure 10. The frontier orbitals of DAP and DAQ, as well as their copper complexes. Chloride was used as the counter-ion.

In both DAP and DAQ, the copper metal centre was coordinated to the amine groups as well as two chloride ions. As expected, the HOMO electron density moves toward the copper centre in both cases, which indicates that the HOMO is no longer located on the anthracene backbone, but is now located on the copper $d_{x^2-y^2}$ orbital (since copper adopts a distorted square-planar configuration which leans toward a tetrahedral geometry). Both DAP and DAQ have a Cu-N bond length of 2.1 Å, and a Cu-Cl bond length of 2.2 Å. In both the non-complexed and the complexed cases, the LUMO density is quite similar, which further supports the fact that the only changes that occurred were to the non-bonding orbitals. The

red shifts observed in the $n \rightarrow \pi^*$ transition is also supported by the changes in the calculated frontier orbital molecular energies before and after complexation (Table 1).

	HOMO Energy (eV)	LUMO Energy (eV)	Band Gap (eV)
DAP	-5.4839	-1.9247	3.5592
Cu-DAP	-6.6677	-3.3241	3.3436
DAQ	-5.5465	-2.4689	3.0776
Cu-DAQ	-6.7169	-3.6988	3.0181

Table 1. Frontier orbital energies and band gaps for DAP, DAQ, and its copper complexes.

In both DAP and DAQ, relaxation of both the HOMO and the LUMO occurs, indicating that the ground state energy of the ligand decreases after complexation with the copper metal centre. The band gaps also decrease after complexation which indicates that a red shift will occur in the $n \rightarrow \pi^*$ transition energy (since the HOMO is a non-bonding copper d orbital).

Based on these results, it is concluded that copper interacts with both DAP and DAQ. The interaction changes the electronic properties of both ligands significantly, and either of them would be appropriate for use in a chemiresistive sensor for the detection of copper in drinking water.

4.3 - Sensor Results

The relaxation of the HOMO energy upon complexation, as well as the red shift in the UV/vis spectrum indicates that complexation will increase hole density in the FLG film, which will lead to an increase in current. The changes in response relative to the baseline for both DAP and DAQ were compared to determine which of the two would be more suitable for sensing (Figure 11).

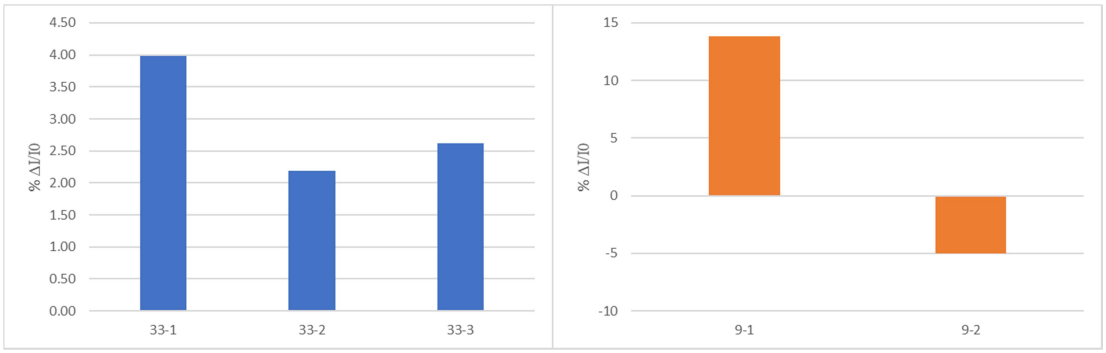

Figure 11. Relative responses (compared to the 0 ppm baseline) of DAP functionalized sensors (blue) and DAQ functionalized sensors (orange) to 1 ppm Cu^{2+}. X-axis labels are sensor identification numbers corresponding to the experiment number and sensor number from the produced batch.

DAP gave a consistent response of 2% to 4% (average 2.93%) for the three sensors that were tested. DAQ had one sensor which gave a very large response of 13.81%, and another sensor with a negative response of -5.03%. Although DAP did not give as significant of a response, the responses were more consistent than the DAQ. Therefore, DAP functionalization was used as the primary method of copper detection for all further testing.

DAP functionalized sensors were tested between a range of 10 ppb to 10 ppm to determine whether they would have a stepwise response with respect to the copper concentration in solution (Figure 12).

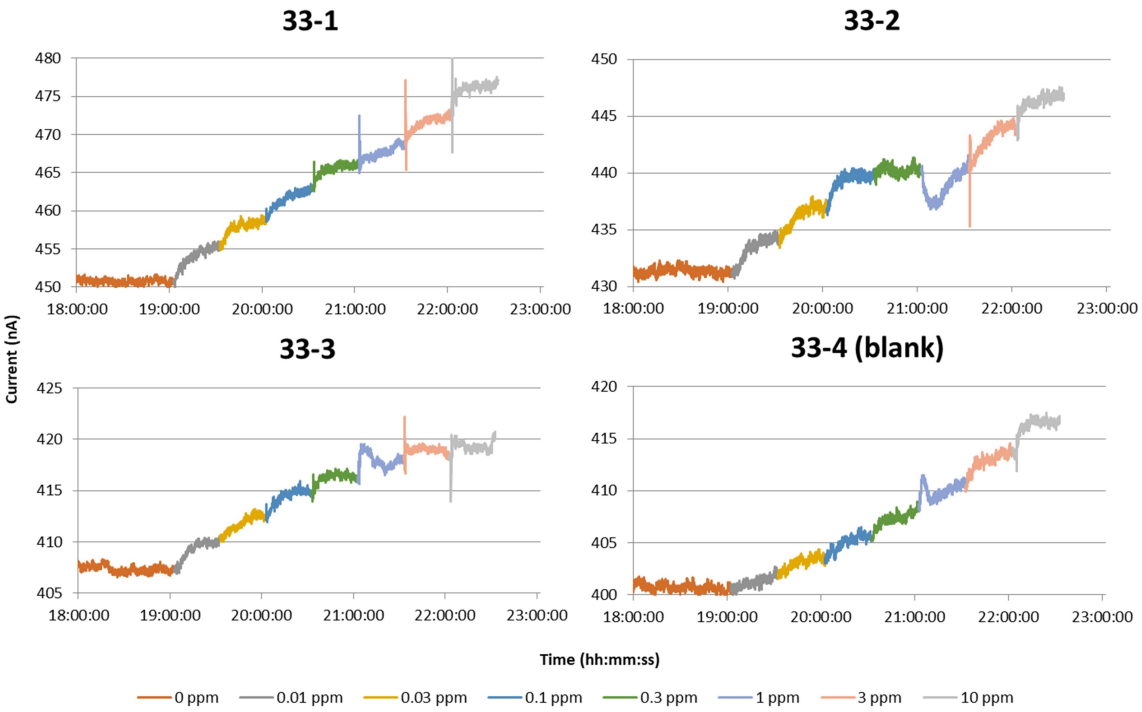

Figure 12. Current responses of the three DAP functionalized sensors (sensors 33-1, 33-2, 33-3) as well as a blank sensor (33-4) with respect to changing concentrations of copper over time.

As predicted by theoretical calculations and the UV/vis spectra, the current stepped up as copper concentration increased in solution, which indicates the existence of an electrostatic gating mechanism between the Cu-DAP complex and the FLG film it is adsorbed onto. As the relaxation of the HOMO occurs in the adsorbed DAP, coulombic attraction between the electron-rich ligand and the holes in the FLG film decreases, which will increase the current. The blank also gives a similar, albeit a less distinct, response to the functionalized sensors, which supports this mechanism (copper is positively charged, and will induce the same effect onto the film). The main difference between the functionalized and the blank sensors is that the functionalized sensors show discrete step ups in current, whereas the blank shows an upward drift with no distinct steps. Using these responses, a calibration curve can be created with a function to be able to interpolate concentration values in real water samples based on the current obtained. One such function is the Langmuir Isotherm (6),

$$\theta_A = \theta_{A,m} \frac{K_{eq}^A[A]}{1+K_{eq}^A[A]} \quad (6)$$

The Langmuir isotherm assumes that the adsorbate (in our case the complexation of copper) in solution acts as an ideal gas in isothermal conditions and binds to distinct, equal and independent sites. In this function, θ_A is the occupancy of sites, $\theta_{A,m}$ is the saturation point, K is the equilibrium constant, and [A] is the concentration of the adsorbate.[42] It is also assumed that current, which is what is being measured, is linearly correlated to the coverage of the surface. This would mean that the proportionality constant for the linear relation is included in the equilibrium constant of the adsorbate. Since copper forms a 1:1 complex with DAP, this would be a fair assumption. Consequently, the formation of a 1:1 complex would also allow for a first-order type exponential decay fit (7),

$$\theta_A = \theta_{A,m}\left(1 - e^{-k_A[A]}\right) \quad (7)$$

In this function, $\theta_{A,m}$ is the saturation point and k_A is the rate constant.[43] A more empirical approach for a calibration curve is the Freundlich isotherm, which correlates the concentration of the analyte to the mass ratio of the analyte to the surface. The isotherm is given by the following function (8).[44]

$$\frac{x}{m} = K[A]^{\frac{1}{n}} \quad (8)$$

In this function, x/m is the mass ratio of the analyte to the surface. K and n are proportionality constants for a given surface at a given temperature. The assumption here is that the relative current change is linearly correlated to the mass ratio of the analyte to the surface. The relative current changes for all of the functionalized sensors were plotted (blue dots) and a Langmuir, exponential, and Freundlich fit were plotted together with them (Figure 13).

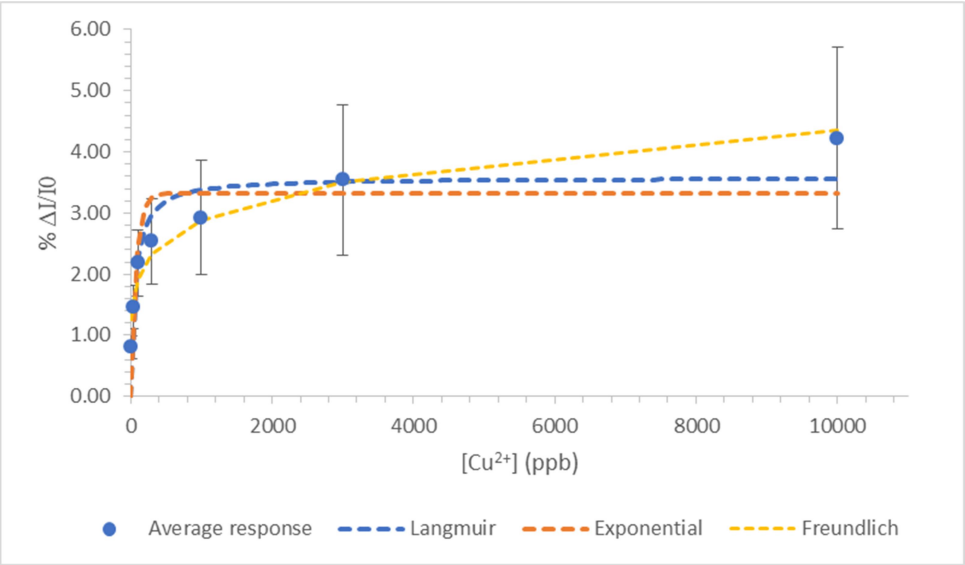

Figure 13. Average response of the three functionalized sensors (blue dots) with their standard deviation (error bars) plotted alongside the Langmuir function (blue dashed line), first order exponential decay function (orange dashed line), and Freundlich function.

The three functionalized sensors deviated significantly in their respective sensor responses, which can be seen with the rather large error bars. This is due to the inherent differences in the sensors (FLG surface area, uniformity, etc.). Using Excel's built in Solver add-in, the coefficients for the Langmuir, first order exponential decay, and Freundlich functions were found, as well as their R^2 Values (Table 2).

	$\theta_{A,m}$	K^A_{eq}	k_A	K	n	R^2
Langmuir	3.58%	0.0169 ppb^{-1}	-	-	-	0.879
First order	3.32%	-	0.0133 s^{-1}	-	-	0.772
Freundlich	-	-	-	0.8352	5.5745	0.957

Table 2. Parameters and R^2 values for the Langmuir, first order exponential decay, and Freundlich functions.

Although both the Langmuir and exponential decay functions offer a moderately decent fit as seen by their respective R^2 values, they will not suffice for quantification in a real sample setting (R^2 values of 0.95 or greater would be preferable). Freundlich gave a much better R^2 value, however this function is an empirical function, and does not give any insight into the saturation and surface coverage of the FLG film. This combined with the relatively low response (maximum 4% for 10 ppm), the large variation in response between

sensors, and the current spikes present at higher concentrations in the raw data indicate the need for optimization of the sensor. This need for optimization becomes more apparent when attempting to reset the sensors. Since the amine groups of DAP are predicted to have a pK_a of 4.74, reducing the pH of the aqueous solution will drive equilibrium away from copper chelation and toward protonation of the amine groups (Figure 14).[45]

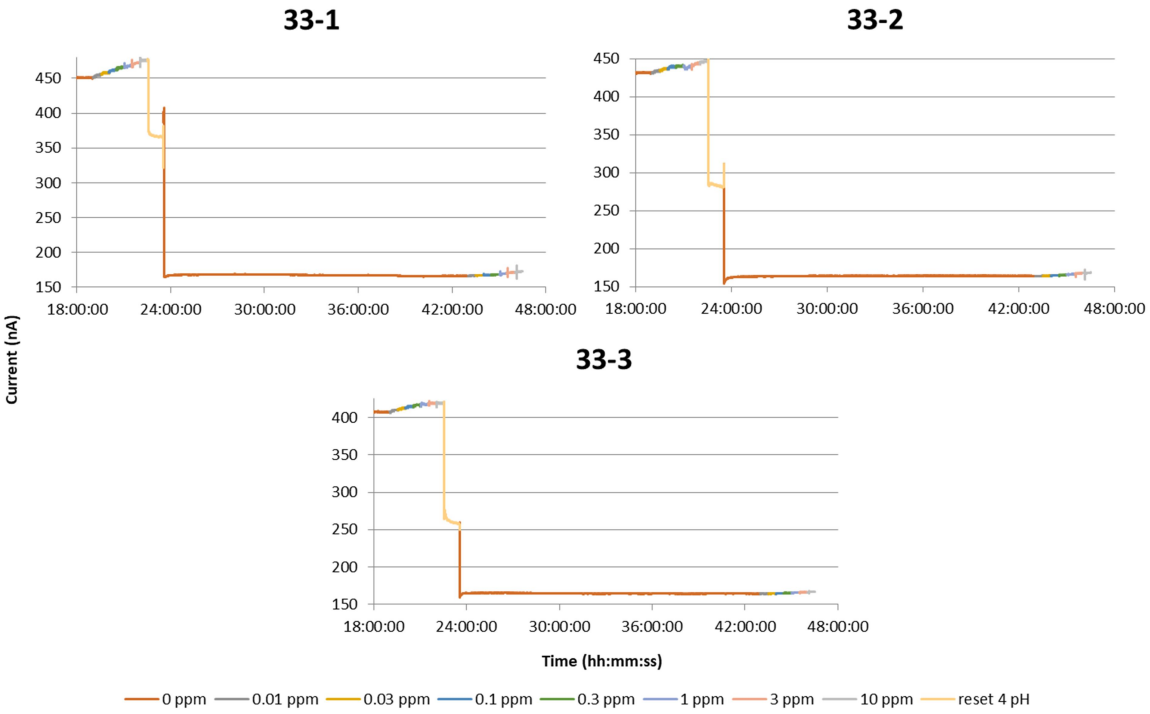

Figure 14. Sensor data of the three functionalized sensors including the reset with a pH 4 solution.

The reset had greatly damaged the sensor, shown by the large drop in baseline current. Nevertheless, there was still a response after the reset, which indicates that it was successful (in a way). The only difference in the responses before and after the reset was the magnitude of the response, which had decreased due to damage of the graphite film surface.

An attempt to optimize the sensor signal was made by varying the saturation of the ligand in the acetonitrile solution. Saturation points used were 100%, 20%, 4%, and 0.8%. The rationale behind this optimization was borne out of the concern that a saturated solution

may lead to the formation of a ligand multilayer on the FLG surface rather than a SAM, which would adversely affect the sensor response (Figure 15). Another thing to consider is the self assembly of poly (*o*-phenylenediamine) oligomers in solution when the concentration of DAP is high, which could be prevented by reducing the saturation of the ligand solution.[46]

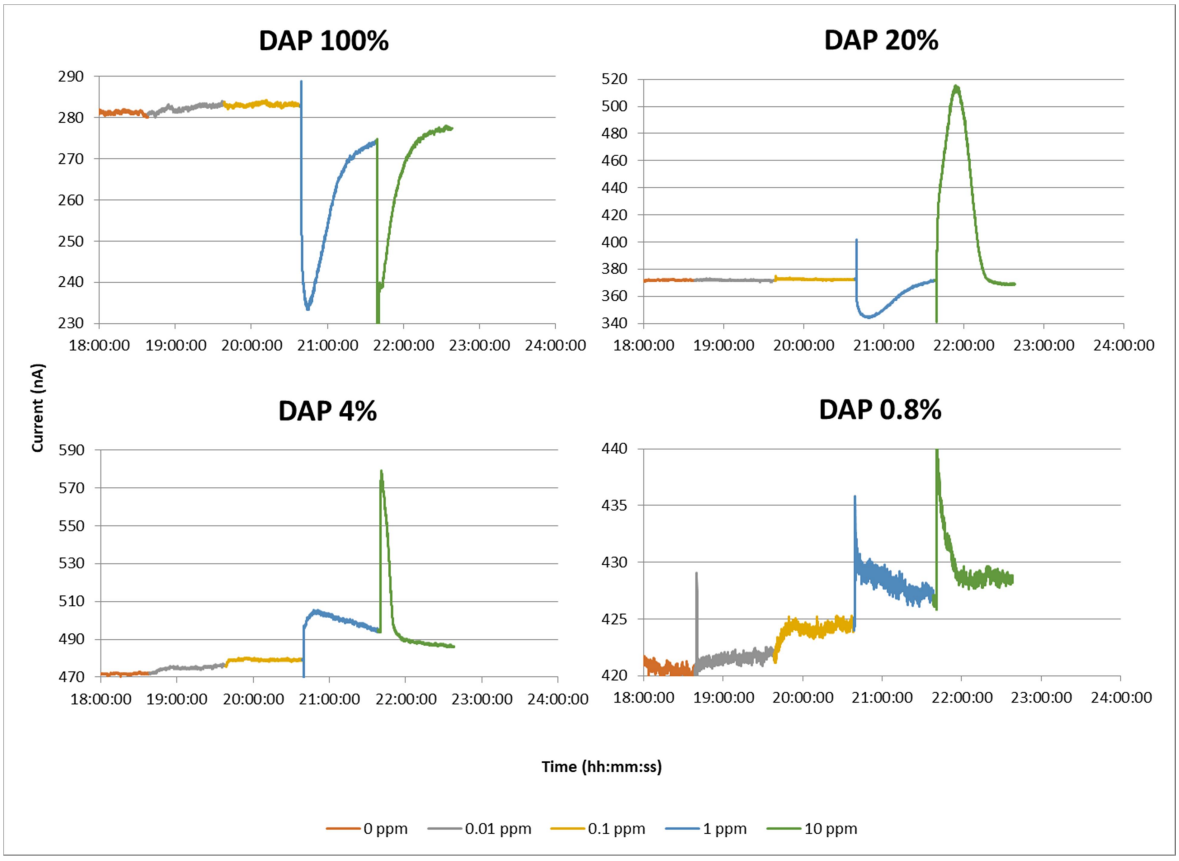

Figure 15. Sensor response for different saturations of ligand solution. Doping protocol for each was the same as mentioned previously.

Based on these results, lower concentrations will give more consistent stepwise responses with respect to the baseline. At 4% and 0.8% saturated, the ligand solutions performed best at lower concentrations, which indicates the formation of a SAM as opposed to a multilayer. At higher concentrations, however, the sensor functionalized with a 4% saturated DAP solution shows a very erratic behaviour and some drift in current. This is also seen in the sensor functionalized with the 0.8% saturated DAP solution albeit to a lesser extent. The signal for this sensor also becomes noisier at the higher concentrations, which

will be an issue when attempting to distinguish the copper detection signal from background noise.

4.4 - Summary

Both DAP and DAQ were tested as potential ligands to be used on a chemiresistive sensor utilizing FLG as its transducing material. Theoretical DFT calculations as well as UV/vis spectroscopy confirm the existence of a complex between copper and both DAP and DAQ. Complexation induced relaxation of the frontier orbital energies as well as a redshift in the $n \rightarrow \pi^*$ peak in their respective UV/vis spectra. The chemiresistive sensors were then functionalized with each ligand for comparison. Although DAQ gave higher responses, DAP was more consistent, and was used for further testing (DAQ may be revisited later on to investigate the effects of sensor optimization on its response). A step-up calibration curve was produced between the range of 10 ppb to 10 ppm for three functionalized sensors (four sensors in total; one sensor was left non-functionalized as a control). The sensor responses were able to be fit by a Langmuir function, a first-order exponential decay function, and a Freundlich function. However, the variation between sensors was quite significant, and the fits were below an R^2 value of 0.95 (save for the Freundlich function, which is ill defined and empirical in nature), making these sensors insufficient for commercial use. Resetting the sensors was attempted with an acidic solution, which damaged the sensor. Optimization of the functionalization was performed using four different ligand saturations in acetonitrile: 100%, 20%, 4%, and 0.8%. The 4% and 0.8% functionalized sensors performed well at lower concentrations of copper but behaved very erratically at higher concentrations of copper. At present, these sensors would not be appropriate for use, and requires further development.

5 - SILVER

Chemiresistive detection of silver ions in aqueous media**

Johnson Dalmieda[1], Ana Zubiarrain-Laserna[1], Devanjith Ganepola[1], P. Ravi Selvaganapathy[2], Peter Kruse[1]*

[1]*Department of Chemistry and Chemical Biology, McMaster University, Hamilton L8S 4M1, Canada*

[2]*Department of Mechanical Engineering, McMaster University, Hamilton L8S 4M1, Canada*

*Author to whom correspondence should be addressed, email: pkruse@mcmaster.ca

**This is the 2nd revised submission.

Keywords: Water Quality; Heavy Metal Sensing; Silver; Cation Sensing; Graphene; Chemiresistive Sensor

Abstract

Silver is used as a water disinfectant in hospital settings as well as in purifiers for potable water. Although there are no strict regulations on the concentration of silver in water, adverse effects such as argyria and respiratory tract irritation have been correlated to excess silver consumption. Based on this, the levels of silver in water are recommended to be maintained below 100 ppb to ensure safety for human consumption. In this work, we present a silver sensor for use in aqueous media that utilizes bathocuproine, a silver selective chromophore, adsorbed onto few-layer graphene (FLG) flake networks for the chemiresistive detection of silver. Complexation of silver to bathocuproine modulates the conductivity of the FLG film, which can be probed by applying a small voltage bias. The decrease in resistance of the film correlates with the concentration of silver in solution between 3 ppb and 1 ppm. Exposing the sensor to a lower pH resets the sensor, allowing it to be reused and reset multiple times. This sensor demonstrates a new pathway to chemiresistive cation sensing using known selective complexing agents adsorbed onto graphitic thin films. This concept can be expanded to the detection of other relevant analytes in domestic, industrial and environmental water sources.

1. Introduction

Metallic silver is commonly used in water filters to reduce the growth of biofilms within the filter itself. Silver (I) ions are used as an effective disinfectant for potable water, giving a $\log_{10}$ reduction for *L. pneumophilia, P. aeruginosa,* and *E. coli* of 2.4, 4, and 7, respectively.[1] Hospitals use copper-silver ionization for *Legionella* control in their hot water systems.[2] On the other hand, silver is not an essential metal for humans, and exposure should be limited to avoid adverse effect such as argyria[3] and respiratory tract irritation.[4,5] In the environment, high concentrations of silver salts can pose a threat to various aquatic organisms. The median lethal concentration (LC_{50}) is 58 ppb for fish and 4.8 ppm for nematodes. Crustaceans are the most sensitive however, with an LC_{50} of 0.85 ppb.[6] Currently there are no guidelines for silver ions in drinking water, and the World Health Organization (WHO) has set a health advisory (not a guideline value) of 100 ppb. The only country with a Maximum Allowable Content (MAC) is Germany, whose drinking water regulations (Trinkwasserverordnung) prescribe a MAC of 80 ppb.[7]

Several methods are currently available for the quantification of silver (I) ions in water. Lee et. al. functionalized a quartz crystal microbalance (QCM) with a suitable oligonucleotide for the detection of silver (I) in aqueous solution, resulting in a limit of detection (LOD) of 100 pM (0.01 ppb) and a limit of quantification (LOQ) of 1 nM (0.1 ppb).[8] Colorimetric approaches to silver (I) detection include use of dyes such as a water-soluble organometallic polyelectrolyte (LOD=54 ppb)[9], Tween-20 functionalized gold nanoparticles (LOD=43 ppb)[10], a Rhodamine B derivative (LOD=14 ppb)[11], and an anthracene derivative.[12] Electrochemical methods include ion selective electrodes (ISE) utilizing copper (II) ionophore (I) (LOD=65 ppt)[13] or calixarene derivatives (LOD=10 ppm)[14], as well as anodic stripping voltammetry (ASV), such as one developed by Schildkraut et. al., which utilized a carbon paste electrode to determine silver (I) in surface water (LOD=0.2 ppb)[15], and one developed by Zejli et. al., which used a polythiophene-functionalized platinum electrode (LOD=60 ppb).[16] For ultra trace detection of silver (I) in water, standard methods exist such as inductively coupled plasma-mass spectrometry (ICP-MS) (EPA method 200.8), inductively coupled plasma-absorption emission spectroscopy (ICP-AES) (EPA method 200.7), and flame atomic absorption spectroscopy (FAAS) (EPA method 7000B) (CASRN 7440-22-4).

Although these methods, as well as many more[17,18], have been used for silver (I) detection, there are various limitations that need to be addressed. QCM sensors are not reusable, as they fail to reproduce their frequency shifts upon repeated exposure to silver (I). Colorimetric methods suffer from matrix effects in real samples that may hinder the colorimetric response or quench the fluorescence of the sensor molecules. ISE's and ASV require reference electrodes, which are easily damaged and require frequent recalibration and maintenance. The standard laboratory methods such as FAAS, ICP-MS, and ICP-AES, although highly sensitive and selective, require elaborate instrumentation and sample workup, effectively ruling out *in situ* measurements.

Here we propose the use of chemiresistive sensors[19] functionalized with a silver (I) ion selective ligand to detect silver (I) ions in aqueous media with sufficient sensitivity, specificity, and robustness. Chemiresistive sensors are based on modulating the electronic structure of the sensor films itself, obliviating the need for counter or reference electrodes. In our device, a percolation network of exfoliated few-layer graphene (FLG) flakes is connected to two copper contacts at either end and exposed to the silver ions such that only the FLG and not the contacts interact with the ions.[20] The reason FLG is used as the transducing element for this sensor is due to its high conductivity and strength. The aromaticity of graphene also allows for easy functionalization through adsorption of aromatic molecules. Adsorption of these ion selective molecules does not inhibit the ballistic transport (transport without electric resistivity) of the elctrons, making functionalized graphite very appealing as a transducing element.[21] To functionalize the FLG, silver (I)-specific ligands, such as bathocuproine, can be adsorbed onto the film and interact with it electronically, imparting selectivity while preventing interactions with interfering ions.[22,23] Bathocuproine will add electron density to the FLG, effectively n-doping it. As silver ions bind to the bathocuproine on the FLG surface, changes in the energy levels of bathocuproine occur. This will cause a decrease in the resistance of the film. As the analyte concentration increases, so do the amount of complexed silver (I) ions, and the magnitude of the resistance change. We have previously demonstrated this principle to detect free chlorine in aqueous media using oligoanilines adsorbed onto carbon nanotubes or graphitic films.[24,25] The linear range for these sensor devices was from 60 ppb to 60 ppm, providing sufficient sensitivity for drinking water applications.[26] The novelty of this sensor lies in the fact that physisorption of the selective molecule is what drives the response rather than a direct bond to the transducing element, as is common in other chemiresistive sensors.[27] This is also the first time bathocuproine has been used for silver (I) detection rather than the previously reported copper (I), which requires reducing agents to facilitate sensing.[28] The development of an aqueous silver (I) sensor is a departure from the redox-based response exhibited by the free chlorine sensor to a complexometric based response, which can be used as a template for detection of various other metal cations.

2. Experimental

2.1. Materials

FLG was prepared from natural graphite powder (-200 mesh, 99.9999% trace metals basis, Alfa Aesar). 96% bathocuproine, silver (I) nitrate, iron (II) chloride tetrahydrate, sodium phosphate monobasic monohydrate, zinc (II) chloride, copper (II) chloride, magnesium chloride hexahydrate, and calcium chloride dihydrate were purchased from Sigma Aldrich. Sodium sulphate, sodium chloride, sodium hydroxide, and sodium nitrate were purchased from Caledon. Potassium chloride

and sodium bicarbonate were purchased from EMD Millipore. Ultrapure water (18.2 MΩ·cm) was obtained from a Millipore Simplicity UV water purifier unit. 1 M nitric acid was prepared by diluting 68% nitric acid (ACS reagent grade) with purified water. All organic solvents used were HPLC grade.

Standard solutions for the salts were prepared by dissolving the appropriate mass into 100 mL of purified water. The bathocuproine solution was prepared by dissolving the ligand into 30 mL of either methanol or acetonitrile until the solution is saturated. Since bathocuproine dissolves at a slower rate in acetonitrile, the solution was left in the dark overnight to dissolve.

Sensor devices were fabricated using twin frosted glass slides (purchased from VWR), freshly prepared exfoliated graphite, a 9B pencil, ¼" wide EMI Copper Foil Shielding Tape (3M #1181), and Sylgard 184 (Dow Chemical; silicone elastomer base was mixed with the curing agent in a 10:1 ratio).

2.2. Spectroscopic Characterization

UV-Vis spectra were obtained by mixing 2 mL of 5.0×10^{-5} M bathocuproine in acetonitrile with 5 mL of a 100 ppm solution of silver (I) nitrate in purified water. The solution was then transferred to a quartz cuvette, and analysed using an Orion Aquamate 8000 spectrophotometer over a range of 200-500 nm.

Raman spectra of drop cast FLG films were recorded on a Renishaw inVia Raman spectrometer using a 514 nm laser and a 50× objective at 10% power with 3 accumulations over 30 seconds each.

Bathocuproine powder, a bathocuproine sample reacted with silver nitrate (as described for UV-Vis spectroscopy, then rinsed and dried), and a set of sensors underwent analysis by X-ray photoelectron spectroscopy (XPS) in order to confirm the functionalization of the films and to gain more insight into the sensing mechanism. The samples were analyzed using a Kratos AXIS Ultra X-ray photoelectron spectrometer. XPS survey spectra were obtained from an area of approximately 300 x 700 μm using a pass energy of 160 eV. XPS high resolution spectra were obtained from an area of approximately 300 x 700 μm using a pass energy of 20 eV. The devices sent for analysis were exposed to the same sequence of solutions. However, they were removed from the solutions at different stages. All devices were rinsed with ultrapure water at the end and they were stored under an inert nitrogen atmosphere until the time of analysis. All spectra were charge corrected to the C 1s binding energy of 284.5 eV for C=C.

2.3. Synthesis of exfoliated FLG

Exfoliated FLG flakes were prepared using a literature procedure.[29] 40 mg graphite was added to 15 g of 30% (w/w) isopropanol:water mixture in a 20 mL capped glass vial and sonicated in a bath sonicator (Elmasonic P30H Ultrasonic Cleaner) for six hours at 80 kHz (100% power) and 30 °C using the sweep setting.

The suspended FLG flakes were then centrifuged for 5 minutes at a relative centrifugal force (RCF) of 14100 × g (14500 rpm) in an Eppendorf MiniSpin plus centrifuge to separate the bulk unexfoliated graphite. The supernatant (with the exfoliated FLG) was retained, and re-centrifuged for 15 minutes at 14100 × g. The supernatant of the second centrifugation step (containing smaller, defect-rich graphene flakes) was discarded and the precipitate retained for sensor fabrication.

2.4. Sensor fabrication

Figure 1a shows an exploded view of the different components that make up a sensor. First, the glass slides were cleaned with methanol (Figure 2a) and two pencil graphite patches were drawn using a 9B pencil on opposite sides of the frosted side in order to decrease the contact resistance between the FLG films and the copper tape (Figure 2b). Then, the precipitate of exfoliated FLG was re-suspended in an isopropanol-water mixture and drop casted until a resistance of 10 – 20 kΩ was achieved (overall film size 21 × 18 mm: bare graphite 8 × 18 mm, pencil reinforcements 6.5 × 18 mm). The drop casting was performed on a hotplate at 100 °C to accelerate solvent evaporation (Figure 2c). Next, two adhesive copper tape strips were attached over the pencil contact reinforcements from end to end of the glass slide (Figure 2d). The sensors were packaged by masking the copper contacts with a thin layer of silicone elastomer. In order to prevent the elastomer from spreading over the FLG film, it was let to partially cure (approx. 6 hours at room temperature) so as to acquire a thicker consistency prior to application. The sensors were placed on a hotplate at 60 °C until the elastomer was completely cured (Figure 2e). A picture of a finished sensor is shown in Figure 1b. Images of the deposited FLG films were obtained with FESEM (JEOL JSM-7000F, Figures 1c and 1d), which show a network of FLG platelets arranged parallel to the glass slide. Raman spectroscopy was also used to study the quality of the FLG films (Figure 1e). The spectrum shows peaks characteristic of graphitic materials (namely the G, 2D and D + D'' bands). The absence of a shoulder in the 2D band suggests that the films consist of few layer graphene and not graphite, for which it should split into $2D_1$ and $2D_2$ components.[30] Finally, the D, D' and D + D' bands indicate that defects have been introduced in the flakes during processing. Some of these defects are related to the size of the platelets (i.e. edge defects).[31]

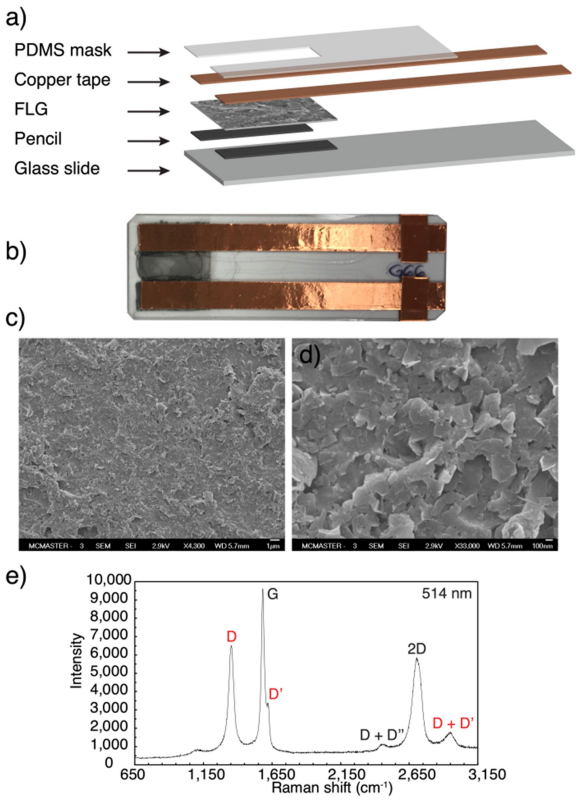

Figure 1. a) Components of a sensor. **b)** Picture of a finished sensor. **c – d)** FESEM images of the few layer graphene (FLG) film at different magnifications: **c)** × 4,300 and **d)** × 33,000. **e)** Raman spectrum of the FLG film. The peaks labelled in black are characteristic of FLG, while the peaks labelled in red indicate the presence of defects.

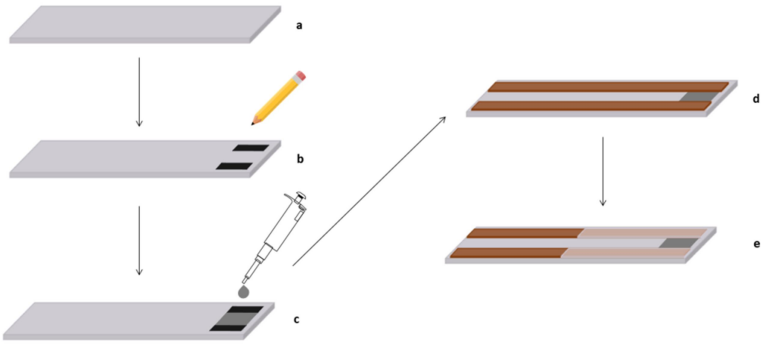

Figure 2. Detailed instructions for the fabrication of the chemiresistive sensor. **a)** Prepare and clean a twin-frosted glass slide. **b)** Draw two thick pencil pads on either end of the glass slide using a 9B pencil. **c)** Drop cast the exfoliated graphite between the pencil pads at 100°C. **d)** Apply conductive copper tape lengthwise along the sensor overlapping the pencil pads. **e)** Apply PDMS over the copper tape at 60°C and allow to cure.

2.5. Sensor Characterization

An eDAQ EPU452 Quad Multi-Function isoPod with USB (purchased from eDAQ Inc) was used for data collection and was set to a polarization of 10 mV over a current range of 2000 nA. The sensors were run using the "Biosensor" configuration. A pH probe and a conductivity probe were also purchased from eDAQ Inc as part of an ER7006 Multisensor Kit. The pH probe was calibrated using two buffer solutions with pH 4 and pH 7 at 25 °C. The conductivity probe was calibrated using a 0.1 M KOH solution with a cell constant of 0.1 cm^{-1}. The eDAQ was connected to a computer via a USB serial controller for data acquisition and processing.

For the calibration experiment, four sensors were run in parallel. The sensors were first dipped in either methanol or acetonitrile in a glass jar for 5 minutes to wet the FLG surface. The sensors were then removed from the solvent, and three of the sensors were dipped into a solution of bathocuproine in either methanol or acetonitrile (the same solvent as used for wetting) for 3 hours to functionalize the FLG surface. The fourth sensor was placed back into the same solvent used for wetting and was used as a blank for control. After 3 hours, the sensors are removed from their respective solutions, and dried with a heat gun (pointed at the backside of the sensor). The sensors were then placed into separate glass jars filled with 50 mL of purified water and a stir bar. Each sensor was oriented facing the stir bar, with the sensor and the stir bar on opposite sides of the glass jar. The water was stirred, and the sensors were left overnight for 18-24 hours to equilibrate. Once equilibrated, appropriate amounts of the 100 ppm stock silver nitrate solution were added such that the Ag^+ ion concentration of the solution in the glass jars was 3 ppb. This was left for 1 hour, during which the current increased, and equilibrated after ~15 minutes. The same was done for 10 ppb, 30 ppb, 100 ppb, 300 ppb, and 1 ppm of Ag^+. To reset the sensors and return them to the 0 ppm baseline, the sensors were removed from the Ag^+ ion containing solution, placed into four jars with 30 mL of HNO_3 solution diluted from the 1M stock solution to a pH of 3, and left for one hour. The sensors were then removed from the pH 3 solution, rinsed with purified water, and placed into 50 mL of stirring purified water in glass jars for 18-24 hours (overnight) to equilibrate once more.

For the interference experiments, six sensors (four functionalized, two blank), as well as a pH probe and a conductivity probe were placed into a 1 L Pyrex bowl filled with 500 mL of stirring purified water and left overnight for 18-24 hours to equilibrate. The stir bar was placed at the centre of the bowl, with the sensors surrounding the perimeter of the bowl facing towards the centre. To test the pH response, a 1 M NaOH solution was used to adjust the pH to 10. Once the pH was set to 10, the sensors were left to run for one hour. The pH was then lowered to 9 using 1 M HNO_3 and was once again left for one hour. This was done for each pH value down to a pH of 3. To test for interferences, the purified water was treated with 1 M HNO_3 and sodium bicarbonate solution to adjust the pH and conductivity to 6.7 and 31 µS/cm, respectively (based on levels typically found in surface waters, such as Duchesnay Creek[32]). A stock solution of the interfering ion was then pipetted into the Pyrex

bowl until the desired concentration was achieved. This was left for 20 minutes, after which the pH was dropped to 3 using 1 M HNO_3 to reset the sensors. The sensors were left to reset for 20 minutes, and then removed from the pH 3 solution. This was replaced by a fresh solution of stirring purified water with the pH and conductivity adjusted using 1 M HNO_3 and sodium bicarbonate and left for 20 minutes before adding the next interfering ion.

3. Results and Discussion

3.1. Sensing principle

The sensing principle for this sensor is based on the formation of a complex between bathocuproine (Figure 2 inset) and silver (I). Bathocuproine has been used as an exciton blocking layer in organic photovoltaics and organic semiconductor devices. This is due to its large bandgap of 3.5 eV, with the LUMO lying at a potential of 3.5 eV. However, when a silver layer is in contact with a bathocuproine layer in an organic diode, the formation of the silver-bathocuproine complex allows for efficient electron transport despite the large band gap.[33] This occurs due to the stabilization of the LUMO caused by the complex, which in an organic diode causes the LUMO of the bathocuproine layer to line up with the Fermi level of the silver layer, allowing for efficient electron transport.[34] In our sensor device, bathocuproine is adsorbed onto a p-type graphene surface through π-π stacking. As the bathocuproine adsorbs, the current through the FLG flake network decreases due to charge transfer occurring from the bathocuproine to the graphene layer. Holes are the primary charge carriers on FLG surfaces that have been exposed to ambient, and a decrease in hole density in the film will lead to a decrease in current. Once the sensor is exposed to Ag^+ ions, the positively charged complex that forms acts as an "electron trap", with charge transfer occurring from the graphene surface to the newly formed silver-bathocuproine complex. This increases the hole density in the film, which consequently increases the current.[35]

The formation of a silver-bathocuproine complex can be seen in the UV-Vis spectrum (Figure 3). As the silver (I) complexes, the peak at 286 nm experiences an increase in the absorbance, which indicates an increase in the transmission probability of the electrons after complexation due to the additional energy level between the HOMO (now the HOMO-1 of the complex) and the LUMO provided by the Ag^+ ion. Further evidence of complex formation comes from high resolution XPS data of the N 1s peak (Figure S1). While most nitrogen atoms in the pure bathocuproine powder have a 1s binding energy compatible with imines, the silver (I) complex shows an increase in the N 1s binding energy, similar to an amine or amide (the nitrate and nitrite peaks stem from the counter ions of the silver salt due to the use of $AgNO_3$). In contrast, for bathocuproine molecules adsorbed onto FLG films as part of a sensor before and after exposure to 1 ppm of Ag^+ ions, there is no such shift in binding energy, as the binding energy of N 1s in the adsorbed bathocuproine already resembles an

amine (Figure S2). Any electronic changes of the molecule during complex formation are directly handed through to the substrate. While Ag^+ ions struggle to interact with the non-functionalized sensor, as evidenced by a very small Ag 3d XPS peak (left side of Figure S3) and a low Ag / N atomic ratio (Table 1), they readily interact with bathocuproine-functionalized FLG films (right side of Figure S3). The silver in the adsorbed bathocuproine complex has an Auger parameter compatible with silver (0), meaning that it acted as an electron acceptor, or p-dopant as described above. This charge transfer between the graphene film and the silver-bathocuproine complex drives the response of the sensor.

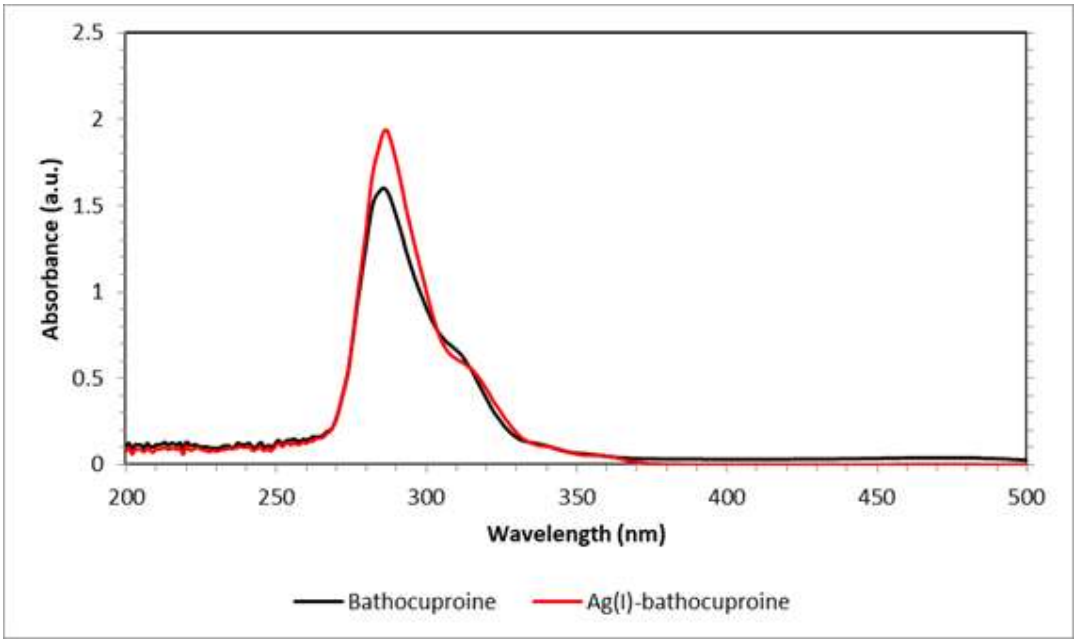

Figure 3. UV-Vis spectra of bathocuproine (black) and the silver (I)-bathocuproine complex (red). Inset: Structure of bathocuproine. The complex with silver will be formed by interaction with the two nitrogen atoms.

Sample	Ag / N atomic ratio
Non-functionalized sensor	0.00
Non-functionalized sensor + 1 ppm Ag^+	0.30
Non-functionalized sensor + 1 ppm Ag^+ + pH 3 HNO_3 reset	0.17
Functionalized sensor	0.00
Functionalized sensor + 1 ppm Ag^+	1.40
Functionalized sensor + 1 ppm Ag^+ + pH 3 HNO_3 reset	0.25

Table 1. Sample composition based on XPS survey spectra (Ag 3d, N 1s) of bathocuproine and silver-bathocuproine complex powder samples as well as non-functionalized and functionalized sensors preserved at different stages of the sensing procedure. The Ag / N ratio was calculated from atomic% values.

3.2. Silver sensing and sensor optimization

The increase in hole density as Ag^+ ions bind to bathocuproine allows for quantification of Ag^+ ions in aqueous media. The concentration of Ag^+ ions in solution correlates with an increase in current through the sensor over a tested range of 3 ppb to 1 ppm, as seen during calibration of the sensor (Figure 4). Each increase in concentration gave a step up in current, which can be correlated to the concentration of Ag^+ ions in solution. This agrees with the behaviour predicted by the charge transfer mechanism between the graphene and bathocuproine once complexed to silver (I). This behaviour is highly reproducible across multiple functionalized devices (Figure S4), while unfunctionalized ("blank") sensor devices do not show any reliable or reproducible response over the tested Ag^+ ion concentration range. Furthermore, blank sensors tend to show visible signs of metallic silver deposition even at low silver concentrations (glittery appearance, Figure S5, right side) resulting in significant noise (Figure S4) on the sensor signal, while functionalized sensors can be used repeatedly without noise or signs of silver deposition (Figure S5, left side).

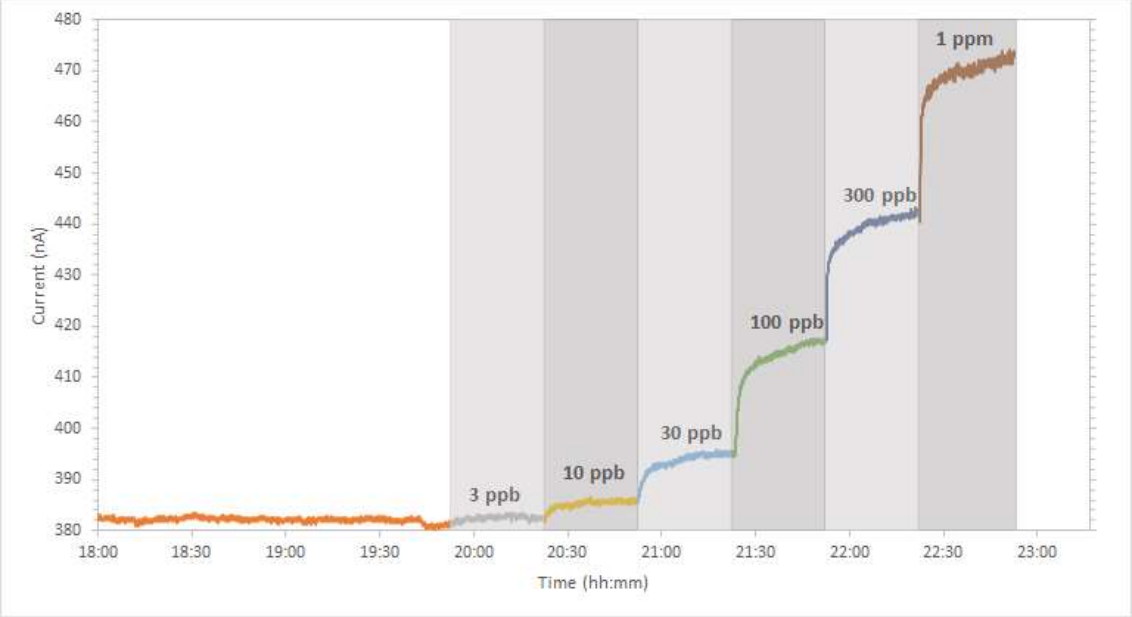

Figure 4. Current response to different concentrations of silver (I) in solution. Concentrations below 30 ppb took ~15 minutes to reach a stable current value. Above this, stabilization only took ~5 minutes.

To ensure that optimal sensor performance is achieved, the functionalization of the sensors was optimized. Bathocuproine is known to dimerize in solution. The occurrence of a dimer or trimer occurs when the sp^2 hybridized imino groups of one bathocuproine monomer bond to the out-of-plane phenyl group of another monomer. This removes one active binding site (the silver (I) binds to the imine nitrogens in the molecule) and causes aggregates of the bathocuproine to clump up onto the FLG film, affecting further adsorption of other bathocuproine monomers and detection of Ag^+

ions.[36] In concentrated solutions of bathocuproine, these aggregates can form heterogeneous multilayers on the graphene surface rather than a uniform self-assembled monolayer. The solution concentration will affect whether the bathocuproine molecules prefer to interact with each other in solution or with the graphene surface, so this parameter must be accounted for.[37,38] With this in mind, eight different sensors were evaluated, four with methanol and four with acetonitrile. The bathocuproine solution saturations for each solvent were 100%, 20%, 4%, and 0.8% relative to a fully saturated solution in the respective solvent. Sensors were exposed to the different bathocuproine solutions for 3 hours, and sensor performance was then analyzed in water by adding calculated amounts of Ag^+ aqueous stock solution to ultra pure water (Figure S6).

The sensors fabricated using 4% solutions had the largest and most reliable responses relative to the 0 ppm baseline over the widest Ag^+ concentration range for both methanol and acetonitrile. Acetonitrile was chosen as a solvent because it causes lesser swelling of the PDMS used as a dielectric protective layer than methanol.[39] Therefore, all subsequent devices used to characterize sensor performance (including Figure 3 and XPS data) were functionalized using a 4% (relative to fully saturated) bathocuproine solution in acetonitrile.

3.3. pH and conductivity response

Since the bathocuproine molecule has two imino groups, protonation will occur at low pH due to the presence of a lone pair on each of the nitrogen atoms. Based on the pK_a of neocuproine (5.79), it can be anticipated that the Ag^+ ion sensor would behave as a "proton sensor" below a pH of 6.[40] To confirm this, the response of the sensor to various pH was assessed to determine the optimal working range of the sensors. The responses were averaged between the four functionalized sensors and the two blank sensors. The error bars represent the standard deviation between replicates (Figure 5a).

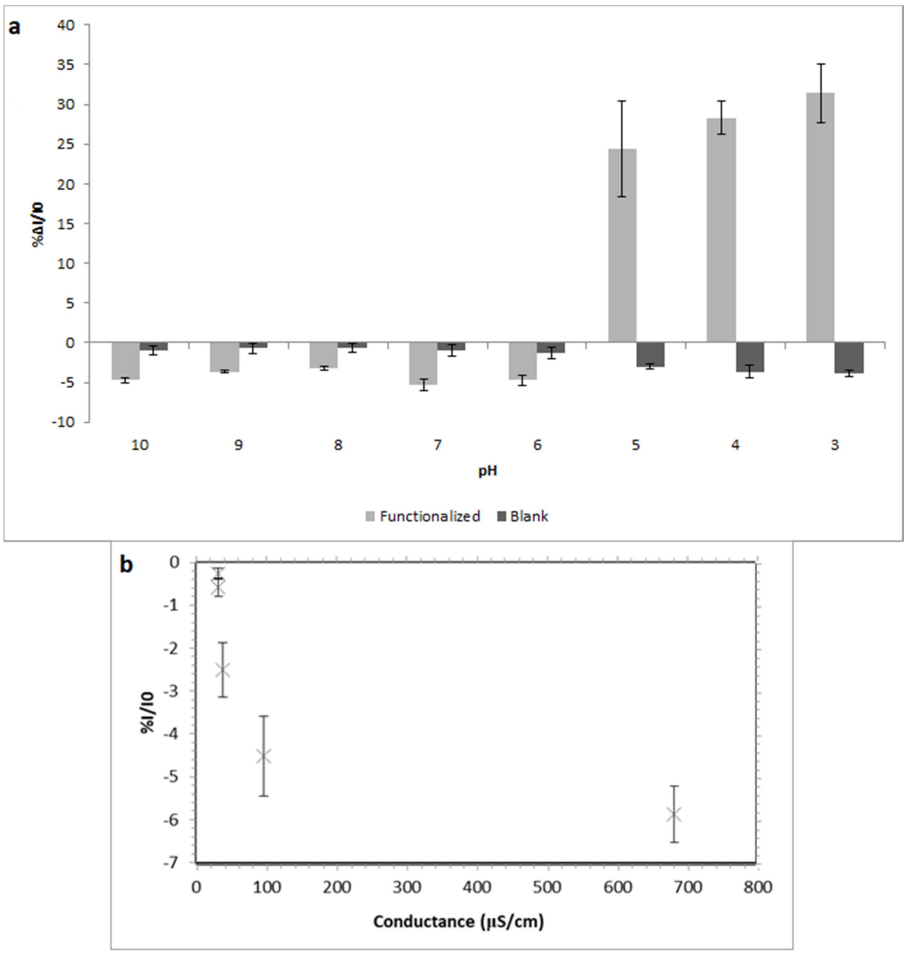

Figure 5. a) Comparison of the sensor response to changes in pH. Only the bathocuproine functionalized sensors exhibit a change in response direction from decreasing to increasing, confirming that functionalization has occurred and that a pH reset is possible. **b)** Sensor response due to conductivity of the aqueous solution. A response in the opposite direction of the silver (I) response indicates the presence of an electrostatic gating effect in the presence of high-conductance aqueous samples.

From pH 10 to 6, there was no significant change in sensor response, indicating that it was stable over that range. However, once the pH changed from 6 to 5, a response of 24% (relative to the 0 ppm baseline) was seen, with the response increasing to 28% at pH 4, and 31% at pH 3. Based on these findings, the working range of this sensor is established to be from pH 6 to pH 10. Below pH 6 the bathocuproine adsorbed onto the FLG begins to protonate, while silver (I) hydroxide will start precipitating above pH 10. The sensor responses in Figure 3 are given relative to a baseline of purified water in the absence of added ionic species. After addition of dilute NaOH to adjust the pH to 10, the ionic strength of the solution is significantly increased, further increasing as HNO_3 is added to reduce the pH. The resulting increase in conductance of the solution is the cause for the observed reduction in sensor film conductivity.

The conductance of the aqueous sample has to be taken into consideration because the ionic strength of the solution impacts the electrochemical double layer that is formed at surfaces in contact with it, including the surface of the chemiresistive sensors. A higher ionic strength would lead to a more compact double layer, leading to electrostatic gating of the resistive film.[41] Depending on the doping state and surface structure of the film, this may increase or decrease its resistance. A different impact on the sensors is also possible, if part of the current through the sensor was able to bypass it and flow through the analyte solution, thus adding a parallel resistance (potentially even lower than the original film) and thus leading to a marked decrease in resistance (i.e. increase in sensor current). The sensor response was thus tested as a function of conductivity by gradual addition of sodium bicarbonate to increase the ionic strength of the aqueous solution in the absence of Ag^+. The current response is shown to decrease with increasing conductance (Figure 5b), thus ruling out the possibility of a short circuit of the sensor current through the solution. This is consistent with our previous reports that short circuits though a conductive aqueous solution can be avoided by applying a sufficiently low voltage bias across the chemiresistive film.[19] An electrostatic gating effect from a more compact electrochemical double layer is confirmed, although smaller than the analyte response and opposite in sign. The ionic strength or conductivity of the analyte solutions will have to be taken into account when the sensor is calibrated, but since the response quickly saturates, this should not be an issue in practice.

3.4. Sensor reset and reuse

The reliance of this sensor on complexation of bathocuproine to Ag^+ ions makes its response time dependent on the time required to establish the binding equilibrium. At pH values higher than the pK_a of bathocuproine, the rate of dissociation of the silver-bathocuproine complex is much too slow, making a return to the baseline current quite time consuming. To rectify this, the sensor was reset back to the baseline using an acidic solution. Reducing the pH of the solution to less than 5.8 should drive equilibrium toward protonation of the imine groups in the ring structure and away from complexation toward Ag^+ ions. To reset the sensor, a pH 3 solution of HNO_3 was used (nitric acid was used to prevent precipitating silver (I) salts from solution by the anions associated with other acids) (Figure 6a). The sensors were kept in the pH 3 solution for one hour to allow for sufficient time to reset. While there was some baseline drift during the first cycle of the sensor (Figure S7), after the initial reset the baseline had stabilized at ~355 nA, returning to the same value after the two subsequent resets. This behaviour was reproducible in multiple devices (Figure S7). The percent changes post-reset also remained quite similar to their previous values, which show that this sensor can be reset and reused multiple times. Resetting can also be done in a reagent-less fashion through amperometric pH regulation. This method would be most useful for remote, online monitoring of water systems.[42-45]

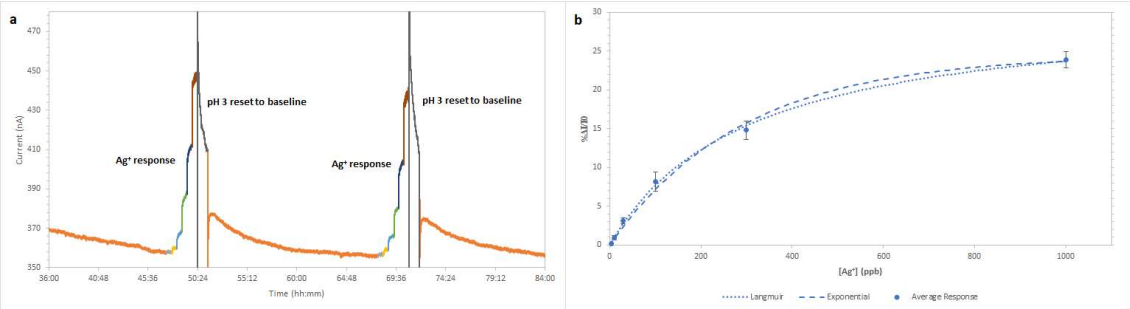

Figure 6. a) Sensor reset with pH 3 HNO_3. It takes 1 hour for the sensor to reach the previous baseline, after which silver (I) can be spiked into solution once again. **b)** Average relative change in current, with the Langmuir and exponential decay function plotted alongside.

XPS analysis was also performed on bare and bathocurpoine-functionalized FLG sensor films at three different stages of the sensing process: (1) after functionalization (or equivalent exposure to pure acetonitrile) and overnight exposure to water; (2) after subsequent exposure to 1 ppm of Ag^+ ions and (3) after subsequent resetting for 1 hour at pH 3. The Ag / N atomic ratio determined from the normalized Ag 3d and N 1s peaks in the survey spectra (Table 1) shows that the functionalized sensors adsorb significantly more silver upon exposure. Furthermore, the adsorption onto the sensor is almost completely reversible for the functionalized sensors only. The small residual amount of silver on the functionalized sensors after reset at pH 3 for 1 hour is likely correlated to defects in the sensing film and explains the observation that the first reset of any new device is incomplete, unlike those of subsequent cycles (Figure S7). It nevertheless does not appear to impede further function of the device.

3.5. Analytical performance

The changes in current relative to the baseline can be correlated to the concentration of Ag^+ ions in solution. This correlation can take the form of a function that can be used to interpolate or extrapolate the concentration with any given change in current. Based on the underlying mechanism two functions can be considered for this calibration curve, namely the Langmuir isotherm and a first-order reaction function (exponential). The Langmuir isotherm assumes that the adsorbate (in our case the complexation of Ag^+) binds to distinct and independent sites (1), and that the sensor response is directly related to the concentration of bound species.

$$\theta_A = \theta_{A,m} \frac{K_{eq}^A[A]}{1+K_{eq}^A[A]} \quad (1)$$

In this function, θ_A is the occupancy of sites, $\theta_{A,m}$ is the saturation point, K is the equilibrium constant (corrected for the sensor response function), and [A] is the concentration of the adsorbate. Since Ag^+ ions form a 1:1 complex with bathocuproine, this would be a fair assumption.[46]

Alternatively, the formation of a 1:1 complex can also be modelled by a first-order type exponential decay fit (2).

$$\theta_A = \theta_{A,m}(1 - e^{-k[A]}) \quad (2)$$

In this function, θ_A is the product formed, $\theta_{A,m}$ is the maximum amount of product that can be formed, and k is the rate constant.[47] In this empirical relationship the assumptions of coverage being limited to a monolayer and proportional sensor response are removed, but the inclusion of (0, 0) in the calibration curve as well as the asymptotic behaviour (saturation) of the sensor response at high concentration are maintained. The average relative current changes of the same sensor between reset cycles were plotted (blue dots) and a Langmuir and exponential fit were plotted together with it (Figure 6b).

The Langmuir curve gave constant values of 30.87% for $\theta_{A,m}$ and 0.0033 M^{-1} for K^{A}_{eq}, with an R^2 of 0.9982. The first order exponential decay curve gave constant values of 24.45% for $\theta_{A,m}$ and a value of 0.0034 $M^{-1}s^{-1}$ for k, with an R^2 value of 0.9939. The Langmuir fit indicates that the sensor will saturate at a relative current of 30.87%, with 1 ppm of Ag^+ resulting in a current change of 23.92±1.05%. The exponential model has an even lower saturation current change of 24.45%, which would indicate that the sensor response will saturate beyond 1 ppm for the Ag^+ ion sensor. The current changes were reproducible, with the values having a standard deviation no greater than 1.24% over the three reset-step up cycles. The limit of detection - calculated using an s/σ ratio of 3 - was determined to be 3 ppb. The response of the sensor was also linearized by plotting the concentration of Ag^+ against the ratio of the Ag^+ concentration to the current response, and was found to have a linear range of 30 ppb to 1 ppm (Figure S8). It should be noted that the linear range for the sensor is irrelevant since the calibration will be fit to a Langmuir Isotherm.

As the concentration exceeded 1 ppm, reduction of Ag^+ to elemental Ag occurred due to the flow of current in the FLG film. This was evident from large noise in the sensor response (Figure S6), as well as a glittery appearance of the exposed sensors similar to the non-functionalized sensor shown in Figure S5. Thus, the effective maximum measurable concentration for this sensor is 1 ppm.

3.6. Interferences

The sensors were tested against a range of common interfering ions to determine feasibility for use in environmental and industrial settings (Figure 7a). The following interferant concentrations were used, based on common concentrations in real samples [32]: SO_4^{2-} (250 ppm), Fe^{2+} (1 ppm), Cl^- (100 ppm), PO_4^{3-} (1 ppm), NO_3^- (50 ppm), K^+ (1 ppm), Zn^{2+} (1 ppm), Cu^{2+} (1 ppm), Mg^{2+} (1 ppm), Ca^{2+} (10 ppm). Each interferant was tested individually in the given order, with sensors being reset and rinsed between interferants. At the end, the sensor response to 100 ppb of Ag^+ ions was also

tested. All devices thus underwent 11 sensing and reset cycles over 15 hours for the purpose of this experiment (in addition to overnight rest periods in water), showing no signs of degradation and fully responding to Ag^+ ions at the end. No significant interference was found from the interferants at the tested concentrations, with the exception of Cu^{2+}, which at 1 ppm was shown to give almost half of the response of 100 ppb of Ag^+ ions. Copper is directly above silver on the periodic table. Due to their chemical similarity it does not surprise that copper would interfere with the silver (I) sensor response. However, it has a preference for an oxidation state of +2, whereas bathocuproine only binds to metals with a d^{10} electron configuration and a +1 oxidation state, making the sensors more selective toward silver (I) in an oxidizing environment (presence of dissolved oxygen). In environmental water, Cu^{2+} is also very sparse, with concentrations rarely exceeding the low-ppb levels.[32] If the concentration of Cu^{2+} were to become an issue, there are many commercially available Cu^{2+} sensors that can detect down to 50 ppb (such as the LaMotte Low Range Copper Test Kit) which can be used in tandem with the Ag^+ sensor. Another potential solution is a chemiresistive sensor array using a neocuproine functionalized sensor, which is known to complex with Cu^{2+}.[48] This sensor can be used concurrently with the Ag^+ sensor to determine both Cu^{2+} and Ag^+ simultaneously. Sensors tested with neocuproine show a good response for Cu^{2+} with negligible interference from Ag^+ (Figure S9, S10). Although further characterization is required, the neocuproine functionalized sensor is a potential solution to the interference from Cu^{2+}.

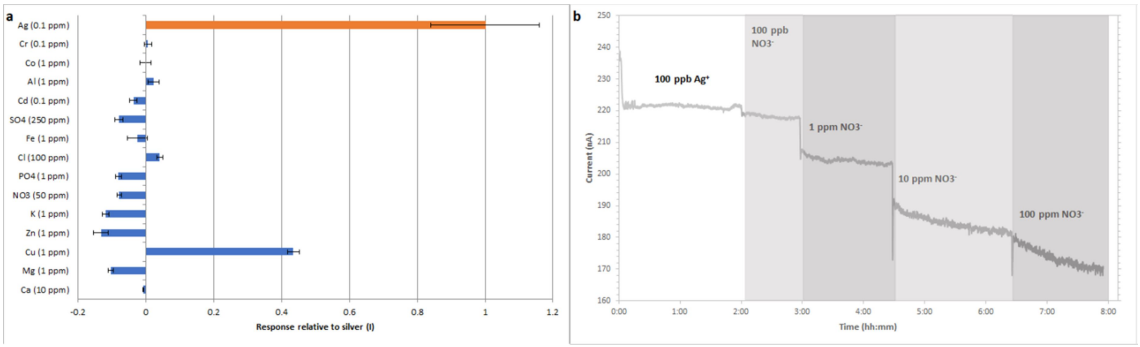

Figure 7. a) Interferences with their relative responses compared to silver (I). The interferences were run in a bicarbonate/nitrate background, with a conductance value of 31 µS/cm and a pH of 6.7. **b)** Current response to different concentrations of nitrate in solution with a constant background of 100 ppb silver (I).

3.7. Real sample analysis

Real sample analysis was conducted using water collected from Spencer creek, a water source in the Westdale area in Hamilton, Ontario. A calibration curve was prepared prior to testing the real water sample by using purified water with its conductance and pH adjusted with sodium bicarbonate and nitric acid, respectively (adjusted to a pH value of 8.7 and conductivity of 203 µS/cm). The difference between this calibration curve and the one shown in Figure 4 is that the one in Figure 4 did

not have its pH and conductivity adjusted. A portion of the real water sample was acidified with nitric acid [49] and sent for testing for Ag+ ions using ICP-MS as the laboratory standard method for metal ion analysis, in addition to sample aliquots that were spiked with additional 20 ppb, 50 ppb or 80 ppb of Ag+ (Table 2, full analysis report in the Supporting Material).

Added (ppb)	Found by sensor (ppb)	Found by ICP-MS (ppb)	Recovery (%)
0	<3.0	<0.2	-
20	21.8±0.9	23.7	108.8±4.4%
50	53.4±6.9	45.2	106.8±13.9%
80	79.0±1.9	81.0	98.7±2.4%

Table 2. Real sample and spike tests for the silver (I) sensor.

The chemiresistive sensors were able to detect Ag^+ ions in all of the spiked samples, with recovery values of 108.8±4.4%, 106.8±13.9%, and 98.7±2.4% for the 20 ppb, 50 ppb or 80 ppb spiked samples respectively (responses from the real sample were interpolated using a Langmuir calibration function made in pH and conductivity adjusted water). Another potential use for the sensor is anion testing, where Ag^+ is preconcentrated on the surface through complexation with the adsorbed bathocuproine, and the Ag-bathocuproine complex is used toward anion detection (mainly nitrates since it has a formal charge of -1, and will be in the preferred orientation for the complex). Based on the ion chromatography data obtained (Table 3), the main anions of concern are chloride, nitrate, and sulfate (at the levels detected, all of the silver salts formed with these anions should be soluble).

Anion	Amount (ppm)
F^-	0.12
Cl^-	103
NO_3^-	0.79
SO_4^{2-}	64.1
PO_4^{3-}	<0.01

Table 3. Ion chromatography results for the real water sample.

To test the potential impact of anions on the sensor response, the devices were exposed to increasing amounts of nitrate while the concentration of Ag^+ ions remained constant at 100 ppb (Figure 7b). From this test, it is apparent that the sensor current decreases with increasing amounts of nitrate. In our real sample, nitrate was present at a concentration of 790 ppb (Table 3), which will result in a response reduction of about 2%.

Another interesting observation from the nitrate interference experiment results in Figure 8b is that the sensor responses were much faster than for Ag^+ ions. The shorter time constant is consistent with an electrostatic gating mechanism from the negatively charged nitrate ions accumulating near the sensor surface. This is similar to the conductivity response in Figure 4, but much higher in magnitude. The higher magnitude of the current results from preferential interactions of the nitrate ions with the

bathocuproine-silver (I) complex. Nitrate is always present in all our experiments as a counter ion to Ag^+, but now its concentration is significantly increased. Furthermore, the distinction between the electrostatic gating and charge transfer doping mechanisms is highlighted by the differing (in speed and sign) responses of our devices.[20]

Method	LOD (ppm)	Linear Range (ppm)	Reference
Fluorescent/Colorimetric	0.014	0.014-0.539	[11]
Potentiometric	10	17-1710	[14]
Anodic Stripping Voltammetry	0.060	0.070-1	[16]
Chemiresistive	0.003	0.030-1	This work

Table 4. Our method of silver (I) detection compared with other methods.

4. Conclusion

A chemiresistive sensor was demonstrated for the detection of aqueous Ag^+ ions. Due to the phenanthroline backbone of the bathocuproine, it could be stably adsorbed onto a percolation network of exfoliated FLG flakes forming a chemiresistive film. The binding of bathocuproine to Ag^+ ions was confirmed by UV-Vis spectroscopy. The sensors were calibrated over a range from 3 ppb to 1 ppm, fitting to both a Langmuir isotherm and a first-order exponential decay function, providing R^2 values of 0.9982 and 0.9939 respectively. Interference studies demonstrated strong selectivity for Ag^+ ions over other cations commonly found in surface waters. The limit of detection (LOD) for this sensor calculated using the s/σ ratio is 3 ppb, and the detection range goes from 30 ppb to 1 ppm (Table 4). The sensors can detect Ag^+ ions in an approximate pH range of 10 to 6 but will not respond to particulate silver species. Sensors can be reset by exposure to low pH and reused, thus enabling continuous online monitoring applications. Many of the current limitations of this sensor have to do with the heterogeneity of the film and the method used to deposit the Ag^+ specific molecule. Drop casting the exfoliated graphite onto the glass slide can lead to differences in uniformity between sensors, which would mean that each sensor will need its own unique calibration curve, rather than one universal curve. Deposition through dip coating is also quite ill defined since we assume that a self-assembled monolayer (SAM) is formed [50], which may not necessarily be true since there are many orientations in which the molecules can form on the FLG film. Much work is left to be done in terms sensor parity, as well as defining the nature of the adsorption of the molecule on the surface and the effect of adsorbate orientation with respect to sensor response. Nevertheless, the development of this sensor platform opens up a new pathway toward aqueous metal cation sensing, and through modification of the adsorbate can be used to detect many other analytes.

Supplementary material

See supplementary material for additional and replicate sensing data, XPS spectra and real water sample analysis by ICP-MS and ion chromatography.

Acknowledgements

The authors thank David J. H. Emslie for fruitful discussions, as well as Dipankar Saha, Arjun Rego, and Jonah Halili for their support. The authors are indebted to Dr. Mark Biesinger at Surface Science Western for assistance with XPS. Electron microscopy was performed at the Canadian Centre for Electron Microscopy (also supported by NSERC and other government agencies). The authors thank Activation Laboratories Ancaster for analyzing the rain water runoff sample. The authors also acknowledge financial support from the Natural Sciences and Engineering Research Council of Canada through the Discovery Grant Program (award number RGPIN06145-18), as well as the Canada First Research Excellence Fund project "Global Water Futures".

References

[1] J. S. Kim, E. Kuk, K. N. Yu, J.-H. Kim, S. J. Park, H. J. Lee, S. H. Kim, Y. K. Park, Y. H. Park, C.-Y. Hwang, et al. Antimicrobial Effects of Silver Nanoparticles, Nanomed. Nanotechnol., Biol. Med. 3 (2007) 95–101.

[2] S. Triantafyllidou, D. Lytle, C. Muhlen, J. Swertfeger, Copper-silver ionization at a US hospital: Interaction of treated drinking water with plumbing materials, aesthetics and other considerations, Water Res. 102 (2016) 1-10.

[3] J. P. Marshall, Systemic Argyria Secondary to Topical Silver Nitrate, Arch. Dermatol. 113 (1977) 1077.

[4] G. D. DiVincenzo, C. J. Giordano, L. S. Schriever, Biologic Monitoring of Workers Exposed to Silver, Int. Arch. Occup. Environ. Health 56 (1985) 207–215.

[5] Agency for Toxic Substances and Disease Registry, Toxicological Profile for Silver, 1990.

[6] O. Bondarenko, K. Juganson, A. Ivask, K. Kasemets, M. Mortimer, A. Kahru, Toxicity of Ag, CuO and ZnO Nanoparticles to Selected Environmentally Relevant Test Organisms and Mammalian Cells in Vitro: A Critical Review, Arch. Toxicol. 87 (2013) 1181–1200.

[7] World Health Organization, Silver as a Drinking-Water Disinfectant, 2018.

[8] S. Lee, K. Jang, C. Park, J. You, T. Kim, C. Im, J. Kang, H. Shin, C.-H. Choi, J. Park, et al. Ultra-Sensitive in Situ Detection of Silver Ions Using a Quartz Crystal Microbalance, New J. Chem. 39 (2015) 8028–8034.

[9] C. Qin, W.-Y. Wong, L. Wang, A Water-Soluble Organometallic Conjugated Polyelectrolyte for the Direct Colorimetric Detection of Silver Ion in Aqueous Media with High Selectivity and Sensitivity, Macromol. 44 (2011) 483–489.

[10] C.-Y. Lin, C.-J. Yu, Y.-H. Lin, W.-L. Tseng, Colorimetric Sensing of Silver (I) and Mercury (II) Ions Based on an Assembly of Tween 20-Stabilized Gold Nanoparticles, Anal. Chem. 82 (2010) 6830–6837.

[11] A. Chatterjee, M. Santra, N. Won, S. Kim, J. K. Kim, S. B. Kim, K. H. Ahn, Selective Fluorogenic and Chromogenic Probe for Detection of Silver Ions and Silver Nanoparticles in Aqueous Media, J. Am. Chem. Soc. 131 (2009) 2040–2041.

[12] M. Chae, A. Czarnik, Fluorometric Chemodosimetry. Mercury (II) and Silver (I) Indication in Water Via Enhanced Fluorescence Signaling, J. Am. Chem. Soc. 114 (1992) 9704–9705.

[13] N. Rubinova, K. Chumbimunitorres, E. Bakker, Solid-Contact Potentiometric Polymer Membrane Microelectrodes for the Detection of Silver Ions at the Femtomole Level, Sens. Actuators B Chem. 121 (2007) 135–141.

[14] K. O'Connor, G. Svehla, S. Harris, M. McKervey, Calixarene-Based Potentiometric Ion-Selective Electrodes for Silver, Talanta 39 (1992) 1549–1554.

[15] D. Schildkraut, P. Dao, J. Twist, A. Davis, K. Robillard, Determination of Silver Ions At Submicrogram-Per-Liter Levels Using Anodic Square-Wave Stripping Voltammetry, Environ. Toxicol. Chem. 17 (1998) 642–649.

[16] H. Zejli, J. Cisneros, I. Naranjo-Rodriguez, K. Temsamani, Stripping Voltammetry of Silver Ions At Polythiophene-Modified Platinum Electrodes, Talanta 71 (2007) 1594–1598.

[17] P. Kruse, Review on Water Quality Sensors, J. Phys. D 51 (2018) 203002.

[18] J. Dalmieda, P. Kruse, Metal Cation Detection in Drinking Water, Sensors 19 (2019) 5134.

[19] A. Mohtasebi, P. Kruse, Chemical Sensors Based on Surface Charge Transfer, Phys. Sci. Rev. 3 (2018) 20170133.

[20] A. Zubiarrain-Laserna, P. Kruse, Graphene-Based Water Quality Sensors, J. Electrochem. Soc. 167 (2020) 037539.

[21] Geim, A. K. Graphene: Status and Prospects. Science 2009, 324 (5934), 1530–1534.

[22] E. Hoque, T. Chowdhury, P. Kruse, Chemical in Situ Modulation of Doping Interactions between Oligoanilines and Nanocarbon Films, Surf. Sci. 676 (2018) 61–70.

[23] T. Saito, Transport of Silver(I) Ion through a Supported Liquid Membrane Using Bathocuproine as a Carrier, Sep. Sci. Technol. 33 (1998) 855–866.

[24] A. Mohtasebi, A. D. Broomfield, T. Chowdhury, P. R. Selvaganapathy, P. Kruse, Reagent-Free Quantification of Aqueous Free Chlorine via Electrical Readout of Colorimetrically Functionalized Pencil Lines, ACS Appl. Mater. Interfaces 9 (2017) 20748–20761.

[25] E. Hoque, L. H.-H. Hsu, A. Aryasomayajula, P. R. Selvaganapathy, P. Kruse, Pencil-Drawn Chemiresistive Sensor for Free Chlorine in Water, IEEE Sens. Lett. 1 (2017) 4500504.

[26] L. H.-H. Hsu, E. Hoque, P. Kruse, P. R. Selvaganapathy, A Carbon Nanotube Based Resettable Sensor for Measuring Free Chlorine in Drinking Water, Appl. Phys. Lett. 106 (2015) 063102.

[27] Gong, J.-L.; Sarkar, T.; Badhulika, S.; Mulchandani, A. Label-Free Chemiresistive Biosensor for Mercury (II) Based on Single-Walled Carbon Nanotubes and Structure-Switching DNA. Applied Physics Letters 2013, 102 (1), 013701.

[28] Moffett, J. W.; Zika, R. G.; Petasne, R. G. Evaluation of Bathocuproine for the Spectro-Photometric Determination of Copper(I) in Copper Redox Studies with Applications in Studies of Natural Waters. Analytica Chimica Acta 1985, 175, 171–179.

[29] U. Halim, C. R. Zheng, Y. Chen, Z. Lin, S. Jiang, R. Cheng, Y. Huang, X. Duan, A Rational Design of Cosolvent Exfoliation of Layered Materials by Directly Probing Liquid–Solid Interaction, Nat. Commun. 4 (2013) 2213. doi: 10.1038/ncomms3213.

[30] A. C. Ferrari, J. C. Meyer, V. Scardaci, C. Casiraghi, M. Lazzeri, F. Mauri, S. Piscanec, D. Jiang, K. S. Novoselov, S. Roth, A. K. Geim, Raman Spectrum of Graphene and Graphene Layers, Phys. Rev. Lett. 97 (2006) 187401.

[31] M. S. Dresselhaus, A. Jorio, A. G. Souza Filho, R. Saito, Defect characterization in graphene and carbon nanotubes using Raman spectroscopy, Philos. Trans. R. Soc. A Math. Phys. Eng. Sci. 368 (2010) 5355–5377.

[32] Government of Ontario, Provincial Water Quality Monitoring Network Website https://www.ontario.ca/environment-and-energy/map-provincial-stream-water-quality-monitoring-network (accessed 10 April 2020).

[33] B. R. Patil, M. Ahmadpour, G. Sherafatipour, T. Qamar, A. F. Fernández, K. Zojer, H.-G. Rubahn, M. Madsen, Area Dependent Behavior of Bathocuproine (BCP) as Cathode Interfacial Layers in Organic Photovoltaic Cells, Sci. Rep. 8 (2018) 12608. doi: 10.1038/s41598-018-30826-7.

[34] H. Yoshida, Electron Transport in Bathocuproine Interlayer in Organic Semiconductor Devices, J. Phys. Chem. C 119 (2015) 24459–24464.

[35] S. Mao, J. Chang, H. Pu, G. Lu, Q. He, H. Zhang, J. Chen, Two-Dimensional Nanomaterial-Based Field-Effect Transistors for Chemical and Biological Sensing, Chem. Soc. Rev. 46 (2017) 6872–6904.

[36] F. Shojaie, Theoretical Studies on Dimerization Reactions of 4, 7-Diphenyl-1,10-Phenanthroline (BPhen) and Bathocuproine (BCP) in Organic Semiconductors, Semiconductors 48 (2014) 1051–1062.

[37] D. K. Schwartz, Mechanisms and Kinetics of Self-Assembled Monolayer Formation, Annu. Rev. Phys. Chem. 52 (2001) 107–137.

[38] N. Rozlosnik, M. C. Gerstenberg, N. B. Larsen, Effect of Solvents and Concentration on the Formation of a Self-Assembled Monolayer of Octadecylsiloxane on Silicon (001), Langmuir 19 (2003) 1182–1188.

[39] J. N. Lee, C. Park, G. M. Whitesides, Solvent Compatibility of Poly(Dimethylsiloxane)-Based Microfluidic Devices, Anal. Chem. 75 (2003) 6544–6554.

[40] Z. Xiao, J. Brose, S. Schimo, S. M. Ackland, S. L. Fontaine, A. G. Wedd, Unification of the Copper(I) Binding Affinities of the Metallo-Chaperones Atx1, Atox1, and Related Proteins, J. Biol. Chem. 286 (2011) 11047–11055.

[41] I. Heller, S. Chatoor, J. Männik, M. A. G. Zevenbergen, C. Dekker, S. G. Lemay, Influence of Electrolyte Composition on Liquid-Gated Carbon Nanotube and Graphene Transistors, J. Am. Chem. Soc. 132 (2010) 17149–17156.

[42] L. T.-H. Kao, H.-Y. Hsu, M. Gratzl, Reagentless pH-Stat for Microliter Fluid Specimens, Anal. Chem. 80 (2008) 4065–4069.

[43] R. Hagedorn, J. Korlach, G. Fuhr, Amperometric pH Regulation - a Flexible Tool for Rapid and Precise Temporal Control over the pH of an Electrolyte Solution, Electrophoresis 19 (1998) 180–186.

[44] E. L. May, A. C. Hillier, Rapid and Reversible Generation of a Microscale pH Gradient Using Surface Electric Fields, Anal. Chem. 77 (2005) 6487–6493.

[45] K. Morimoto, M. Toya, J. Fukuda, H. Suzuki, Automatic Electrochemical Micro-pH-Stat for Biomicrosystems, Anal. Chem. 80 (2008) 905–914.

[46] D. A. H. Hanaor, M. Ghadiri, W. Chrzanowski, Y. Gan, Scalable Surface Area Characterization by Electrokinetic Analysis of Complex Anion Adsorption, Langmuir 30 (2014) 15143–15152.

[47] A. Leike, Demonstration of the Exponential Decay Law Using Beer Froth, Eur. J. Phys. 23 (2001) 21–26.

[48] Gouda, A. A.; Amin, A. S. Copper(II)–Neocuproine Reagent for Spectrophotometric Determination of Captopril in Pure Form and Pharmaceutical Formulations. Arabian Journal of Chemistry 2010, 3 (3), 159–165.

[49] USEPA, 1994. Method 200.8: Determination of Trace Elements in Waters and Wastes by Inductively Coupled Plasma - Mass Spectrometry, Revision 5.4. Environmental Monitoring Systems Laboratory, Office of Research and Deveopment, Cincinnati, OH.

[50] Barlow, S. M.; Raval, R. Complex Organic Molecules at Metal Surfaces: Bonding, Organisation and Chirality. Surface Science Reports. (2003) 201–341.

6 - LEAD

Lead is a toxic contaminant in water and can lead to various cardiovascular and reproductive effects, as well as the hindrance of neurological development in children. To be able to monitor lead in water, the FLG sensors developed were functionalized with three different ligands: pyrogallol red, 6,7,8,9,10,11,12,13,14,15,16,17-dodecahydro-1,21-methanodibenzo[n,q][1,4,7,10,13]pentaazacyclooctadecine-22,23(5H)-dione (Ligand β), and 4-nitrobenzoic acid(6-oxo-6-H-[1,10]phenanthroline-5-ylidene)-hydrazide (Receptor 1). Pyrogallol red has been used for the detection of lead via atomic absorption spectroscopy by way of a functionalized activated carbon column.[47] Receptor 1 is a phenanthroline-based ligand that was shown to have a selective colorimetric response to lead in aqueous solution. This ligand was tested in collaboration with Mae Masters, an undergraduate thesis student during the 2019-2020 academic year.[48] As with copper (Chapter 4), UV/vis spectroscopy and theoretical calculations were employed. Following this, sensors functionalized with each ligand were run. In this chapter we discuss the results obtained.

6.1 - Experimental

6.1.1 - Computational Details

Theoretical calculations were performed using Gaussian09 and visualized in Gaussview 5.0. To optimize the structures of the three ligands, ground state DFT calculations were used with the B3LYP functional and the 6-31G(d,p) basis set. In the case of the lead complexes, the non-metallic components of the complexes (C, H, N, O, S, Cl) were optimized with the 6-31G(d,p) basis set, while the lead metal centre was optimized with SDD for the sake of computational efficiency. Optimization was done in gas phase in a vacuum.

6.1.2 - UV/vis Spectroscopy

UV/vis spectroscopy was done using an Orion Aquamate 8000. The solutions of pyrogallol red in ethanol and Receptor 1 in acetonitrile were made such that their concentrations were $5x10^{-5}$ M. A stock solution of $4.82x10^{-4}$ M (100 ppm) was made by adding the requisite amount of lead (II) chloride into 100 mL of ultrapure water (obtained from a Millipore Simplicity UV). The UV/vis spectrophotometer was calibrated to a 1:1 solution of solvent:water. To obtain the spectra of the ligand on its own, 1 mL of the prepared ligand solution was mixed with 1 mL of ultrapure water. For the complex, 1 mL of the ligand solution was mixed with 1 mL of the stock lead solution and left for 2 minutes to ensure that the lead and the ligand has ample time to interact. The spectra were obtained between a range of 200 nm to 800 nm for pyrogallol red and 300 nm to 600 nm for Receptor 1 (as well as their complexes). The spectrum for Ligand β could not be obtained due to its low product yield during synthesis.

6.1.3 - Synthesis[48]

Synthesis of 1,10-phenanthroline-5,6-dione:

The following syntheses were performed using a modification of the literature. Phenanthroline monohydrate (0.6746 g, 3.4033 mmol) and potassium bromide (1.0133 g, 8.5151 mmol), along with a stir bar was added to a dry 50 mL round-bottom flask. Everything in the flask was then cooled to 0^{o}C using an ice bath, after which 10 mL of cold fuming sulfuric acid was added in a dropwise manner through the use of a Pasteur pipette. Once gas had stopped evolving from the flask, it was removed from the ice bath, placed into an oil bath heated to 30^{o}C, and stirred. After the reaction mixture had heated to 30^{o}C, 5 mL of concentrated nitric acid (68% w/w) was added dropwise through the use of a Pasteur pipette to the flask while stirring. After addition of nitric acid, a condenser was affixed to the round-bottom flask, and the mixture was heated to 40^{o} C for 3 hours followed by heating at 88^{o}C for 1 hour. The condenser was then removed to allow for bromine to evaporate out of solution, and the reaction mixture was heated for another 4 hours. After all the bromine had evaporated out of the mixture, the bright yellow solution was cooled to room temperature and left overnight. The next day, the mixture was poured onto crushed ice and then neutralized first with solid NaOH beads, and then with a saturated sodium bicarbonate solution so that the pH would be about 6-7 (at this point light orange solid had appeared). The solid was separated out of solution through solvent extraction with DCM as the organic phase, and the organic phase was dried with sodium sulfate. The solvent was then removed through the use of a rotary evaporator to afford a yellowish-orange powder (0.4469 g, 62.48%).

Synthesis of 4-nitroethylbenzoate:

This step involved the Fischer esterification between 4-nitroethylbenzoic acid and ethanol. 4-nitrobenzoic acid (1.0472 g, 6.2662 mmol), along with 30 mL anhydrous ethanol and 3 drops of fuming sulfuric acid was added to a dry 50 mL round-bottom flask. A condenser was affixed, and the reaction mixture was refluxed for 13 hours. Once the mixture had cooled down, ethanol was removed through the use of a rotary evaporator, and saturated sodium bicarbonate solution was added to remove unreacted acid and/or aqueous impurities. The solution was then vacuum filtered to give an off-white powder (1.2442 g, 101.7% yield).

Synthesis of 4-nitrobenzhydrazide:

This step involved the Wolff-Kishner reduction of the previously produced 4-nitroethylbenzoate. To a dry 50 mL 2-neck flask was added 4-nitroethylbenzoate (0.6047 g, 3.0983 mmol) and 30 mL ethanol. A condenser was attached, and the reaction mixture was brought to reflux. Then, 2 mL of hydrazine monohydrate was added dropwise through a syringe, and the reaction was refluxed for 2 hours. After cooling, ethanol was evaporated *in vacuo*, and the resulting yellow powder was rinsed in water. The mixture was then vacuum filtered to afford a yellow powder (0.1667 g, 0.2970%).

Synthesis of 4-nitrobenzoic acid(6-oxo-6-H-[1,10]phenanthroline-5-ylidene)-hydrazide (Receptor 1):

1,10-phenanthrolinedione (0.1017 g, 0.4838 mmol) and 4-nitrobenzhydrazide (0.0783 g, 0.4322 mmol) was added to a dry 100 mL round-bottom. The flask was put under an N_2 atmosphere using a balloon, after which 50 mL of anhydrous methanol was added using a

needle. The reaction mixture was stirred at room temperature for 77 hours, after which a pale-yellow precipitate had appeared. After vacuum filtering and washing with cold methanol, a pale-yellow powder was obtained (0.0232 g, 14.55%; Figure 16).

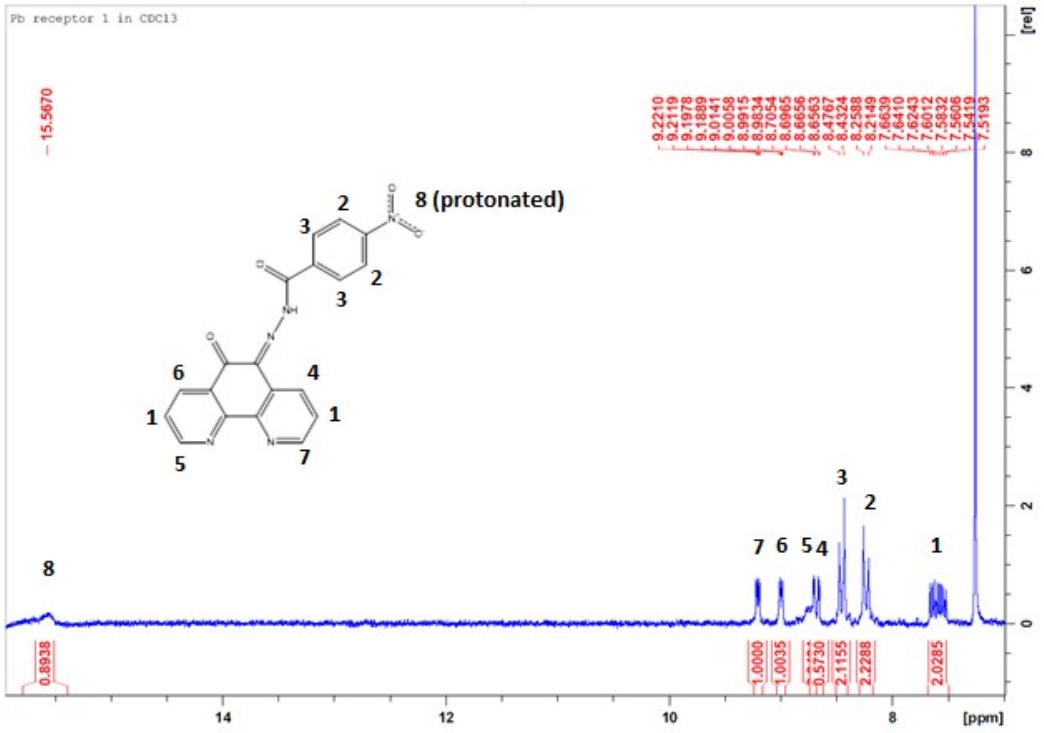

Figure 16. ^{1}H-NMR spectra of Receptor 1 in $CDCl_3$.

6.1.4 - Sensor Testing

Much like the silver sensors, the sensors used for lead were first dipped into their respective solvents (ethanol for pyrogallol red and acetonitrile for Receptor 1) for 5 minutes. After this, they were dipped into a 4% saturated solution of each ligand for 3 hours to functionalize the surface. As previously observed, the increase in electron density due to ligand adsorption will decrease the current output of the sensor (Figure 17).

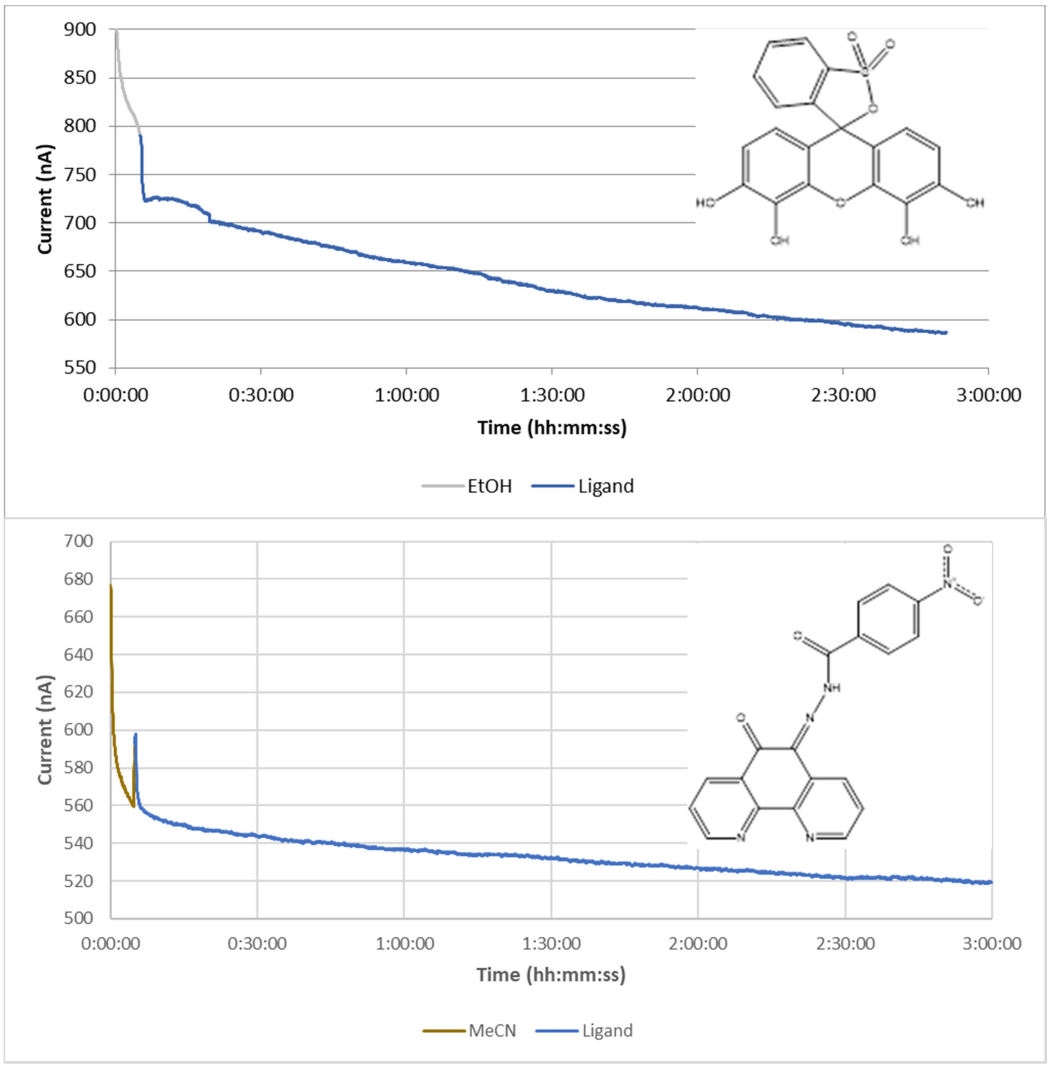

Figure 17. Functionalization of the sensors with pyrogallol red (top) and Receptor 1 (bottom). Insets are the corresponding molecular structures. A decrease in current is observed when the sensors were dipped in solvent (first five minutes), followed by a larger decrease in current during functionalization.

After functionalization, the sensors were removed from the ligand solution, dried with a heat gun, and placed into a stirring vial filled with 18.2 MΩ·cm water overnight for 18 to 24 hours to allow for equilibration with the surrounding air. Once equilibrated, a known amount of the stock lead solution was pipetted into the water. This increased the concentration of lead in the water solution, which would hypothetically increase the current which was displayed on the computer output.

6.2 - UV/vis and DFT calculations

Both pyrogallol red and Receptor 1 had colorimetric responses to lead in a mixed solvent:water solution (ethanol for pyrogallol red and acetonitrile for Receptor 1) (Figure 18). Due to its low product yield, a UV/vis spectrum was unable to be obtained for Ligand β.

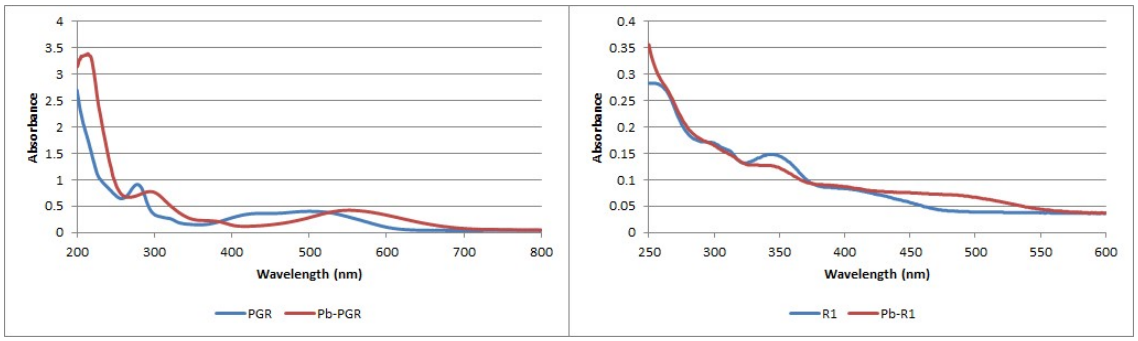

Figure 18. UV/vis spectra of pyrogallol red and its lead complex (left), and Receptor 1 and its lead complex (right).

It should be noted that the large peak at ~200 nm corresponds to free lead ions in solution. The entire spectrum for pyrogallol red redshifts upon complexation with lead. The peak at 278 nm for pyrogallol red ($\pi \rightarrow \pi^*$ transition) is redshifted by 16 nm upon lead complexation. The peak at 500 nm ($n \rightarrow \pi^*$ transition) is also redshifted, albeit by a greater amount (51 nm). Peak broadening is also seen in the $\pi \rightarrow \pi^*$ transition for pyrogallol red after complexation. For Receptor 1, quenching is seen at 343 nm ($\pi \rightarrow \pi^*$ transition), coupled with an enhancement in the absorbance at 483 nm ($n \rightarrow \pi^*$ transition) and an isosbectic point at 376 nm, indicating the formation of a new complex. The formation of these complexes were also observed through DFT calculations (Figure 19).

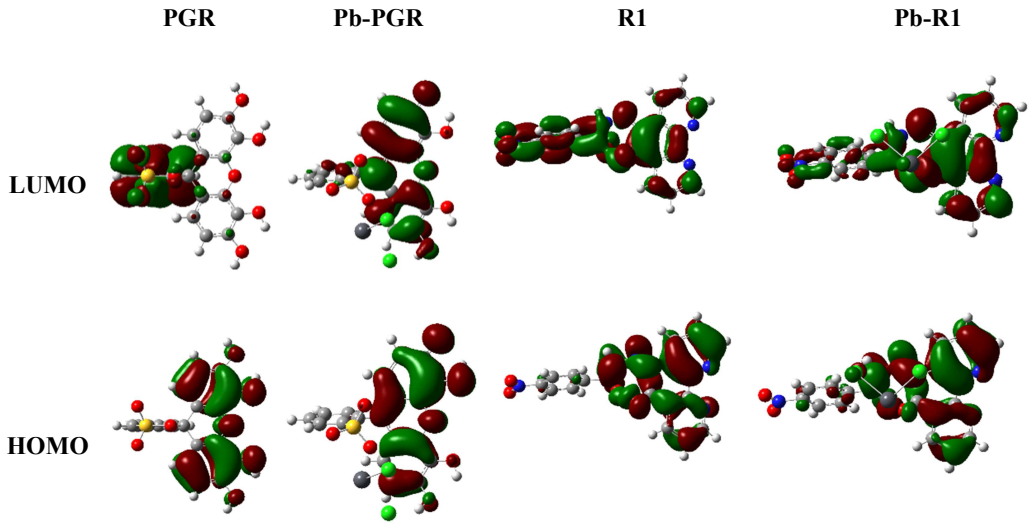

Figure 19. The frontier orbitals of pyrogallol red (PGR and Receptor 1 (R1), as well as their lead complexes. Chloride was used as the counter-ion.

When observing pyrogallol red, one can see that the HOMO electron density is situated on the anthracene backbone and the hydroxy groups located around it, which is to be expected since these are non-bonding electrons. The LUMO electron density is located around the out-of-plane sulfate group, which falls in line with the fact that the sulfate group is electron-withdrawing by induction (the sulfur atom is in a +5 oxidation state). As pyrogallol red interacts with lead, oxidation of the sulfonate ester group occurs, accompanied by a ring opening of the sulfate group.[49] This time, in both the HOMO and the LUMO, electron density is located around the anthracene backbone. Receptor 1 has its HOMO electron density located about the phenanthroline backbone as well as on the carbonyl and azide groups, due to the non-bonding electrons within those orbitals. The LUMO electron density is spread out across the whole molecule. Upon complexation to lead, there is no particular interaction with the HOMO. There is, however, an overlap in the LUMO with a p-orbital from the lead, which is indicative of an interaction. The frontier orbital energies and their band gaps were also recorded for pyrogallol red and receptor 1 (Table 3).

	HOMO Energy (eV)	LUMO Energy (eV)	Band Gap (eV)
PGR	-5.8428	-1.4319	4.4109
Pb-PGR	-3.1369	-0.4558	2.6811
R1	-6.6921	-3.3231	3.3690
Pb-R1	-7.0599	-3.8273	3.2326

Table 3. Frontier orbital energies and band gaps for pyrogallol red (PGR), Receptor 1 (R1), and its lead complexes.

In both cases, a decrease in band gap is seen which falls in line with the redshift observed in the UV/vis spectra. Complexation of lead to pyrogallol red gives a predicted redshift of 181 nm, which is quite larger than the actual shift of 51 nm. This may be due to the equilibrium constant of the ring opening mechanism induced by lead, which would mean that there was still unreacted pyrogallol red in the solution. The shift for Receptor 1 is predicted to be 15 nm, which is lower than the actual shift of 140 nm. This indicates the existence of other transitions that may not have been accounted for in the DFT calculations.

6.3 - Sensor Results

Much like copper (Chapter 4) and silver (Chapter 5), lead complexation is expected to lead to an increase in hole density and current in the FLG film for all three ligands. Pyrogallol red was the first ligand tested out of the two (Figure 20).

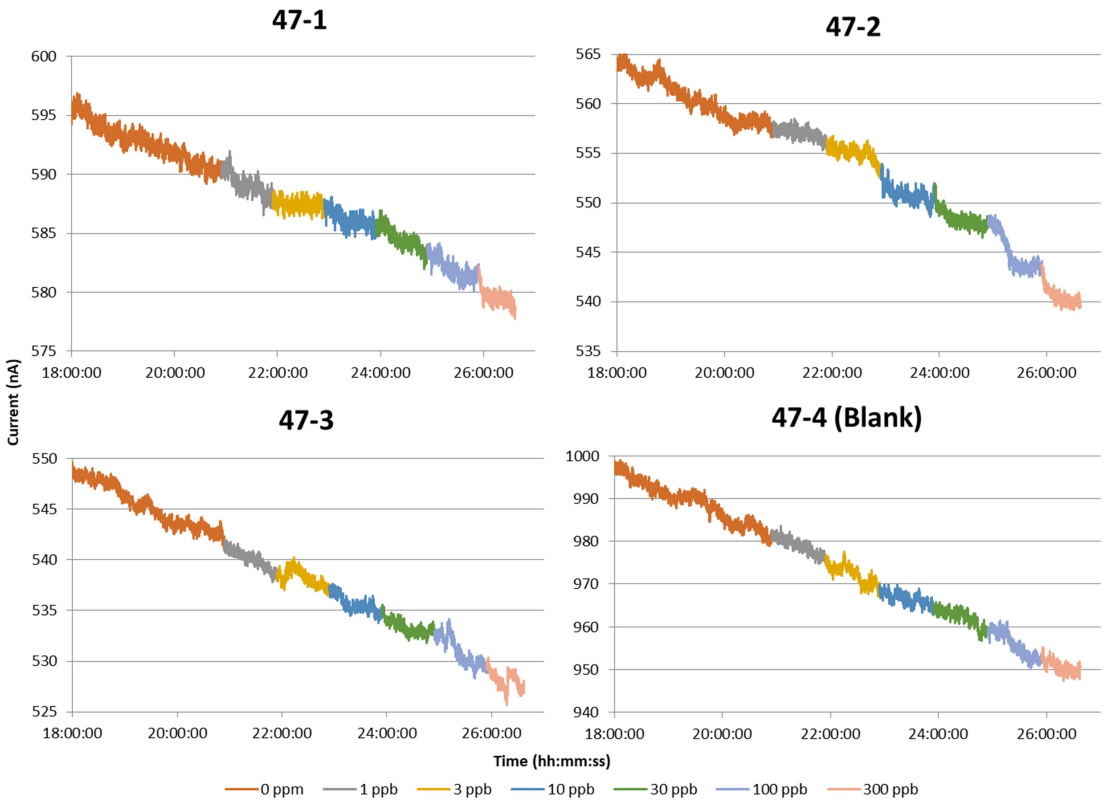

Figure 20. Current responses of three pyrogallol red functionalized sensors (sensors 47-1, 47-2, 47-3) as well as a blank sensor (47-4) with respect to changing concentrations of lead over time.

Although the UV/vis gave a clear response, there was no discernible signal from the sensors, indicating that binding does not occur when the pyrogallol red is immobilized on the FLG film. Adsorption onto the film may adversely affect the preferred binding geometry of the lead pyrogallol red complex, preventing lead binding and leading to the lack of response. Alternatively, a response in the UV/vis spectrum may not translate directly to sensor response since the ligand is free in solution rather than immobilized on a surface. Whatever the case may be, it is concluded that pyrogallol red is not an appropriate ligand for lead detection in water.

The final ligand tested for lead detection was Receptor 1 (Figure 21). Since the phenanthroline system worked well for silver detection, an attempt was made to utilize this for the detection of lead. Some changes to the experimental method that were made were: the 0 ppm Millipore water baseline was treated with HEPES buffer and kept at a pH of 7.4 (to ensure consistency with the publication the ligand was based on), and the concentration range started from 100 ppt to determine if ultra-trace detection was possible.

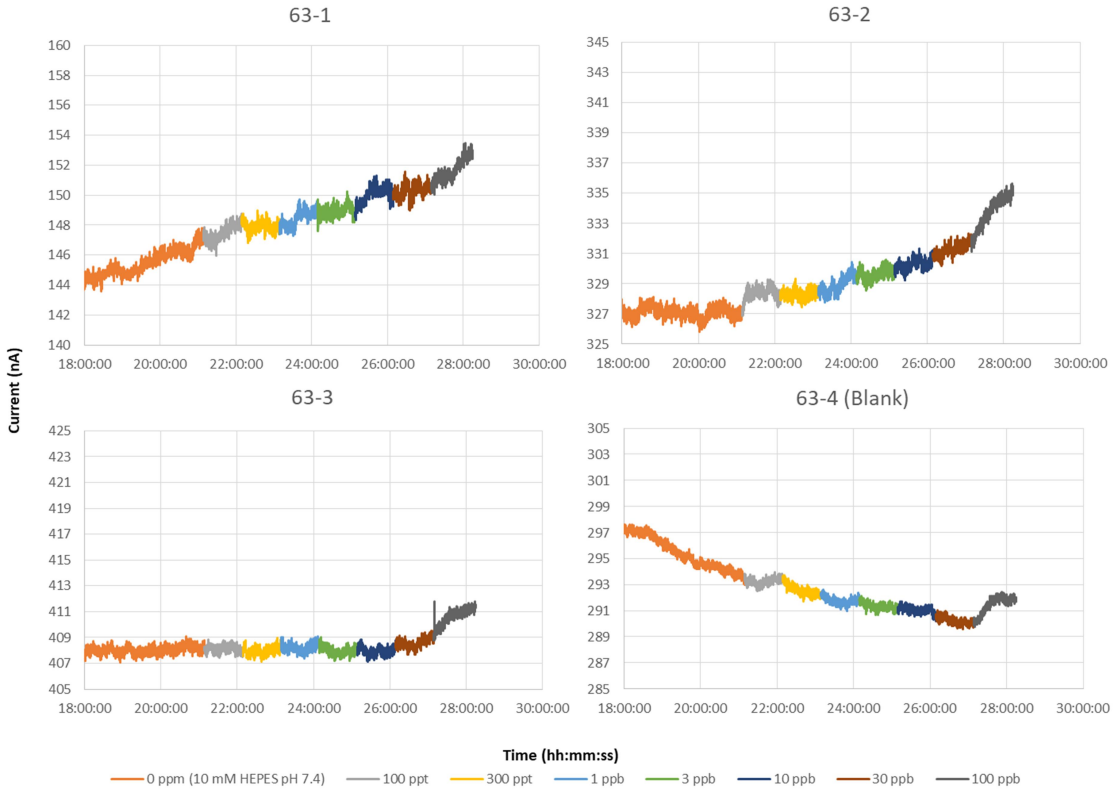

Figure 21. Current responses of three Receptor 1 functionalized sensors (sensors 63-1, 63-2, 63-3) as well as a blank sensor (63-4) with respect to changing concentrations of lead over time.

Much like the previous two ligands, there was not any discernible response for Receptor 1 with respect to increasing lead concentrations. A small response is seen at 100 ppb; however, this is also present in the blank sensor which indicates that the FLG film itself

will detect lead at higher concentrations, and that this response should not be attributed to the ligand.

6.4 - Summary

Two different ligands were tested for their ability to detect lead when adsorbed onto an FLG-based chemiresistive sensor: pyrogallol red and Receptor 1. Pyrogallol red and Receptor 1 exhibited a response in the UV/vis spectrum when exposed to lead, with pyrogallol red showing quenching behavior that is expected of lead, and Receptor 1 exhibiting the formation of a new peak when complexed. When adsorbed onto the FLG film and tested in solution, the two ligands were not able to detect the increasing concentrations of lead, apart from Receptor 1 at 100 ppb (although the blank sensor also had the same response). Further research is required to develop a functioning lead sensor.

7 - MERCURY

Mercury is a contaminant in water that is known to cause dermatitis and eczema upon skin contact, as well as irreversible damage to the nervous system when consumed in relatively large amounts. FLG sensors were used once again to investigate the possibility of online detection and quantification of mercury in aqueous solution. The ligand used to functionalize the FLG film is a rhodamine 6G-based ligand that is shown to be selective to mercury in a mixed dimethylformamide:water solution, with a quantitative fluorescence response.[50] This ligand was tested in collaboration with Maryam Darestani-Farahani, a graduate student in the Kruse group who began her research in Fall 2019. As with all previous metal cations, UV/vis spectroscopy was employed to determine the feasibility of the ligand. In this chapter we discuss the results obtained.

7.1 - Experimental

7.1.1 - UV/vis Spectroscopy

UV/vis spectroscopy was done using an Orion Aquamate 8000. The UV/vis experiment done for mercury is quite different from previous experiments. Rather than testing for a response by oversaturating the ligand with the metal cation, a series of concentrations between 10 μM and 200 μM were tested with a stock 10 μM solution of the ligand to determine if the UV/vis spectrum obtained will give a quantitative response to mercury. The UV/vis spectrophotometer was calibrated to a 1:1 solution of DMF:water. To obtain the spectra of the ligand on its own, 1 mL of the prepared ligand solution was mixed with 1 mL of ultrapure water. For the different concentrations of mercury, the stock mercury

solution (1 mM) was diluted to the requisite concentration. 1 mL of the diluted mercury solution was then mixed with 1 mL of the 10 μM ligand solution and left for two minutes to ensure that the mixture has ample time to interact. The spectrum was obtained between the range of 400 nm to 600 nm.

7.1.2 - Synthesis

Synthesis of Rhodamine 6G hydrazide[51]*:*

Rhodamine 6G (0.9616 g, 2 mmol) and 35 mL ethanol were added to a 50 mL round-bottom flask. The solution was stirred at room temperature, and 3.1 mL hydrazine monohydrate was added. After this, the mixture was heated to reflux for 2 hours. 5 minutes into refluxing, the solution went from dark purple to light pink. The solution was left to cool overnight. After cooling, pink precipitate was present, which was filtered and washed three times with 15 mL of 50% ethanol. The resulting powder was left to dry under vacuum over P_2O_5, and recovered (0.7761 g, 93.72%).

Synthesis of mercury ligand[52]*:*

Rhodamine 6G hydrazide (0.4396 g, 1 mmol) and 30 mL methanol were added to a 50 mL round-bottom flask, which was stirred and brought to a boil. 2-pyridine carbaldehyde (0.1 mL) was then added along with 5 drops of glacial acetic acid. After 2 hours, the resulting white solid was filtered off, washed with methanol/diethyl ether (1:1), and dried in vacuum over P_2O_5 to recover the final product (0.4075 g, 76.40%; Figure 22).

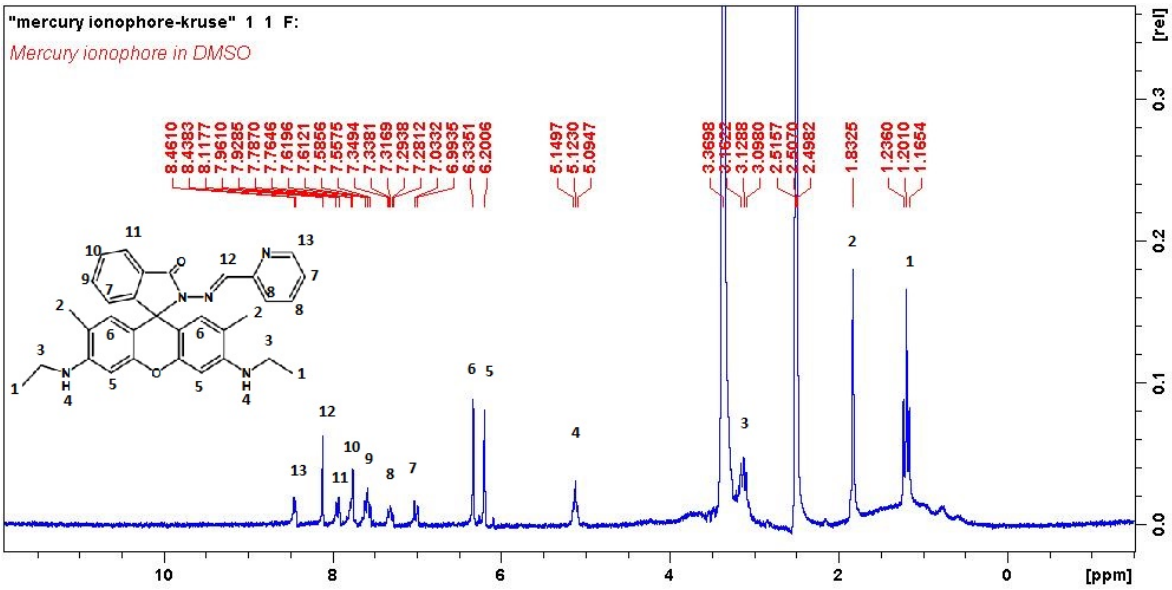

Figure 22. ^{1}H-NMR spectra of the Rhodamine 6G-based mercury ligand.

7.1.3 - Sensor Testing

Sensor testing for this ligand was much different than the previous ligands tested for lead, silver, and copper. First, the sensors were dipped in DMF solvent for 5 minutes, as usual. However, since DMF is non-polar, it was unclear how this would affect the functionalization protocol previously employed. Polar solvents are known to stabilize delocalized electrons in solution, which allows for some control over orientation. Non-polar solutions do not have this effect, so the orientation of the molecule is unknown.[53] To ensure optimal functionalization, the sensors were dipped in a 400 µM ligand solution for 24 hours (Figure 23). As previously observed, a decrease in current is observed as the sensor is functionalized.

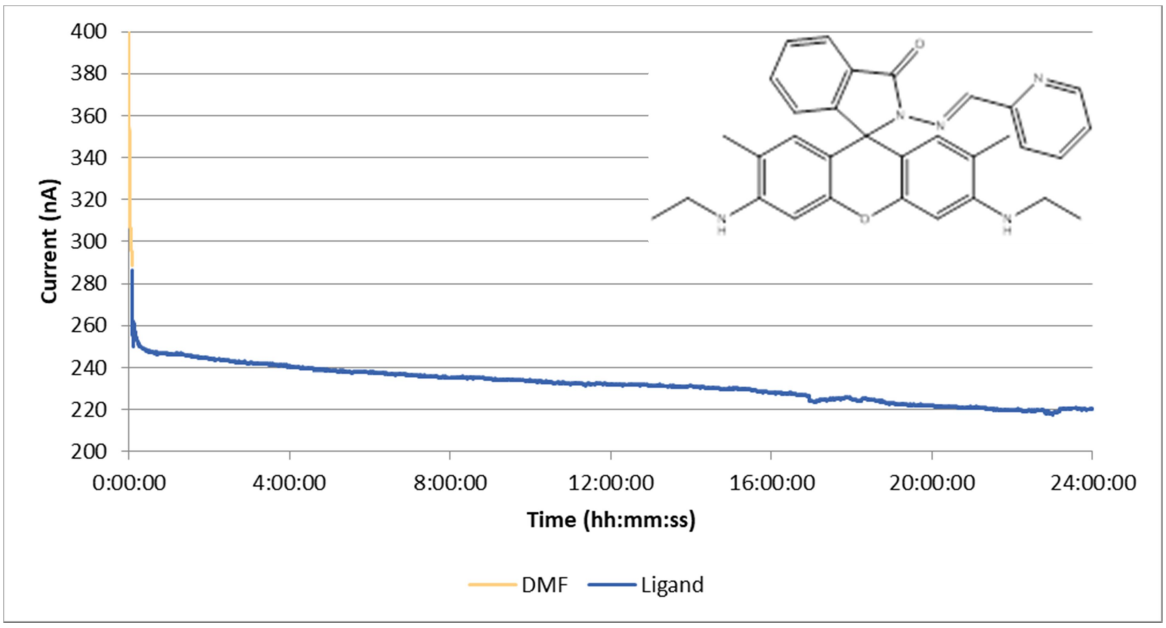

Figure 23. Functionalization of the sensors with the Rhodamine 6G-based ligand. Inset is the corresponding molecular structure. A decrease in current is observed when the sensors were dipped in solvent (first five minutes), followed by a larger decrease in current during functionalization.

After functionalization, the sensors were removed from the ligand solution, dried under low pressure in a fume hood, and placed into a stirring vial filled with 18.2 MΩ·cm water overnight for 18 to 24 hours to allow for equilibration with the surrounding air. Once equilibrated, a known amount of the stock mercury solution was pipetted into the water. This increased the concentration of mercury in the water solution, which would hypothetically increase the current through the chemiresistive film.

7.2 - UV/vis Spectroscopy

As expected from the paper by Wu et. al., the Rhodamine 6G-based ligand was able to detect mercury quantitatively through an increase in the absorbance at 535 nm (Figure 24). One thing to note is that the UV/vis was not sufficiently sensitive, so the spectrum looks quite jagged.

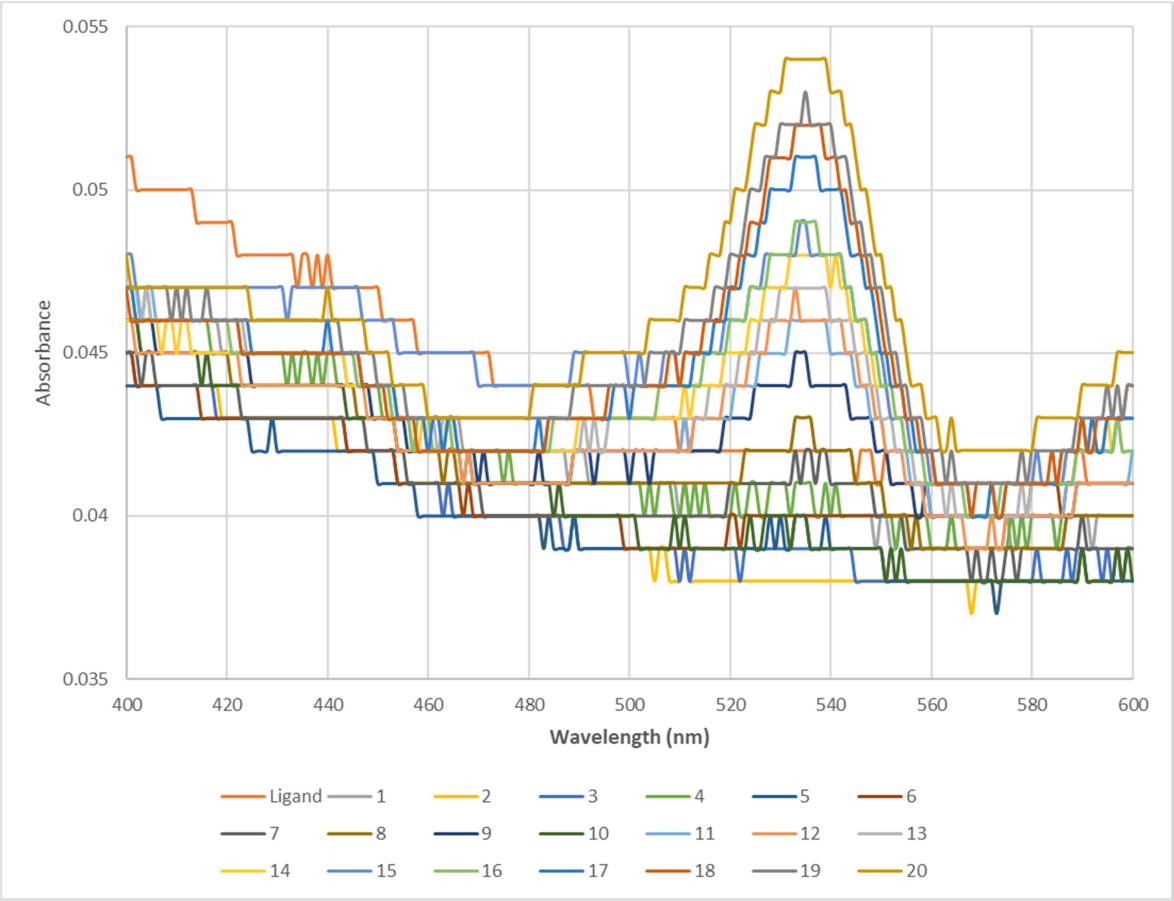

Figure 24. UV/vis spectrum of the Rhodamine 6G-based ligand and the mercury complex with different equivalents of mercury added. [R6G ligand] =10 μM; range of mercury concentrations go from 10 μM (1 eq.) to 200 μM (20 eq.).

When the concentration is 100 μM (10 eq.) and below, there is no correlation between the concentration of mercury and the absorbance at 535 nm. Above 100 μM (10 eq.), the increase in absorbance at 535 nm begins to follow an upward trend as the concentration of mercury increases. According to the Beer-Lambert law[33] the absorbance at a given wavelength is directly proportional to the concentration of the attenuating species, with the proportionality constant being referred to as the molar extinction coefficient (ε). Based on this, a trendline was formed correlating the concentration of mercury between 100 μM and 200 μM to determine ε (Figure 25).

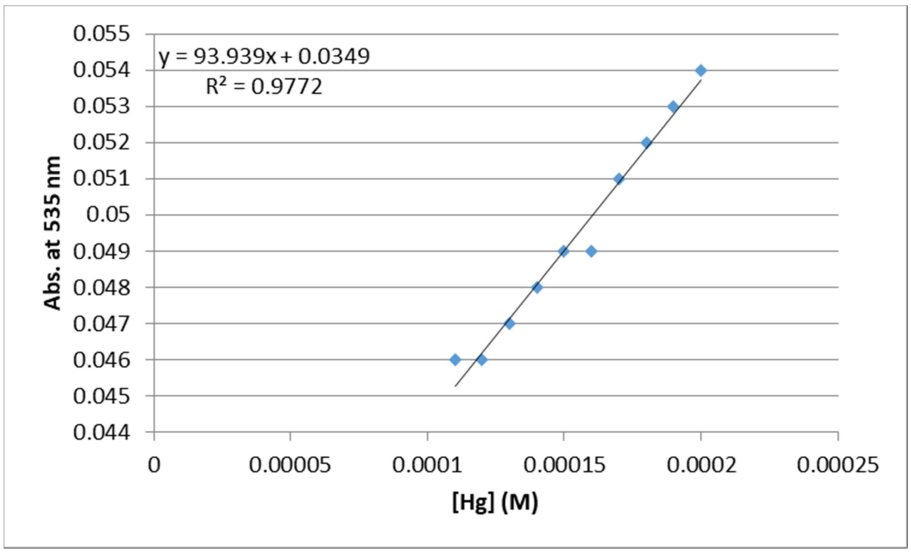

Figure 25. The linear correlation between the concentration of mercury in solution and the absorbance at 535 nm. Inset is the function of the trendline along with its R^2 value.

The linear correlation shows a good fit with an R^2 value of 0.9772. Based on the function provided by Excel and the 1 cm path length of the cuvette, the molar extinction coefficient ε was determined to be 93.939 $M^{-1}cm^{-1}$ which, although on the low side compared to other fluorescent molecules, does indicate a quantitative response towards the presence of mercury.

7.3 - Sensor Results

The sensor was tested in 18.2 MΩ·CM·cm water, and mercury was added from a stock 1 mM solution for concentrations ranging from 100 ppt to 100 ppb (Figure 26).

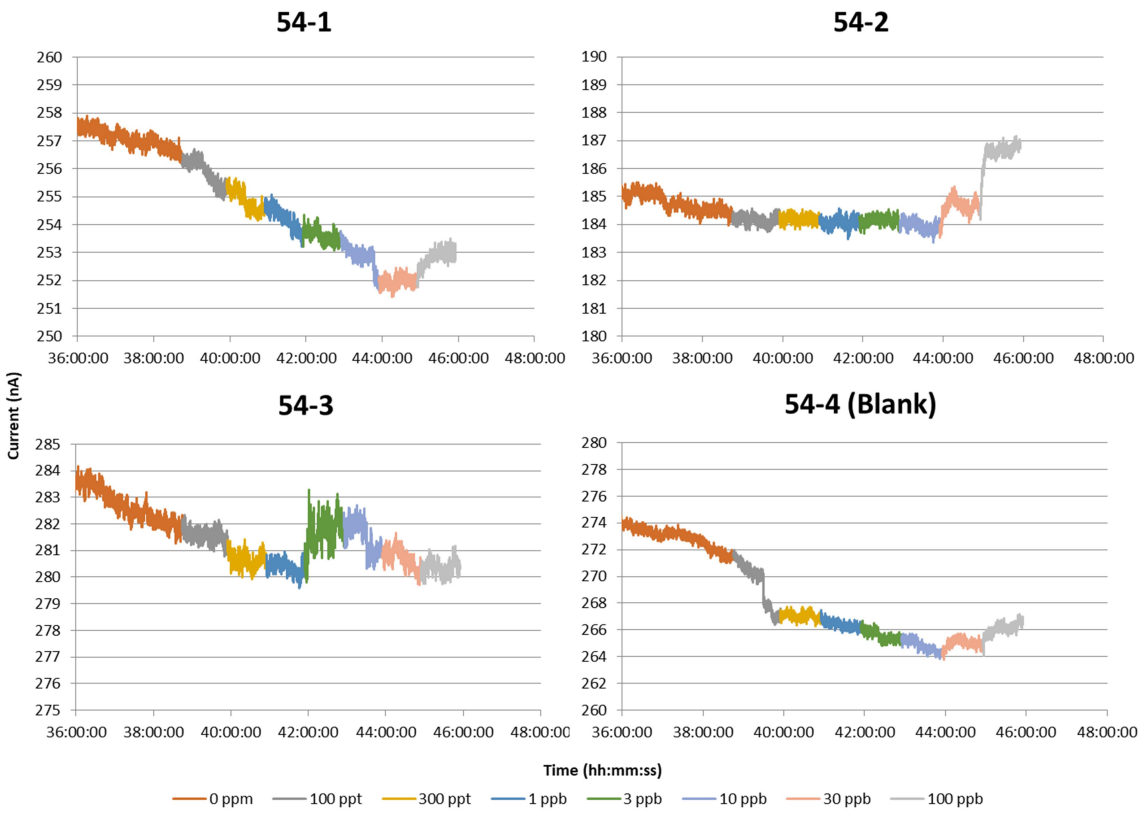

Figure 26. Current responses of three Rhodamine 6G-based ligand functionalized sensors (sensors 54-1, 54-2, 54-3) as well as a blank sensor (54-4) with respect to changing concentrations of mercury over time.

Although the data is noisy, one can conclude that there are no significant responses to mercury (sensors 54-2 exhibited a response at 30 ppb and 100 ppb, however the blank sensor 54-4 has the same response, indicating that the FLG film is responsible for the current change).

7.4 - Summary

A Rhodamine 6G-based ligand was tested as a potential mercury detecting ligand via functionalization of a FLG based chemiresistive sensor. A quantitative response was observed in the UV/vis for the range spanning from 100 µM to 200 µM with a ligand

concentration of 10 μM. When tested on the sensor however, no discernible response was present except for a response at 30 ppb and 100 ppb (which was also present in the blank and cannot be attributed to the ligand). The development of a membrane based chemiresistive sensor (currently being developed by Maryam) may rectify the issues contributing to poor sensor performance. However as of present, further research is required before the development of a chemiresistive mercury sensor.

8 - PHENANTHROLINE BASED LIGANDS: A SYSTEMATIC APPROACH

In previous chapters, attempts have been made to functionalize sensors with ligands that simply show a colorimetric interaction with the metal cation of interest. However, one must also consider many other variables when creating these sensors, such as the binding geometry in solution versus immobilized on a surface and whether the response seen in the UV/vis spectrum can be correlated to charge transfer on the surface of the sensor. Prior to this systematic approach, ligands were chosen simply based on two criteria: polycyclic aromaticity, and colorimetric response. This simplistic approach ignores how surface immobilization may affect binding geometry, and the ability of the ligand to translate an optical response to an electronic one. In Chapter 5, *Chemiresistive Detection of Silver Ions in Aqueous Media*, both bathocuproine and neocuproine were used as an array for the selective detection of both silver and copper ions in water. Bathocuproine would respond primarily to silver with a smaller response toward copper, and neocuproine would isolate the copper signal selectively so that both silver and copper can be accurately quantified. Based on this, it would seem that a study on phenanthrolines and their derivatives would allow for a more rigorous approach toward finding ligands for the detection of other metals. For this study, four derivatives were investigated: phenanthroline, neocuproine, bathophenanthroline, and bathocuproine. These ligands were screened with 15 different metals through UV/vis and chemiresistive sensing. Computational calculations and calibration curves were done for the metals that exhibited a response based on the screening. In this chapter we discuss the results obtained.

8.1 - Experimental

8.1.1 - UV/vis Spectroscopy

UV/vis spectroscopy was done using an Orion Aquamate 8000. The ligand solutions were made such that their concentrations in acetonitrile were $5x10^{-5}$ M. Stock solutions of $1x10^{-3}$ M each of Na^{+}, K^{+}, Ca^{2+}, Mg^{2+}, Co^{2+}, Mn^{2+}, Ni^{2+}, Hg^{2+}, Cd^{2+}, Pb^{2+}, Al^{3+}, Ag^{+}, Cu^{2+}, Zn^{2+}, and Fe^{2+} were made by adding the requisite amount of their respective salts (all chlorides with the exception of $Al_2(SO_4)_3$ and $AgNO_3$) into 100 mL of 18.2 MΩ·CM·cm water. The UV/vis spectrophotometer was calibrated using a 1:1 solution of acetonitrile:water. To obtain the spectra of the ligand on its own, 1 mL of the prepared ligand solution was mixed with 1 mL of 18.2 MΩ·CM water. For the metal on its own, 1 mL of the metal cation solution and 1 mL of 18.2 MΩ·CM water were mixed. For the metal complexes, 1 mL of the ligand solution was mixed with 1 mL of the stock cation solutions and left for 2 minutes to ensure that the metal cations and the ligand had ample time to interact. The spectrum was obtained between a range of 200 nm to 700 nm for all four ligands.

8.1.2 - Screening Process

The screening process for the phenanthroline based ligands was quite similar to the interference study done in Chapter 5. Eight sensors were functionalized as described in Chapter 5 such that there were two sensors for each ligand. These sensors were dipped into one bowl with 500 mL of stirring 18.2 MΩ·cm water and left overnight to allow the water to equilibrate with the surrounding air (~18-24 hours). Then, 500 µL of a chosen metal cation

was added to the solution (the concentration of the metal cation in the 500 mL of water would be 1 μM) and left to run for 40 minutes. Nitric acid was then added to the metal cation solution until the pH reached a value of 3 to allow for resetting. The sensors were left in this acidified solution for 40 minutes. After this, the acidified solution was discarded and the sensors were rinsed. The sensors were then placed for forty minutes into 500 mL of 18.2 MΩ·cm water (which had already been left out to equilibrate). This process was repeated for each metal cation. The relative responses were plotted into Excel, and metal cations that gave a negative or negligible response were discarded. Only the metal cations that gave a consistent positive response passed the screening and underwent further computational study and sensor analysis.

8.1.3 - Computational Details

Theoretical calculations were performed on the metal complexes that had exhibited a response during the screening process. The calculations were done using Gaussian09 and visualized in Gaussview 5.0. To optimize the structures of the four ligands, ground state DFT calculations were used with the B3LYP functional and the 6-31G(d) basis set. In the case of the metal complexes, the non-metallic components of the complexes (C, H, N, Cl) were optimized with the 6-31G(d) basis set, while the metal centres were optimized with SDD for the sake of computational efficiency. Optimization was done in gas phase in a vacuum.

8.1.4 - Sensor Testing

Eight sensors were functionalized such that there were two sensors per ligand. These sensors were placed into a stirring vial with 500 mL of 18.2 MΩ·cm water and left overnight

to equilibrate. To test the conductivity response of the ligands, saturated sodium chloride solution was pipetted into the 500 mL of water to change the conductivity. The tested conductivity range was 100 μS/cm to 30 000 μS/cm. To test the pH, sodium hydroxide solution was added into the 500 mL of water to change the pH to an initial value of 10. This solution was left for an hour, after which nitric acid solution was added to change the pH to 9. This was done for each pH value down to a pH of 3, below which sensor damage is likely. This is due to the decreasing ζ-potential at both low and high pH values, at which the graphene flakes on the surface will prefer to form aggregates in aqueous solution rather than remain on the surface as a flake.[54]

8.2 - UV/vis Screening

Prior to screening with the four phenanthroline based ligands, the UV/vis spectra of the cations by themselves were obtained. This allows for easier determination of peak shifts by eliminating any falsely attributed shifts to the inherent peaks present due to the metal cations themselves (Figure 27).

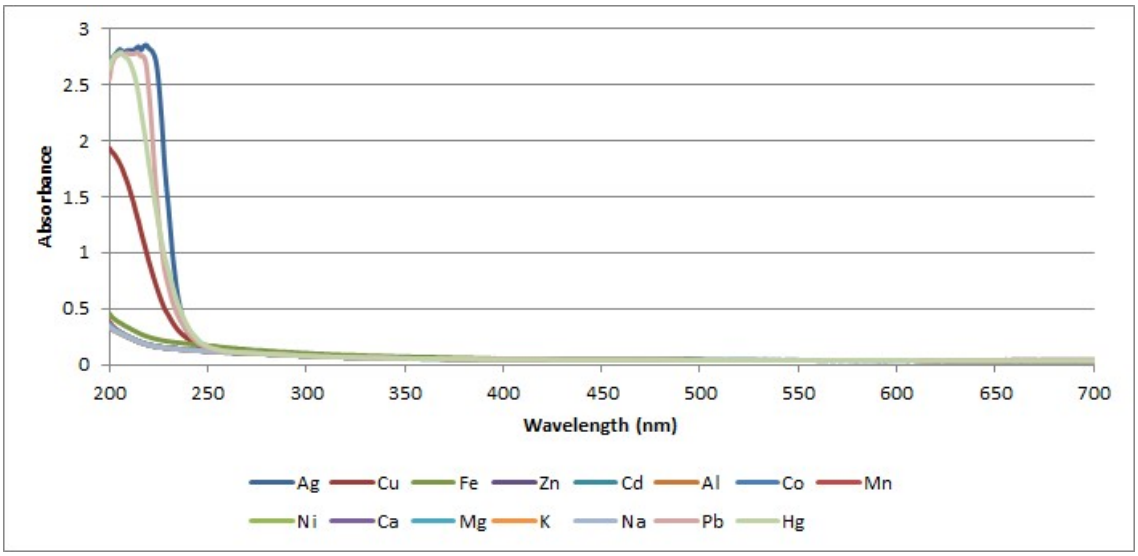

Figure 27. UV/vis spectra of each metal cation solution on their own. Concentration of each metal cation was 1 mM in 18.2 MΩ·CM water.

Many of the metals have no absorbance at any wavelength (which is to be expected since d-d transitions are low in intensity due to the Laporte selection rule, and the spin selection rule in the case of Mn^{2+}). However, a peak between 200 nm to 250 nm is seen for copper, silver, lead, and mercury, which could be due to the ligand-metal charge transfer that occurs when the aqua complexes of those metals are formed. The metals were then tested alongside the four ligands (Figure 28).

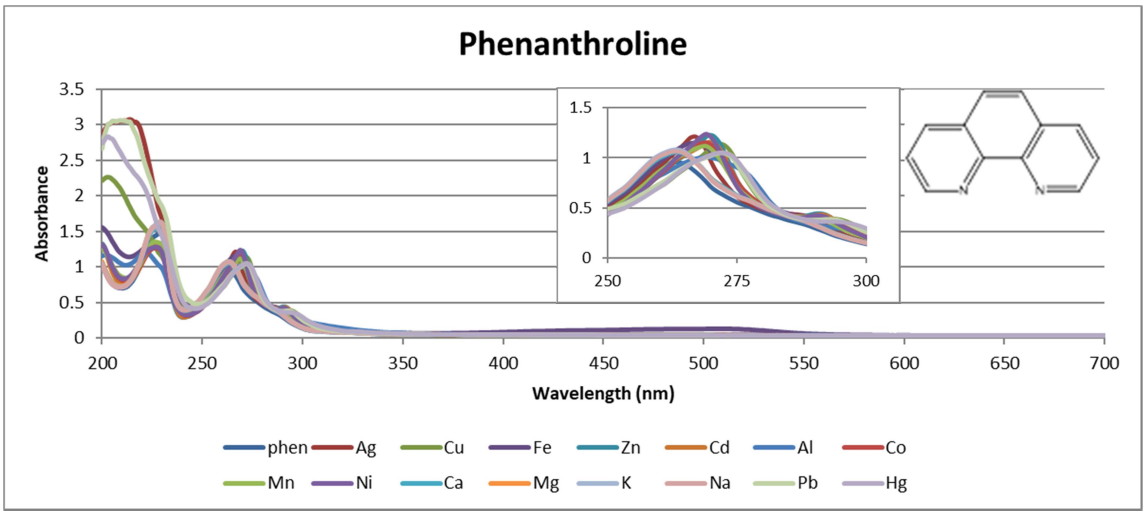
Phenanthroline
Absorbance
Wavelength (nm)
phen Ag Cu Fe Zn Cd Al Co
Mn Ni Ca Mg K Na Pb Hg

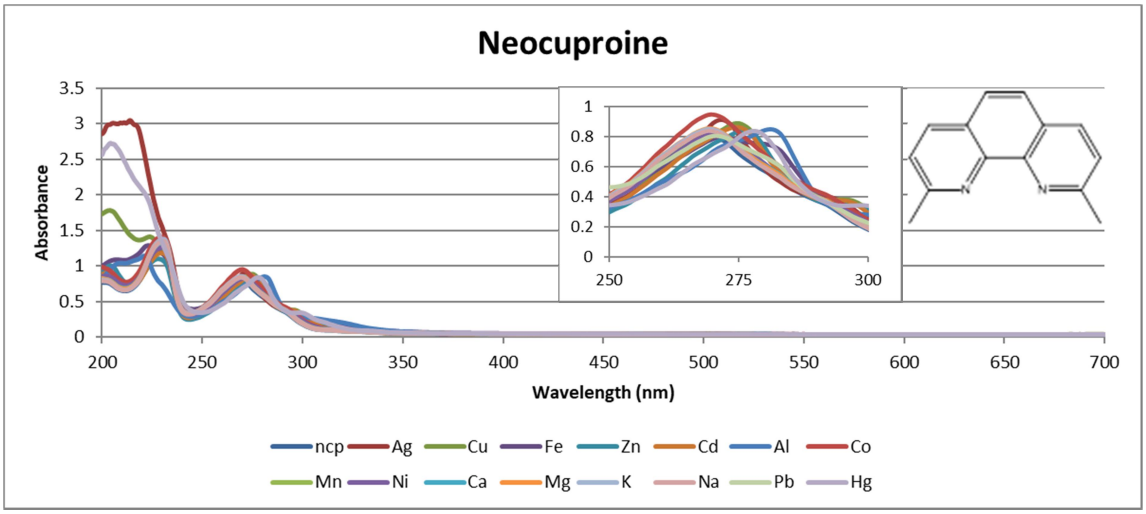
Neocuproine
Absorbance
Wavelength (nm)
ncp Ag Cu Fe Zn Cd Al Co
Mn Ni Ca Mg K Na Pb Hg

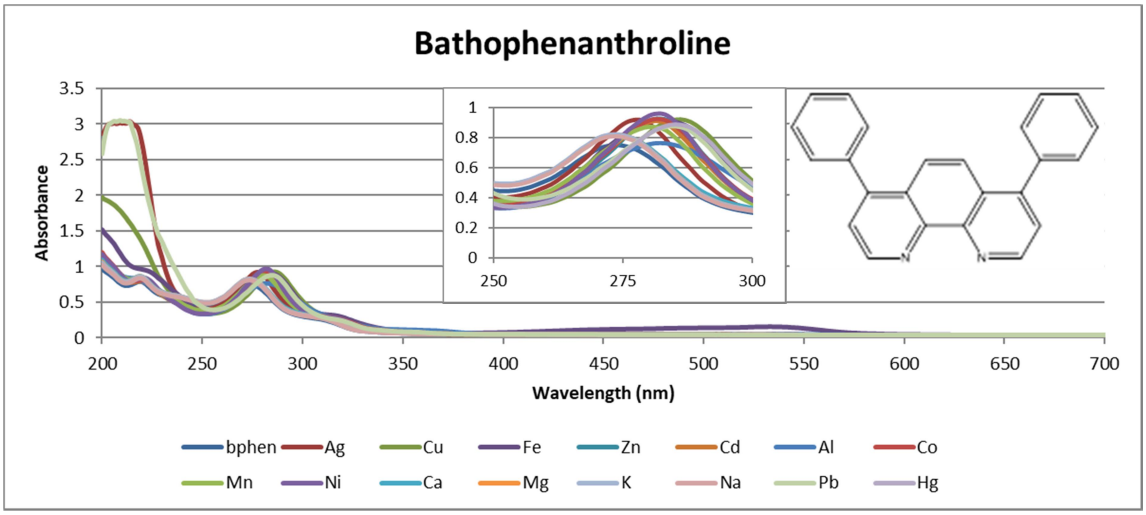
Bathophenanthroline
Absorbance
Wavelength (nm)
bphen Ag Cu Fe Zn Cd Al Co
Mn Ni Ca Mg K Na Pb Hg

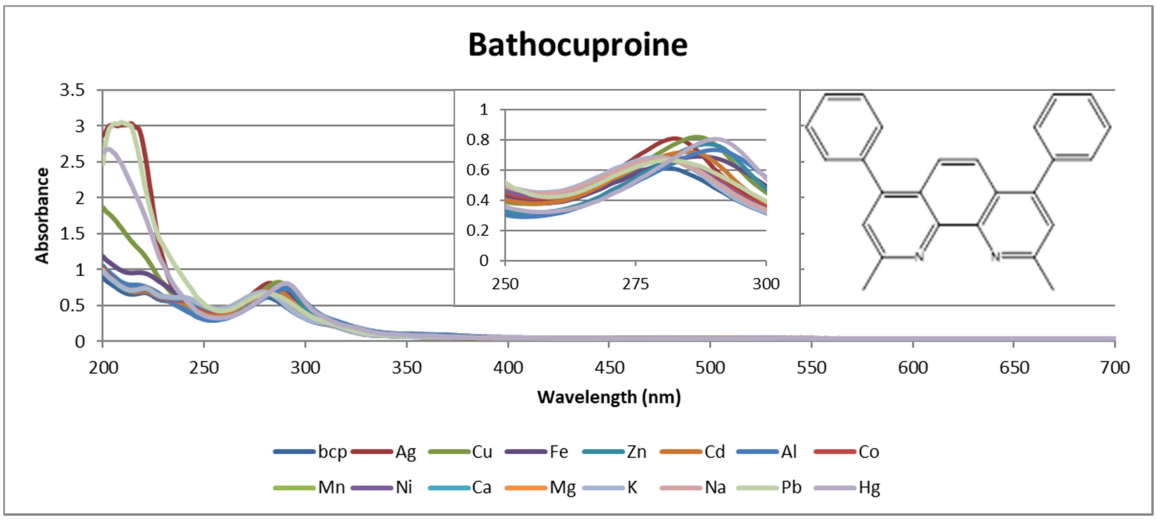

Figure 28. UV/vis spectra of the four ligands along with the 15 metal cations. Inset is the molecular structure of the ligands.

The phenanthroline does not show any major shifts when complexed with Ca^{2+}, Mg^{2+}, Na^{+}, or K^{+}. When Al^{3+} is added, the peak at 263 nm broadens and redshifts by 12 nm. This could be attributed to the possible formation of tris-1,10-phenanthroline aluminum (although formation of the complex under the conditions of this experiment would not be energetically favourable), which is known to absorb in the blue region.[55] All of the transition metal ions seem to interact with the phenanthroline, shifting the peak at 263 nm to a new position at ~275 nm. The formation of a new peak between 295 nm to 300 nm is also observed for all of the transition metal ions. This is expected since phenanthroline is a common ligand for many transition metals.[56] The iron phenanthroline mixture specifically shows a peak in the red region, at 514 nm. Since phenanthroline is used for the spectrophotometric determination of iron in many undergraduate laboratories, this result is trivial.[57]

Ca^{2+}, Mg^{2+}, Na^{+}, and K^{+} also show no signs of interaction with neocuproine. Al^{3+} once again exhibits a redshift of 12 nm for the peak at 272 nm. This time, however, Al^{3+} also shows the formation of a new peak at ~318 nm. It is unsure where this peak arises from, as there are no known complexes of neocuproine with Al^{3+} (although it is possible that the tris-neocuproine aluminum complex had formed). With regards to the transition metals, Co^{2+},

Mn^{2+}, Ni^{2+}, and Pb^{2+} do not show any response in the UV/vis, indicating that the methyl groups adjacent to the binding sites increases selectivity towards certain metal cations (particularly d^9 and d^{10} metals). Ag^+, Cu^{2+}, Zn^{2+}, Cd^{2+} and Hg^{2+} all show a similar response. Ag^+ induces an increase in absorbance for the peak at 268 nm and the formation of a new peak at 298 nm. Cu^{2+} redshifts the peak at 268 nm by 8 nm to a new value of 276 nm, and also forms the new peak at 294 nm. Zn^{2+}, Cd^{2+}, and Hg^{2+} are all part of the same group in the periodic table, so it is unsurprising that all three have very similar responses: a redshift of the peak at 268 nm by 7 nm to a new value of 275 nm, and a new peak arising between 298 nm and 300 nm. Fe^{2+} broadens the peak at 268 nm and begins to form a new peak further down at ~320 nm (although this peak is quite small). Based on this data, it seems that neocuproine is quite selective towards d^9 and d^{10} metals.

Bathophenanthroline once again shows no response towards Ca^{2+}, Mg^{2+}, Na^+, and K^+. Exposure to Al^{3+} shifts the peak at 276 nm by 10 nm to a new value of 286 nm, as well as forming a new peak at 363 nm indicating the tris complex has formed with bathophenanthroline as well. Co^{2+}, Mn^{2+}, Ni^{2+}, and Pb^{2+} all show similar responses, with an increase of the absorbance and a peak shift for the peak at 276 nm by 5 nm to a new value of 281 nm. Ag^+ shows an increase in the absorbance at 276 nm. Cu^{2+} redshifts the peak at 276 nm by 13 nm to a new value of 289 nm accompanied by an increase in absorbance. The peak at 313 nm for bathophenanthroline also redshifts by 11 nm when interacting with Cu^{2+}. Zn^{2+}, Cd^{2+}, and Hg^{2+} all show the same response: an increase in absorbance and a shift of the peak at 268 nm by 16 nm to a new value of 284 nm. The peak at 311 nm also shifts by 8 nm to its new position at 319 nm. Fe^{2+} exhibits the most significant change in the UV/vis, with an increase in absorbance and a peak shift for the peak at 268 nm by 20 nm to a new value of 288 nm. A new peak also appears at 534 nm in the visible region. Since bathophenanthroline

is commonly used for the spectrophotometric detection of Fe^{2+}, this is not a surprising result.[58]

As expected, based on previous results, Ca^{2+}, Mg^{2+}, Na^{+}, and K^{+} have no response with bathocuproine. Al^{3+} once again responds, showing an increase in absorbance and a peak shift of 16 nm for the peak at 278 nm to a new value of 294 nm. In this case, Co^{2+}, Mn^{2+}, Ni^{2+}, and Pb^{2+} do not respond, possibly due to steric hindrance from the methyl groups adjacent to the imine binding sites. Both Ag^{+} and Cu^{2+} increase the absorbance at 278 nm, with Cu^{2+} also shifting the peak by 12 nm to its new position at 290 nm. Zn^{2+}, Cd^{2+}, and Hg^{2+} all show similar responses, increasing the absorbance slightly and shifting the peak at 278 nm by varying amounts: Cd^{2+} shifted the peak by 4 nm to a new value of 282 nm, and Zn^{2+} and Hg^{2+} both shifted the peak by 18 nm to a new value of 296 nm. Fe^{2+} increased the absorbance at 278 nm as well as shifted the peak by 14 nm to its new position at 292 nm. The peak that arises in the visible range for phenanthroline and bathophenanthroline is not present possibly due to the methyl groups adjacent to the imine binding sites (much like neocuproine).

8.3 - pH and Conductivity

The pH and conductivity response of the four ligands on the sensors was observed to determine an optimal working range for sensor response. In Chapter 5, the impact of conductivity on the double layer and, consequently, the baseline current was discussed.[59] However, the range of conductivity was quite limited. For this experiment, the conductivity range was increased to a maximum value of 30 000 μS/cm (Figure 29).

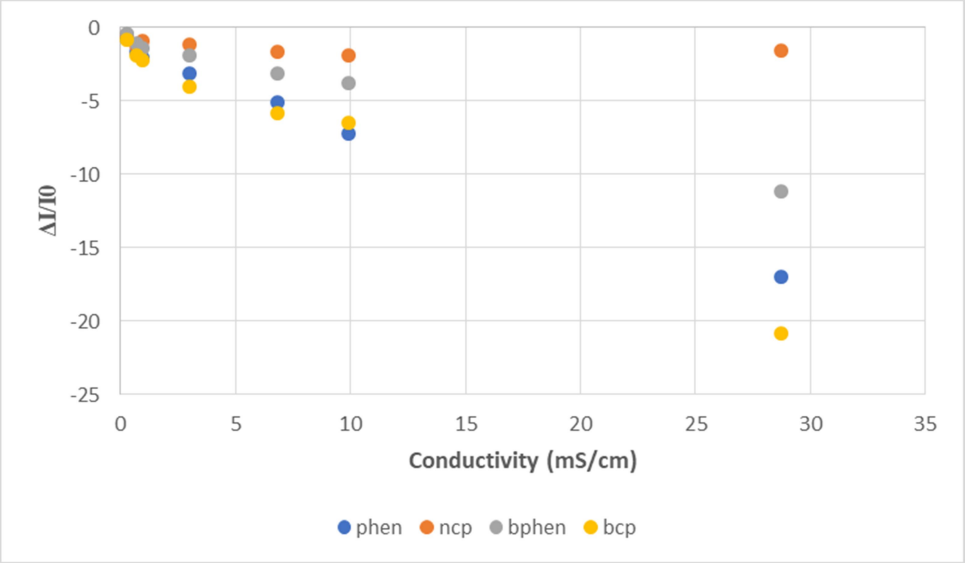

Figure 29. Conductivity response of sensors doped with phenanthroline (phen), neocuproine (ncp), bathophenanthroline (bphen), and bathocuproine (bcp).

The current decreases for all ligands as expected. However, the saturation that was expected to occur at ~700 µS/cm does not occur. Instead, the current response follows a linear negative response as conductivity increases. This indicates that contraction of the double layer continues even at extremely high conductivity values.[60] Curiously, neocuproine does not seem to be affected as much by the extreme conductivity values, seemingly saturating at 10 000 µS/cm. It is unclear as to why neocuproine follows this trend considering the structural similarity of all four ligands, however it seems the presence of either methyl groups or phenyl groups will decrease conductivity response. The presence of both at the same time however will increase the conductivity response, which is seen when comparing the slopes of their trend lines (Table 4).

	Slope (nA*cm/µS)	R^2
Phenanthroline	-0.5331	0.9956
Neocuproine	-0.0273	0.3168
Bathophenanthroline	-0.3597	0.9929
Bathocuproine	-0.6712	0.9888

Table 4. Current response slopes and R^2 values for the four phenanthroline based ligands.

The pH of the solution is also another factor to consider when discussing the chemiresistive sensors because not only is it important to know what the working pH range of the sensor must be, but one must know the effects of the pH on the binding constant of the phenanthroline ligands and the metal cations, as well as changes in the sensing behaviour. The pK_a of phenanthroline is known to be 4.86[61], and since the other ligands have unknown pK_a, it is assumed that theirs would also be between pH 4.8-6. To test this hypothesis, a pH test was run with all four ligands to determine the pH at which the sensor would be able to "reset"; allow equilibrium to lean toward protonation rather than metal complexation (Figure 30). The baseline chosen here is 18.2 MΩ·cm water that has been left overnight to equilibrate (a pH value of 5.7 and a conductance value of 3 µS/cm).

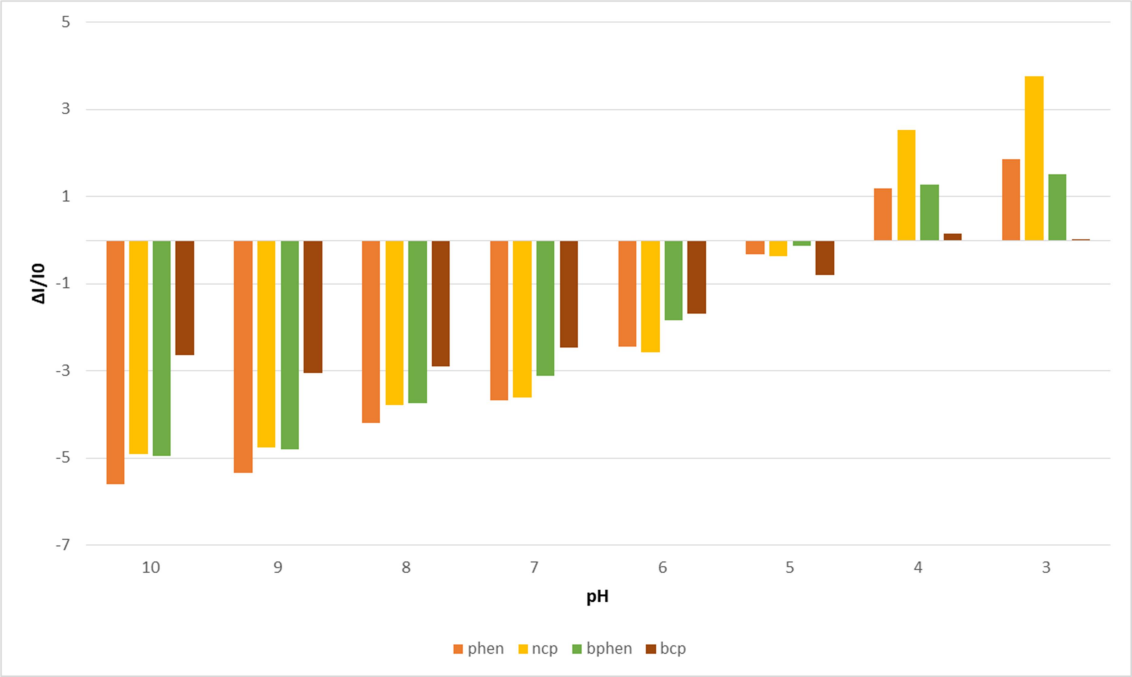

Figure 30. Current responses of the four ligands to different pH values.

The response when exposed to basic pH levels is negative relative to the previously established baseline, which indicates that conductivity is what drives the response at those pH values. This negative response continues to get smaller as the pH decreases due to the

reduction of OH^- ions as the neutralization reaction occurs in solution. Once the pH reaches a value of 4, the response shifts in the positive direction, which means that between pH values of 5 to 4 the ligand preferentially protonates rather than complexing to the metal cation in solution. This means that a pH range of 5 to 10 would be most appropriate for sensor testing (with values above pH 10, many metal cations form hydroxides), and a pH below 5 would allow for resetting these sensors.

8.4 - Sensor Screening

As mentioned earlier, a response in the UV/vis screening may not directly translate to a response when tested with a sensor. Al^{3+} for example forms a tris complex with phenanthroline. When phenanthroline is immobilized on an FLG surface, this will not be possible. Therefore, a separate screening experiment is required to determine which metals would be feasible for sensing with the four phenanthroline-based ligands (Figure 31).

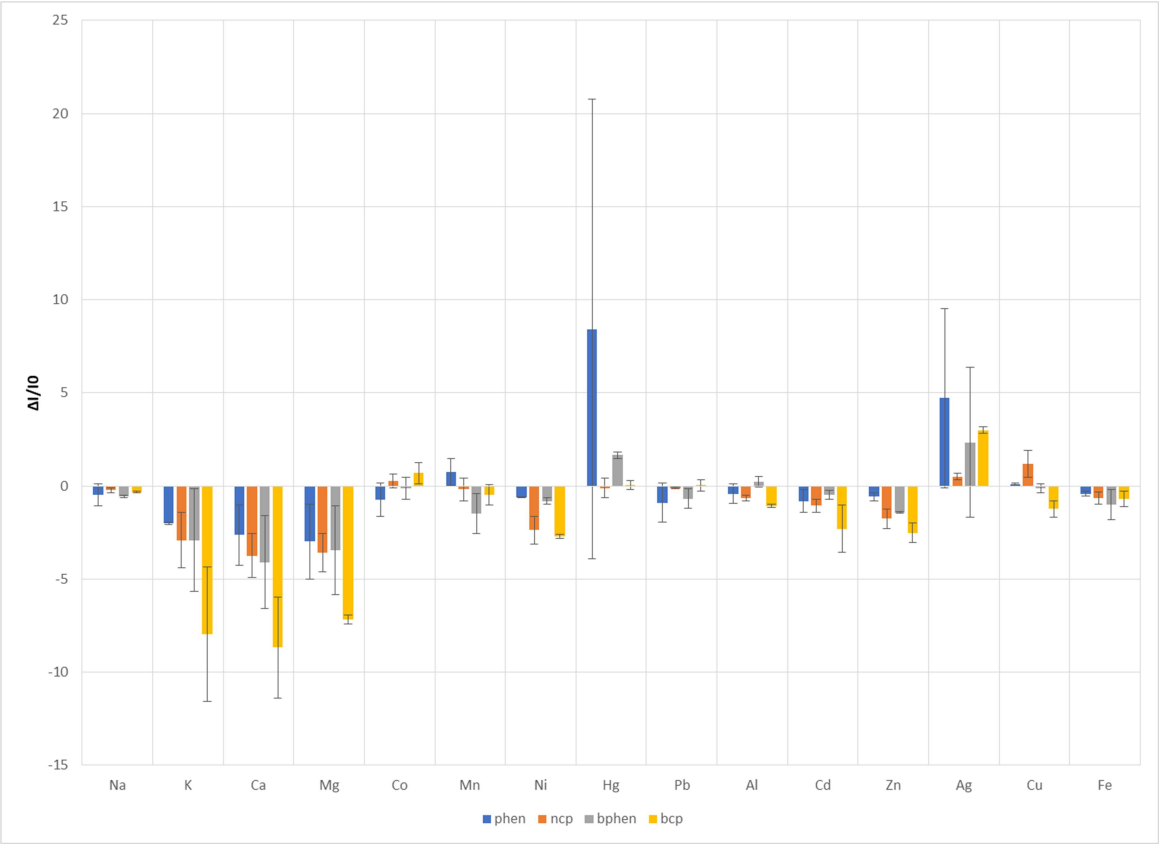

Figure 31. The sensor screening experiment performed with the phenanthroline-based ligands. 1 µM of each metal cation was added to the solution.

Metals that had responded before in the UV/vis spectra, such as Co^{2+}, Mn^{2+}, Ni^{2+}, Pb^{2+}, Al^{3+}, Cd^{2+}, Zn^{2+}, and Fe^{2+}, now no longer show a response when adsorbed onto the FLG film, indicating that binding geometry plays a much larger role in sensor performance than previously thought. On the other hand, metals that have not exhibited a response in the UV/vis, such as K^{+}, Ca^{2+}, and Mg^{2+}, now show a negative response (although the error bars are quite large). This shows that water hardness may have an effect on sensor response, particularly with bathocuproine. The metals that do respond are Ag^{+} (with bathocuproine, 2.99%), Cu^{2+} (with neocuproine, 1.18%), and Hg^{2+} (with bathophenanthroline, 1.65%) at a concentration of 1 µM. The Ag^{+} and Cu^{2+} sensing has already been investigated in Chapter 5 and was an expected outcome. Hg^{2+}, however, was not expected to respond. However upon

further inspection, it was found that bathophenanthroline has a weak electrostatic attraction to mercury through the resonance-stabilized imine groups, which quenches the photoluminescence of bathophenanthroline aggregates in solution.[62] Although the response is quite low when compared to the concentration of Hg^{2+} in water (1 μM or 200 ppb), it offers a suitable starting point for the development of a Hg^{2+} chemiresistive sensor.

8.5 - DFT Calculations

For the metal cations and ligands that had passed screening (Ag^{+} with bathocuproine, Cu^{2+} with neocuproine, and Hg^{2+} with bathophenanthroline), DFT calculations were performed to determine the manner in which the electronic structure of the ligand changes when complexed with its specific metal cation (Figure 32). All of the complexes were mono-ligand complexes since this is the most likely binding mode on the surface.

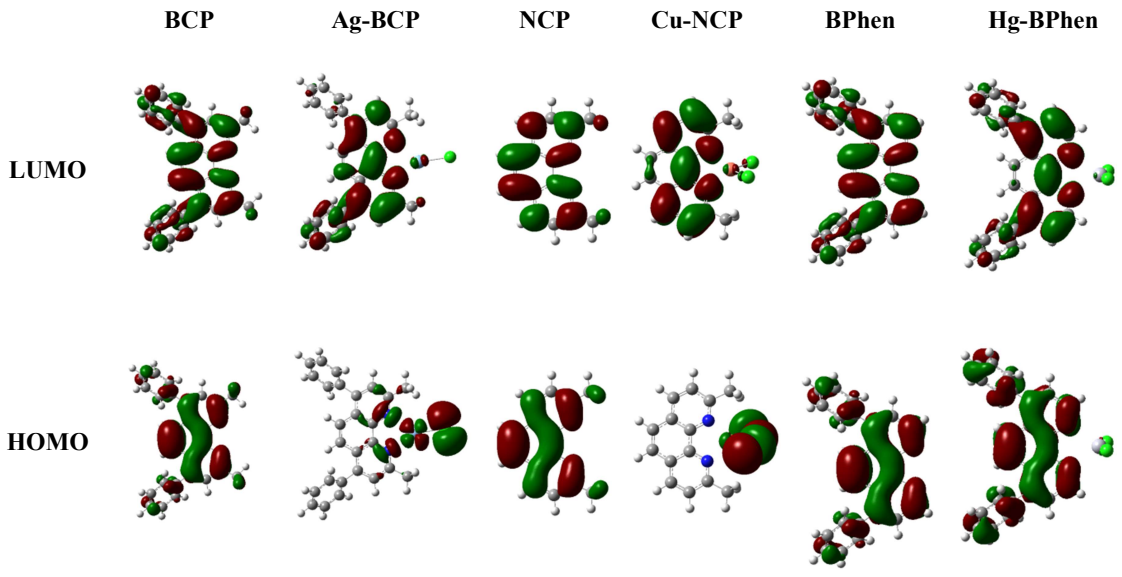

Figure 32. The HOMO and LUMO of bathocuproine (BCP), neocuproine (NCP), and bathophenanthroline (BPhen) as well as their metal complexes. Chloride was used as the counter ion in all three cases.

The electronic distributions of the three phenanthroline based complexes are quite similar. The HOMO and the LUMO electron density are spread over the phenanthroline backbone, with some minor contribution from the phenyl and methyl substituents. Once complexed, both the Ag-BCP and Cu-NCP complexes experience a change in the HOMO electron density, which is now located on the metal centre. Ag-BCP has some contribution from the imine groups, whereas the HOMO in Cu-NCP is exclusively centred on the metal centre. This difference could be because Ag^{+} adopts a d^{10} electron configuration, whereas Cu^{2+} adopts a d^{9} configuration. This leads to the loss of degeneracy in the spin states of the Cu^{2+} electrons.[63] Therefore, both the α-HOMO (pictured above in Figure 32) and the β-HOMO must be considered for the Cu-NCP complex (Figure 33).

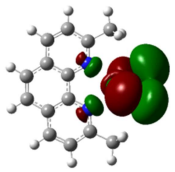

Figure 33. The β-HOMO of Cu-NCP.

Here, the interaction between the Cu^{2+} metal centre and the imine groups on neocuproine is clearer. There is now an obvious contribution from the imine groups indicating the existence of an interaction. The LUMO for both the Ag-BCP and Cu-NCP complexes also experiences a change in the electron density, which is now being pulled toward the metal centre in both cases. The HOMO of the Hg-BPhen complex is relatively unchanged, and there is only minimal contribution from the Hg^{2+} metal centre in the complex, so it is unclear what could lead to an interaction between Hg^{2+} and bathophenanthroline. Energy values for the orbitals have also been calculated to determine the degree to which complexation affects orbital energy (Table 5).

	HOMO Energy (eV)	LUMO Energy (eV)	Band Gap (eV)
BCP	-5.7870	-1.2846	4.5024
Ag-BCP	-5.3670	-2.2158	3.1512
NCP	-5.9598	-1.2446	4.7152
Cu-NCP	-6.4075	-2.5796	3.8279
BPhen	-5.9759	-1.4659	4.5100
Hg-BPhen	-6.6796	-2.2273	4.4523

Table 5. Frontier orbital energies and band gaps for BCP, NCP, BPhen and their metal complexes.

In all cases, the band gap decreases as complexation with the metal cation occurs; this is to be expected. Binding with the lone pairs on the imine groups will stabilize the molecule and decrease HOMO energy. The energy for the Ag-BCP complex increases compared to the free bathocuproine, however. It was shown that the Ag-BCP complex, used to improve electron transport in the bathocuproine layer in organic semiconductors, exhibited an increase in the HOMO and a decrease in the LUMO to align with the Fermi level of the silver electrode.[64] The band gap for each molecule decreases as well, due to the crystal field splitting that occurs when the metal complexes with the ligand.

8.7 - Summary

A systematic method of discovering new ligand molecules was introduced in the hopes that sensor molecule discovery could be made more efficient. Since phenanthroline-based systems show promise, four different phenanthroline derivatives: phenanthroline, neocuproine, bathophenanthroline, and bathocuproine, were tested. UV/vis screening of the phenanthroline derivatives with 15 different metals were performed. Transition metals and metalloids seemed to interact more frequently than the alkali metals and alkaline earth metals. Steric hindrance from the methyl groups adjacent to the binding sites in neocuproine and bathocuproine lead to increased binding preference towards certain metals such as copper and silver, respectively. pH experiments with the four ligands show a change in response polarity between pH values of 5 and 4, which fall in line with the experimental pK_a values of

phenanthroline molecules. Conductivity tests show a linear decrease in sensor response with the increase of solution conductance due to the double layer contraction (neocuproine seems to resist this change at higher conductance values, however). When the four ligands were tested on sensors, three responses were seen that were considered significant: neocuproine and copper, bathophenantroline and mercury, and bathocuproine and silver. DFT calculations were performed on the three molecules and their respective complexes to determine the nature of their interaction. All three of the ligands on their own have quite similar HOMO and LUMO electron density distributions. When complexed with their respective metals, the HOMO of bathocuproine with silver is located around the silver metal centre, with contribution from the imine binding sites, as expected. The HOMO of the neocuproine and copper is located exclusively around the metal centre, which is explained by the loss of spin-state degeneracy since copper adopts a d^9 electron configuration in the +2 oxidation state. When looking at the β HOMO electron density distribution, the contribution from the imine groups becomes clearer. Bathophenanthroline and mercury is unique in that there is no apparent interaction between the ligand and metal, save for some contribution from mercury in the LUMO of the complex. This is despite the fact that mercury shows an interaction with bathophenanthroline in both the UV/vis spectra and the sensor screening results. Further inquiry is required to determine the reason for this discrepancy.

9 - SUMMARY

9.1 - Conclusion

In CHAPTER 1, a review article, *Metal Cation Detection in Drinking Water*, was appended, which introduced and elaborated upon the importance of metal cation detection, as well as recent advances made toward that end. In CHAPTER 2 current methods, as well as their drawbacks were also introduced, and FLG based chemiresistive sensors were offered as an alternative approach toward online detection of cations in water. The concept of chemiresistivity was explained, as well as the use of metal cation selective ligands adsorbed onto the FLG film for selective analyte detection. One particular family of ligands, phenanthrolines, was introduced as a possible option toward the systematic selection of ligands. Justification was also offered for the use of FLG as a transducing film when constructing the chemiresistive sensor. In CHAPTER 3, the general concepts behind DFT, UV/vis spectroscopy, and XPS were explained and the use of these methods were justified in their aid toward ligand selection and sensor performance. This chapter also included instructions on the synthesis of an exfoliated FLG suspension and the fabrication of a chemiresistive sensor for use in aqueous media.

CHAPTER 4 expanded upon Ana Zubiarrain Laserna's research on the chemiresistive detection of copper in aqueous media. For the first time in the Kruse Research Group, DFT was employed as an indicator for the feasibility of a ligand when used on a chemiresistive sensor platform. Two different ligands, DAP and DAQ, were chosen as potential copper selective ligands. Both ligands had shown good responses in the UV/vis spectrum and had promising results given by DFT calculations. When both ligands were screened for copper selectivity, DAP was chosen as the main ligand due to its more consistent response. When

testing against various concentrations of copper in water, step ups in current were observed (these step ups were also present in the non-functionalized sensor, albeit with a far lower response). These step-ups were fit to a Langmuir isotherm, first order decay function, and a Freundlich isotherm. Although they gave moderately good fits, the R^2 values for both the Langmuir and first order functions were below 0.95, and would not be suitable for mass production. The Freundlich isotherm had a better fit, but since it is an empirical function it would not be sufficient for a calibration curve. Attempts to reset the sensor led to sensor damage as seen by the large sharp drop in current (however the sensor continued to respond to copper despite the damage).

CHAPTER 5 was an appended manuscript, *Chemiresisitive Detection of Silver Ions in Aqueous Media*, which was submitted to Sensors and Actuators B: Chemical. The manuscript outlines a successful attempt at a chemiresistive silver sensor based on a bathocuproine functionalized FLG film. UV/vis spectroscopy was used to confirm the formation of a silver-bathocuproine complex. From there, deposition optimization was performed, and a 4% saturated bathocuproine solution was found to functionalize the solution best. pH and conductivity tests were performed to determine the response to the pH and conductivity of solution. Using these tests, it was determined that the working range of the sensor was between pH 6 and pH 10. A negative response was observed when conductivity increased, indicating an electrostatic gating effect on the FLG film. As the concentration of silver increased in solution, so did the current passing through the sensor. The current changes were fit to a Langmuir and first order decay function, where they both had very good correlation (both R^2 values were above 0.95). Interference tests show that the sensor is very selective to silver, with a minor response interference from copper. When testing in a real water sample, the sensor underestimated the amount of silver in solution. This was attributed to the presence of excess anions in the real water sample which could precipitate silver out of the water or

suppress the silver response. The sensor test with nitrate proved the suppression of the silver response. Nevertheless, this silver sensor is a first step toward chemiresistive cation detection in water.

CHAPTER 6 was the attempt at creating a lead sensor using three different ligand molecules: pyrogallol red, Ligand β, and Receptor 1. These tests were done in collaboration with Mae Masters. UV/vis spectroscopy and DFT calculations show favourable results when the ligands were exposed to lead. When running the sensors however, there was no discernible response for any of the ligands.

CHAPTER 7 discusses an attempt at making a chemiresistive mercury sensor. This was done in collaboration with Maryam Darestani-Farahani. The ligand tested was a Rhodamine 6G based ligand. A UV/vis calibration curve was formed and the molar extinction coefficient of the ligand was determined. Although the ligand was rather weak, the UV/vis spectra showed that it had potential to be a viable mercury sensor. No response was seen when tested with the sensor, however, indicating that the ligand may not be appropriate on a chemiresistive sensing platform.

In CHAPTER 8, a more systematic approach to finding new ligands was investigated. This new method, based on phenanthroline derivatives, would allow for more efficient selection of ligand molecules which would allow for the detection of many different cations. First, four different derivatives (phenanthroline, neocuproine, bathophenanthroline, and bathocuproine) were screened with 15 different cations through UV/vis spectroscopy and chemiresistive sensor testing. What was found was that neocuproine and copper, bathophenanthroline and mercury, and bathocuproine with silver gave the best responses. DFT calculations were done on the metal complexes that had passed the screening to determine the change in electron density and band gap as complexation occurred. Once this

was done, pH and conductivity tests were performed on the sensors. The sensors responded to pH as expected, and a pH range of 5 to 10 was determined as the best range for sensor use. The increase in conductivity decreased the current in a linear fashion, as expected.

9.2 - Future Work

Reproducibility of the copper sensor was the main issue, as many sensors were tested but only a few gave a favourable response. The reliability of DAP as a copper ligand is brought into question due to this. One potential replacement for DAP is neocuproine, which is known to selectively bind to copper in solution.[65,66] This ligand has also responded to copper during the phenanthroline screening test. Neocuproine should be investigated as a potential copper ligand through further reproducibility testing as well as interference and real sample tests. XPS can also be employed to investigate the nature of complexation on the FLG surface.

In the case of lead, anthracene-based ligands show a lot of promise for use in a chemiresistive sensor. One possible ligand that can be used is N-methyl-2-(9,10-dimethylanthryl)-thiohydroxamic acid. The ligand has a low fluorescence yield which doesn't change upon complexation with lead. However, the UV peak redshifts by 28 nm after complexation, indicating a change in the electronic structure of the ligand. This ligand is also not water soluble, which ensures it stays on the FLG film rather than coming off and dissolving into solution.[67] Another possible ligand is a TTF-π-pyridine derivative, which consists of two pyridine groups bridged together by a tetrathiafulvalene molecule. The interaction between the pyridine and the lead changes the colour from yellow to purple, as well as increases the oxidation potential of the ligand. This indicates a large change in the

electronic structure of the ligand, which could mean large current changes in a chemiresistive sensor for smaller concentrations, which is important for lead sensors.[68]

Progress is being made with the creation of a mercury sensor through Maryam Darestani-Farahani's research on ion-selective membranes. These membranes, similar to membranes used in ISE's, are being looked into as an alternative to pure chemiresistive sensors. The main benefit of using a membrane over directly functionalizing the FLG film is the degree of freedom that the ligand has. When immobilized on the FLG film, the sensor is very restricted on how it binds with the metal cation. This means that ligands that form complexes in solution may not form complexes when immobilized on a surface. With membranes, the ligands are able to bind more freely to the metal cations, increasing the potential response of the sensor.[69]

With respect to phenanthrolines, calibration curves will need to be formed with the cations that exhibited a response to determine whether the response is quantitative. Further experimentation with XPS, X-ray diffraction (XRD), and Raman spectroscopy may also be necessary. After this, anions and organic contaminants would be the next logical step for a target analyte. The complexes formed between neocuproine and copper, bathophenanthroline and mercury, and bathocuproine and silver may be used for anion and organic molecule detection in solution. Neocuproine copper complexes have been used for the detection of ascorbic acid[70] and nitrate/nitrite.[71] Metal bathophenanthroline complexes have also been used for the detection of uric acid in biological samples.[72] This path could allow for the development of a new class of sensors based on metal complexes rather than ligands themselves.

Although much work is required, FLG based chemiresistive sensors open many opportunities towards the quantification of many different parameters in water. These sensors

are cheap and offer good performance, making them very attractive towards ensuring the availability of clean water for all.

REFERENCES

(1) Udhayakumari, D.; Velmathi, S.; Sung, Y. M.; Wu, S. P. Highly Fluorescent Probe for Copper (II) Ion Based on Commercially Available Compounds and Live Cell Imaging. *Sensors Actuators, B Chem.* **2014**, *198*, 285–293. https://doi.org/10.1016/j.snb.2014.03.063.

(2) Hsu, L. H. H.; Hoque, E.; Kruse, P.; Ravi Selvaganapathy, P. A Carbon Nanotube Based Resettable Sensor for Measuring Free Chlorine in Drinking Water. *Appl. Phys. Lett.* **2015**, *106* (6). https://doi.org/10.1063/1.4907631.

(3) Halim, U.; Zheng, C. R.; Chen, Y.; Lin, Z.; Jiang, S.; Cheng, R.; Huang, Y.; Duan, X. A Rational Design of Cosolvent Exfoliation of Layered Materials by Directly Probing Liquid-Solid Interaction. *Nat. Commun.* **2013**, *4*. https://doi.org/10.1038/ncomms3213.

(4) European Action towards Leading Centre for Innovative Materials. EAgLE – WP 4.1 and 4.2 -XPS AtIF-PAN.

(5) Dalmieda, J.; Kruse, P. Metal Cation Detection in Drinking Water. *Sensors (Switzerland)*. 2019. https://doi.org/10.3390/s19235134.

(6) Mohtasebi, A.; Kruse, P. Chemical Sensors Based on Surface Charge Transfer. *Physical Sciences Reviews*. 2018. https://doi.org/10.1515/psr-2017-0133.

(7) Love, J. C.; Estroff, L. A.; Kriebel, J. K.; Nuzzo, R. G.; Whitesides, G. M. Self-Assembled Monolayers of Thiolates on Metals as a Form of Nanotechnology. *Chemical Reviews*. 2005, pp 1103–1169. https://doi.org/10.1021/cr0300789.

(8) Lawrance, G. A. *Introduction to Coordination Chemistry*; 2009. https://doi.org/10.1002/9780470687123.

(9) Banerjee, S. Phenazines as Chemosensors of Solution Analytes and as Sensitizers in Organic

Photovoltaics. *Arkivoc*. 2016, pp 82–110. https://doi.org/10.3998/ark.5550190.p009.347.

(10) Vvedensky, D. D. Symmetry and Spectroscopy. *Encycl. Spectrosc. Spectrom.* **2016**, 396–400. https://doi.org/10.1016/B978-0-12-409547-2.12172-9.

(11) Sammes, P. G.; Yahioglu, G. 1,10-Phenanthroline: A Versatile Ligand. *Chemical Society Reviews*. 1994, pp 327–334. https://doi.org/10.1039/CS9942300327.

(12) Phifer, C. C.; McMillin, D. R. The Basis of Aryl Substituent Effects on Charge-Transfer Absorption Intensities. *Inorg. Chem.* **1986**, *25* (9), 1329–1333. https://doi.org/10.1021/ic00229a008.

(13) Preston, H. S.; Kennard, C. H. L. Stereochemistry of Rigid Chelate-Metal Complexes. Part II. Crystal Structure of Di-μ-Chloro-Sym-Trans-Dichloro-Bis-(2,9-Dimethyl-1,10- Phenanthroline)Dinickel(II)-2-Chloroform. *J. Chem. Soc. A Inorganic, Phys. Theor. Chem.* **1969**, 2682–2685. https://doi.org/10.1039/J19690002682.

(14) Bănică, F. G. *Chemical Sensors and Biosensors: Fundamentals and Applications*; 2012. https://doi.org/10.1002/9781118354162.

(15) Dobson, P. J. Nanosensors: Physical, Chemical, and Biological, by Vinod Kumar Khanna. *Contemp. Phys.* **2012**, *53* (4), 391–392. https://doi.org/10.1080/00107514.2012.689351.

(16) Wohltjen, H.; Barger, W. R.; Snow, A. W.; Jarvis, N. L. Vapor-Sensitive Chemiresistor Fabricated With Planar Microelectrodes and a Langmuir-Blodgett Organic Semiconductor Film. *IEEE Trans. Electron Devices* **1985**, *ED-32* (7), 1170–1174. https://doi.org/10.1109/t-ed.1985.22095.

(17) Partoens, B.; Peeters, F. M. From Graphene to Graphite: Electronic Structure around the K Point. *Phys. Rev. B - Condens. Matter Mater. Phys.* **2006**. https://doi.org/10.1103/PhysRevB.74.075404.

(18) Graphite and Precursors. *Choice Rev. Online* **2001**, *38* (11), 38-6194-38–6194. https://doi.org/10.5860/choice.38-6194.

(19) Deprez, N.; McLachlan, D. S. The Analysis of the Electrical Conductivity of Graphite Conductivity of Graphite Powders during Compaction. *J. Phys. D. Appl. Phys.* **1988**, *21* (1), 101–107. https://doi.org/10.1088/0022-3727/21/1/015.

(20) Hernandez, Y.; Nicolosi, V.; Lotya, M.; Blighe, F. M.; Sun, Z.; De, S.; McGovern, I. T.; Holland, B.; Byrne, M.; Gun'ko, Y. K.; Boland, J. J.; Niraj, P.; Duesberg, G.; Krishnamurthy, S.; Goodhue, R.; Hutchison, J.; Scardaci, V.; Ferrari, A. C.; Coleman, J. N. High-Yield Production of Graphene by Liquid-Phase Exfoliation of Graphite. *Nat. Nanotechnol.* **2008**, *3* (9), 563–568. https://doi.org/10.1038/nnano.2008.215.

(21) Donkersloot, M. C. A. The Structure of Binary Liquids. The Kirkwood-Buff Theory of Liquid Mixtures, Illustrated on the Basis of the Systems Water/Methanol, Water/Ethanol, and Cyclohexane/2,3-Dimethylbutane, as a Link between Thermodynamic Data and x-Ray and Neutron Scattering . *J. Solution Chem.* **1979**, *8* (4), 293–307. https://doi.org/10.1007/BF00650747.

(22) Lin, S.; Shih, C. J.; Strano, M. S.; Blankschtein, D. Molecular Insights into the Surface Morphology, Layering Structure, and Aggregation Kinetics of Surfactant-Stabilized Graphene Dispersions. *J. Am. Chem. Soc.* **2011**, *133* (32), 12810–12823. https://doi.org/10.1021/ja2048013.

(23) Hohenberg, P.; Kohn, W. Inhomogeneous Electron Gas. *Phys. Rev.* **1964**, *136* (3B). https://doi.org/10.1103/PhysRev.136.B864.

(24) Kohn, W.; Sham, L. J. Self-Consistent Equations Including Exchange and Correlation Effects. *Phys. Rev.* **1965**, *140* (4A). https://doi.org/10.1103/PhysRev.140.A1133.

(25) Becke, A. D. Perspective: Fifty Years of Density-Functional Theory in Chemical Physics. *J. Chem. Phys.* **2014**, *140* (18). https://doi.org/10.1063/1.4869598.

(26) Becke, A. D. Density-Functional Exchange-Energy Approximation with Correct Asymptotic Behavior. *Phys. Rev. A* **1988**, *38* (6), 3098–3100. https://doi.org/10.1103/PhysRevA.38.3098.

(27) Sherrill, C. An Introduction to Hartree-Fock Molecular Orbital Theory http://vergil.chemistry.gatech.edu/courses/chem6485/pdf/hf-intro.pdf.

(28) Lee, C.; Yang, W.; Parr, R. G. Development of the Colle-Salvetti Correlation-Energy Formula into a Functional of the Electron Density. *Phys. Rev. B* **1988**, *37* (2), 785–789. https://doi.org/10.1103/PhysRevB.37.785.

(29) Boys, S. F. A General Method of Calculation for the Stationary States of Any Molecular System. *Proc.*

R. Soc. Lond. A. Math. Phys. Sci. **1950**, *200* (1063), 542–554.

(30) Ditchfield, R.; Hehre, W. J.; Pople, J. A. Self-Consistent Molecular-Orbital Methods. IX. An Extended Gaussian-Type Basis for Molecular-Orbital Studies of Organic Molecules. *J. Chem. Phys.* **1971**, *54* (2), 720–723. https://doi.org/10.1063/1.1674902.

(31) Hay, P. J.; Wadt, W. R. Ab Initio Effective Core Potentials for Molecular Calculations. Potentials for K to Au Including the Outermost Core Orbitale. *J. Chem. Phys.* **1985**, *82* (1), 299–310. https://doi.org/10.1063/1.448975.

(32) Nathan, A. J.; Scobell, A. *How China Sees America*; 2012; Vol. 91. https://doi.org/10.1017/CBO9781107415324.004.

(33) Beer. Bestimmung Der Absorption Des Rothen Lichts in Farbigen Flüssigkeiten. *Ann. Phys.* **1852**, *162* (5), 78–88. https://doi.org/10.1002/andp.18521620505.

(34) Seah, M. P.; Dench, W. A. Quantitative Electron Spectroscopy of Surfaces: A Standard Data Base for Electron Inelastic Mean Free Paths in Solids. *Surf. Interface Anal.* **1979**, *1* (1), 2–11. https://doi.org/10.1002/sia.740010103.

(35) Powell, C. J.; Larson, P. E. Quantitative Surface Analysis by X-Ray Photoelectron Spectroscopy. In *Applications of Surface Science*; 1978; Vol. 1, pp 186–201. https://doi.org/10.1016/0378-5963(78)90014-4.

(36) Krebs, F. C.; Krebs, F. C.; JÃ¸rgensen, M.; Bundgaard, E.; de Bettignies, R.; Krebs, F. C.; Katz, E. A.; Norrman, K.; Bundgaard, E.; Krebs, F. C.; Norrman, K.; Cros, S.; de Bettignies, R.; Firon, M.; Krebs, F. C.; Aernouts, T.; Cros, S.; Krebs, F. C.; Krebs, F. C. Lifetime and Stability Studies. In *Polymer Photovoltaics: A Practical Approach*; 2010. https://doi.org/10.1117/3.737854.ch4.

(37) *Practical Surface Analysis By Auger and X-Ray Photoelectron Spectroscopy.*; 1983.

(38) Sen, S. K.; Sen, S.; Bauer, C. L. Determination of the Oxidation States of Tin by Auger Electron Spectroscopy. *Thin Solid Films* **1981**, *82* (2), 157–164. https://doi.org/10.1016/0040-6090(81)90439-9.

(39) Barlow, S. M.; Raval, R. Complex Organic Molecules at Metal Surfaces: Bonding, Organisation and Chirality. *Surface Science Reports*. 2003, pp 201–341. https://doi.org/10.1016/S0167-5729(03)00015-3.

(40) Satyanarayana, N.; Sinha, S. K. Tribology of PFPE Overcoated Self-Assembled Monolayers Deposited on Si Surface. *J. Phys. D. Appl. Phys.* **2005**. https://doi.org/10.1088/0022-3727/38/18/029.

(41) Zubiarrain-Laserna, A.; Kruse, P. Review—Graphene-Based Water Quality Sensors. *J. Electrochem. Soc.* **2020**, *167* (3), 037539. https://doi.org/10.1149/1945-7111/ab67a5.

(42) Hanaor, D. A. H.; Ghadiri, M.; Chrzanowski, W.; Gan, Y. Scalable Surface Area Characterization by Electrokinetic Analysis of Complex Anion Adsorption. *Langmuir* **2014**, *30* (50), 15143–15152. https://doi.org/10.1021/la503581e.

(43) Leike, A. Demonstration of the Exponential Decay Law Using Beer Froth. *Eur. J. Phys.* **2002**, *23* (1), 21–26. https://doi.org/10.1088/0143-0807/23/1/304.

(44) THORNE, P. C. L. Kapillarchemie: Eine Darstellung Der Chemie Der Kolloide Und Verwandter Gebiete. *Nature* **1932**, *130* (3293), 866–866. https://doi.org/10.1038/130866a0.

(45) Swan, G. A. The Chemistry of Heterocyclic Compounds, Phenazines. *B. Rev.* **2007**, 718. https://doi.org/10.1002/9780470186602.

(46) Sun, X.; Dong, S.; Wang, E. Formation of O-Phenylenediamine Oligomers and Their Self-Assembly into One-Dimensional Structures in Aqueous Medium. *Macromol. Rapid Commun.* **2005**. https://doi.org/10.1002/marc.200500502.

(47) Ensafi, A. A.; Khayamian, T.; Karbasi, M. H. On-Line Preconcentration System for Lead(II) Determination in Waste Water by Atomic Absorption Spectrometry Using Active Carbon Loaded with Pyrogallol Red. *Anal. Sci.* **2003**, *19* (6), 953–956. https://doi.org/10.2116/analsci.19.953.

(48) Goswami, S.; Chakrabarty, R. Highly Selective Colorimetric Fluorescent Sensor for Pb2+. *European J. Org. Chem.* **2010**, No. 20, 3791–3795. https://doi.org/10.1002/ejoc.201000142.

(49) Atala, E.; Velásquez, G.; Vergara, C.; Mardones, C.; Reyes, J.; Tapia, R. A.; Quina, F.; Mendes, M. A.; Speisky, H.; Lissi, E.; Ureta-Zañartu, M. S.; Aspée, A.; López-Alarcón, C. Mechanism of Pyrogallol Red Oxidation Induced by Free Radicals and Reactive Oxidant Species. A Kinetic and Spectroelectrochemistry Study. *J. Phys. Chem. B* **2013**, *117* (17), 4870–4879. https://doi.org/10.1021/jp400423w.

(50) Wu, D.; Huang, W.; Duan, C.; Lin, Z.; Meng, Q. Highly Sensitive Fluorescent Probe for Selective Detection of Hg 2+ in DMF Aqueous Media. *Inorg. Chem.* **2007**, *46* (5), 1538–1540. https://doi.org/10.1021/ic062274e.

(51) Yang, X. F.; Guo, X. Q.; Zhao, Y. B. Development of a Novel Rhodamine-Type Fluorescent Probe to Determine Peroxynitrite. *Talanta* **2002**, *57* (5), 883–890. https://doi.org/10.1016/S0039-9140(02)00120-0.

(52) Yang, Y. K.; Yook, K. J.; Tae, J. A Rhodamine-Based Fluorescent and Colorimetric Chemodosimeter for the Rapid Detection of Hg2+ Ions in Aqueous Media. *J. Am. Chem. Soc.* **2005**, *127* (48), 16760–16761. https://doi.org/10.1021/ja054855t.

(53) Ungnade, H. E. The Effect of Solvents on the Absorption Spectra of Aromatic Compounds. *J. Am. Chem. Soc.* **1953**. https://doi.org/10.1021/ja01098a051.

(54) Li, Q.; Chen, B.; Xing, B. Aggregation Kinetics and Self-Assembly Mechanisms of Graphene Quantum Dots in Aqueous Solutions: Cooperative Effects of PH and Electrolytes. *Environ. Sci. Technol.* **2017**, *51* (3), 1364–1376. https://doi.org/10.1021/acs.est.6b04178.

(55) Kumar, R.; Dvivedi, A.; Bhargava, P. Synthesis and Characterization of a New Photoluminescent Material, Tris-[1-10 Phenanthroline] Aluminium. In *AIP Conference Proceedings*; 2016; Vol. 1728. https://doi.org/10.1063/1.4946075.

(56) Brandt, W. W.; Dwyer, F. P.; Gyarfas, E. C. Chelate Complexes of 1,10-Phenanthroline and Related Compounds. *Chem. Rev.* **1954**, *54* (6), 959–1017. https://doi.org/10.1021/cr60172a003.

(57) Fortune, W. B.; Mellon, M. G. Determination of Iron with O-Phenanthroline: A Spectrophotometric Study. *Ind. Eng. Chem. - Anal. Ed.* **1938**, *10* (2), 60–64. https://doi.org/10.1021/ac50118a004.

(58) Seamer, P. A. Estimation of Mgm. Quantities of Iron in Culture Medium, Using Bathophenanthroline. *Nature* **1959**, *184* (4686), 636–637. https://doi.org/10.1038/184636a0.

(59) Heller, I.; Chatoor, S.; Männik, J.; Zevenbergen, M. A. G.; Dekker, C.; Lemay, S. G. Influence of Electrolyte Composition on Liquid-Gated Carbon Nanotube and Graphene Transistors. *J. Am. Chem. Soc.* **2010**, *132* (48), 17149–17156. https://doi.org/10.1021/ja104850n.

(60) Heller, I.; Chatoor, S.; Männik, J.; Zevenbergen, M. A. G.; Dekker, C.; Lemay, S. G. Influence of Electrolyte Composition on Liquid-Gated Carbon Nanotube and Graphene Transistors. *J. Am. Chem. Soc.* **2010**, *132* (48), 17149–17156. https://doi.org/10.1021/ja104850n.

(61) Durand, J.; Zangrando, E.; Stener, M.; Fronzoni, G.; Carfagna, C.; Binotti, B.; Kamer, P. C. J.; Müller, C.; Caporali, M.; Van Leeuwen, P. W. N. M.; Vogt, D.; Milani, B. Long-Lived Palladium Catalysts for CO/Vinyl Arene Polyketones Synthesis: A Solution to Deactivation Problems. *Chem. - A Eur. J.* **2006**, *12* (29), 7639–7651. https://doi.org/10.1002/chem.200501047.

(62) Mazumdar, P.; Das, D.; Sahoo, G. P.; Salgado-Morán, G.; Misra, A. Aggregation Induced Emission Enhancement from Bathophenanthroline Microstructures and Its Potential Use as Sensor of Mercury Ions in Water. *Phys. Chem. Chem. Phys.* **2014**, *16* (13), 6283–6293. https://doi.org/10.1039/c3cp54563f.

(63) Patel, R. N.; Singh, Y.; Singh, Y. P.; Butcher, R. J.; Kamal, A.; Tripathi, I. P. Copper(II) and Nickel(II) Complexes with N′-[(Z)-Phenyl(Pyridin-2-Yl)Methylidene]Acetohydrazide: Synthesis, Crystal Structures, DFT Calculations and Antioxidant Effects. *Polyhedron* **2016**, *117*, 20–34. https://doi.org/10.1016/j.poly.2016.05.036.

(64) Yoshida, H. Electron Transport in Bathocuproine Interlayer in Organic Semiconductor Devices. *J. Phys. Chem. C* **2015**, *119* (43), 24459–24464. https://doi.org/10.1021/acs.jpcc.5b07548.

(65) Ashtari, P.; Wang, K.; Yang, X.; Huang, S.; Yamini, Y. Novel Separation and Preconcentration of Trace Amounts of Copper(II) in Water Samples Based on Neocuproine Modified Magnetic Microparticles. *Anal. Chim. Acta* **2005**, *550* (1–2), 18–23. https://doi.org/10.1016/j.aca.2005.06.048.

(66) Shariati, S.; Golshekan, M. Dispersive Liquid-Liquid Microextraction of Copper Ions as Neocuproine Complex in Environmental Aqueous Samples. *Acta Chim. Slov.* **2011**, *58* (2), 311–317.

(67) Chae, M.; Yoon, J.; Czarnik, A. W. Chelation-Enhanced Fluorescence Chemosensing of Pb(II), an Inherently Quenching Metal Ion. *J. Mol. Recognit.* **1996**, *9* (4), 297–303. https://doi.org/10.1002/(sici)1099-1352(199607)9:4<297::aid-jmr335>3.3.co;2-y.

(68) Xue, H.; Tang, X. J.; Wu, L. Z.; Zhang, L. P.; Tung, C. H. Highly Selective Colorimetric and Electrochemical Pb2+ Detection Based on TTF-π-Pyridine Derivatives. *J. Org. Chem.* **2005**, *70* (24), 9727–9734. https://doi.org/10.1021/jo051091r.

(69) Rundle, C. C. A Beginners Guide to Ion-Selective Electrode Measurements. *Data Process.* **2011**, No. May 2000, 1–30.

(70) Güçlü, K.; Sözgen, K.; Tütem, E.; Özyürek, M.; Apak, R. Spectrophotometric Determination of Ascorbic Acid Using Copper(II)-Neocuproine Reagent in Beverages and Pharmaceuticals. *Talanta* **2005**, *65* (5), 1226–1232. https://doi.org/10.1016/j.talanta.2004.08.048.

(71) Gallego, M.; Silva, M.; Valcárcel, M. Determination of Nitrate and Nitrite by Continuous Liquid-Liquid Extraction with a Flow-Injection Atomic-Absorption Detection System. *Fresenius' Zeitschrift für Anal. Chemie* **1986**, *323* (1), 50–53. https://doi.org/10.1007/BF00531131.

(72) Hassan, S. S. M.; Rizk, N. M. H. Miniaturized Graphite Sensors Doped with Metal-Bathophenanthroline Complexes for the Selective Potentiometric Determination of Uric Acid in Biological Fluids. *Analyst* **1997**, *122* (8), 815–819. https://doi.org/10.1039/a701038i.

APPENDIX

SUPPLEMENTAL MATERIAL

Chemiresistive detection of silver ions in aqueous media

Johnson Dalmieda[1], Ana Zubiarrain-Laserna[1], Devanjith Ganepola[1], P. Ravi Selvaganapathy[2], Peter Kruse[1]*

[1]*Department of Chemistry and Chemical Biology, McMaster University, Hamilton L8S 4M1, Canada*

[2]*Department of Mechanical Engineering, McMaster University, Hamilton L8S 4M1, Canada*

*email: pkruse@mcmaster.ca

Figure S1. Nitrogen 1s high resolution XPS spectra of bathocuproine (left), and the silver-bathocuproine complex (right).

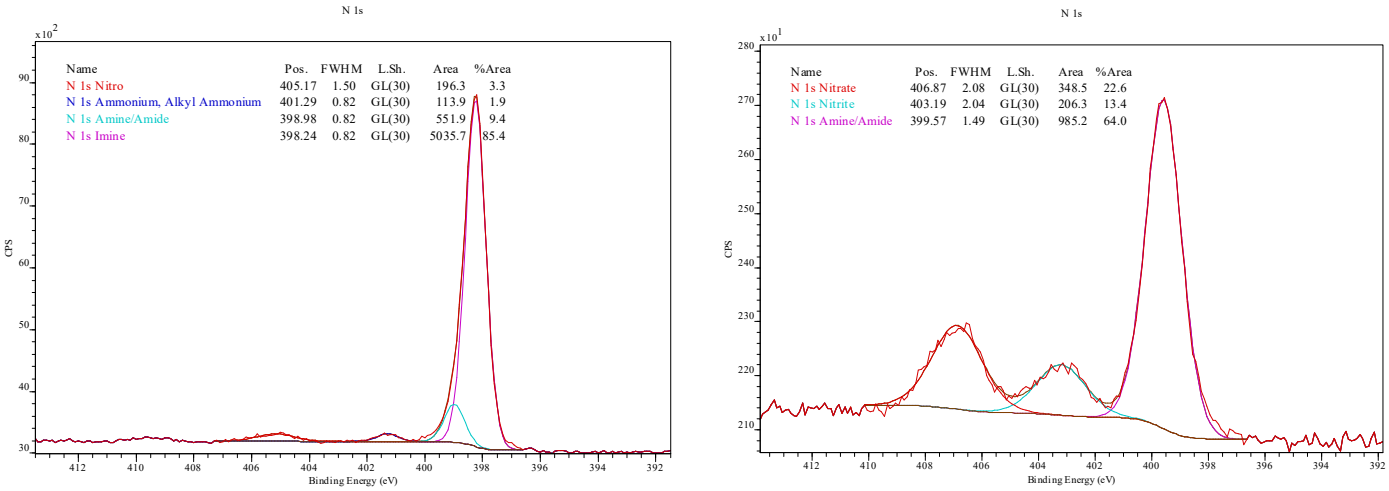

Figure S2. Nitrogen 1s high resolution XPS spectra of the functionalized sensor by itself (left), and the functionalized sensor exposed to silver (right).

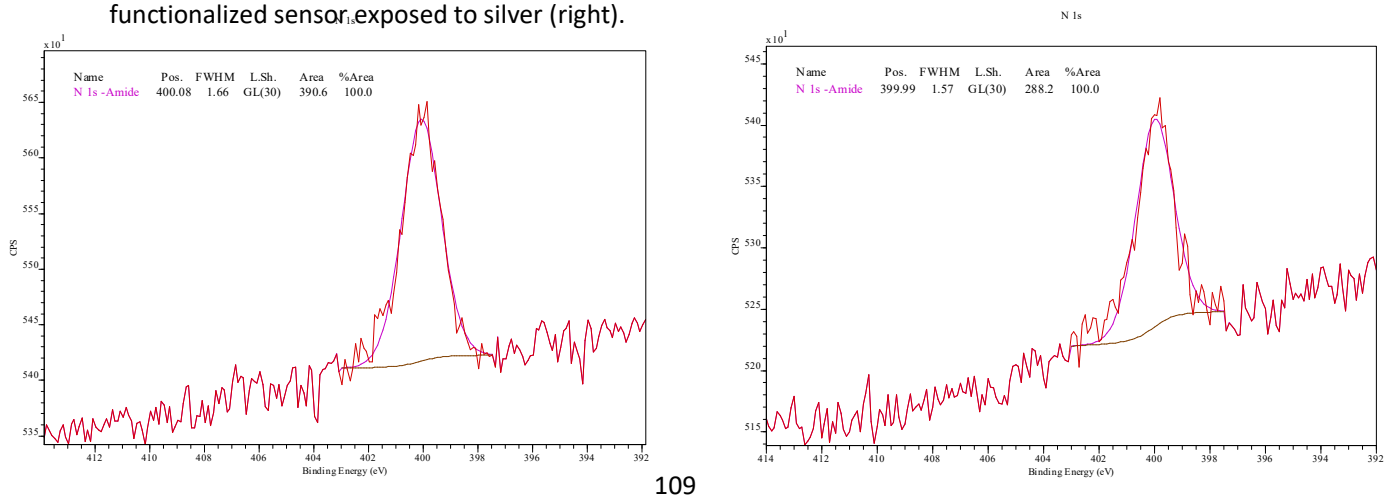

Figure S3. Silver 3d high resolution XPS spectra and Ag MVV Auger peak of the non-functionalized sensor exposed to silver (left), and the functionalized sensor exposed to silver (right).

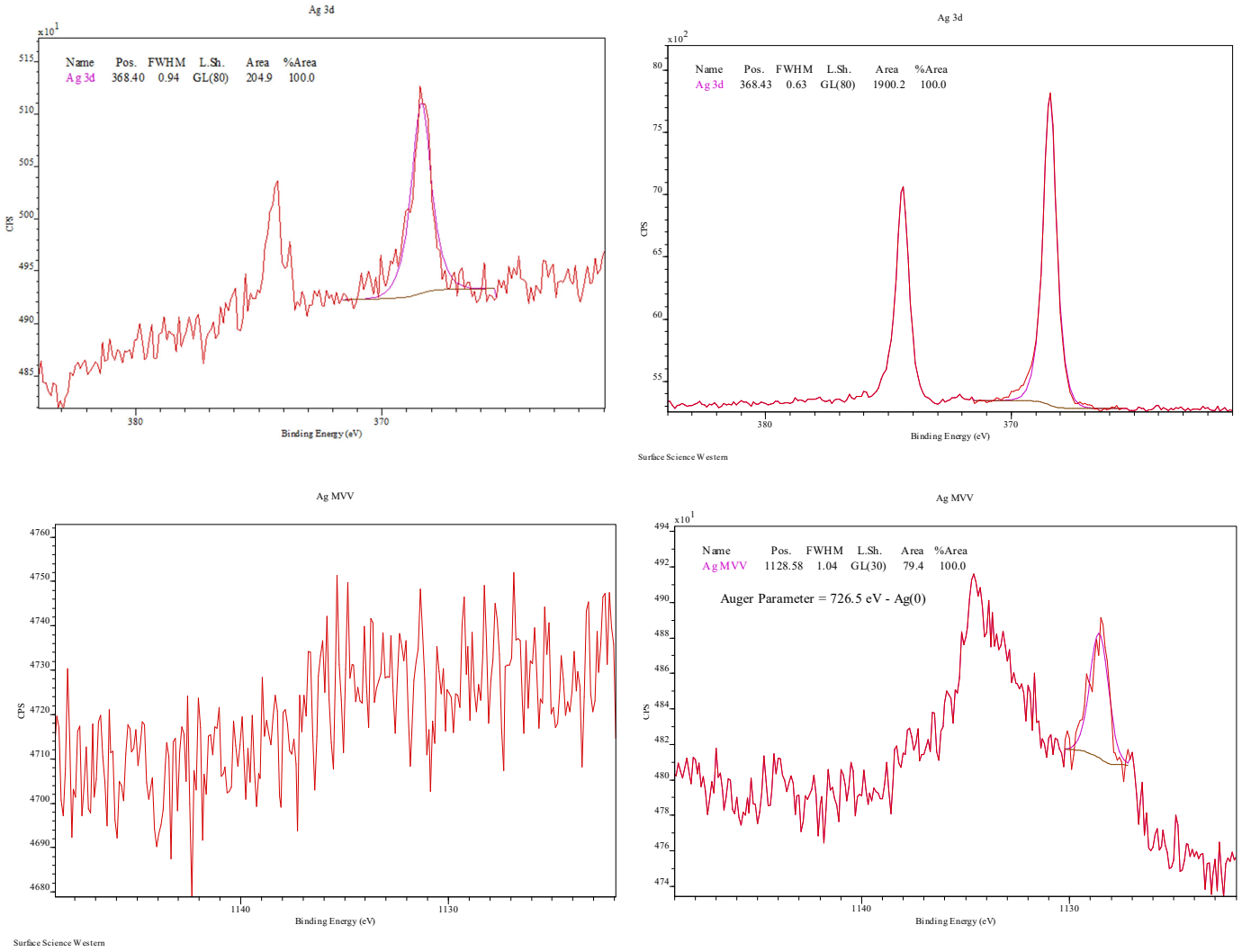

Figure S4. Sensor responses for four bathocuproine functionalized sensors (BC1, BC2, BC3, and BC4), as well as two non-functionalized (blank) sensors. X axes are labelled in the format hour:minutes:seconds. Y axes units are nA (absolute current through the sensor film).

Figure S5. Pictures of the functionalized (left) and the non-functionalized (right) sensor after exposure to 1 ppm silver (I) nitrate in aqueous solution. Metallic silver particles on the non-functionalized sensor film give it a glittery appearance.

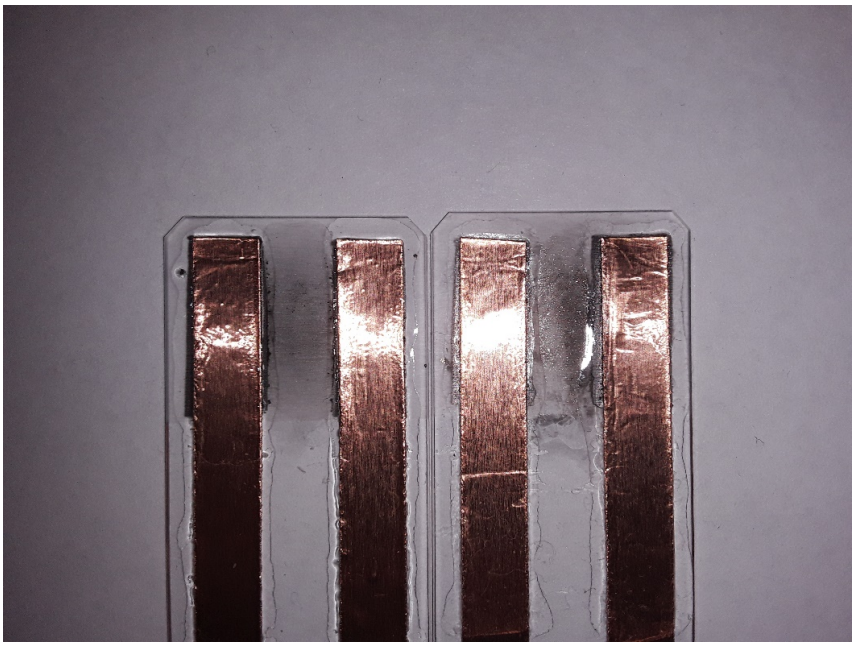

Figure S6. Deposition optimization process of the bathocuproine onto the sensor. The percentage represents the saturation of the bathocuproine in either methanol (MeOH) or acetonitrile (MeCN) solution. X axes are labelled in the format hour:minutes:seconds. Y axes units are nA (absolute current through the sensor film).

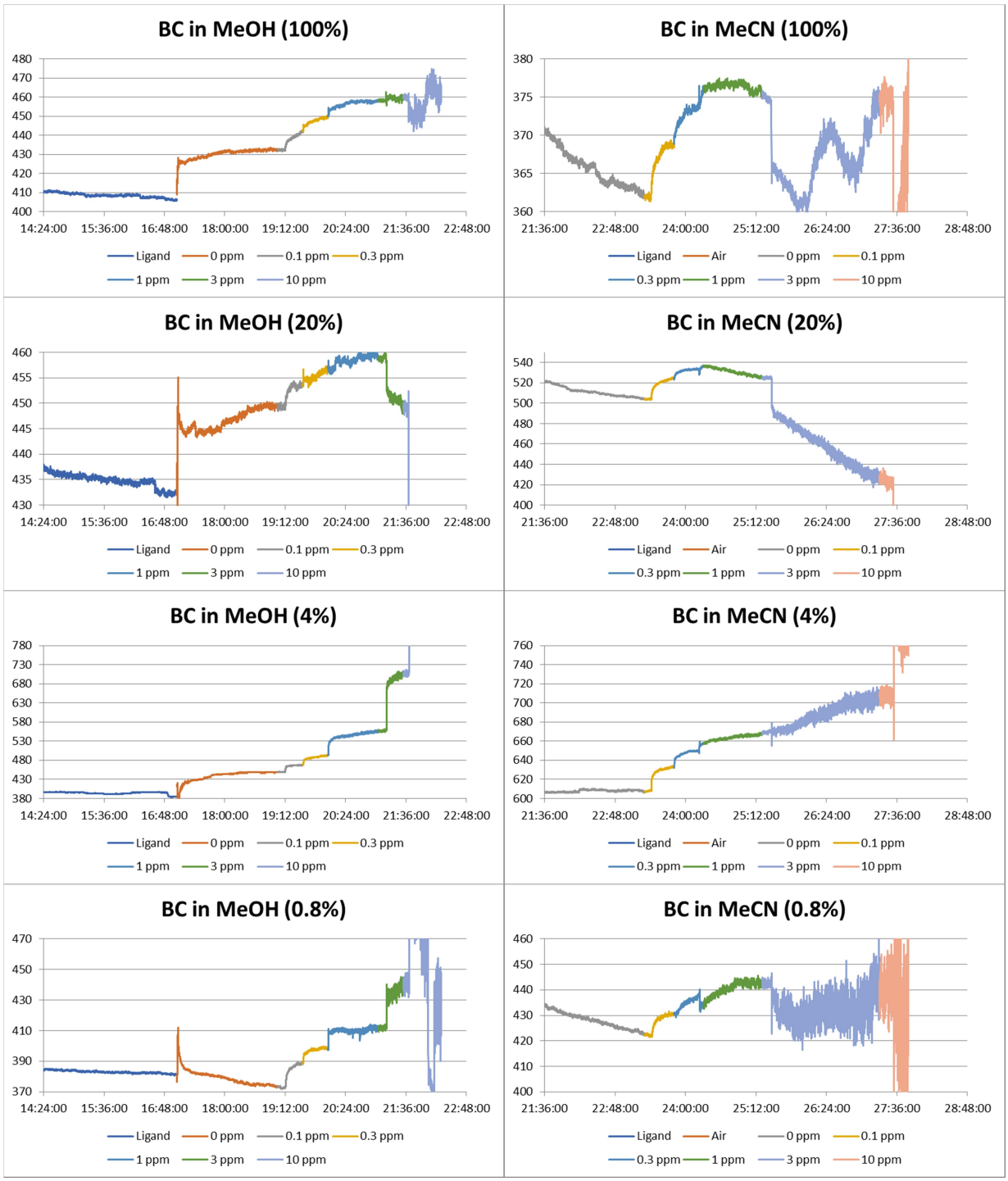

Figure S7. Resetting the four functionalized sensors (BC1, BC2, BC3, and BC4) with pH 3 HNO_3. X axes are labelled in the format hour:minutes:seconds. Y axes units are nA (absolute current through the sensor film).

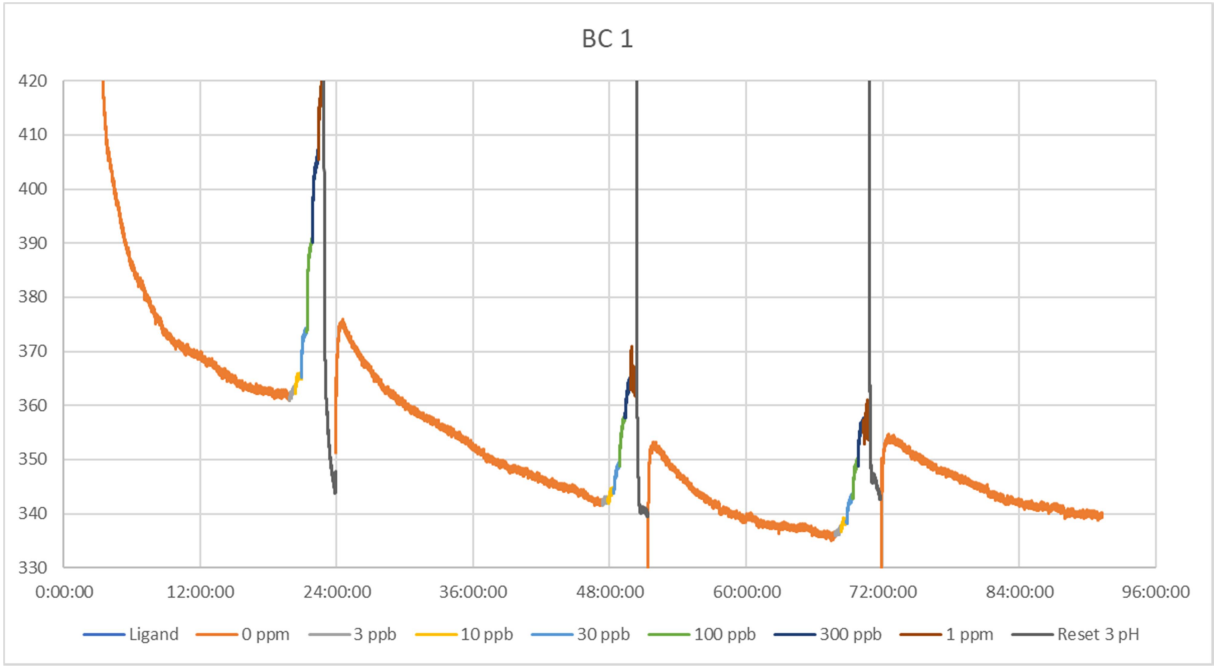

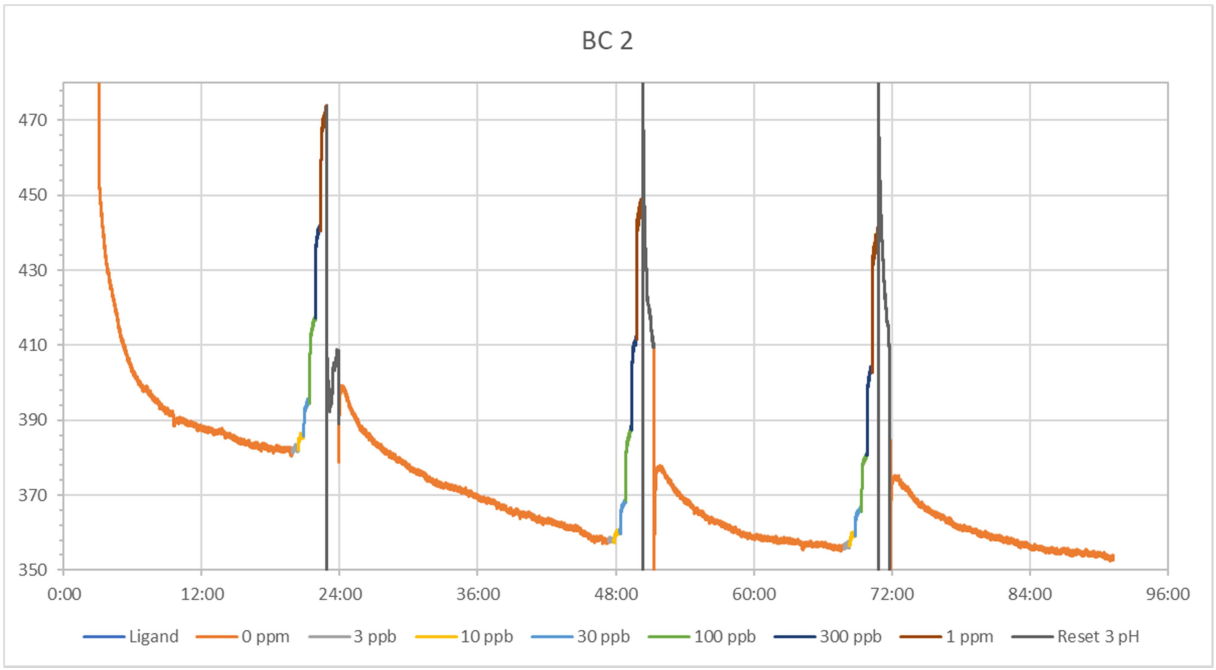

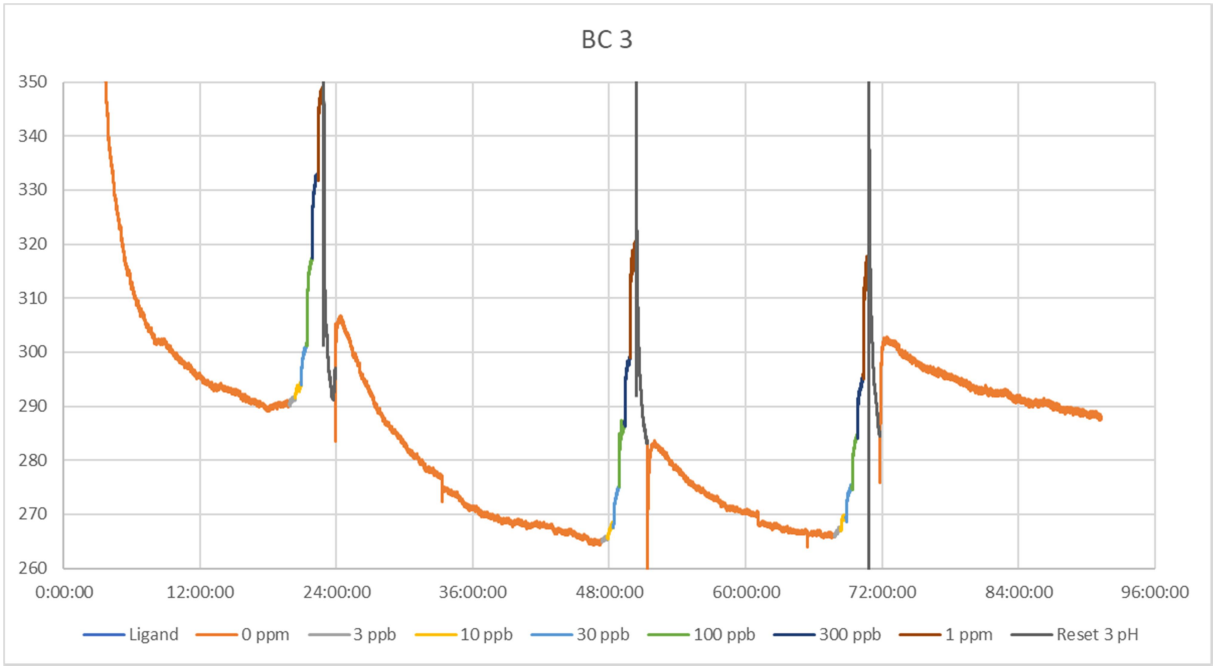
BC 3
350
340
330
320
310
300
290
280
270
260
0:00:00
12:00:00
24:00:00
36:00:00
48:00:00
60:00:00
72:00:00
84:00:00
96:00:00
Ligand
0 ppm
3 ppb
10 ppb
30 ppb
100 ppb
300 ppb
1 ppm
Reset 3 pH

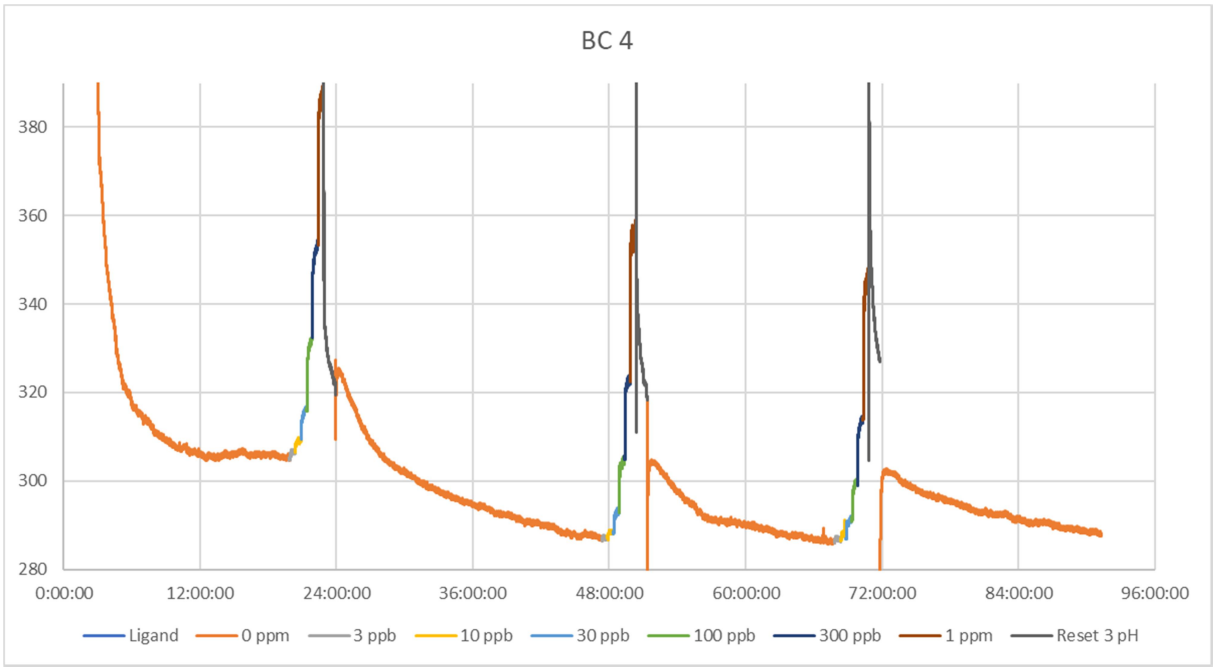
BC 4
380
360
340
320
300
280
0:00:00
12:00:00
24:00:00
36:00:00
48:00:00
60:00:00
72:00:00
84:00:00
96:00:00
Ligand
0 ppm
3 ppb
10 ppb
30 ppb
100 ppb
300 ppb
1 ppm
Reset 3 pH

Figure S8. The linearized response of the Ag^+ sensor. Note that this plot is not appropriate for calibration, its use is to determine the linear range of the sensor.

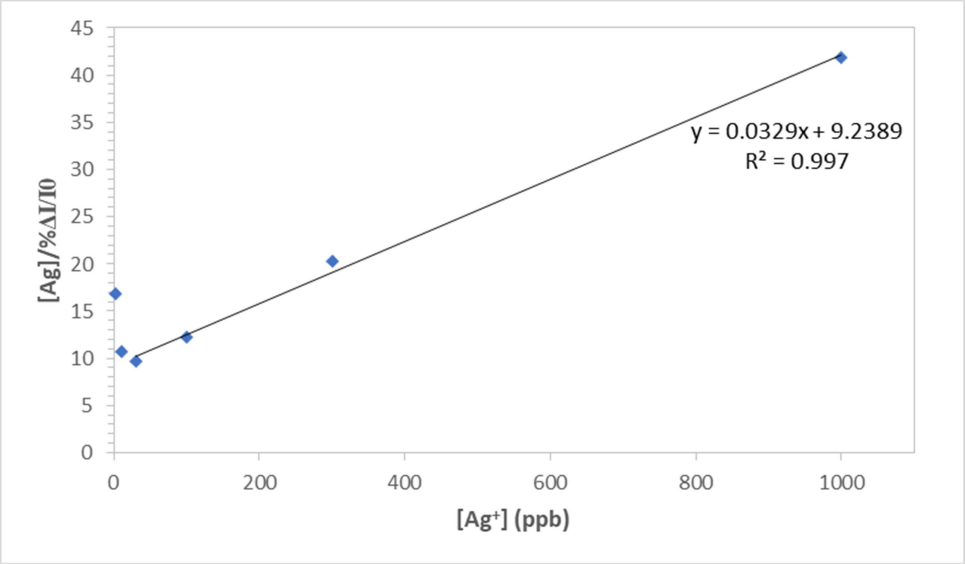

Figure S9. Three replicates of a neocuproine sensor and its response to both copper (II) and silver (I).